KU LEUVEN

FACULTEIT
INGENIEURSWETENSCHAPPEN

Time Domain Reflectometry (TDR) for detecting leakage damage in large engineering structures

Ruben Windey

Academiejaar 2017 – 2018

Master of Science in de ingenieurswetenschappen: materiaalkunde

KU LEUVEN

FACULTEIT INGENIEURSWETENSCHAPPEN

Time Domain Reflectometry (TDR) for detecting leakage damage in large engineering structures

Ruben Windey

Academiejaar 2017 – 2018

Preface

If we knew what it was we were doing, it would not be called research, would it? - A. Einstein

At the moment of writing, I never realised how close the finish line of my student career is right now. Five years ago, I started my incredible journey at the Faculty of Engineering of KU Leuven. By living in the far West(-Vlaanderen), the weekly expedition to Leuven was sometimes a more challenging experience than my lectures and projects as an engineering student. My friends and family often asked me: why didn't you choose to go to study in Ghent, it would have saved you a lot of time and travel misery. Each time I then replied: because personally I prefer the educational mentality and study supervision given in Leuven. After five years, I truly can state this was the best choice I ever made. Maybe using the word best is not completely correct, because this was reserved to my choice for our beloved Department of Materials Engineering. I met numerous fantastic people, participated in a bunch of socially and educationally enriching organisations and discovered engineering could really be considered as a way-of-life instead of just being some study experience. I got the chance to elaborate my research skills during the Honours Program of our Faculty by which I realised my future career would rather be in academia than at a desk or industrial plant. This thesis let me further experience how it feels to participate in on-going research and definitely strengthened my choice to start a PhD next year if possible.

However all these choices and experiences would not have been possible without the support and guidance of several persons. I am grateful to prof. Ingrid De Wolf and prof. Jan Fransaer for their intermediate feedback on my thesis progression. Special thanks go to my thesis supervisor prof. Martine Wevers, who helped me to see the bigger picture of my thesis research and to not get lost too much into details. Her personal and intensive supervision during my first project within the Honours Program was priceless and convinced me to choose for the Master of Materials Engineering. Also Johan Vanhulst, Wout Veulemans, Thomas Lapauw and Sevilia Sunetchiieva deserve a special mention for their valuable support to my thesis. Tom Van der Donck is sincerely acknowledged for providing numerous microscopic images, they could each of them be called small pieces of art. A special thank goes also to Alessia Gennaro and prof. Michael Wübbenhorst for the use of the equipment to perform dielectric spectroscopy at the Department of Physics. The obtained data were essential for a complete understanding of the sensor behaviour. Maybe the most important person to deserve a word of thank is my daily mentor and supervisor dr. Helge Pfeiffer. His ideas and suggestions were limitless and after each of our meetings, new directions and inspirations for my thesis research arose. Without his experience and endless feedback, my thesis would today not have reached the results summarised in the next chapters.

Three other groups of persons also have to mentioned. First, I would like to thank my parents for the study opportunities they offered me and for their support to persevere in my thesis research, which is, as they often said, a sort of final business card of my study career. Also my fellow Materials Engineering students Nick Goossens and Vincent Feyen deserve a special acknowledgement for the numerous discussions we had on our thesis research or during the lectures and exam period. Finally, I would like to thank my (engineering) friends to restore the study-life balance during this intensive period of thesis research.

Ruben Windey

Table of contents

Abstract

During previous research, percolation-based PVA/TiCN and silicone/graphite sensors have been designed and tested at the Department of Materials Engineering at KU Leuven for the detection of water and kerosene leakages. An approximately exponential increase of the DC resistance at the lyotropic percolation threshold allowed a fuse-like detection of the leakage. However, the localisation of the leakage along the sensor length was not possible and hence, the feasibility of a combination with the simple, low-cost and fast nondestructive Time domain reflectometry (TDR) technique was studied within this thesis to localise the leakage spot.

Detection and localisation of multiple leakage spots along both sensors was possible. The differential evolution of the sensor's TDR voltage was monitored during each experiment and compared to the dry sensor. Leakage spot sizes of 10 and 4 cm were clearly detected for respectively the water and kerosene sensor. The proposed sigmoidal fitting method of the differential voltage allowed accurate localisation of the leakage spots. When two leakage spots were simultaneously applied at the sensor, the differential peak for each leakage spot could be distinguished and localised.

A lumped circuit model based on the dimensional and electromagnetic properties of the sensor's constituting layers accurately predicted the reflection of the applied voltage wave at both the sensor entrance and the applied leakage spot. The observed negative differential TDR peak for a water leakage was assumed to be caused by a local increase in the permittivity of PVA. For the kerosene sensor, a positive differential TDR peak was seen, which was attributed to the fuse-like increase of the sensor's resistance due to a kerosene-induced disruption of the percolative graphite network.

TDR was concluded to offer a sensitive detection and accurate localisation solution for leakage monitoring in large engineering structures like fuselages of aircrafts and pipelines. Its combination with DC resistance monitoring allows the lay-out of a distributed sensor network in these structures for low-cost, flexible and continuous Structural Health Monitoring. The sensor's low materials cost of approximately € 1-2/m makes it clearly advantageous over the currently available commercial leakage sensors.

List of figures

List of tables

List of symbols

A	area of cross-section	[m²]
$b(y)$	local width as function of the y-coordinate	[m]
$\vec{B}$	magnetic flux intensity	[T]
c	velocity of light	[m/s]
C'	equivalent capacitance	[F/m]
d	diameter of the wire	[m]
d_{fault}	position of the fault (normally relative to the cable entrance)	[m]
d_i	distance of the ith cable part	[m]
D	distance between the centres of two wires	[m]
$\vec{D}$	electric flux density	[C/m²]
e	exponential function	[-]
e_i	distance error of the ith cable part	[m]
$\vec{E}$	electric field intensity	[V/m]
E_n	normal component of electric field intensity	[V/m]
E_p	tangential component of electric field intensity	[V/m]
f	frequency	[Hz]
f_{eff}	effective frequency	[Hz]
f_{rel}	relaxation frequency	[Hz]
f_r	resonance frequency	[Hz]
f_{3dB}	frequency for which an attenuation of 3 dB of the pulse DC voltage occurs	[Hz]
$F(f)$	Fourier coefficient for frequency f	[V]
G'	equivalent conductance	[S/m]
$\vec{H}$	magnetic field intensity	[A/m]
H_n	normal component of magnetic field intensity	[A/m]
H_p	tangential component of magnetic field intensity	[A/m]
$i(z,t)$	current	[A]
$I(z)$	phasor notation for the spatial-dependent component of the current amplitude	[A]
I_0^+	forward-propagating component of a current wave	[A]

I_0^-	backward-propagating component of a current wave	[A]
j	imaginary unit	[-]
$\vec{J}$	current density	[A/m^2]
l	length	[m]
l_d	pitch length	[m]
L	length of the probe	[m]
L'	equivalent inductance	[H/m]
M_W	molecular weight	[g/mole]
$\vec{M}$	magnetisation density	[A/m]
n	index of refraction	[-]
n	exponent	[-]
N	index of random element (>0)	[-]
p_i	parameter of the sigmoidal curve	[-]
$\vec{P}$	electric polarisation density	[C/m^2]
r_{E_n}	reflection coefficient of normal component of electric field intensity	[-]
r_{E_p}	reflection coefficient of parallel component of electric field intensity	[-]
r_{H_n}	reflection coefficient of normal component of magnetic field intensity	[-]
r_{H_p}	reflection coefficient of parallel component of magnetic field intensity	[-]
R_L	load resistance	[Ω]
R_s	generator resistance	[Ω]
R'	equivalent resistance	[Ω/m]
$R(\theta)$	radius as function of the polar angle	[m]
RH	relative humidity	[%]
RH$_{gt}$	relative humidity for lyotropic glass transition	[%]
RH$_{pt}$	relative humidity for lyotropic percolation threshold	[%]
$\mathfrak{R}$	real part of a complex property	[-]
s	separation between the centers of two wires	[m]
S	modelled property	[-]
t	exponent of power law	[-]
t_{E_n}	transmission coefficient of normal component of electric field intensity	[-]
t_{E_p}	transmission coefficient of parallel component of electric field intensity	[-]

t_{H_n}	transmission coefficient of normal component of magnetic field intensity	[-]
t_{H_p}	transmission coefficient of parallel component of magnetic field intensity	[-]
t_r	rise time	[s]
$t_{r,generator}$	rise time of the wave generator	[s]
$t_{r,oscilloscope}$	rise time of the oscilloscope	[s]
$t_{r,system}$	total rise time of the TDR system	[s]
t_{TOF}	time of flight/round trip time (normally relative to the cable entrance)	[s]
$t_{10-90\%}$	10-90 % (of the wave voltage amplitude) rise time	[s]
T	transmission coefficient for transmission lines	[-]
T	temperature	[° C]
v	wave propagation velocity	[m/s]
$v(z,t)$	voltage	[V]
v_p	phase velocity	[m/s]
$V(z)$	phasor notation for the spatial-dependent component of the voltage amplitude	[V]
V_0^+	forward-propagating component of a voltage wave	[V]
V_0^-	backward-propagating component of a voltage wave	[V]
ΔV	voltage difference	[V]
x	x-coordinate	[m]
$\bar{x}$	x-coordinate of the centre of mass	[m]
x_V	volume fraction	[-]
y	y-coordinate	[m]
$\bar{y}$	y-coordinate of the centre of mass	[m]
Z_L	load impedance	[Ω]
Z_0	characteristic impedance	[Ω]
α	attenuation constant	[Np/m]
α_s	inclination angle	[rad]
β	phase constant	[rad/m]
γ	propagation constant	[Np/m]
Γ	reflection coefficient for transmission lines	[-]
$\Gamma_{corrected}$	corrected reflection coefficient measured at the cable entrance because of the cable losses	[-]
$\Gamma_{measured}$	reflection coefficient measured at the cable entrance	[-]

Γ_z	spatial-dependent reflection coefficient for transmission lines	[-]
$|\Gamma|$	magnitude of the reflection coefficient for transmission lines	[-]
δ	skin depth	[m]
δl	length error	[m]
δ_{res}	time resolution	[s]
δt	time error	[s]
δv	velocity error	[m/s]
$\tan|\delta|$	loss tangent	[-]
Δz	differential element of length	[m]
ε	permittivity	[F/m]
ε_A	permittivity of air	[F/m]
ε_{BW}	permittivity of bound water	[F/m]
ε_C	permittivity of the composite	[F/m]
ε_{eff}	effective permittivity	[F/m]
ε_f	permittivity of the filler	[F/m]
ε_{FW}	permittivity of free water	[F/m]
ε_m	permittivity of the matrix	[F/m]
ε_r	relative permittivity	[-]
ε_S	relative static dielectric permittivity/dielectric constant	[-]
ε_S	permittivity of solid particles	[F/m]
$\varepsilon_{S,matrix}$	dielectric constant of the matrix	[-]
ε_W	permittivity of water	[F/m]
ε_∞	relative dielectric permittivity at infinite frequency	[-]
ε'	real component of the permittivity	[F/m]
ε''	imaginary component of the permittivity	[F/m]
ε_0	permittivity of free space	[8.85 x 10^{-12} F/m]
η	intrinsic impedance	[V/A]
θ_Γ	phase angle of the reflection coefficient for transmission lines	[-]
λ	wavelength	[m]
λ_{min}	minimal wavelength present in the used wave	[m]
μ	magnetic permeability	[H/m]
μ_r	relative magnetic permeability	[-]
μ'	real component of the magnetic permeability	[H/m]

μ''	imaginary component of the magnetic permeability	[H/m]
μ_0	magnetic permeability of free space	[4π x 10^{-7} H/m]
ρ	electric charge density	[C/m^3]
σ	conductivity of the conductor	[S/m]
$\sigma_{dielectric}$	conductivity of the dielectric	[S/m]
σ_{filler}	conductivity of the filler	[S/m]
σ_{matrix}	conductivity of the matrix	[S/m]
ϕ	angle of incidence	[rad]
ϕ	volume fraction of the filler	[rad]
ϕ_A	volume fraction of air	[-]
ϕ_C	volume fraction at the percolation threshold	[-]
ϕ_{FW}	volume fraction of free water	[-]
ϕ_S	volume fraction of solid particles	[-]
ϕ_W	volume fraction of water	[-]
ψ	angle of refraction	[rad]
ω	angular frequency	[rad/s]

Abbreviations

DUT	device under test
EDS	Energy Dispersive Spectroscopy
EM	electromagnetic
EOTPR	electro-optical terahertz pulse reflectometry
FDR	frequency domain reflectometry
FEM	finite element modelling
FEP	fluorinated ethylene propylene
GPR	Ground Penetrating Radar
IC	integrated circuit
MWCNT	multiwall carbon nanotube
NDT	nondestructive testing
OTDR	optical time domain reflectometry
PA	polyamide
PI	polyimide
PCB	printed circuit board

PTFE	polytetrafluoroethylene
PVA	polyvinyl alcohol
PVC	polyvinyl chloride
RADAR	Radio Detection and Ranging
SEM	Scanning Electron Microscopy
SCALINT	Structural Composites and Alloys, Integrity and Nondestructive Testing group
SHM	Structural Health Monitoring
TDR	Time Domain Reflectometry
TEM	transverse electromagnetic mode
TiCN	titanium carbo-nitride
TSV	through silicon via
VSWR	voltage standing wave ratio

Subscripts and superscripts

AC	related to the frequency dependent component of a property
app	apparent
at%	atom percentage
bound water	related to bound water molecules
c	critical, related to the percolation threshold
corr	corrected
cond	related to the conducting components of an electric circuit
DC	related to the frequency independent component of a property
dielectric	related to the isolating dielectric in an electric circuit
dry	related to a property measured when moisture is absent
E	related to the electric field
eff	effective
fault	related to the error made during measurement
filler	minority component of a composite
free water	related to free water molecules
generator	wave generator
H	related to the magnetic field
in	measured at the entrance of an electric circuit
L	related to the load applied to an electric circuit

matrix	majority component of a composite
max	maximum
meas	measured
min	minimum
MAX	determined by the maximum method
MD	determined by the maximum-derivative fitting method
n, p	normal and parallel component of a wave
N	N^{th} node
open	measured in open-circuit condition
oscilloscope	oscilloscope
output	returned from the electric circuit
r	reflected
res	resolution
short	measured in short-circuit condition
sys	system
SF	determined by the sigmoidal fitting method
t	transmitted
TC	determined by the tangent line method
V	volume
x, y, z	related to the spatial coordinates in cartesian space
ZD	determined by the zero-derivative method
0	related to the initial condition or input state
1, 2	related to different electromagnetic media
+, -	forward and backward propagating component of a wave
*	complex conjugate

Mathematical notations

$\vec{a} = (a_1, a_2, a_3)$	vector in cartesian space
a_i	i^{th} component of a vector
a_{ij}	element on i^{th} row and j^{th} column of a matrix
a	scalar or norm of vector
$a_N^{(L,C)}$	value of a property (related to the conductance C or inductance L) at the Nth node.

$$\frac{\partial^n a}{\partial i^n}$$

n^{th} partial derivative with respect to the i-coordinate

$$\nabla \vec{a} = \left(\frac{\partial a_x}{\partial x}, \frac{\partial a_y}{\partial y}, \frac{\partial a_z}{\partial z} \right)$$

gradient of a vector

$$\nabla \times \vec{a} = \left(\frac{\partial a_z}{\partial y} - \frac{\partial a_y}{\partial z}, \frac{\partial a_x}{\partial z} - \frac{\partial a_z}{\partial x}, \frac{\partial a_y}{\partial x} - \frac{\partial a_x}{\partial y} \right)$$

rotor of a vector

$$\nabla . \vec{a} = \frac{\partial a_x}{\partial x} + \frac{\partial a_y}{\partial y} + \frac{\partial a_z}{\partial z}$$

divergence of a vector

$$\nabla^2 \vec{a} = \frac{\partial^2 a_x}{\partial x^2} + \frac{\partial^2 a_y}{\partial y^2} + \frac{\partial^2 a_z}{\partial z^2}$$

Laplace operator applied to a vector

$\vec{a} . \vec{b}$

scalar product of 2 vectors

$\vec{a} \times \vec{b}$

vector product of 2 vectors

Chapter 1

General introduction

Time domain reflectometry (TDR) is a widely used, simple, low-cost and fast nondestructive characterisation and fault localisation technique used for transmission line inspection and characterisation together with the detection of moisture, strain and cracks in engineering constructions and electronic packages. TDR has already been successfully applied for the detection of water leakages in case of buried pipes and transmission lines. However, its application in aircrafts and Structural Health Monitoring is still not fully elaborated.

The goal of this thesis was to investigate the feasibility of leakage detection in large engineering structures by TDR. The main application intended consists of pipelines and floor structures in the aircraft's fuselage, and continues on the research carried out at the Department of Materials Engineering at KU Leuven. A percolation sensor has already been developed that allows accurate detection of a leakage spot based on a fuse-like increase of the DC resistance. However, localisation cannot be carried out with this nondestructive technique and here TDR can play a major role because of its accurate localisation possibilities.

The thesis starts with an exhaustive and summarising literature study in chapter 2-4. Chapter 2 illustrates the economic and social importance of early leakage detections and an overview of the commercially available leakage detecting sensors together with the percolation sensor developed at the Department of Materials Engineering at KU Leuven is given. In chapter 3, the main fundamentals and equations of transmission line theory are discussed. A comprehensive overview of the fundamentals, parameters and applications of TDR is elaborated in chapter 4.

Chapters 5-9 focus on the experimental part of this thesis. The performed experiments together with the used materials and methods are listed in chapter 5. The characterisation and TDR behaviour of the water and kerosene sensor under dry and leakage conditions are discussed in respectively chapter 6 and 7. The observed sensor's TDR signature and the influence of leakages on it is modelled in chapter 8 by using a lumped circuit approach. Chapter 9 gives an overview of the limitations and future challenges of the research carried out within this thesis together with the applicability of TDR to large engineering structures. Finally, the general conclusions of this thesis are summarised in chapter 10. The references and appendices can be found at the end of the thesis.

Chapter 2

Leakage detecting cable sensors

Leakages can cause major damage and long-duration downtimes in industrial structures and public transport facilities. Hence, early detection, localisation and repair of the leakage spot is indispensable. This chapter starts with an elaboration of the socio-economic importance of early leakage detection for Structural Health Monitoring (SHM) in paragraph 2.1 by illustrating possible severe consequences and safety threats based on major leakage incidents and currently applied liquid detection solutions. Next, an overview of the available commercial leakage detecting cable sensors is given in paragraph 2.2. Paragraph 2.3 discusses in detail the design, working principle and characteristics of the percolation sensor developed at the Non-Destructive Testing (NDT) group of the Department of Materials Engineering at KU Leuven together with a summary of the percolation and humidity sensors based on polyvinyl alcohol (PVA) developed at other research institutes. Finally, paragraph 2.4 summarises the major conclusions of this chapter.

2.1. Socio-economic importance of leakage detection for Structural Health Monitoring

Water is everywhere and assures the viability of human life on our planet. Contradictory, water acts in the same time as one of the major threats for humanity (storms, floods, diseases) and can severely damage industrial and electric infrastructure, because its liquid and low-viscosity character make water hard to stop. In our daily living environment, areas of risk for leakages are heating/cooling water supplies and return pipes, drains, fire sprinklers, toilets, basements, roofs and windows, beverage vending machines and overhead pipes (Pentair, 2016). The potential consequences of leakages may not be underestimated: business disruption, service network interruption and network outages, loss of telephone service, damage to furnishings, paper files and records and finally the consequent clean-up costs. 27 % of business outages is attributed to water damage, which is ranked second behind power outage, and the average downtime cost attains 1-2,8 billion dollar a year depending on the industry (RLE Technologies, 2017). Especially in the public transport sector, leakages can cause severe damage and induce long downtimes accompanied by large revenue losses.

Multiple major leakage incidents occurred during commercial flights. One of the most famous is the incident with the Airbus 380 of Qantas in November 2010. During a routine flight from Singapore to Sydney, shrapnel was ejected and pierced part of the wing after one of the Rolls-Royce turbines had failed (Lilley, 2015). Figure 2.1a shows the size of the damage on the wing caused by the shrapnel. Investigation showed that a cracked oil feed stub pipe was the cause of leakage of atomised oil spray, which self-ignited consequently. As a consequence of the incident, Quantas' complete A380 fleet was grounded for 3 weeks and other aircraft operators took the same measure until renewed quality control was improved by Rolls-Royce.

In November 2009, loss of the green hydraulic system and nose wheel steering was noticed in an AVRO JR 100 during taxiing for its flight from Zaventem to Berlin (Federal public Service Mobility and Transport - Air Accident Investigation Unit, 2012). Fluid leaked into the cabin and

contaminated some passengers: 4 persons suffered from skin and face burns and panic broke out among the passengers. Fatigue at a penetrated weld had caused a stainless steel pipe to rupture and green hydraulic fluid leaked into the cabin. Brussels Airlines installed a sealed plastic contained envelope around the hydraulic system pipes as a precautionary measure.

The economic price of structural damages in aircrafts caused by leakages may not be underestimated. Between January 2015 and June 2016, the maintenance reports from the 6-yearly D-check reports for 24 aircrafts at Brussels Airlines were investigated (R. Windey, 2016). Corrosion of one or multiple structural floor components was discovered in 63 % of the inspected aircrafts. Typical corrosion spots are the wet areas, which are situated at the galleys, lavatories and passenger entrance doors. However, seat tracks, floor beams and door sills are also prone to corrosion. The degradation was attributed to stress corrosion cracking of the susceptible aluminium 7076-T6 alloy accelerated by galvanic corrosion and environmental influences (chlorides) due to condensed water, rain water, beverage spillage and the excessive use of cleaning agents. The corrosion spots on one of the investigated door sills are given in figure 2.1b. Most damaged items had to be replaced, for which on average $ 1500 and 40-50 man hours were required. For the door sills, the price increased to almost $ 9000 per item and 100 man hours were required. All item and labour costs taken into account, a mean cost of $ 47 000 for an A319 and $ 35 000 for an A320 was attained. However, the lost revenues of approximately $ 100 000 a day were not taken into account. Knowing that the delivery time of a new sill is on average 1.5 week and that some parts even have a lead time up to 6 months, the importance of pre-catastrophic failure and leakage detection should be clear.

(a)   (b)
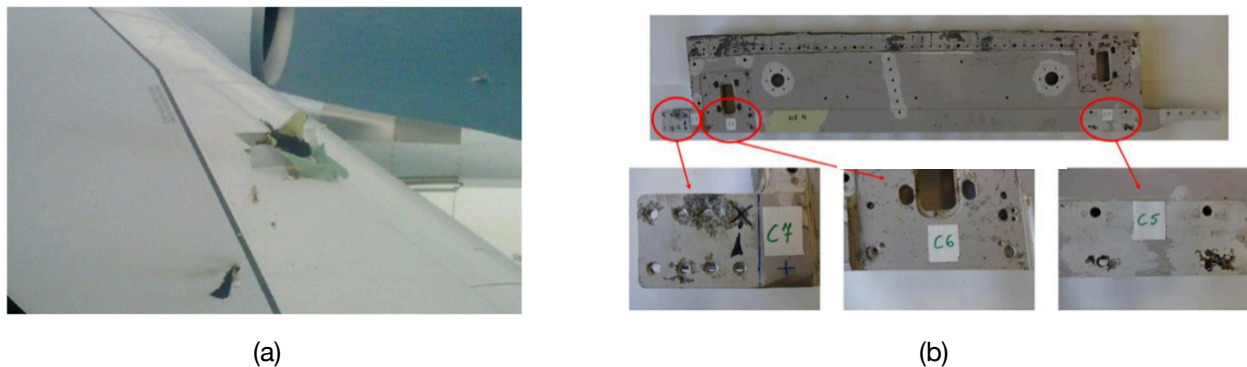
Figure 2.1a. Damaged wing of Qantas' Airbus 380 in November 2010 due to the impact of shrapnel ejected from a failed turbine (Lilley, 2015). Figure 2.1b Stress corrosion spots (dark grey and brown) and on a door sill of an A320 of Brussels Airlines due to leakage of water, beverages and cleaning agents (R. Windey, 2016).

Currently, predictive maintenance forms a high priority in the Maintenance, Repair and Overhaul (MRO) industry to avoid unnecessary aircraft inspections (Versteele - Sabena Aerospace, 2017). The commonly used NDT techniques in commercial aviation are eddy current testing, embedded electrical crack gauges, ultrasonic Lamb waves, optical fibres for acoustic emission monitoring, radiography, thermography, liquid penetrant testing and magnetic particle inspection (I. Pitropakis, 2015). Digitalisation and connectivity of data are indispensable. New inspection and repair techniques are accompanied by simplified NDT techniques and embedded sensors for SHM. A reduced turn around time, maintenance cost and an increase in aircraft availability are expected results of these innovations. Early failure detection will contribute to safety and advanced quality, and the efficiency of Maintenance and Engineering is based on in-service data monitoring and analysis in order to reduce the non-routine tasks (Reynaert, 2017). Multiple joined projects between research institutes and aircraft operators are started and partnerships between airlines like Brussels Airlines, Lufthansa Technics and TAP Air Portugal arise to efficiently tackle these challenges on a large scale (Vandepitte, 2017).

Since more than one decade, the Structural Composites and Alloys, Integrity and Non-destructive Testing group (SCALINT) of the Department of Materials Engineering at KU Leuven focused on joined projects with Brussels Airlines, Lufthansa Technik and other international aircraft related partners. During the European FP6 Aircraft Integrated Structural Health Assessment (AISHA) and FP7 AISHA II project, the long-term material behaviour of aircraft structures was investigated concerning corrosion and damage developed during mechanical and thermal loading (Pfeiffer, 2017). KU Leuven partners in other projects were the Department of Physics (SHM via photo-acoustics and photo thermal techniques), KULAK (Non-linear Elastic Wave Spectroscopy), Vives Kortrijk (Non-contact air coupled Ultrasound) and the Materials Technology Cluster in Ghent and Aalst (contactless 3D measurement of deformations by Digital Image Correlation).

2.2.   Commercial leakage sensors

As illustrated in the previous paragraph, the early detection of leakages is of major economic importance for many industries and public services. Hence, multiple companies have developed leakage detecting sensors and solutions based on hydrostatic pressure testing (no leakage localisation is possible), tracer gas (check the leakage into the soil), double containment pipes (expensive) and comparison of modelled pressure and flow rates to experimental values. However, the suppliers of cable based sensors are rather scarce. The TraceTek Leak Detection and Locating system from Raychem (UK) is widely used in commercial, environmental and industrial applications (Pentair, 2016; Raychem, 2017). The sensor consists of a cross-linked conductive polymer (no susceptibility to corrosion) surrounding a fluoropolymer core. Two isolated signal wires and a non-isolated semiconductive sensing wire are wound around the cylindrical-shaped polymer. A fixed current is applied and when a spillage of a liquid occurs, a short arises through the conductive liquid causing the travelled distance on the non-isolated sensing wire, and hence the measured voltage over the sensor to drop, from which the leakage spot position is derived. The working principle is illustrated is figure 2.2.

Different versions of the sensor exist for measuring water (TT1000), aqueous chemicals, acids and other hazardous fluids with water content (TT3000), diesel, petrol, jet fuel, lubricant oil and other hydrocarbons (TT5000), organic solvents (TT5001) and strong acids and bases (TT7000). The sensor's main advantages are the very quick drying time of 15 seconds, the high accuracy and precision (better than 0.1 %), the reliable and flexible distributed sensing network and the fully supervising circuit due to the simple and modular installation accompanied by capabilities for multiple circuiting. The sensor has been applied in medical environments (dialysis ward), unoccupied apartments (the Shard, London), fuel lines in harbours (Queensland, Australia and San Jose, USA), pipelines (Tanzania and Chile), fuel storage tanks (France) and historical sites (HM Treasury and Cabinet War Rooms, London) (Aquilar, 2017). The sensor has also been installed at Madrid Airport since 2003 for the detection and localisation of fuel leakages under the concrete to avoid complete excavation of the taxiway, hence saving costs related to leakage source detection, repair, repaving and environmental contamination (Key Publishing Ltd, 2005).

A similar sensor design and operation principle is used by other suppliers and user-friendly in-service monitoring is allowed by tailored software. RLE Technologies' SeaHawk system (USA) is able to detect conductive fluids, water and chemicals, and is currently applied at the University of Northern Colorado, Tramell Crow Company (an estate agency in the USA) and Expedient (a data center in the USA) (RLE Technologies, 2017).

(a)	(b)	(c)
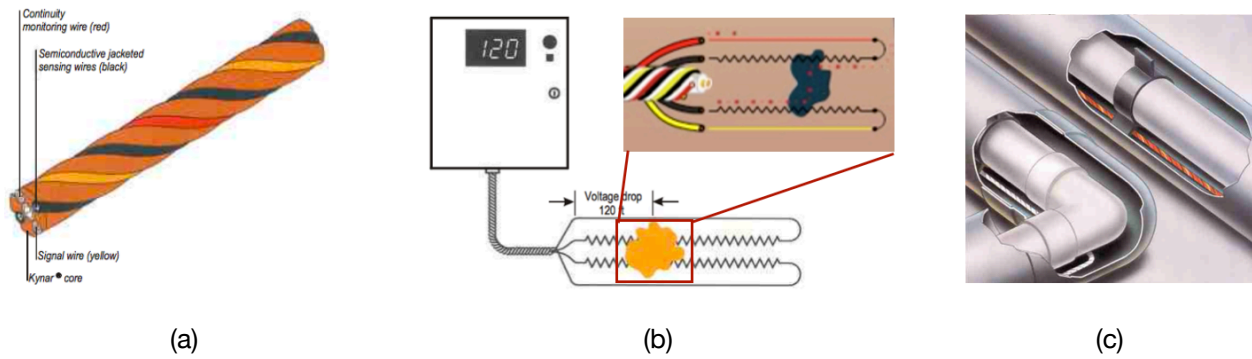
Figure 2.2a and 2.2b. Raychem's TT1000 liquid detection cable consisting of a polymer core surrounded by 2 isolated signal wires (red and yellow) and 1 non-isolated sensing wire (black). A possible leakage spot will cause a short conductive path of the applied fixed current through the spilled liquid, causing a voltage drop from which the position of the leakage spot is derived (Aquilar Ltd, 2008; Raychem, 2017)). Figure 2.2c. Application of the liquid detection cable in a pipeline environment (Raychem, 2017).

TTK (France) developed sensors for the detection of water (FG-ECS), acids (FG-AC) and hydrocarbons (FG-OD) (TTK, 2017). The sensor's reaction time of 5 minutes for highly volatile hydrocarbons (petrol) and 20 minutes for lowly volatile hydrocarbons (diesel) allows quick response and action of the operators. The drying time of approximately 10 seconds assures the immediate readiness for further use after leakage. The sensor design of the FG-ECS and SeaHawk water sensing cables are shown in figure 2.3a and 2.3b.

The major drawback of these accurate and sensitive sensors is their high market price and the limited lengths in which they are available (normally up to 15-50 m) (HW group, 2017; Pentair, 2016). HW group's WLD water sensor (Czech Republic) is available for $ 2000/50m (HW group, 2017 and True Path Technologies, 2017). Aquentis provides water detection sensing cables with a price of $140/10 m (Aquentis, 2017). Despite the high sensitivity and accuracy of the sensors, a full network of sensor cables is required for early water detection and to be consequently advantageous over common local sensors, which is illustrated is figure 2.3c.

It is clear that the high cost and limited lengths of the commercially available leakage detecting sensor cables form a major drawback for their wide application in industrial (pipelines, fuel storage facilities) and public environments (estates, airports and historical sites). Hence, tailored sensor designs with high accuracy and sensitivity, but that are still producible at a mediocre and economically attractive price are required.

(a)	(b)	(c)
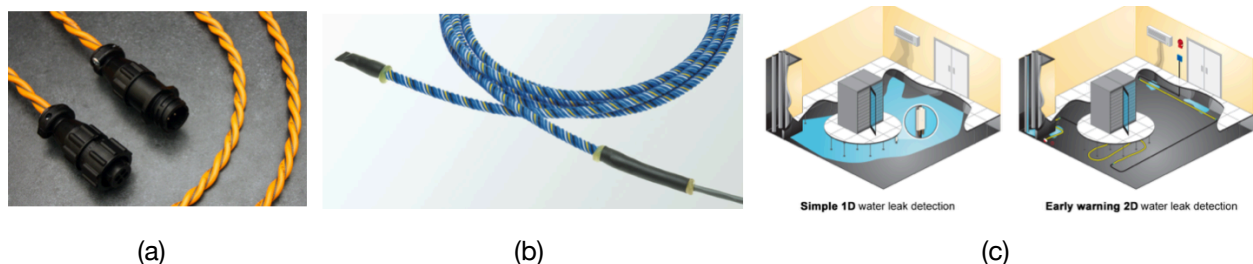
Figure 2.3a. RLE Technologies' SeaHawk water sensing cable (RLE Technologies, 2017). Figure 2.3b. TTK's FG-ECS water sensing cable (TTK, 2017). Figure 2.3c, The advantage of a sensor network lay-out over a simple local sensor for early water detection becomes clear (HW group, 2017).

2.3. Leakage detection based on percolation theory

2.3.1. Overview of percolation theory

Percolation is the theory of connectivity of conducting particles in randomised lattice structures and the corresponding evolution of certain properties when reaching a state of global connectivity (G. De Lescluze, 2017; C. W. Nan, 2010). The theory of percolation for heterogeneous media describes that a number of individual clusters arise at low volume fractions forming isolated minor phase networks partially extending throughout the matrix. By increasing the particle volume fraction, these individual networks steadily grow and suddenly, upon reaching the percolation threshold, one minor phase cluster spans the whole matrix and a state of global connectivity is reached. The percolation principle is illustrated in figure 2.4a en 2.4b (G. De Lescluze, 2017; H. Pfeiffer, 2012b).

(a)   (b)
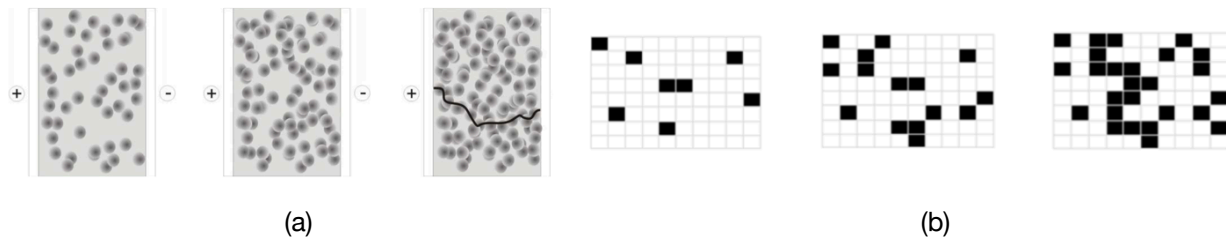
Figure 2.4a. Simplified scheme of the creation of percolation conductivity for randomly dispersed spherical particles (H. Pfeiffer, 2012). Figure 2.4b. Representation of site percolation, the percolation threshold is reached in the figure to the right (G. De Lescluze, 2017).

The physical properties of the composite dramatically change upon the onset of percolation, particularly when the difference between the properties of the constitutive phases is large. The formation of the percolation network immediately results in a nonlinear scaling of transport properties (e.g., electrical or thermal conductivity and diffusion) (C. Siegmund, 1999). For example, the conductivity of polypropylene filled with copper particles changed 12 orders of magnitude when the percolation threshold was exceeded (A. Boudenne, 2005). Other properties such as the dielectric constant or optical nonlinearity significantly change even before the percolation threshold is reached. Large enhancements in the relative dielectric permittivity in the order of 100 and more have been observed for a number of dielectric ceramic composites like $Ca[(Li_{1/3} Nb_{2/3})_{1-x}Ti_x]O_{3-\delta}/Ag$ (4.10^5 at 1 MHz) and $Bi_{1.5}ZnNb_{1.5}O_7/Ag$ (10^5 at 1 MHz) (C. W. Nan). Microcapacitor networks near percolation are the physical reason of the non-linear behaviour. A very thin layer of dielectric is present between the neighbouring conductive filler particles, which causes an abnormally large capacitance. The physical properties of percolative materials are commonly described by the power-law given in equation (2.1). Equations (2.2) and (2.3) specifically apply to the conductivity of the composite, whereas equation (2.4) describes the dielectric behaviour. Geometrical properties of the minor phase such as the particle size and shape influence the position of the percolation threshold (C. W. Nan, 2010).

$$S \propto \left(\phi - \phi_c\right)^t \tag{2.1}$$

$$\sigma = \sigma_{filler}\left(\phi - \phi_c\right)^t \quad \phi > \phi_c \tag{2.2}$$

$$\sigma = \sigma_{matrix} \left(\phi_c - \phi \right)^{-t} \quad \phi < \phi_c \tag{2.3}$$

$$\varepsilon_S = \varepsilon_{S,matrix} \left| \phi_c - \phi \right|^{-t} \tag{2.4}$$

with S the modelled property, ϕ the volume fraction of the minor phase fillers, ϕ_c the percolation threshold, t a critical exponent, σ the conductivity of the composite, σ_i a pre-exponential factor based on the conductivity of the insulating matrix or conductive filler particles, ε_S the dielectric constant of the composite and $\varepsilon_{S,matrix}$ the dielectric constant of the insulating/dielectric matrix.

Percolative materials are applied as antistatic media, electromagnetic shields, thermal fuses and pressure or strain sensors (A. Boudenne, 2005; K. K. Kim, 2015; I. Tsuyumoto, 2011). In the field of electrical engineering, the concept of percolation is also known to describe the phenomena causing leakage paths and oxide breakdown in dielectric layers (R. Degraeve, 1998; R. Degraeve, 2004).

2.3.2. Percolation sensor developed by the Materials Engineering Departement of the KU Leuven

The NDT group of the Materials Engineering Department of KU Leuven strongly focuses its research on SHM solutions. In 2012, a leakage sensor was created for the detection of water, but also the presence of other harmful liquids as petrol, Coca Cola and Skydrol could be measured (H. Pfeiffer, 2012a). The sensor is patented at the US Patent and Trademark Office, patent number 8,963,565 (USPTO, 2015), and also an international patent via the EPO was just granted. Whereas detecting sensors are frequently used in other engineering structures, their application in aircrafts is currently limited because the price of such sensors often exceeds the maintenance cost of the damaged structure (H. Pfeiffer, 2014). However, the materials cost of the developed sensor was estimated on only € 1-1.5/m, for sure not considering development, staff, overhead and tax costs. The main principle is based on the collapse of the percolation conductivity of the composite, providing a fuse-like change in the DC resistance of the sensor. An advantage is that accurate resistance measurements or not longer required, only relevant changes on a logarithmic scale on the baseline variation are important.

The sensor composite consists of conducting and hydrophobic TiCN particles (70/30 wt% TiC-TiN, 1.2-2 μm) and an insulating and hydrophilic PVA matrix due to the hydroxyl groups in its chemical structure. For the detection of Skydrol, a phosphate-ester-based hydraulic liquid, an acrylic acid polymer with embedded copper or nickel was used, whereas the detection of kerosene and mineral oils required a rubber composite containing graphite or graphite coated nickel particles (H. Pfeiffer, 2014).

Figure 2.5a shows the sorption isotherms derived for equilibration of the sensor in different levels of relative humidity (RH). For higher volume fractions, the water absorption decreased due to the hydrophobicity of the TiCN particles. The anhydrous percolation threshold was found to be 0.23 vol%. For high volume fractions, a large increase in resistance occurred for high RH, approximately 80 %, because the lyotropic percolation threshold was reached: interaction due to absorption between the water solvent and the matrix causes a fuse-like resistance increase. This lyotropic threshold increased with higher volume fractions of TiCN, which is easily explained since more water is required to interrupt the percolation network (G. De Lescluze, 2017). One can assume that the lyotropic percolation threshold is partially triggered, or at least promoted by the

hydration driven lyotropic glass–rubber transition, which is shown in figure 2.5b (H. Pfeiffer, 2012a). The glass-transition always preceded the percolation threshold and approximately a difference of RH of 20% was observed. It is believed that the typical increase in the mobility of polymer chains (second order phase transition) at the glass transition helps the interruption with the percolating network by facilitating water diffusion.

(a)   (b)
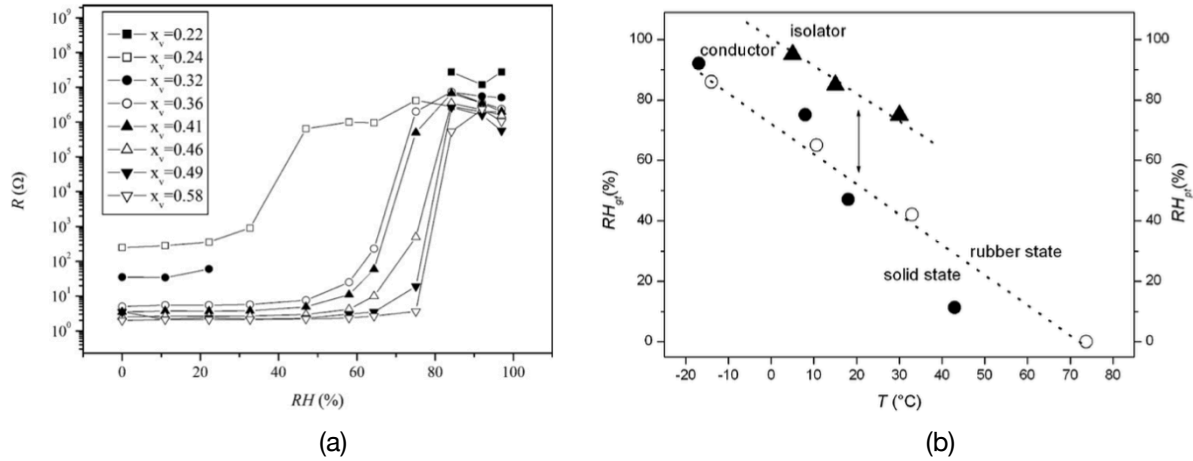
Figure 2.5a. Resistance for the different TiCN/PVA mixtures as a function of humidity. The captions in the legend present the volume fraction of TiCN. For lower volume fractions, the lyotropic percolation threshold occurred for lower levels of RH (H. Pfeiffer, 2012a). Figure 2.5b. Relationship between the temperature dependence of the humidity-driven (lyotropic) glass transition, RH_{gt}, of pure PVA (solid circles, open circles other work) and of the corresponding (lyotropic)percolation threshold RH_{pt} (triangle) for TiCN/PVA mixtures at a volume fraction of $x_{v,TiCN}$ = 40% (H. Pfeiffer, 2014).

In the currently used sensor design, a volume fraction of 0.46 was chosen because the lyotropic percolation threshold occurred for a RH of 80 %, which is significantly above the normal RH of 40-50 % in air, the latter being reached during boarding of the aircraft. During the flight, a RH of 10-20% is normally reached in the cabin at an altitude of 10 km (I. Pitropakis, 2015). However, in the cargo space temperatures can decrease significantly and condensation of water is possible, which will cause lyotropic percolation.

The evolution of the DC resistance was measured as function of time for a Coca Cola (most aggressive liquid in aircraft operations within the cabin) droplet of 0.7 ml. After 25 minutes, the resistance exponentially increased and reached a maximum of $10^{6.5}$ Ω , before decreasing again to $10^{1.1}$ Ω and subsequently increasing again to a limit value of less than 10^7 Ω (G. De Lescluze, 2017). The spike after the percolation threshold was attributed to the competition between the collapse of the percolating TiCN network and the creation of a conductive water percolation network. The total resistance curve is given in figure 2.6a (H. Pfeiffer, 2014).

Also Skydrol was used as spilled liquid. Similar resistance curves as for water were observed. However, no residual conductance and spike was observed because of the absence of electrolytic properties of the oil, and a limit value of 10^8 Ω was reached. Percolation occurred at the given sensor dimensions and temperature after approximately 15 minutes. The resistance curve as a function of time is given in figure 2.6b (H. Pfeiffer, 2014). Remarkable is the fluctuating fraction of the curve around the percolation curve. This was believed to be a macroscopic effect of the Brownian motion, but this effect still requires further research.

The developed sensor was consequently applied in operational airliners (Lufthansa) and in chemical plants (BASF at Antwerp harbour) (H. Pfeiffer, 2014). Only periodic inspection on a

regular base was done. The measured resistance curve as a function of time is given in figure 2.7c together with the sensor lay-out in figure 2.7a and 2.7b (H. Pfeiffer, 2014). Each peak corresponds to a leakage accompanied by the subsequent drying. Another advantage of the sensor not be mentioned yet, is its buffer capacity to retain the spilled liquid and hence, protecting the surrounding floor structure. The results were so convincing that Lufthansa-Techniks adapted its maintenance procedures for floor structures in order to reduce the maintenance and repair costs.

(a)   (b)
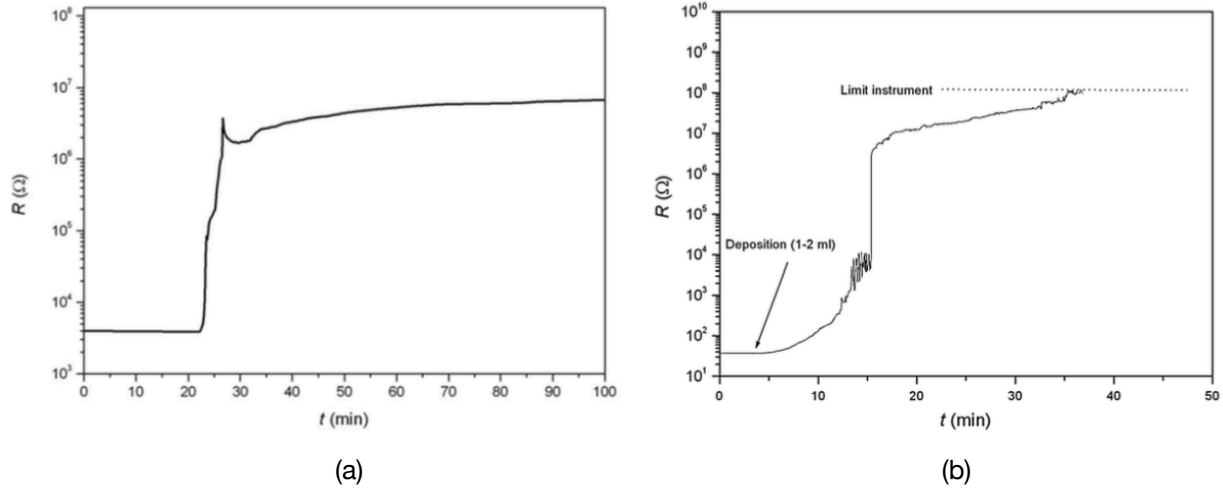
Figure. 2.6a. Drop-like exposure of the sensor to an aqueous liquid (cola) at room temperature (H. Pfeiffer, 2014). Figure 2.6b. Time-dependent percolation threshold of a thick layer of the nickel/acrylic composite after exposure to Skydrol (H. Pfeiffer, 2014).

For the chemical plant, the sensor was installed inside the isolation of the pipeline at the bottom (H. Pfeiffer, 2014). The reference resistance of the 3 m long sensor was 10-30 kΩ, whereas its value increased exponentially to orders of MΩ in wet conditions. 2-3 days were used as interval for inspection.

Besides its durability, which was tested by a fatigue and tensile test, its ability to detect high RH levels, flexibility and easiness of production, installation and data collection over large areas are together with the independence of electromagnetic and mechanical interference the main advantages of the sensor (I. Pitropakis, 2015). However, the temperature influence on the glass transition forms a minor drawback.

(a)   (b)   (c)
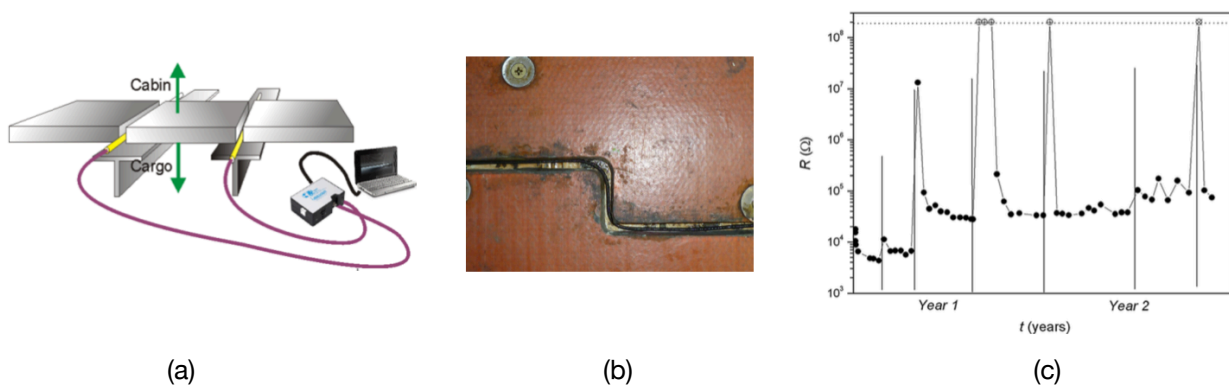
Figure 2.7a and 2.7b. Sensor lay-out in an operational aircraft at Lufthansa (Boeing 737). The sensor was installed under the joint notches of the floor panels (H. Pfeiffer, 2014). Figure 2.7c. Resistance measured over a period of 2 years in an operational aircraft. Consecutive periods of leakage and drying are observed (H. Pfeiffer, 2014).

9

2.3.3. Percolation sensors developed by other research institutes

Little research activities have been attributed to the development of similar percolation sensors as the one designed by the Materials Departement at the KU Leuven. However, 2 successful examples developed at foreign universities can be found in literature.

In 2011, I. Tsuyumoto and Y. Iida from the Kanazawa Institute of Technology in Ishikawa, Japan, developed a low-cost and durable percolation sensor consisting of a random mixture of insulating montmorillonite particles (5-120 µm) and conducting carbon particles (5 µm) (I. Tsuyumoto, 2011). Water absorption in the montmorillonite caused a sigmoidal change in resistivity in the range of Ω/cm to MΩ/cm due to the swelling of the insulating phase, which is shown in figure 2.8a.

K. P. Yoo et al. from the Korea University in Seoul, South-Korea, designed in 2011 a novel resistive-type humidity sensor based on a mixture of highly conducting multiwall carbon nanotubes (MWCNT) and insulating polyimide (PI) (K. P. Yoo, 2010). The percolation threshold occurred for a volume fraction of 0.05 wt% of MWCNT accompanied by a decrease in resistivity from the MΩ tot kΩ range, after which a linear change in resistivity was observed for increasing RH, which is shown in figure 2.8b.

(a)   (b)
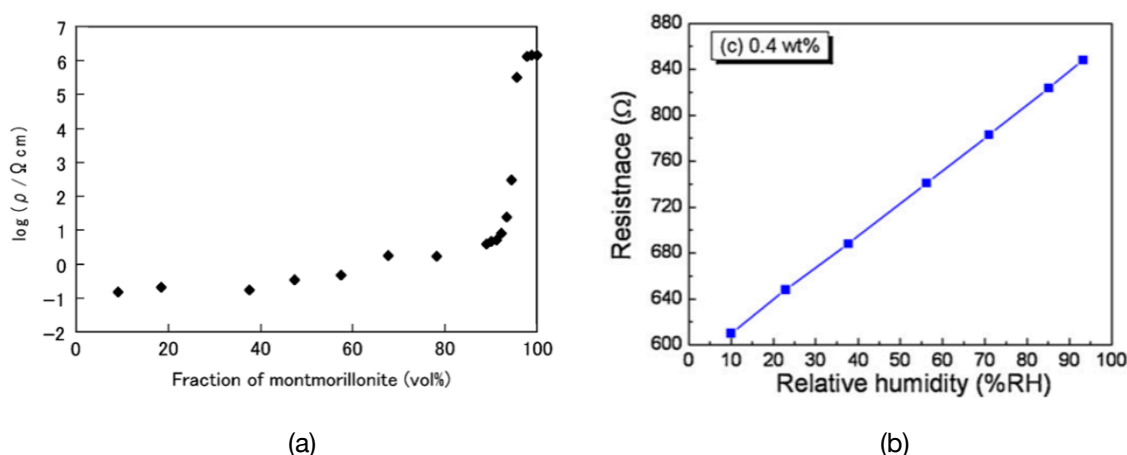
Figure 2.8a. Resistivity of the montmorillonite-carbon composite as a function of the volume fraction of the montmorillonite (I. Tsuyumoto and Y. Iida, 2011). Figure 2.8b. Dependence of the AC resistance on the RH for 0.4 wt% MWCNT (K. P. Yoo, 2010). The first sensor showed a fuse-like resistance behaviour, whereas for the latter one a linear behaviour was observed.

2.3.4. Humidity sensors based on PVA developed by other research institutes

As a hygroscopic polymer, 2 researches were found in which PVA was chosen as the humidity sensing material layer. E. M. Amin, N. C. Karmakar, and B. Winther-Jensen developed a coplanar waveguide, which is a centre strip line sandwiched between two dielectric substrates, with PVA as one of the dielectric layers (E. M. Amin, 2013). The sensitivity of the PVA-based sensor was found to be twice the value of the commercially available Kapton-based ($C_{12}H_{12}N_2O$) sensor. The frequency shift that was noticed for increasing RH levels was attributed to the increase in permittivity of PVA, which is already 75 % for a RH of 20 % for pure PVA.

A second example was provided within the research of T. Li, X. Dong et al. (T. Li, 2013). A photonic crystal fibre-model interferometer was used. The change in permittivity of the PVA and hence, also the refractive index caused interference when recombination of the sensor's core and cladding modes at the end of the photonics crystal fibre occurred. A linearly increasing total shift of 40.9 pm/RH % was measured.

2.4. Conclusions

This chapter stressed the importance of Structural Health Monitoring for the accurate, quick and reliable detection of leakages to avoid major damage and long-duration downtimes in industrial structures and public transport facilities. An overview of the available commercial leakage detecting cable sensors was given from which it was clear the high cost is a major drawback for their wide application. Hence a cheap, durable and reversible sensor was successfully developed at the Non-Destructive Testing group of the Department of Materials Engineering at KU Leuven based on the phenomenon of percolation in a composite of conducting filler particles in an insulating matrix. The absorption of water by the hygroscopic polyvinyl alcohol matrix caused the destruction of the percolating network of titanium carbo-nitride particles at the lyotropic percolation threshold due to the swelling, which was accompanied by a fuse-like increase in the DC resistance of not less than four orders of magnitude. The combination of PVA and the ceramic TiCN particles had not been used before by other authors. For the detection of kerosene and mineral oil a similar sensor was designed with respectively a rubber and an acrylic acid polymer as matrix material. Only a few projects on percolation-based and PVA-based humidity sensors were performed at other research institutes. However, the reported examples were successful and showed a sensitive, accurate, durable and low-cost (fuse-like) humidity sensor based on the theory of percolation and by choosing a hygroscopic matrix material to be possible .

Chapter 3

Transmission line theory

Time domain reflectometry (TDR) is based on the reflection of generated voltage pulses by impedance mismatches along its propagation path. The investigated Device Under Test (DUT) or used cable sensor can often be considered as a coaxial cable or as parallel wires. Hence, an in-depth understanding of the propagation characteristics of Electromagnetic (EM) waves along transmission lines is indispensable.

All electromagnetic, acoustic and particle waves scatter, diffract and interfere on their propagation path (J. Lekner, 2016). Reflection is the result of constructive interference of many scattered or diffracted waves originating from scatters in a stratified medium. A many-body approach is hard to apply. Hence, a replacement of the collection of scatters by effective media with frequency and position dependent properties in unavoidable. This approach leads to the formulation of a set of partial differential equations which subsequently have to be solved in combination with the appropriate boundary conditions. This chapter is mainly based on the analysis of A. Von Hippel - *Dielectrics and Waves (*A. Von Hippel, 1954*)* and S. H. Hall and H. L. Heck - *Advanced Signal Integrity for High-Speed Digital Designs* (S. H. Hall, 2009), unless stated otherwise. Paragraph 3.1 gives an overview of the basic electromagnetic fundamentals of Maxwell's equations and wave propagation. The boundary conditions causing reflection and refraction are derived for EM waves. Paragraph 3.2 gives a detailed analysis of transmission line theory: the concept of equivalent or lumped circuit parameters is discussed leading to the telegrapher's equations. The reflection coefficient is defined and directly related to the equivalent circuit parameters. Also the principle of standing waves is discussed. Finally, the theory of network analysis is shortly treated in paragraph 3.3.

3.1. Electromagnetic fundamentals

3.1.1. Maxwell's equations

The foundation of all electromagnetic theory is described by Maxwell's equations. The differential form of Maxwell equations together with the supplementary equations that comprehend the properties of media other than free space are summarised in appendix A.1.

3.1.2. Wave propagation

When studying Maxwell's equations, it becomes apparent that Faraday's and Ampère's law are coupled: a changing electric field will produce a changing magnetic field and vice versa. This mutual interaction is responsible for the propagation of an EM wave. In the transverse electromagnetic mode (TEM), the electrical and magnetic fields are orthogonal and have no components in the propagation z-direction. If the width of the transmission line is smaller than a quarter of the wavelength, the TEM assumption is accurate (J. A. Strickland, 1970). A further simplification of Maxwell's equations can be made if the time variation is assumed to be steady-

state sinusoidal or time harmonic in nature, which results in plane waves. The solutions for the electric and magnetic fields consist of a sinusoidal part based on the phase constant β and an exponentially decaying part based on the attenuation constant α, which is related to conductive and dielectric resistance losses, both combined in the complex propagation constant $\gamma = \alpha + j\beta$.

Each wave is a linear combination of a forward-propagating and a backward-propagating component. The intrinsic impedance η in a medium depends on the ratio of the electric and magnetic field, respectively denoted by E and H, and is comparable to the classic AC impedance.

$$\eta = \frac{E}{H} = \sqrt{\frac{\mu}{\varepsilon}} \tag{3.1}$$

3.1.3. Reflection of EM waves

Generally, when an EM wave encounters a region with different EM properties, a portion of the wave will be reflected and a portion will be transmitted due to energy conservation. At the interface between two non-conducting media, the incident, reflected and transmitted electric and magnetic field are connected by the boundary condition concerning the continuity of the tangential component, which results in Snell's law of reflection and refraction together with Fresnel's equations.

The field vectors are as defined in the TEM perpendicular to each other and to the direction of incidence, but their orientation relative to the plane of incidence can still be arbitrarily chosen. Therefore, each field vector is decomposed into two components, an n-component normal to the plane of incidence and a p-component parallel to the plane of incidence, which are both shown in figure 3.1 (A. Von Hippel, 1954).
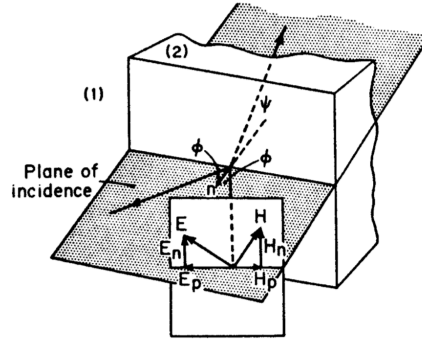
Figure 3.1. Decomposition of the incident beam into an n-component (normal to the plane of incidence) and a p-component (parallel to the plane of incidence) (A. Von Hippel, 1954).

Define the reflection and transmission coefficients, respectively denoted by r and t, as the ratio of the amplitude of respectively the reflected and the transmitted amplitude at the boundary to the incident amplitude, which are both given in equations (3.2) and (3.3).

$$r_{E_n} = \frac{E_{r_n}}{E_{i_n}} = \frac{\eta_2 \cos(\phi) - \eta_1 \cos(\psi)}{\eta_2 \cos(\phi) + \eta_1 \cos(\psi)} = -r_{H_p} \quad \text{and} \quad r_{E_p} = \frac{E_{r_p}}{E_{i_p}} = \frac{\eta_2 \cos(\psi) - \eta_1 \cos(\phi)}{\eta_2 \cos(\psi) + \eta_1 \cos(\phi)} = -r_{H_n} \tag{3.2}$$

$$t_{E_n} = \frac{E_{t_n}}{E_{i_n}} = \frac{2\eta_2 \cos(\phi)}{\eta_2 \cos(\phi) + \eta_1 \cos(\psi)} = \frac{\eta_2}{\eta_1} t_{H_p} \quad \text{and} \quad t_{E_p} = \frac{E_{t_p}}{E_{i_p}} = \frac{2\eta_2 \cos(\phi)}{\eta_2 \cos(\psi) + \eta_1 \cos(\phi)} = \frac{\eta_2}{\eta_1} t_{H_n} \tag{3.3}$$

For perpendicular incidence, which is an assumption made for transmission lines constrained in the propagation z-direction for straight cables, the angle of incidence ϕ and refraction ψ are both

zero and the distinction between the n- and p-component disappears resulting in the commonly used expressions (3.4) and (3.5) for the reflection and transmission coefficient.

$$r_E = \frac{E_r}{E_i} = \frac{\eta_2 - \eta_1}{\eta_2 + \eta_1} = -r_H \tag{3.4}$$

$$t_E = \frac{E_t}{E_i} = \frac{2\eta_2}{\eta_2 + \eta_1} = \frac{\eta_2}{\eta_1}t_H \tag{3.5}$$

A relation for both the electric and magnetic field exists between the reflection and transmission coefficient according to equations (3.6) and (3.7).

$$t_E - r_E = 1 \tag{3.6}$$

$$t_H - r_H = 1 \tag{3.7}$$

3.2. Transmission lines

The process of solving Maxwell's equations is often cumbersome and forms a real challenge for the circuit analyst in case of complex geometry and boundary conditions. Hence, the conversion of the complex investigated system into equivalent or lumped circuit elements in the simple world of voltages and currents offers an attractive alternative approach (E. Bogatin, 2011).

3.2.1. Telegrapher's equations

All interconnects can be treated as transmission lines consisting of a signal and return conductor. Basically, the transmission line is divided in N equal differential elements, as shown in figure 3.2 (F. Farahmand, 2012a), which can each be characterised by 4 equivalent or lumped parameters: a resistance R' [Ω/m], a capacitance C' [F/m], an inductance L' [H/m] and a conductance G' [S/m] per unit length. In this lumped parameter approach, the series inductance will take the changes in the magnetic field into account caused by the changing current in the closed loop formed by the transmission line. The effect of the changing voltage, dielectric properties of the medium in between the conductors and their close spacing is represented by a shunt capacitance. A series resistance takes the attenuation along the conducting lines due to the DC resistance and the skin effect into account. Finally, any losses due to the conductive properties of the dielectric are taken into account by a conductance in parallel with the capacitance (F. Farahmand, 2012b).

By applying Kirchhoff's voltage and current law in each differential element, a relation between the current and voltage at the entrance and exit of the Nth differential element can be derived. Solving these coupled linear second-order differential equations leads to solutions that have the same form as for the electric and magnetic field. These are standing waves caused by the interference of a forward-propagating and back-propagating wave, respectively denoted by + and -. The complex propagation constant is directly related to the lumped circuit parameters. A detailed derivation of the Telegrapher's equations and the next expressions for both the propagation constant and characteristic impedance is given in appendix A.2.

$$\gamma = \alpha + j\beta = \sqrt{(R' + j\omega L')(G' + j\omega C')} \tag{3.8}$$

Equation (3.9) is considered as the fundamental formula of transmission line theory and gives the characteristic impedance Z_0 as the ratio of forward-propagating voltage and current waves.

$$Z_0 = \frac{V_0^+}{I_0^+} = -\frac{V_0^-}{I_0^-} = \sqrt{\frac{R' + j\omega L'}{G' + j\omega C'}} \tag{3.9}$$

(a) Parallel-wire representation

(b) Differential sections each Δz long

(c) Each section is represented by an equivalent circuit
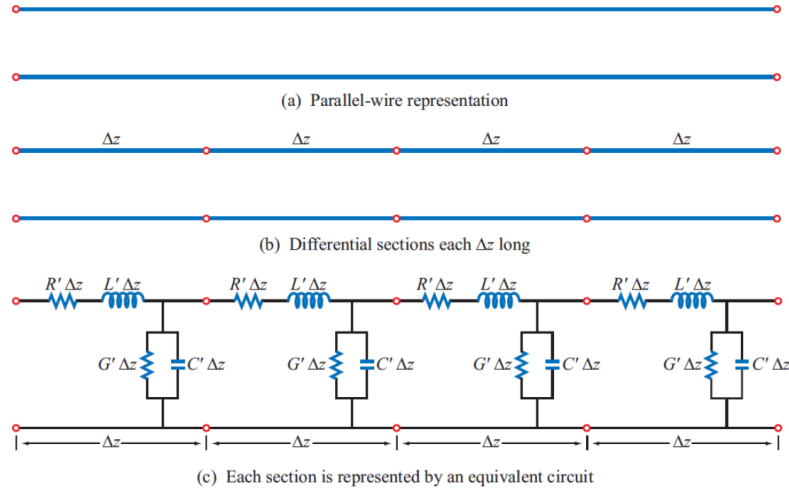
Figure 3.2. Concept of a transmission line divided into *N* differential elements, each with length *Δz* (F. Farahmand, 2012a).

3.2.2. Reflection of voltage and current waves

The similarity between the intrinsic impedance defined in equation (3.1) and the characteristic impedance in equation (3.9) is clear and hence, exactly the same expressions as for the reflection and transmission coefficient defined in equation (3.2) and (3.3) are found for perpendicular incidence of the voltage and current wave, where η_1 is replaced by Z_0 and η_2 by Z_L, which is the characteristic impedance of the mismatched load attached to the transmission line.

$$\Gamma = \frac{V_0^-}{V_0^+} = \frac{Z_L - Z_0}{Z_L + Z_0} \tag{3.10}$$

$$T = \frac{V_0^+ + V_0^-}{V_0^+} = \frac{2Z_L}{Z_L + Z_0} \tag{3.11}$$

Due to energy conservation, the voltage and current must be constant across the boundary (a change in voltage/current is caused by a change in electric/magnetic field) (E. Bogatin, 2011). Hence, the sum of the incident and reflected wave must equal the transmitted wave, both having the same voltage and current amplitude. An overview of the modulus and phase angle of the reflection coefficient $\Gamma = |\Gamma|e^{j\theta_\Gamma}$ depending on the type of impedance mismatch is given in table 3.1 (F. Farahmand, 2012b). Note that the value of the reflection coefficient directly measured from the TDR waveform is the average reflection coefficient over all frequencies present in the incident and reflected signal (MOHR, 2017).

3.2.3. Transmission line properties

The (relative) permittivity ε_r for a conductor consists of a real component ε' responsible for the capacitive character and an imaginary component ε'' responsible for conductive losses due to its conductivity σ (vacuum is denoted by 0). The total dielectric constant can then be written as:

$$\varepsilon_r = \varepsilon_r' - j\varepsilon_r'' = \varepsilon_r' - j\frac{\sigma}{\omega\varepsilon_0} \tag{3.12}$$

The real and imaginary part of the permittivity are related via the loss tangent:

$$\tan|\delta| = \frac{\varepsilon''}{\varepsilon'} \tag{3.13}$$

Table 3.1. Modulus $|\Gamma|$ and phase angle θ_Γ of the reflection coefficient $\Gamma = |\Gamma|e^{j\theta_\Gamma}$ depending on the type of impedance mismatch (F. Farahmand, 2012b).

Type of impedance mismatch $\mathbf{Z_L}$	$\mathbf{|\Gamma|}$	$\mathbf{\theta_\Gamma}$
(non)	0 (no reflection)	irrelevant
$(\alpha + j\beta)Z_0$	$\sqrt{\dfrac{(\alpha - 1)^2 + \beta^2}{(\alpha + 1)^2 + \beta^2}}$	$\tan^{-1}\left(\dfrac{\beta}{\alpha - 1}\right) - \tan^{-1}\left(\dfrac{\beta}{\alpha + 1}\right)$
∞ (open)	1	$0°$ (in phase)
0 (short)	1	$\pm 180°$ (phase opposition)
$jx = \dfrac{1}{j\omega C}$	1	$\pm 180° - 2\tan^{-1} x$
$jx = j\omega L$	1	$\pm 180° + 2\tan^{-1} x$

The phase velocity of a wave is defined in equation (3.14) and can be written in terms of the imaginary part of the propagation constant, where μ_r is the relative permeability.

$$v_p = \frac{\omega}{\beta} = \frac{c}{\sqrt{\mu_r \varepsilon_r}} \qquad (3.14)$$

3.2.4. Equivalent circuit parameters

For a good conductor, the attenuation factor is significant due to the high conductivity. The total equivalent resistance is an averaging root-sum-square function dependent on both its DC and AC behaviour, the latter one caused by the skin effect and becoming significant for high frequencies (E. Bogatin, 2011).

Non-ideal conductor effects due to surface roughnesses cause additional resistance losses and can be taken into account by using (emperical) models like the Hammerstad, Hemispherical or Huray model.

The exact values of the equivalent circuit parameters depend on the geometry of the used wires and their configuration. In general, all geometries of wires can be mainly divided into two types of transmission lines: either the open wire/parallel-conductor/two-wire lines, either the coaxial/ concentric line (where the skin effect plays a major role) (R. D. Straw, 2000). Table 3.2 gives the formulas to calculate these parameters for a coaxial cable and for two parallel cables, for which the geometric properties are shown in figure 3.3 (F. Farahmand, 2012b).

The determination of the equivalent circuit parameters becomes more difficult when more complex geometries are used. Another common cable design is a helical structure where the outer conductor is wound around the central inner conductor. The inclination angle α_S between the central conductor and the outer wire created electrical and magnetic fields which are not longer perpendicular to the central axis of the inner conductor. The calculation of these fields is not easily analytically done and often finite element modelling (FEM) is required. R. Papazyan, P.

Pettersson and D. Pommerenke observed that the screen design not significantly affects the cable losses (R. Papazyan, 2007). A somewhat longer propagation time was seen because of the longer distance to travel due to the inclination angle. The damping was also higher and increased with a decreasing pitch l_d, which is the axial distance required for the helix to complete one winding as can be seen in figure 3.5 (H. Kaden, 1959).

Table 3.2: calculation of the equivalent circuit parameters based on the geometric properties and lay-out of the wires . $\mathbf{R_s} = \sqrt{\dfrac{\mu_c \omega}{2\sigma}}$ and the DC resistance contribution is neglected (F. Farahmand, 2012b).

Equivalent parameter	Coaxial cable		Parallel wires	
R'	$\dfrac{R_s}{2\pi}\left(\dfrac{1}{a}+\dfrac{1}{b}\right)$	(3.15)	$\dfrac{2R_s}{\pi d}$	(3.19)
L'	$\dfrac{\mu}{2\pi}\ln\left(\dfrac{b}{a}\right)$	(3.16)	$\dfrac{\mu}{\pi}\ln\left[\dfrac{D}{d}+\sqrt{\left(\dfrac{D}{d}\right)^2-1}\right]$	(3.20)
C'	$\dfrac{2\pi\varepsilon}{\ln\left(\dfrac{b}{a}\right)}$	(3.17)	$\dfrac{\pi\varepsilon}{\ln\left[\dfrac{D}{d}+\sqrt{\left(\dfrac{D}{d}\right)^2-1}\right]}$	(3.21)
G'	$\dfrac{2\pi\sigma_{dielectric}}{\ln\left(\dfrac{b}{a}\right)}$	(3.18)	$\dfrac{\pi\sigma_{dielectric}}{\ln\left[\dfrac{D}{d}+\sqrt{\left(\dfrac{D}{d}\right)^2-1}\right]}$	(3.22)
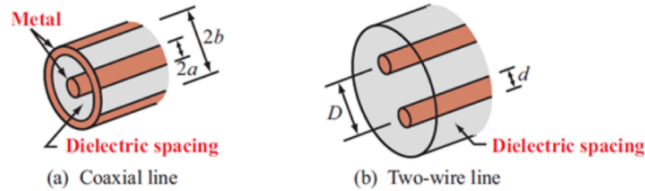
Figure 3.3. Geometric properties of the wires and the dielectric medium used for the calculation of the equivalent circuit parameters in table 3.2 (F. Farahmand, 2012b).

For the twisted pair model, in which two wires are helically interwoven, approximate equations were also derived from the parallel wire model based on the diameter d of the wires and the separation D between the centres of the wires (EEWeb, 2017; Helukabel, 2018).

$$Z_0 = \frac{120}{\sqrt{\varepsilon_r}} ln\left(\frac{2D}{d}\right) \tag{3.23}$$

$$L' = 4.10^{-7} ln\left(\frac{2D}{d}\right) \tag{3.24}$$

$$C' = \frac{2.78.10^{-11}\varepsilon_r}{ln\left(\frac{2D}{d}\right)} \tag{3.25}$$

3.2.5. Standing waves

The local constructive and destructive interaction of the forward- and backward propagating wave causes the creation of standing waves, which are locally only varying in time and do not seem to

propagate in space. Depending on the type of the load mismatch, a node is observed at the end of the transmission line for the voltage (short: the electric field must be zero in a perfect conductor to avoid infinite current) or for the current (open: the magnetic field must be zero because no current is allowed to flow in the isolating free space). For impedance mismatches between these two limiting cases, standing waves can also be observed. However, at the nodes the field doesn't obtain a zero amplitude, it can rather be seen as a superposition of a DC constant voltage or current and a sinusoidal wave. Figure 3.4a shows possible mismatch cases resulting in the creation of standing waves, from which it should be clear that the voltage reaches a maximal amplitude where the current cancels out and vice versa, because they are 90° out of phase (TPub, 2017).

The maximal attainable value of the voltage amplitude is two times the applied voltage and is obtained in one of the limiting cases (open or short). It is important to stress that these equations only hold for lossless transmission lines, because any attenuation will cause the amplitude of the forward- and backward-propagating wave to dampen in space, resulting in a complex standing wave pattern.

The Voltage Standing Wave Ratio (VSWR), which is the ratio of the maximal and the minimal measured voltage amplitude at a position along the transmission line, gives also information on the reflection coefficient (MOHR, 2017).

3.3. Network analysis

At low frequencies, the modelling of the electric circuit by lumped elements such as capacitors, inductors and resistors resulting in equivalent circuit parameters works well. However, at higher frequencies, resonance and dielectric losses can become significant. The much easier analysis in the frequency domain by using a frequency dependent transfer function instead of performing a convolution operation on the impulse response function in the time domain is a major advantage. Network analysis is used for a complete frequency characterisation of interconnects and components.

3.3.1. Reflection coefficient in the frequency domain

The frequencies for which the real part of the reflection coefficient is maximal can also be calculated, which gives information on the equivalent circuit parameters and can be in turn used to calculate other transmission line properties like the phase velocity, characteristic impedance and dielectric constant.

3.3.2. Scattering parameters

Network theory is based on the property that a linear time-invariant system can be completely characterised by parameters only evaluated at the input and output of the system. The S-parameters, which give a relation between the injected and returned power waves and have a close relation to reflection coefficients, are widely used since their popularisation in the 1960s by K. Kurokawa (K. Kurokawa, 1965). Also a relation between the voltage and current at the entrance and exit of each port exists and is given by the ABCD-matrix (C. L. Pin, 2015).
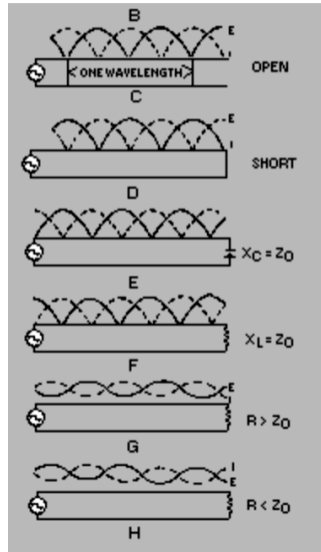
Figure 3.6a. Creation of standing waves of the electric and magnetic field, which are 90° out of phase, for which the position of the nodes is dependent on the load mismatch. The voltage and current are respectively shown by the full and dashed line (TPub, 2017).

3.4. Conclusions

The fundamentals of the propagation, reflection and transmission of electromagnetic waves in media with different electromagnetic properties was summarised. Each discontinuity in these properties will cause a partial reflection of the propagating electric and magnetic field at the interface between the two regions of non-matching properties. Based on the equivalent or lumped parameter approach, in which an equivalent resistance, conductance, capacitance and inductance per unit length were defined, expressions for the characteristic impedance of a transmission line and for both the reflection and transmission coefficient were determined. The relation of each of these four parameters with the physical properties of the conducting wires and the in-between dielectric were elaborated for the parallel wire, coaxial and twisted pair wire transmission line. Hence, the conversion of the complex investigated system into equivalent or lumped circuit elements in the simple world of voltages and currents offers an attractive alternative approach to solving Maxwell's equations. Also the principle of standing waves and their relation with the type of load mismatch were discussed. Finally, this chapter shortly treated the theory of network analysis in which the advantage of transmission line analysis in the frequency domain was made clear.

Chapter 4

Time Domain Reflectometry

Time Domain Reflectometry (TDR) is a widely used NDT technique for characterisation and failure localisation. TDR was initially applied to transmission wires and cables. However, a vast array of applications exists nowadays, varying from moisture or salt content determination, crack growth monitoring and liquid level detection to the detection of shorts and failures in electronic packages and interconnects. This chapter starts with the basics of TDR and shows how localisation of an impedance discontinuity is performed based on the received wave voltage signal in time. Paragraph 4.2 contains a brief history of TDR, which found its origin in Ground Penetrating Radar (GPR) and is nowadays replaced by the more accurate Electro-Optical Terahertz Pulse Reflectometry (EOTPR). Next, the most important parameters influencing the accuracy and performance of TDR are discussed. Paragraph 4.4 explains the complementary Frequency Domain Reflectometry (FDR) technique, after which modelling and simulation examples of TDR are given for complex geometries and transient waves based on solving Maxwell's equations. Finally, paragraph 4.6 gives a comprehensive overview of (current) TDR applications.

4.1. History of TDR

Pulse reflection method, pulse echo method or TDR are terms applied to what is referred to as cable radar (Megger, 2013). Originally the acronym Radio Detection And Ranging (RADAR) was applied to the method for detection of aircrafts and for determining their range and velocity by analysing the reflections of radio waves, which is now used in airport radar systems and police radar guns (Keysight Technologies, 2017). TDR was first suggested by Rohrig in 1931 for cable fault detection and this remained its main area of application for over 40 years until it was suggested as a solution to other engineering problems (L. Bengtsson, 2017). In the 1980s a wide use of TDR started for the determination of the soil water content by using the higher frequency range of 100-200 MHz (K. Kupfer, 2005). Also a large interest from the mining industry arose to detect caving hazards in coal mine roofs (L. Bengtsson, 2017). Because simple approximated relations between the dielectric soil properties and the water content were early established, TDR became the most used method. The geological community started to use TDR for monitoring and predicting landslide hazards (L. Bengtsson, 2017). TDR is widely applicable and data collection is easily automated. A drawback is the strong dependence of the accuracy and precision on the waveform and on the used interpretation methods in software (J. Behari, 2005).

Ground Penetrating Radar (GPR) has a similar operating principle to TDR, but the transmitter and receiver can be located on or above the ground. GPR was originally intended for following the moving wetting front to monitor changes in the soil water content (J. Behari, 2005). GPR is used for determining material thicknesses, detecting cables or steel wires and localising the water table or frost depth. It seems the TDR technique is based on GPR, which was developed earlier.

The maximal attainable rise time (which is defined in paragraph 4.3) with TDR is about 35 ps and results in a bandwidth of 20 GHz, which equals to a resolution of 500 μm. This is clearly a problem when the failure is situated in the vicinity of the interconnect bumps in electronic packages,

because the reflection from these interconnects and the failure discontinuity will overlap (Y. Cai, 2010). Y. Cai et al. introduced Electro Optical Terahertz Pulsed Reflectometry (EOTPR) as an innovative tool for fault localisation of defects based on electro-optics and photoconductive switches that produce a high frequency delta-pulse (E. Kowalczuk, 2014). The system achieved a resolution of 10 μm and a rise time of 5.7 ps. Figures 4.1a and 4.1b clearly show the higher resolution attainable by using EOTPR instead of TDR (Y. Cai, 2010). Because of the complexity of electronic packages, always a Known Good Device (KGD) is required to allow comparison of a bare substrate to a good and a failed package to determine whether the failure occurred inside the substrate, at or after the solder bumps (M. Y. Tay, 2012).

TeraView produces commercially available EOTPR systems like the EOTPR 2000 for imaging and analysis of semiconductor and flip-chip packages or Through Silicon Vias (TSV) (TeraView, 2017). An accuracy of 5 μm together with a rise time smaller than 6 ps is assured. The company provides EOTPR solutions for NDT applications (thickness and uniformity measurements of coatings and structure analysis of composites and ceramics), the pharmaceutical industry (inline control), the solar industry, medical imaging, homeland security (detection of explosives and noxious gasses, personal and mail scanning) and material characterisation (metamaterials and electron carriers).

Optical Time Domain Reflectometry (OTDR) measures the attenuation of back-scattered laser pulses at the faults for localisation of the fibre damage. This technique has an accuracy between centimetres to meters and is for example used in submarine power cables (T. Worzyk, 2009). OTDR techniques were developed to overcome the limited resolution and accuracy of TDR. Ultrasound could also be used, which was illustrated for the monitoring of compressive strains in membranes (R. A. Peterson, 1998).

(a)   (b)
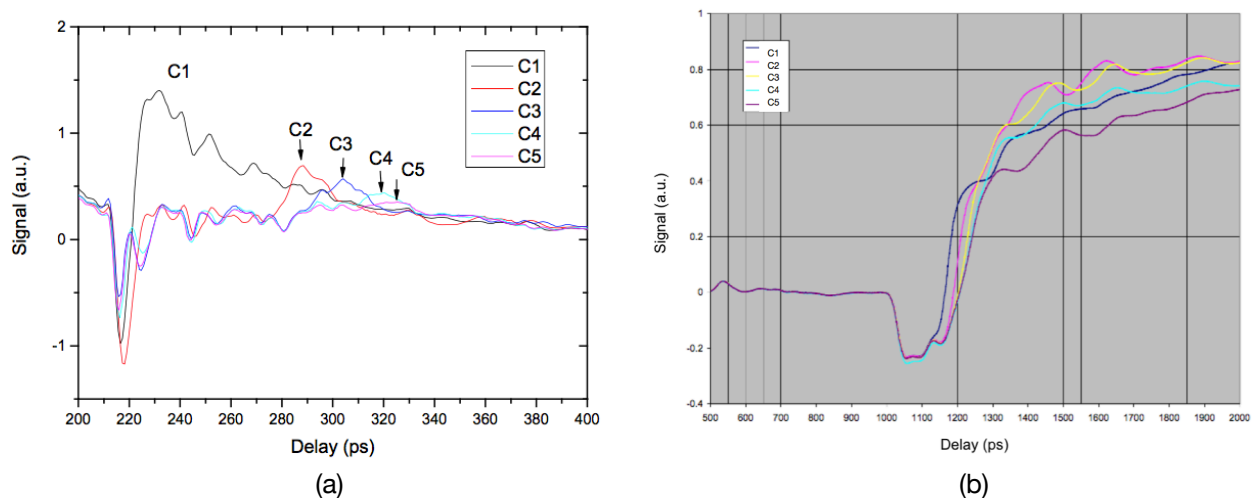
Figure 4.1a and 4.1b. Respectively EOTPR and TDR signals obtained for multiple intentionally created cuts on a package by Focused Ion Beam. With EOTPR the reflections from cut 1 to cut 5 are clearly separated, which is not possible for the TDR signal, and the locations of those failures can be determined from their peaks (Y. Cai, 2010).

4.2. TDR basics

Time Domain Reflectometry, abbreviated by TDR, is a NDT technique used by designers for signal integrity analysis and system performance determination, whereas the failure analyst uses TDR for fault detection and localisation (Electronic Device Failure Analysis Society, 2004). TDR provides an

electronic signature instead of an optical image of the investigated system, the so-called Device Under Test (DUT). In TDR, a transient voltage wave is injected on the DUT and the voltage at the entrance of the DUT is monitored. Hence, the sum of the injected and reflected voltage wave is probed. As discussed in chapter 3, reflections occur at impedance mismatches, which can be real or imaginary. The amplitude and orientation (positive/negative) of the reflected voltage wave depends on the four equivalent circuit parameters R', C', L' and G'. A change in characteristic impedance is caused by cable damage, water ingress, a different cable type, improper cable installation or manufacturing flaws (Megger, 2013). Cable faults are almost always broadband with preferential attenuation of the higher frequencies and indicate a change in geometry of the conductor, a change in the dielectric properties of the insulator and/or a partial or complete interruption of the conductor (MOHR, 2017). The signal modification depends on the attenuation and phase shift. Often the detected reflected voltage is converted and shown as the reflection coefficient. The time after which an impedance discontinuity is detected, can be related to the position of the discontinuity by the main equation of TDR, if the time at which the voltage wave is injected in the system is denoted as time zero:

$$d_{fault} = \frac{v\, t_{TOF}}{2} \tag{4.1}$$

where v is the wave propagation velocity on the DUT, t_{TOF} is the time of flight or round trip time, which is the time between the detection of the cable entrance and the discontinuity and d_{fault} is the position of the discontinuity in the DUT measured from the cable entrance (Megger, 2013).

A typical setup for TDR exists of a wave generator, an oscilloscope and additional probes and fixtures. Supplementary analysis software can also be used (Electronic Device Failure Analysis Society, 2004). Figure 4.2 shows the typical TDR setup where an additional connecting cable is installed between the DUT and the oscilloscope and where an open-circuit load is applied (S. H. Hall, 2009). For transmission line testing, a matched impedance system is used: both the generator resistance R_S and the load resistance R_L match the characteristic impedance of the line at their connection points (J. A. Strickland, 1970). If not, additional reflections will occur at the boundaries between the source, load, connecting cables and the inspected line (DUT), which complicates the signal analysis. Typically a voltage between 10-20 V is applied, but also a lower amplitude is possible (Megger, 2013; MOHR, 2017). Commonly, a source and connecting cable impedance of 50 Ω are used (S. H. Hall, 2009; MOHR, 2017; J. A. Strickland, 1970).
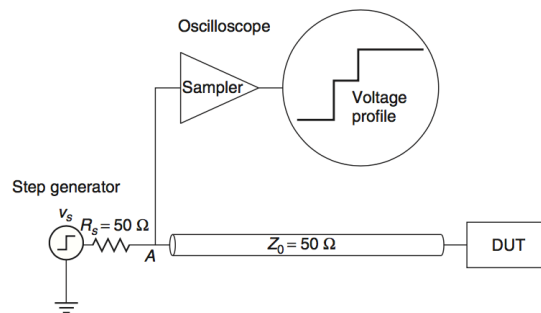
Figure 4.2. Typical TDR setup consisting of a wave generator and an oscilloscope with an additional connection cable to characterise the DUT. An open-circuit load is applied after the DUT, hence a complete positive reflection of the incident voltage wave is expected at the DUT end (S. H. Hall, 2009).

TDR offers a more intuitive and direct look at the DUT than other NDT techniques (Agilent Technolgies, 2017a). Information on the nature of the impedance mismatch (resistive, inductive, capacitive) and its position are obtained together with broadband information. For detecting multiple faults it is better to test the cable from both entrances. An open-circuit load is less

appropriate for cable testing because of unwanted absorption by free space, rather replace it by a short-circuit load (Agilent Technologies, 2017b; Radiodetection, 2017). The TDR accuracy is determined by the system's step response, interconnect reflections, DUT losses, step amplitude accuracy, baseline corrections and accuracy of the reference impedance (Tektronix, 2017).

Multiple back reflections, which are referred to as ghost reflections, occur due to the back and forth propagation of the reflected voltage wave between discontinuities and cause the TDR signature to be less clear. These ghost reflections form a major limitation of TDR. Figure 4.3 shows typical TDR voltage waveforms obtained for a line with multiple discontinuities (Agilent Technologies, 2017b). The orientation (positive/negative), size and waveform of a reflection are related to the type of impedance mismatch present in the system. A comprehensive overview of the possible types of non-reactive (resistive) and reactive (capacitive and inductive) impedance mismatches is given in figures 4.4 and 4.5 (Electronic Device Failure Analysis Society, 2004).

A step-like detected reflection originates from discrete components or loose connectors with a single resistance value, whereas a continuously changing reflection indicates a distributed resistance and occurs on a larger part of the line tested. A series inductance results in a positive reflection, while a parallel resistance causes a negative reflection (J. A. Strickland, 1970).
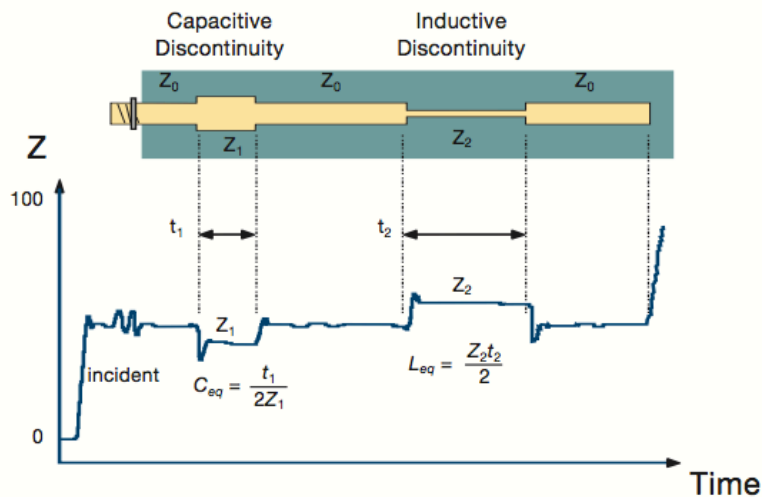
Figure 4.3. Typical oscilloscope (impedance [Ω]) view of the detected voltage waveform for a line with multiple discontinuities (Agilent Technologies, 2017b). Geometric, capacitive and inductive discontinuities are shown.
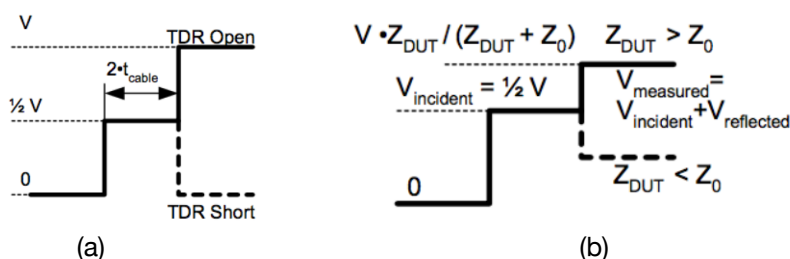
Figure 4.4a and 4.4b. Overview of the possible reflections caused as a function of the type of non-reactive (resistive) impedance mismatch (Electronic Device Failure Analysis Society, 2004). An initial voltage pulse of magnitude 1/2 V was used.
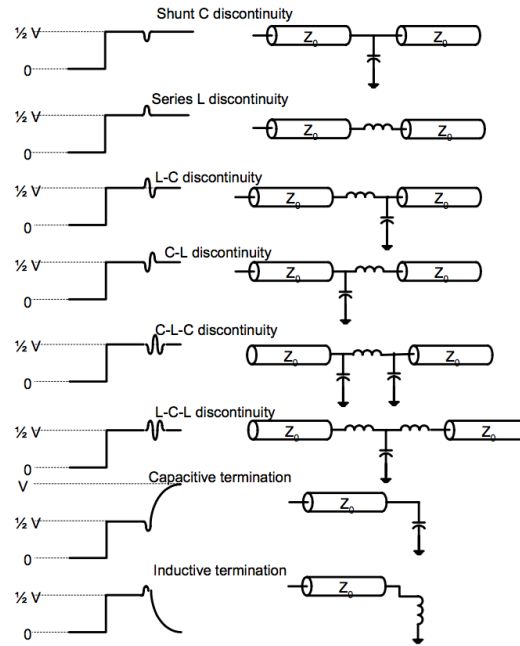
Figure 4.5. Overview of the possible reflections caused as a function of the type of reactive impedance mismatch (Electronic Device Failure Analysis Society, 2004).

4.3. TDR parameters

Multiple parameters influence the performance, accuracy and distortion of the detected TDR voltage wave form. This paragraph discusses the influence of the bandwidth, resolution, rise time, time of flight, pulse width, signal aberrations and the used measurement equipment.

4.3.1. Rise time

The 10-90 % rise time (relative to the attained voltage of the produced spike) is defined in equation (4.2) and can be determined by using the frequency for which an attenuation of 3 dB of the pulse DC voltage occurs, like in a low-pass filter (S. H. Hall, 2009).

$$t_r = t_{10-90\%} = \frac{0.35}{f_{3dB}} \qquad (4.2)$$

A 10-90% rise time of 200 ps results in a bandwidth of 1.75 GHz. The lower frequency components are suppressed by losses or interference with noise in the line, hence 20 kHz is a practical lower limit of the frequency band (J. D. Cooper, 2016). If the distance between two impedance discontinuities is short compared to the width of the pulse's leading edge, the reflections appear to smear out (E. Bogatin, 2011). The best TDR systems provide rise times smaller than 9 ps resulting in a resolution of 1.5 mm (Agilent Technologies, 2017b).

4.3.2. Resolution

A distinction between the amplitude resolution and the time resolution has to be made. Amplitude resolution refers to the ability of a TDR system to display a reflection caused by a discontinuity that produces a very small reflection coefficient (J. A. Strickland, 1970). It is the value of the

reflection coefficient that is equivalent to the amplitude of the displayed noise. For a distributed discontinuity, noise limits the amplitude resolution. Normally, a single discontinuity can be seen if the voltage wave passes along it in a time frame at least equal to one-fifth or one-tenth of the signal's rise time (Electronic Device Failure Analysis Society, 2004).

Time resolution is the minimal time spacing between two equal point discontinuities which gives rise to a 50 % value in between the two received signals of the maximal signal for the point discontinuity (J. A. Strickland, 1970). Time resolution is primarily determined by the system's (10-90 %) rise time (MOHR, 2017). For a rise time of 140 ps, a resolution of 10 mm can be obtained which can be checked with equation (4.3) (D. A. Robertson, 2005). High frequency generators allow resolutions of 2.5-3 mm for rise times down to 30-40 ps (Electronic Device Failure Analysis Society, 2004).

$$\delta_{res} = \frac{v\,t_r}{2} \tag{4.3}$$

4.3.3. Bandwidth

The large bandwidth and the long lines inspected with TDR cause significant attenuation, relaxation and partial reflection resulting in distortion of the signal (J. D. Cooper, 2016). Dispersion is the frequency dependence of the propagation velocity and will result in a smearing out of the pulse. At low or constant frequencies the dispersion effect is neglected or absent, but for sharp transitions and accurate localisation, high frequency components or desirable. A perfectly sharp transition of the received signal occurs when an idealised pulse or step function is used with zero rise time. However, this results in an infinite frequency spectrum with values of the Fourier coefficients for an idealised square wave decaying according to equation (4.4) (S. H. Hall, 2009).

$$F(f) = \frac{\sin(2\pi f)}{\pi f} \tag{4.4}$$

Commonly an effective frequency f_{eff} is used to determine the dielectric parameters. A first method is more pragmatic and compares the measured value of the permittivity obtained from fitting tangent lines to the waveform with the permittivity obtained from the frequency domain dispersion curve, assuming the complex part of the permittivity to be small (D. A. Robinson, 2005). A more theoretic method uses the rise time of the reflected signal and was suggested in a Tektronix application note, which is comparable to equation (4.2) derived for the 10-90 % rise time (J. A. Strickland, 1970).

$$f_{eff} = \frac{\ln\left(\frac{0.9}{0.1}\right)}{2\pi\,t_r} = \frac{0.35}{t_r} \tag{4.5}$$

4.3.4. Time of Flight

The time of flight (TOF) or round trip time, sometimes expressed as delay, is the time it takes for a test signal to travel a certain distance through a medium (Megger, 2013). This parameter may seem easily to derive from the curve of the reflected signal, but actually is considered as one of the main sources of uncertainty in TDR. Accurate TOF measurements are still an open issue. Traditionally the tangent line method was used, which is based on the time resulting from the intersection of the horizontal line drawn at the bottom of the signal before a reflection occurs and the tangent line drawn at the inflection point determined by the first maximum in the derivative during the reflection spike. The velocity derived from this 'extrapolated onset' corresponds to the phase velocity of the injected wave packets (ideally a pulse) on the transmission line (N. Giaquinto, 2015). D. A. Robinson et al. proposed to use the time corresponding to the apex of the derivative in the spike (maximum-derivative method), which is related to the group velocity of the

wave packet (G. M. D'Aucelli, 2017; D. A. Robinson, 2005). Also the time point where the derivative becomes zero just before the reflection spike is a valid choice (N. Giaquinto, 2015). Figure 4.6 shows the time point derived from these three methods (N. Giaquinto, 2015). N. Giaquinto et al. showed the zero-derivative to be the most appropriate when the cable parameters are known, whereas for an unknown cable the tangent method is better. The velocity derived from the maximum-derivative is always lower than the one derived from the tangent method, which is in turn always smaller than the velocity corresponding to the zero-derivative method.
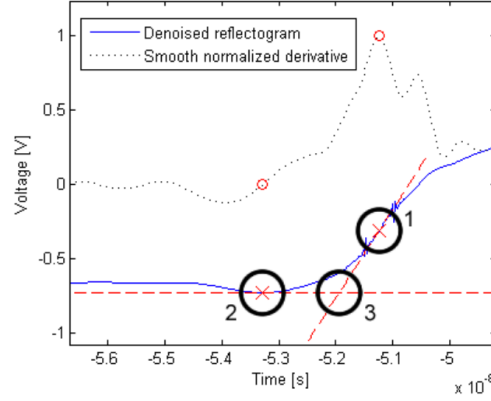
Figure 4.6. Illustration of the three methods for deriving the TOF by determining a characteristic time point for each reflection spike. 1: maximum-derivative method, 2: zero-derivative method and 3: tangent line method (N. Giaquinto, 2015).

The accuracy of the localisation is mainly dependent on the TOF and the propagation velocity, which are strongly dependent on the method used for determining the TOF and frequency dependence of the propagation velocity on the permittivity. A Three-Stake method was proposed by Megger to improve the accuracy by measuring the reflected signal from both cable entrances (Megger, 2013). This method is based on the proportionality of the distance error e to the distance d and allows an improved prediction of the fault's location (or stake) starting from the estimated distance between the fault and each cable entrance. The method is illustrated in figure 4.7 (Megger, 2013).

$$e_1 = d_3 \frac{d_1}{d_1 + d_2} \quad \text{and} \quad e_2 = d_3 \frac{d_2}{d_1 + d_2} \tag{4.6}$$

$$d_{fault} = d_1 + e_1 = d_2 + e_2 \tag{4.7}$$
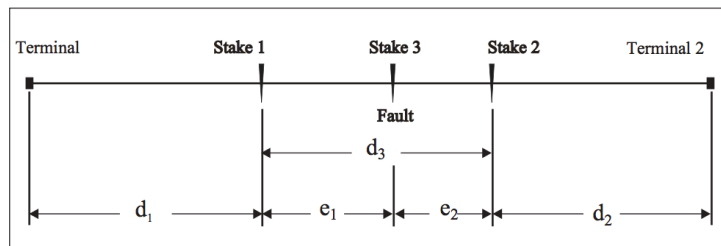
Figure 4.7. Illustration of the Three-Stake method with indication of the required parameters (Megger, 2013).

4.3.5. Pulse width

A longer pulse period results in larger cable lengths that can be investigated, because more energy is injected in the Device Under Test (DUT). However, this involves a decrease in accuracy (Megger, 2013). A pulse width of 2 ns, 10 ns, 100 ns and 1,000 ns respectively allow investigation lengths of 150 m, 230 m, 610 m and 1830 m (Radiodetection, 2017). However, the generated

pulse takes a certain amount of time and distance to launch. This distance is known as the blind spot. Larger pulse widths result in larger blind spots. A pulse width of 2 ns, 10 ns, 100 ns and 1,000 ns respectively result in blind spots of 1.8 m, 4.3 m, 16.8 m and 131 m (Radiodetection, 2017). A pulse width between 80 ns and 100 µs is often applied (Megger, 2013).

4.3.6. Signal aberrations

The response to reactive mismatch loads or defects can only be seen for a limited time and creates transient short-duration pulses that can be characterised by using time constants. Imperfections on these curves are caused by stray capacitances and inductances present in the circuit environment (J. A. Strickland, 1970). N. Giaquinto et al. used wavelet decomposition for preliminary denoising of the reflectograms before determining the TOF (N. Giaquinto et al., 2015).

Ringing is seen after each discontinuity detection and is caused by multiple reflections between two impedance discontinuities. Ringing can be distinguished from a small amplitude impedance discontinuity by looking to the signal after when an open end is detected: superposition of the multiple reflections and the completely reflected voltage pulse occurs. This periodic presence of parasitic multiple reflections is the most common signal integrity problem and is inherent to the TDR method (E. Bogatin, 2011; A. Cataldo, 2011). Back reflections can be eliminated by using impedance deconvolution algorithms, for example layer peeling/dynamic deconvolution (Electronic Device Failure Analysis Society, 2004; MOHR, 2017). Overshoot of the pulse is also a problem (Agilent Technolgies, 2017a).

4.3.7. Measurement equipment

Currently two manufacturers of high-end TDR systems, namely Agilent Technologies and Tektronix, are commercially available (Electronic Device Failure Analysis Society, 2004). High bandwidths of 20 GHz and more are required for accurate localisation. Adequate TDR equipment is already available for approximately $ 900 (A. Cataldo, 2017).

Important factors of the wave generator are the pulse rise time and edge speed (group velocity). The bandwidth of both the wave generator and the oscilloscope limit the attainable rise time (Agilent Technologies, 2017b).

$$t_{r,system} = \sqrt{t_{r,generator}^2 + t_{r,oscilloscope}^2} \qquad (4.8)$$

Average systems produce a system 10-90 % rise time down to 35 ps resulting in a resolution of 5 mm (relative permittivity of one). Use calibration, which means the baseline signal for the studied system is subtracted from the monitored signal to see the applied variations, to minimise the effect of fixtures, probes, connections and other measurement equipment (Agilent Technologies, 2017b). Attenuation due to cables placed before the DUT can be corrected according to equation (4.9) (A. Cataldo, 2011).

$$\Gamma_{corrected} = e^{2\alpha l}\Gamma_{measured} \qquad (4.9)$$

Always remember that the most oscilloscopes are not protected against overvoltage. Precautions have to be taken in order to prevent damage from high (capacitive) charges left on coaxial cables created during manufacture testing (J. A. Strickland, 1970; Megger, 2013).

4.4. Frequency Domain Reflectometry

Frequency domain Reflectometry (FDR) does not locate discontinuities on a distance basis and shows some unique advantages over TDR (J. A. Strickland, 1970). When complementary used to TDR, an extended transmission line characterisation is possible. In FDR, two resonant discontinuities closely spaced together can be clearly separated. However, TDR can show the presence of discrete discontinuities and determine their values better. Also small changes in impedance are better discernible (such as too tight clamping). Both techniques detect single discrete reactances, but the accuracy of FDR is higher. The Voltage Standing Wave Ratio (VSWR) is determined by both TDR and FDR, but TDR can speed-up the tests by selecting the resonance frequencies that have to be tested in FDR. FDR allows direct interpretation of the obtained data, is easy to assemble, requires a lower power consumption and is inexpensive. However, FDR techniques are cumbersome and not handy (J. Behari, 2005).

M. Shafiq et al. determined the propagation velocity on a 154 m medium voltage cable by using the Quarter Wavelength (QWL) method as described in equation (3.14) and by measuring the fundamental resonance frequency f_r, resulting in equation (4.10) (M. Shafiq, 2013). The propagation velocity equalled $1.53.10^8$ m/s.

$$v = 4lf_r \qquad (4.10)$$

The propagation velocity is mainly dependent on the cable dimensions, type and additives of the isolation, the resistance of conductors and the structure of the neutral conductor (corrosion is possible). A typical value is half of the velocity of light (Megger, 2013).

4.5. Modelling and simulating TDR

For more complex transmission line designs and dispersion sensitive materials, computational modelling and simulations are indispensable. Pulses with a sub-ns rise time propagate in higher-order modes where the TEM approximation is not longer valid and hence, dedicated Maxwell solvers are required. However, the price of commercial codes attained values between \$ 10,000 and \$ 50,000. The classic approach consists of solving the telegrapher's equations by using partial differential equations and the equivalent circuit parameters. D. Pommerenke and S. Sakaguchi gave an overview of possible EM field analysis techniques, which are divided for discretisation in space and evolution in time (same techniques complemented by frequency domain methods) (D. Pommerenke, 2002). Main causes of calculation errors are dispersion, the skin effect, an inappropriate discretisation or incorrect dielectric properties. The models should always be tested against simplified analytical methods to check if energy/charge are conserved and if convergence occurs if a quasi-static solution exists.

G. M. D'Aucelli, E. Piuzzi and A. Cataldo used a Matlab simulator to measure arbitrary profiles of equivalent circuit parameters by matching the simulations to TDR experiments. The numeric transfer function for the used probe was determined. By solving a set of nodal equations for each differential block along the probe, the reflected voltage detected in the time domain could be simulated. Care should be taken in choosing the length of a differential block. Equation (4.11) can be used and is based on the wave propagation velocity.

$$\Delta z = \frac{c\, t_r}{10\sqrt{\varepsilon_r}} \qquad (4.11)$$

C. W. Hsue and T. W. Pan proposed the use of a recursive method to determine the characteristic impedance across the line by dividing the reflected signal in differential signals assumed to be constant in each time increment (C. W. Hsue, 1997).

Y. Li, P. Wagenaars et al. discretised a transmission line with a non-uniform cross-section and defined a characteristic impedance and propagation constant to completely characterise each differential part of the line (Y. Li, 2012).

Finally, K.C. Lee, J. Alton and M. Igarashi modelled a flawless replica of the Device Under Test (DTU) in the absence of an experimental equivalent. This was used to calculate the transient EM behaviour on a 3D IC package through solving of Maxwell's equation (K.C. Lee, 2015).

4.6.   Applications of TDR

4.6.1.   Transmission line characterisation

A step signal was used to determine the characteristic impedance of a long transmission line by changing the load resistance until reflections were absent (J. A. Strickland, 1970). TDR is best used for shorter cables because of high frequency attenuation, dispersion and noise become significant for longer cables (M. Shafiq, 2013). However, the conductor losses dominate, certainly for high frequencies where the skin effect becomes important (Tektronix, 2017).

The reflection coefficient can be estimated by the apparent or effective permittivity, which is discussed in paragraph 4.6.2, if the Device Under Test (DUT) is connected to a (resistance and inductance) matched cable (A. Cataldo, 2011). The capacitance and inductance of an electronic package (S. Corey, 2000) and high speed interconnects (X. Zeng, 2007) were also calculated by using the integrated voltage difference between the TDR signal and a reference wave. For the capacitance, an open-circuit reference was used, whereas for the inductance a short-circuit reference was required.

M. Cauwe, J. De Baets and A. Van Calster performed high frequency characterisation of embedded active components in Printed Circuit Boards (PCB) by measuring the characteristic impedance, attenuation coefficient and permittivity (M. Cauwe, 2006). Polymer films with thicknesses in the micrometer range were characterised by J. Obrzut and R. Nozaki based on permittivity measurements (J. Obrzut, 2006).

4.6.2.   Soil water content and moisture measurements

Water consists of polar molecules and hence, a frequency dependent permittivity can be expected due to the electric and orientation (dipole) polarisation (J. Behari, 2005). The real part of the permittivity is little dependent on the frequency, whereas the complex part is small and insignificant unless for saline soils (because of their conductivity). The wave propagation velocity as a function of the dielectric properties is given in equation (4.12) (J. Behari, 2005; D. A. Robinson, 2005):

$$v = \frac{c}{\left[\frac{1}{2}\varepsilon'\left(1 + \left(1 + \tan^2|\delta|\right)^{\frac{1}{2}}\right)\right]^{\frac{1}{2}}} \quad \text{and} \quad \tan|\delta| = \frac{\left(\varepsilon'' + \frac{\sigma}{\omega\varepsilon_0}\right)}{\varepsilon'} \tag{4.12}$$

with ε'' as the pure imaginary part of the permittivity, which is related to relaxation processes and not to the dielectric's conductivity. For very high frequencies the loss tangent reduces to zero and the wave propagation velocity can be written as a function of an apparent or effective permittivity ε_{eff}.

$$v = \frac{c}{\sqrt{\varepsilon_{eff}}}$$ (4.13)

For frequencies sufficiently lower than the relaxation frequency, this parameter approximately equals the real part of the permittivity. From the effective frequency defined in equation (4.5), the apparent permittivity is determined and used to calculate the propagation velocity, which can in turn be used for localisation of the impedance discontinuity when the time of flight (TOF) is known. The velocity in soils is on average $0.6\text{-}1.5.10^8$ m/s (J. Behari, 2005). The dependence of the soil's effective permittivity on the volumetric water fraction can be modelled by a Topp-like equation (K. Kupfer, 2005).

Multiple dielectric relaxation models exist: Debye, Cole-Cole (often used in the food industry for quality control and measuring the dielectric parameters), Havrilick-Negami and Cole-Davidson (A. Cataldo, 2011; D. A. Robinson, 2005)). The Debye model is used for permanent and induced molecular dipoles. If the relaxation frequency increases, the dispersion is larger and the tangent lines used for the determination of the TOF have a lower slope, resulting in a decreased TOF. However, only a few materials behave purely polarly, which is taken into account in the Cole-Cole model by introducing an additional relaxation parameter α.

$$\varepsilon = \varepsilon_\infty + \frac{\varepsilon_S - \varepsilon_\infty}{\left(1 + j\frac{f}{f_{rel}}\right)^{1-\alpha}}$$ (4.14)

where ε_S and ε_∞ are respectively the static permittivity and permittivity at infinite frequency.

For water, a distinction between bound and free water molecules has to be made (J. Behari, 2005). Bound water molecules are adsorbed to the surface of particles and consequently, the dipoles are constrained because of electrostatic interaction between the functional groups within the particle molecule and the water molecule. Water molecules that are located several molecular layers away from the particles can relatively easily move because of the fast decreasing interactions with the functional groups with distance and hence, are referred to as free water molecules. Table 4.1 gives the Cole-Cole parameters for free and bound water. The dielectric constant is lower for bound water because the constrained water molecules are less free to rotate and react to the applied electric field. For ice, the f_{rel} is even lower and has a value close to 10^4 Hz. The relaxation time of bound water is dependent on the thickness of the water film and obtains the same value as for free water for a thickness of 10 times the diameter of a water molecule.

For increasing temperatures, ε_S decreases, whereas f_{rel} increases because of the higher thermal vibration energy of the water molecules, which improves their movability (A. Andryieuski, 2015).

Table 4.1. Cole-Cole parameters for free and bound water (J. Behari, 2005).

Paremeter	f_{rel} [Hz]	α [-]	ε_s [-]	ε_∞ [-]
free water	1.66×10^{10}	0.01	80.4	4.23
bound water	1.71×10^5	0	57.9	3.15

The soil is a composite matter existing of multiple components. Birchak's model is a simple mixing law based on the volumetric fractions of water ϕ_W, solid particles ϕ_S and air ϕ_A (K. Kupfer, 2005).

$$\sqrt{\varepsilon} = \phi_W\sqrt{\varepsilon_W} + \phi_S\sqrt{\varepsilon_S} + \phi_A\sqrt{\varepsilon_A} \tag{4.15}$$

More complex mixture models like the one of Maxwell and De Loor are more accurate.

A more accurate volumetric mixing model was based on the volumetric fractions ϕ of air (A), solid particles (S), bound (BW) and free water (FW) is given in equation (4.26) (A. Cataldo, 2011):

$$\varepsilon^\alpha = (1 - \phi_A)\varepsilon_S^\alpha + (\phi_A - \phi_{FW})\varepsilon_A^\alpha + (\phi_W - \phi_{FW})\varepsilon_{BW}^\alpha + \phi_{FW}\varepsilon_{FW}^\alpha \tag{4.26}$$

where α is a parameter to take the geometry and the polarisation medium into account and ϕ_W is the total volume fraction of water.

A. Dawson monitored the water content in road structures during 7 months in Iceland with TDR and GPR (A. Dawson, 2008). The moisture content was again determined by using the Topp equation (K. Kupfer, 2005).

TDR can also be used to measure the liquid levels in storage tanks, because the propagation property depends on the apparent permittivity of the travelled medium, which changes when absorbing water. L. Bengtsson proposed to wrap the waveguide-pair around a cylinder in order to increase the travelled distance to the cable end and hence, increasing the sensitivity (L. Bengtsson, 2017). The probe design is shown in figure 4.8. The TOF, when compared to straight waveguides, is increased by a factor $\sin(\varphi)$ and is given by equation (4.17), where v_A and v_L are the propagation velocities in the air and the liquid and φ the inclination angle.

$$t_{TOF} = \frac{2l}{v_A \sin(\varphi)} + \frac{2}{\sin(\varphi)}\left(\frac{1}{v_L} - \frac{1}{v_A}\right) \tag{4.17}$$
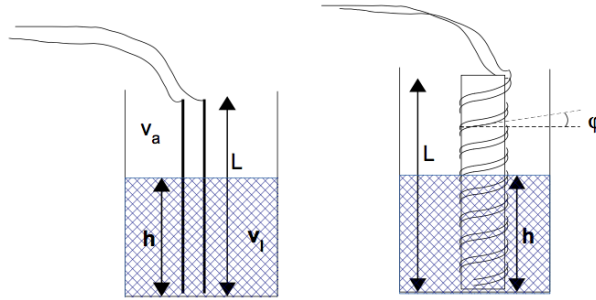
Figure 4.8. Parameters used for the determination of the liquid level. The innovative design with a wound waveguide-pair is shown on the left and results in a higher sensitivity compared to the classic straight waveguide-pair on the right (L. Bengtsson, 2017).

A. Cataldo et al. measured the water content of construction materials before pouring them into the concrete mixture (A. Cataldo, 2017b). This allows the addition of the optimal amount of water to obtain the best mechanical properties. The moisture content (related to the probability of bacteria) of cereals was determined by using TDR in order to assess their health safety and quality (A. Cataldo, 2017a). The large difference between the relative permittivity of water (approximately 80) and dry cereals (approximately 3.8) will cause a decrease of the wave propagation velocity (A. Cataldo, 2011). Hence, the measured length of the cable will be higher than its real value when using the propagation velocity along the probe measured in the dry state.

B. E. Clothier and S. R. Green monitored the change in soil water content in the root zone of a kiwifruit vine in New-Zeeland (B. E. Clothier, 1994). Apparently, a change in the spatial pattern of water uptake occurred as a response of the plants on the application of irrigation water. Finally, the water content of sand was determined by a change in conductivity by P. A. Ferré, J. D. Redman and D. L. Rudolph (P. A. Ferré, 1998).

4.6.3. Soil salinity content determination

Comparable to the determination of the water content of soils, the salt concentration can be measured based on the change in dielectric permittivity due to the interaction of the salt ions and the water molecules. However, the large conductivity of the dissociated salts causes a significant increase in the attenuation constant along the inspection cables (F. N. Dalton, 1986). S. B. Jones, J. M. Wraith and D. Or illustrated the influence of salt concentration and the volume fraction of water on the detected reflection coefficient, which is shown in figures 4.9a and 4.9b (S. B. Jones, 2002). A change of -300% was measured for the reflection coefficient when the conductivity of the soil increased form 0 to 12 dS/m. The apparent cable length clearly increased because of the water-dominated permittivity, which decreased the wave propagation velocity according to equation (4.13).

A similar approach was used by J. O. Payero, D. D. Tarkalson and S. Irmak to monitor the loss of nitrates and nitrogen to ground and surface water (J. O. Payero, 2006). Nitrogen-rich fertilisers are a major environmental and agronomic concern. A decrease in the reflection coefficient indicated a loss due to the increase in bulk electric conductivity of the soil.

(a)   (b)
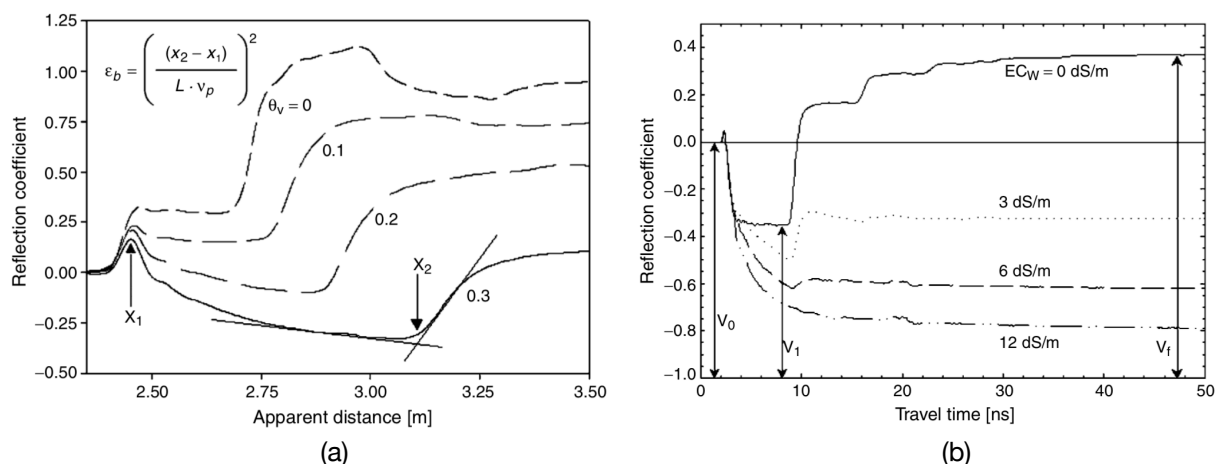
Figure 4.9a. Influence of the volume fraction of water on the detected apparent cable length. A significant increase in the length is observable due to the decreased wave propagation velocity (S. B. Jones, 2002). Figure 4.9b. Influence of the salt concentration of the soil on the detected reflection coefficien. A significant decrease in is observable due to the increased conductivity of the soil (S. B. Jones, 2002).

4.6.4. Leakage detection

A. Cataldo et al. evaluated a TDR-based system for leakage detections along a 100 m buried cast iron pipe (A. Cataldo, 2012). Two leakage spots were applied and their apparent position was derived from the reflected signal. Both leakages spots were observable and could be distinguished from each other. The strongly increased permittivity of the soil due to the water absorption caused a negative reflection which is larger and broader when locally more water was

supplied. 2 Figure 4.10 gives the measured reflection coefficient as a function of the apparent length.
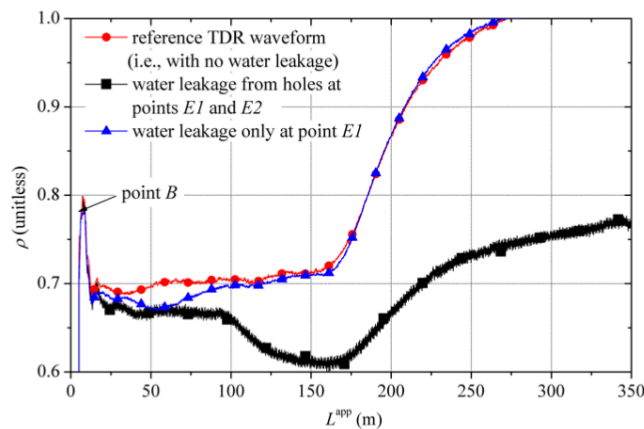
Figure 4.10. Measured reflection coefficient due to leakages in a buried pipe as a function of the apparent length (A. Cataldo, 2012).

Multiple reasons exist for the deterioration of a transmission line cable, but they all naturally age, especially at high temperatures. Treeing in the cross-linked polyethylene insulation is caused by moisture, electrical stresses and protrusions in the isolation (Megger, 2013). A water tree cannot be detected by partial discharge testing and the classic cable health techniques like the withstand test, DC measurement and dissipation factor all required off-line testing. TDR offers an interesting alternative and can detect water trees years before complete failure occurs (K. W. Burkes, 2015). K. W. Burkes, E. B. Makram and R. Hadidi used the equivalent circuit parameter approach to derive the presence and size of a water tree based on the increase in capacitance (closer spacing of the conductors via the water) and causes a negative voltage reflection.

H. M. Hashemian reported the application of TDR in combination with an LCR meter in nuclear power plants for cable diagnostics and the detection of anomalous signals reflected from thermocouples and neutron detectors (H. M. Hashemian, 2006). The main goal was to determine whether the problem was situated inside or outside the reactor vessel, which is critical to assess the degree of safety risk.

The water sealing elements of dams and the infiltration levels of a water basin were also monitored by TDR (K. Kupfer, 2005). The moisture front progress and density determination of snow layers form other applications of TDR in the field of leakage detection.

4.6.5. Failure of transmission lines

The very first application of TDR was the localisation of faults in electric cables. Crack growth and crack sizes can also be monitored with TDR (L. Huakang, 2017). The crack decreases the cross section of a cable and causes an increase in resistance. Also a capacitive effect is coupled to the crack due to the separation of the planes of the crack. TDR is also being used for the localisation of faults along submarine power cables (T. Worzyk, 2009). All landmarks of an electric cable are also measured, like splices, wyes and T-taps, which is illustrated in figure 4.11 (Megger, 2013). The change of the impedance profile over time can also be caused by connector damage and corrosion (MOHR, 2017). Any fault reduces the accuracy of localisation of subsequent faults along the line because of the reduction in pulse amplitude (MOHR, 2017).

However, never dig a hole for inspection of the failed transmission line solely based on TDR: too many variables like the exact propagation velocity, the exact cable route and the accuracy of the used TDR system are not exactly known (Megger, 2013).
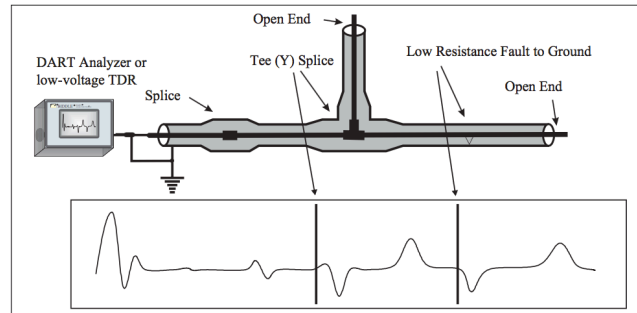
Figure 4.11. Illustration of the influence of landmarks (splices, low resistance paths to ground) on the measured TDR signal (Megger, 2013).

4.6.6. Failure of microelectronics, electronic packages and interconnects

TDR was primarily used in microelectronics for the characterisation and validation of packaging and component interconnects (Electronic Device Failure Analysis Society, 2004; D. H. Jung, 2013; Roderick P. Cruz 2004). The accurate localisation properties and visual nature of TDR form a major advantage over classic failure analysis techniques for electronic packages and interconnects like X-ray and Scanning Acoustic Microscopy (SAM) (Electronic Device Failure Analysis Society, 2004). It allows quick failure isolation with very little preparation of the Device Under Test (DUT) and is therefore often used for complex packaging systems with a number of interconnects, as flip chip bumps, Ball Grid Array (BGA) joints, Through Silicon Vias (TSVs), sockets and wire bonded devices. Other advantages are an improved detection rate, a largely increased probability of successfully developing the root cause of failure and a more timely respond of the corrective action team to the failure (M. K. Chen, 2006; H. T. Devarajulu, 2017; Electronic Device Failure Analysis Society, 2004; W. Yuan, 2007). A TDR measurement together with an X-ray image of a short between two solder bumps is shown in figure 4.12a and 4.12b to illustrate the ease of localising a failure in a complex microelectronic system (Electronic Device Failure Analysis Society, 2004).

4.6.7. Others

G. Pandey et al. used TDR for monitoring the resin flow front in vacuum assisted resin transfer moulding (G. Pandey, 2013). Detection was based on the high permittivity of the dipoles of the monomers, which causes a clear negative reflection of a high frequency pulse at the flow front. The curing of the monomers could also be monitored based on the restriction of the dipole rotation, which decreases the permittivity again.

Between 2007 and 2009, the alpEWAS project developed and tested a 3D warning system for early detection of alpine unstable slopes for landslide monitoring (F. Wenzel, 2014). The deformations of the coaxial cables, which are a herald of a possible landslide, cause changes in the geometry of the cable probe resulting in a changed wave reflection pattern.

A coaxial cable sensor was developed for the detection of cracks and strains in reinforced concrete structures based on the topology change of its outer conductor, which increases the inductance (S. Sun, 2009). The deformations caused changes in the measured TDR voltage wave.
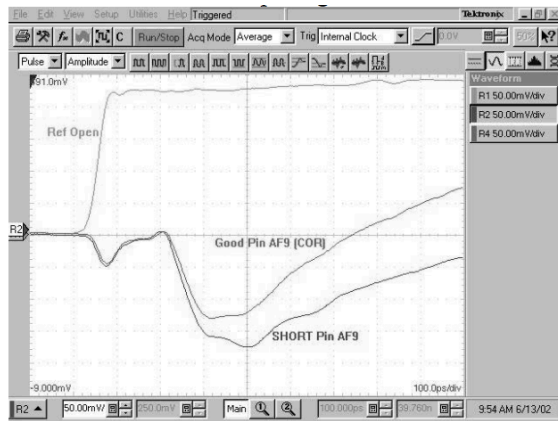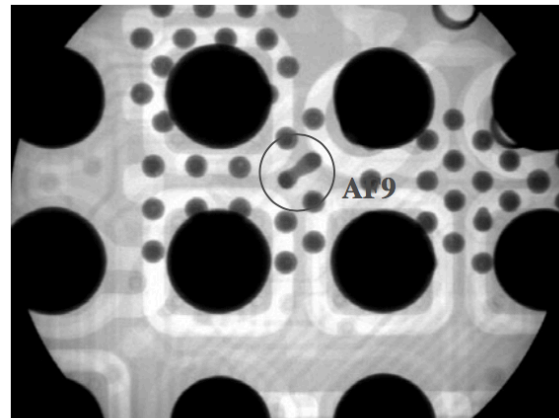
Figure 4.12a and 4.12b. Respectively TDR measurement and X-ray image of a short (denoted by AF9) between 2 solder bumps in an electronic package. The short can clearly be localised by comparing the TDR signal for the good and short-circuited package. Comparison with the reference signal for an unconnected package shows the short is situated inside the package (Electronic Device Failure Analysis Society, 2004).

Crack lengths of 5 mm could already be noticed. S. Miau-Bin investigated the influence of different load conditions on concrete and accompanying fracture formation based on the relative movement of the concrete blocks (S. Miau-Bin, 1990).

4.7. Conclusions

This chapter gave an overview of the fundamentals of Time Domain Reflectometry (TDR) and explained why typically a wave generator, an oscilloscope and calibrated connecting cables are required in addition to the Device Under Test (DUT). Localisation of the fault or discontinuity is possible due to the measured reflection coefficient which can be related to the position of the discontinuity based on the time of flight and the wave propagation velocity. Multiple parameters influence the performance, accuracy and distortion of the detected TDR voltage wave form, namely the bandwidth, resolution, rise time, time of flight, pulse width, signal aberrations and the used measurement equipment. The resistive (resistance and dielectric conductance) and reactive (capacitance and inductance) elements along the inspected transmission line directly influence these parameters. The complementary Frequency Domain Reflectometry technique was also studied and modelling and simulation examples of TDR were given for complex geometries and transient waves based on solving Maxwell's equations.

Time Domain Reflectometry was initially applied to transmission wires and cables and found its origin in Ground Penetrating Radar. However, a vast array of applications exists nowadays, varying from moisture or salt content determination, crack growth monitoring and liquid level monitoring to the detection of shorts and failures in electronic packages and interconnects.

Chapter 5

Materials and methods

This thesis continues the research carried out within the NDT group of the Department of Materials Engineering of KU Leuven concerning the production and characterisation of accurate, sensitive and durable percolation sensors for leakage detection. The past years, several bachelor, master and PhD thesisses focused on the characterisation of the PVA/TiCN percolative composite by measuring the fuse-like resistance behaviour during water absorption or by constructing the phase diagram, including the glass transition, of the ternary PVA/TiCN/water system based on the conductivity (G. De Lescluze, 2017; I. Pitropakis, 2015; H. Pfeiffer, 2012a; W. Tala Taza, 2012). It was generally concluded that the exponential resistance change in the neighbourhood of the lyotropic percolation threshold was an accurate and sensitive property to monitor the moisture absorption by the PVA. However, unlike the detection of water ingress, no localisation of the leakage was allowed based on the resistance change measured between the entrance and end of the sensor. Also the detection of kerosene and Skydrol leakages was monitored with similar rubber-based percolative sensors, for which also only detection and no localisation was possible. Hence, the main research question of this thesis is to assess whether detection and localisation is possible by using TDR based on the changing sensor's characteristic impedance in the area of leakage.

Two percolative sensor designs will be characterised and used for leakage experiments. First, a redesigned prototype of the PVA/TiCN sensor for both water detection and localisation is considered. Next, a conductive nickel coated graphite silicone rubber is examined for both the detection and localisation of kerosene. The same procedure and experiments will be carried on both sensors out to assess and compare the ability of detection and the accuracy of localisation.

5.1. Sensor 1: PVA/TiCN for detection of water

The sensor design is similar to the tailored sensor used within the previous PhD and thesis research that was described in paragraph 2.3.2 (H. Pfeiffer, 2012a; W. Tala Taza, 2012). However, a nylon cord was not longer used: instead a *viscose* protected wire was coated with the PVA/TiCN composite that was previously developed for a partner in the chemical industry. On top of the sensor, a layer of PVA was applied for protection and to speed-up the water absorption (T. A. Papadopoulos, 2013). To make TDR possible, an isolated conductive wire was helically wound around the sensor establishing in this way a twisted-pair cable scheme. Figure 5.1 shows the renewed sensor design. According to the manufacturing data and the research data on the used PVA/TiCN composite, the suggested lay-up and composition of the sensor is given in table 5.1. The sensor lay-up is illustrated in figure 6.2 of the next chapter. Additionally, the original nylon sensor was examined for comparison with the new sensor design. The suggested lay-up and composition of the nylon-based sensor is given in table 5.2.

5.1.1. Dimensional and compositional characterisation of the sensor's cross-section by Scanning Electron Microscopy

Microscopic analysis is carried out to verify the compositional and dimensional data supplied by the manufacturers for a complete and accurate determination of the sensor lay-up. Two cross-sections of the central sensor wire were made and embedded in epoxy before grinding and polishing. One cross-section of the surrounding conductor was made additionally. Imaging was done in a Nova 600 NanoLab Scanning Electron Microscope (SEM) at a voltage of 20 kV and a current of 2.4 nA. Chemical point and area analysis was performed by Energy Dispersive Spectroscopy (EDS).

Additionally, a cross-section of the original nylon-based sensor was examined by SEM and EDS. The same imaging conditions were applied.
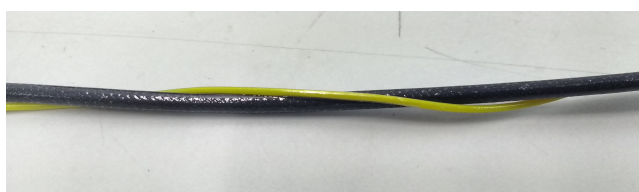
Figure 5.1. Detail of the investigated percolative PVA/TiCN sensor for the detection of water. An isolated conductive wire (yellow) was helically wound around a central wire coated by PVA/TiCN and an additional layer of PVA (black) to establish a twisted pair cable.

Table 5.1. Suggested lay-up and composition of the water detecting viscose-based sensor based on the manufacturing data.

layer	Composition	Dimensions	Manufacturer/source
inner conductor	conductor covered by twined textile (viscose)	-	(Kabel Schmidt, 2018)
PVA/TiCN percolating composite	80 wt% TiCN 20 wt% PVA	-	(HC Starck, 2018) (Acros Organics, 2018)
PVA protection	pure PVA (95.5-96.5 % hydrolysed) (M_W of 85-124 kg/mole)	-	(Acros Organics, 2018)
outer conductor	tinned annealed copper wire PVC insulation	diameter: 1.2 mm	(Farnell, 2014)

5.1.2. Materials cost of the sensor

In order to allow comparison of the designed percolative humidity sensor to the commercially available alternatives mentioned in paragraph 2.2, the materials cost of the sensor per meter was calculated, keeping for sure in mind that the final price must also contain development costs, labour costs as well as overhead and taxes. The diameter of each layer was estimated from the SEM images and together with the materials price per unit volume or unit mass provided by the manufacturers and density data found in literature, an estimation of the complete sensor's materials cost can be made.

Table 5.2. Suggested lay-up and composition of the water detecting nylon-based sensor based on the manufacturing data.

layer	Composition	Dimensions	Manufacturer/source
inner conductor	conductor covered by FEP or PTFE - type ASNE 0261	diameter: 0.75-0.84 mm	(Nexans, 2003)
nylon cord	-	-	(CheapRope, 2018)
PVA/TiCN percolating composite	80 wt% TiCN 20 wt% PVA	-	(HC Starck, 2018) (Acros Organics, 2018)
PVA protection	pure PVA (95.5-96.5 % hydrolysed) (M_W of 85-124 kg/mole)	-	(Acros Organics, 2018)
outer conductor	tinned annealed copper wire PVC insulation	diameter: 1.2 mm	(Farnell, 2014)

5.1.3. TDR signature of the measuring set-up

TDR baseline signature

As discussed in paragraph 4.1, a complete measuring system for TDR consists of a wave generator, an oscilloscope, connecting cables and the Device Under Test (DUT). A DPO 4034 Tektronix oscilloscope (maximal 10-90 %rise time of 1 ns) and a 33250A Agilent Technologies (maximal 10-90 %rise time of 8 ns) wave generator were used (Agilent Technologies, 2000; Tektronix, 2009). The oscilloscope and wave generator were connected by an 1 or 2 m long RG 58 C/U coaxial cable which had a characteristic impedance of 50 Ω (Huber+Suhner, 2007). A splitter was inserted between the coaxial cable to divide the voltage wave between the oscilloscope and the DUT. A BNC-to-banana adapter was placed between the splitter and the oscilloscope. Both the splitter and adapter had a characteristic impedance of 50 Ω (Pasternack, 2018). The inner conductor was chosen as signal conductor, whereas the helical outer conductor acted as the return conductor. An open-circuit load was applied at the end of the sensor. The complete measuring system and its constituting electrical components are shown in figure 5.2.

A square wave was chosen, which is a commonly used wave form as was described in paragraph 4.1, with a period of 4,167 μs and an amplitude of 10 V. The oscilloscope signal was averaged using 512 samples.

Wave propagation velocity and TOF

The reflected voltage wave was recorded and the reflection coefficient at the entrance of the sensor was calculated. The wave propagation velocity was derived based on the different methods summarised in paragraph 4.3.4 for the determination of the TOF. A new additional method was introduced based on fitting a sigmoidal curve on the cable entrance and end, hence using the inflection point as the characteristic time for calculating the TOF. The phenomenon of dispersion of the initial pulse causing a sigmoidal flattening of the sharp edge was the physical basis to choose this fit. Equation 5.1 gives the mathematical expression for the selected sigmoidal fitting curve.

$$V(t) = \frac{p_1}{1 + e^{-p_2(t-t_0)}} + p_3 \qquad (5.1)$$

where t_0 is the inflection time and p_i is a fitting parameter. The length of the sensor was measured with a measuring tape. The impedance spectrum for frequencies between 10 kHz and 40 MHz was measured with a BODE 100 Omicron Lab VNA to verify the estimated length and show Frequency Domain Reflectometry (FDR) to be a useful (complementary) alternative to TDR based on the resonance frequency defined in equation (4.10).
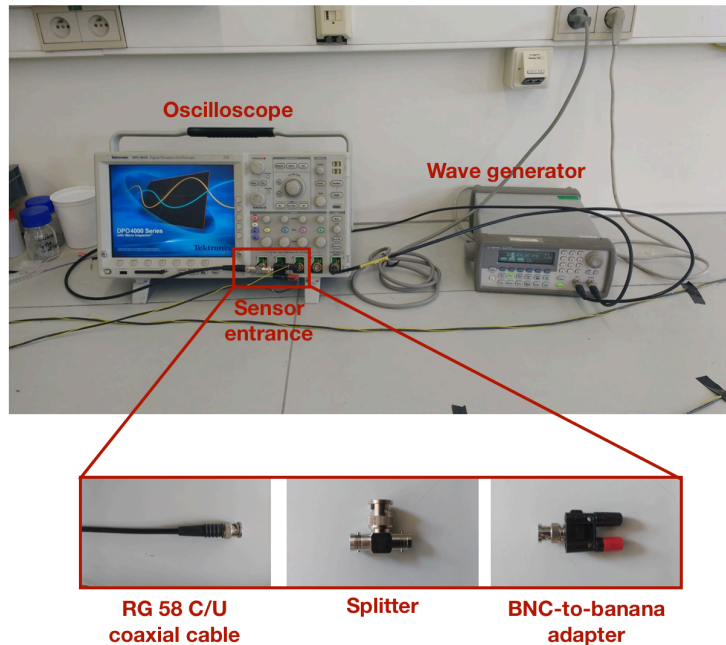
Figure 5.2. Overview of the complete measuring system for the water detecting sensor. It consists of an oscilloscope, wave generator, a connecting coaxial cable, a splitter, a BNC-to-banana adapter and the sensor (DUT).

Influence of sensor entrance and signal conductor

The influence of which side of the sensor functions as entrance (chosen at both sides of the sensor) and the period of the square wave were investigated too. Also the function of the inner conductor as signal conductor and the outer conductor as return conductor were reversed.

Influence of wave frequency and rise time

Normally, a square wave with a period of 5 µs and hence, a frequency of 200 kHz was used. However, it was investigated if an upper limit in the allowable frequency for clear detection and recognition of the sensor's voltage reflectogram exists. This was done by varying the wave frequency into the MHz range and monitoring the voltage reflectogram seen by the oscilloscope. The influence of the rise time on the frequency spectrum present in the wave was also studied.

Uncertainty on wave propagation velocity, TOF and effective permittivity

Uncertainty of the influencing parameters can severely jeopardise the accuracy of the discontinuity localisation. Hence, the uncertainty on the measured TOF and sensor length will be calculated to assess the uncertainty on the derived length/location. An uncertainty of 0.5 cm/20 cm of measured sensor length measured by a measuring tape was chosen based on the experimental average error introduced while measuring the shortest base of a sheet of paper. For the wave propagation velocity, a maximal uncertainty was introduced if the time distance between the inflection point and the time determined by the tangent line method was used. However, when the uncertainty on these time points was derived from the uncertainty of the (fitting) parameters, a

smaller uncertainty will be found for the wave propagation velocity. However, the combined uncertainty on both the sensor length and wave propagation velocity can be calculated according to the theory of uncertainty propagation, denoted by Δ (P. Fornasini, 2008; S. V. Gupta, 2013):

$$\Delta v = \left| \frac{\partial v}{\partial l} \right| \Delta l + \left| \frac{\partial v}{\partial t} \right| \Delta t = v \left(\frac{\Delta l}{l} + \frac{\Delta t}{t} \right) \qquad (5.2)$$

The apparent permittivity will be calculated from equation (4.13) and the uncertainty is equal to equation (5.3).

$$\Delta \varepsilon = \left| \frac{\partial \varepsilon}{\partial v} \right| \Delta v = 2\varepsilon \left(\frac{\Delta v}{v} \right) \qquad (5.3)$$

Lumped parameter model

Finally, the characteristic impedance and consequently the reflection coefficient at the sensor's entrance is estimated based on the materials magneto-electromagnetic properties of the constituting layers of the sensor. The formulas derived for the equivalent parameters, especially the ones reported in table 3.2, will be used to model the sensor as a transmission line.

5.1.4. Water sorption by viscose

It was already shown by multiple authors that PVA is, depending on the temperature range, a very hygroscopic polymer matrix material, especially at the conditions where the sensor is applied. To determine whether the viscose layer should also be taken into account when modelling the influence of water uptake on the dielectric and dimensional properties of the sensor, a simple immersion experiment was carried out (G. De Lescluze, 2017; G. S. Kulagina, 2007; H. Pfeiffer, 2012a; W. Tala Taza, 2012). A 6.7 cm long sample of the viscose protected conducting wire with a weight of 0.858 g (measured with a Gemini Sartorius BP211S balance) was immersed for 45 min in tap water. The weight of the sample was recorded after the sorption measurement to assess the relative mass sorption of water. Next, the viscose textile was removed from the wire and separately tested in a sorption experiment with the same set-up. Finally, a 15 cm long sample of the viscose protected conducting wire was partly immersed in water (exactly 6.7 cm of the wire was present below the water level) to visually estimate the rate of diffusion along the viscose coating. Hence, it is known if the water sorption occurs completely within the time frame of a leakage experiment discussed in paragraph 5.1.6.

5.1.5. Dielectric characterisation of PVA/TiCN, PVA and TiCN by dielectric spectroscopy

Dielectric spectroscopy is a powerful tool to characterise the dielectric behaviour of the investigated materials. The fundamentals of this spectroscopic analysis technique will be explained in the next chapter. However, an overview of the measurements executed within this thesis are given here. Three series of experiments were initiated: low frequency ($< 10^6$) scans for the samples equilibrated in a humidity chamber, temperature-low frequency ($< 10^7$) scans, and temperature-high frequency ($< 10^9$) scans to record the evolution of the dielectric properties.

Low frequency ($< 10^6$) scans in a humidity chamber

A PVA/TiCN coating with the same composition as present within the percolative sensing layer (80wt% TiCN, 20 wt % PVA) was coated on a circular electrode of 40 mm diameter and 2 mm thickness. A humidity chamber was created by using a series of saturated salt solutions, which

are given in table 5.3 together with the RH in the vapour phase above the solutions at 20 °C(L. Greenspan, 1977). All salts were supplied by ChemLab and their required amount for each level of RH was dissolved in 100 ml of deionised water. The saturated salts were chosen such that the lyotrpic percolation threshold, which was estimated to be about a RH of 80% at 20 °C (see figure 2.5b), is included in the RH range covered by the salt solutions. The sample was also equilibrated in room conditions, because the sensor is normally exposed to the surrounding air in the laboratory, for which a RH of 56.8 % was measured (sensor supplied by Farnell). The evolution of the real and imaginary part of the relative permittivity was monitored during the transition to the new RH equilibrium, after the sample was put in a different saturated salt solution, with a Keysight 4284A Precision LCR Meter for 20 Hz to 1 MHz for 0.5 -1 day.

Table 5.3. Used saturated salt solutions together with the RH obtained in the vapour phase above the solutions at 20 °C (L. Greenspan, 1977).

Saturated salt solution	P_2O_5	NaBr	NaCl	KCl	K_2SO_4
RH [%]	≈ 0	59.1	75.5	85.1	97.6

Next, pure PVA was coated on the circular electrode and tested in room conditions, in K_2SO_4 and in the P_2O_5 to examine the effect of the TiCN filler particles on the dielectric behaviour. By following this order of equilibrium RH, all RH levels between almost fully condensed water for the K_2SO_4 and completely dry air for P_2O_5 were momentarily reached. Hence, the drying kinetics are monitored based on the change in the dielectric behaviour.

Temperature-low frequency (< 10⁷) scans

The temperature and frequency dependent behaviour of the PVA/TiCN coating (80wt% TiCN, 20 wt % PVA) was examined by performing for each temperature between -100 °C and 250 °C (steps of 2 °C) a frequency scan between 0.1 Hz and 3 MHz and by recording the real and imaginary part of the relative permittivity together with the conductivity and loss tangent. The measurement was performed in a Novocontrol Alpha analyser. Decalc, a tailored software program written by prof. M. Wübbenhorst, was used for the determination of the glass transition, alpha and beta relaxation of the polymer composite. The temperature was stabilised for each scan by supplying liquid nitrogen to the measuring set-up. The coating was equilibrated in both room conditions and K_2SO_4 to study the influence of water on the dielectric behaviour and observed relaxation peaks.

Pure PVA was also tested with this set-up after equilibration in K_2SO_4 to study the dielectric influence of water on the pure matrix and to compare the results with those obtained for the PVA/TiCN coating, which allows an assessment of the influence of the TiCN filler particles.

Temperature-high frequency (> 10⁶) scans

The temperature and frequency dependent behaviour of the PVA/TiCN coating in room conditions and in K_2SO_4 was also examined for higher frequencies (1 MHz - 1.8 GHz) with a Novocontrol Alpha analyser containing a radio-frequency cell with a coaxial short. Additionally, the pure PVA was studied with this set-up for room conditions.

Pure PVA was also tested with this set-up after equilibration in K_2SO_4 to study the dielectric influence of water on the pure matrix and to compare the results with those obtained for the PVA/TiCN coating, which allows an assessment of the influence of the TiCN filler particles.

Because of the use of dielectric mixture rules within this thesis and because of the large interest on the dielectric behaviour of TiCN at microwave frequencies for current research projects at the

Department of Materials Engineering at KU Leuven, a sample of TiCN was also analysed with this set-up. A disc with a diameter of 3 cm and a thickness of 3 mm was produced starting from the TiCN mixture that was used in the sensor. The disc was densified by Spark Plasma Sintering at 1800 °C for 7 minutes at 50 MPa after it was heated at a rate of 100 °C/minute (which was also used as cooling rate). Next, the disc was sandblasted and made parallel to assure a good connection with the parallel plate electrodes in the dielectric spectroscopic measurements. The relative density was measured by the Archimedes principle with a Gemini Sartorius BP211S balance and Desinfectol (ChemLab). Because of the conductive properties of TiCN, a teflon isolating layer had to be applied between the disc and the electrode to avoid a shortcut between the electrodes and to allow the disc to function as a dielectric.

5.1.6. Water leakage detection and localisation

The series of experiments carried out within this section allow to answer the core research question of this thesis. Is leakage detection of water possible with TDR, especially with the present low cost equipment, and can the leakage spot be localised based on the received voltage reflectogram by TDR? All water leakage experiments can be grouped into three main series of experiments. During series 1 and 3, the DC resistance will also be monitored to detect the leakage when the lyotropic percolation threshold has been reached and hence, to confirm the current leakage detection ability of the sensor based on only the DC resistance.

For all leakage experiments, the same set-up as discussed in paragraph 5.1.3 for the TDR signature of the sensor, was used, which consists of a wave generator, a connecting coaxial cable, an oscilloscope and the sensor (DUT). Additionally, a Fluke 177 Multimeter was connected with clamps to the entrance and end of the sensor to monitor the DC resistance. Because of the isolating protective PVA layer coated on the TiCN sensing layer, the PVA layer had to be locally partially removed with grinding paper to allow a conductive connection between the TiCN layer and the clamps of the multimeter. The influence of the clamps on the TDR signature of the sensor was also examined. At the start of each leakage experiment, the TDR reflectogram of the sensor was recorded and used as a baseline for comparison with the wetted sensor to locate the leakage spot.

Series 1: leakage spots of different size

For all experiments, a square wave with a period of 4,167 µs and an amplitude of 10 V and were used. The load condition of the sensor was always an open-circuit. Four random leakages spots were chosen, which were applied in four separate experiments. However, the distance between them was at least 0.5 m to allow clear distinction of the different spots. The size of the leakage spot was varied between 4 cm (localised leakage) and 1 m (distributed leakage) to study the influence of the leakage spot size. In between each experiment, sufficient time was allowed to assure complete drying of the sensor. Complete drying was assumed when the DC resistance measured over the sensor had approximately reached the value recorded before the experiment. For all experiments, tap water was used.

Figure 5.3 shows a typical wet position in a characteristic industrial application case: harmful water spots usually have a considerable size of approximately 10 cm. Hence, the performed experiments needed to cover the boundary conditions also including smaller and bigger leakage spots.
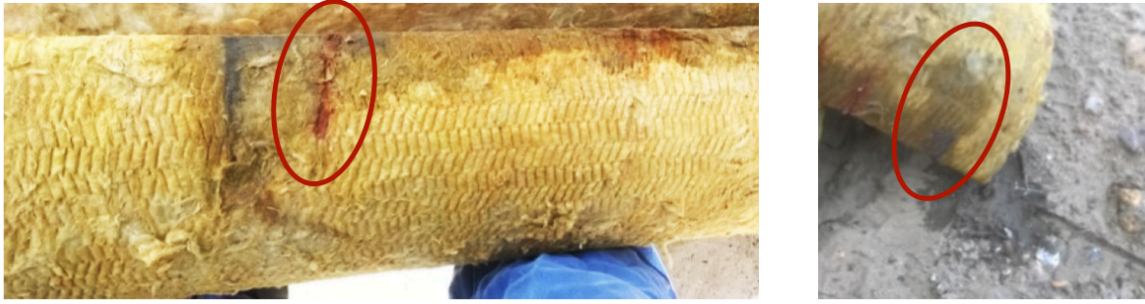
Figure 5.3. Typical wet position, which is indicated by a red circle, in a characteristic application case: harmful water spots usually have a considerable size of approximately 10 cm.

Experiment 1 consisted of the application of 5 droplets of water at a distance of 4.6 m measured form the entrance of the sensor. The leakage spot was covered by a weighing boat and sealed of with tape to avoid expansion of the leakage spot. Every 5 minutes (or every 1 minute when the DC resistance started to increase fast, indicating the lyotropic percolation point) the DC resistance was recorded and the voltage reflectogram was saved on the oscilloscope. The experiment lasted 120 minutes.

Experiment 2 consisted of the application of a wet cotton cloth with a length of 8 cm at a distance of 2.2 m measured form the entrance of the sensor. The leakage spot was covered by a plastic bag and sealed of with tape to avoid expansion of the leakage spot. Every 5 minutes (or every 1 minute when the DC resistance started to increase fast, indicating the lyotropic percolation point) the DC resistance was recorded and the voltage reflectogram was saved on the oscilloscope. The experiment lasted 180 minutes.

Experiment 3 consisted of the application of a 14 cm long spillage of water at a distance of 2.7 m measured form the entrance of the sensor. The leakage spot was left uncovered to visually inspect the expansion of the leakage spot along the sensor and vapour phase. Every 5 minutes (or every 1 minute when the DC resistance started to increase fast, indicating the lyotropic percolation point) the DC resistance was recorded and the voltage reflectogram was saved on the oscilloscope. The experiment lasted 95 minutes.

Experiment 4 consisted of the application of a 1 m long spillage of water at a distance of 4.7 m measured form the entrance of the sensor. The leakage spot was left uncovered to visually inspect the expansion of the leakage spot along the sensor and vapour phase. After 17 hours of exposure to water, the voltage reflectogram was saved on the oscilloscope.

Figure 5.4 gives a visual overview of the location and size of each leakage spot applied. The location of the resistance clamps at the entrance and end of the sensor are also shown.

A MOHR 100 nanopulsor was used once for the detection of a 4 cm wide leakage spot created by wrapping a wet paper around the sensor cloth (same set-up as the other experiments). The lower rise time of 60-100 ps allowed a time resolution of about 1 cm (MOHR, 2017). The nanopulsor was tested to judge the need of a commercially available high-cost wave generator and oscilloscope for the detection of cm-size leakage spots.
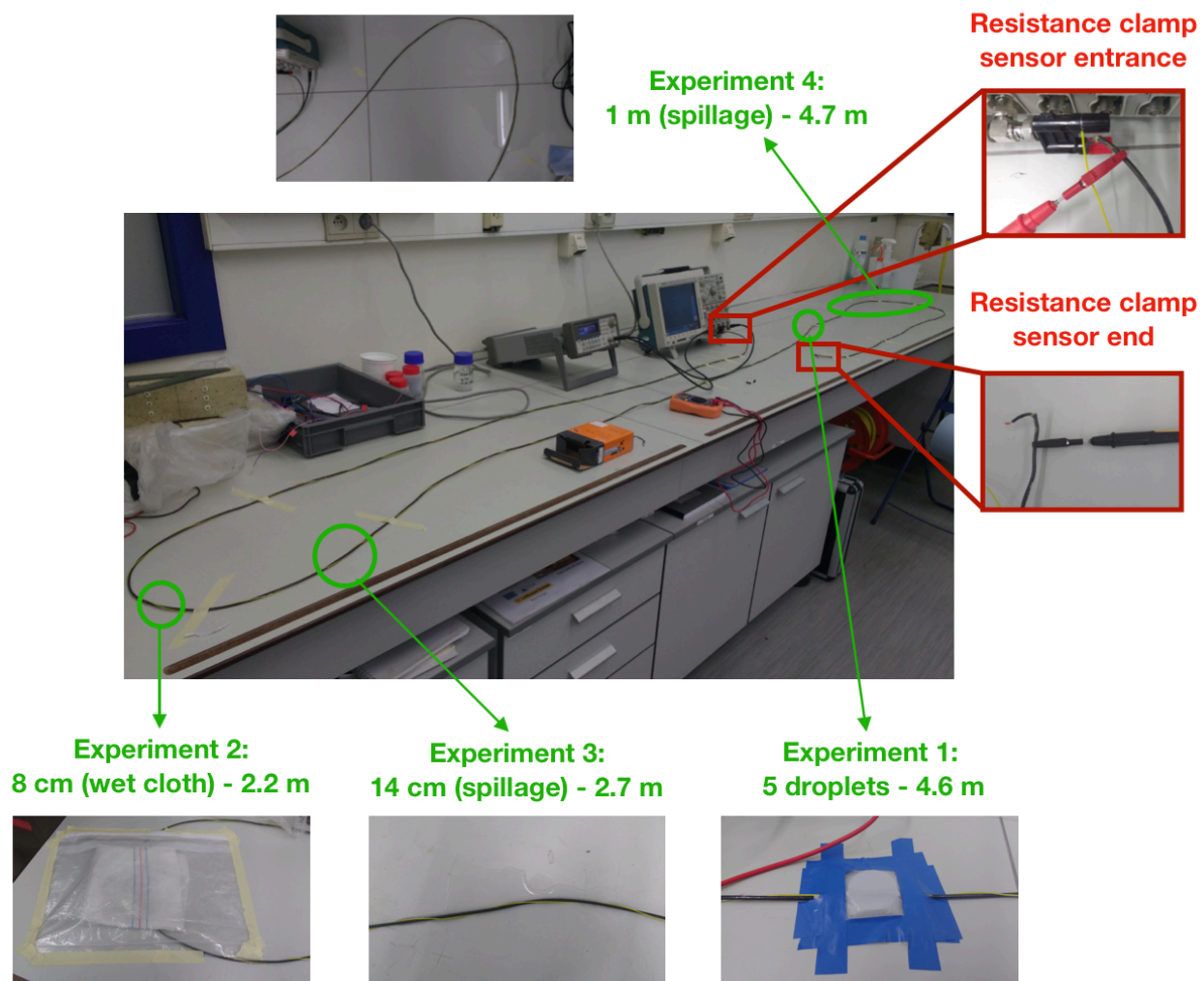
Figure 5.4. Overview of the locations and size of each of the four leakage spots applied in the first series of water leakage experiments. The location of the clamps applied for the DC resistance measurements are also shown at the entrance and end of the sensor.

Series 2: leakage spots of same size at 3 different locations

To support this work, and to show that the results are independent of the operator, the results obtained by Sevilia Sunetchiieva, which were part of her PhD research, were included. Three leakage spots were created along the sensor at a distance of respectively 1.6 m, 3.25 m and 6.7 m. A paper cloth of approximately 20 cm was immersed in water and wound around the sensor representing a good approach to real problems in engineering structure. The cloth was wetted at regular times to avoid drying. Each experiment lasted 1-1.5 hours. For all experiments, a square wave with a period of 5 µs and an amplitude of 10 V and were used. The sample was not averaged. The load condition of the sensor was always an open-circuit. The DC resistance was not monitored. Those 3 experiments were repeated twice to verify the reproducibility of the detected voltage reflectogram. For all experiments, tap water was used. Figure 5.5 shows one of the leakage spots created by winding a wet paper cloth around the sensor.

Series 3: leakage spots of same size at close distance and two simultaneous leakage spots

Based on the successful detection and localisation of the leakage spots created within the PhD research of Sevilia Sunetchiieva, an additional leakage spot was applied at 2.9 m for the first

experiment by again using an immersed paper cloth of approximately 20 cm. The cloth was wetted at regular times to avoid drying. The experiment lasted 100 minutes. The DC resistance and voltage reflectogram were monitored every minute. Tap water was used.

Figure 5.5. One of the leakage spots created within the PhD research of Sevilia Sunetchiieva by winding a wet paper cloth of approximately 20 cm long around the sensor. The paper was regularly wetted to avoid drying.

For the second experiment, two leakage spots were applied simultaneously. The first leakage spot was created at a distance of 2.4 m from the sensor entrance to study the accuracy of localisation compared to the first experiment in which the leakage spot was situated at a distance of 2.9 m from the sensor entrance. An immersed paper cloth of approximately 10 cm was used to study the amplitude resolution of the recorded reflectogram compared to the voltage amplitude of the leakage spot of a 20 cm long immersed paper cloth. Unfortunately, a conductive contact of the clamps with the TiCN sensing layer could not longer be established and hence, the DC resistance was not monitored, which however not reduced the principal value of the test. After 1 hour, the second leakage spot was applied at 5 m to assess the detectability of the sensor when a leakage spot was already present at the same sensor on a location closer to the sensor entrance. The voltage reflectogram was monitored every 15 minutes. Tap water was used.

The sensor's reflectogram before and after the second experiment was recorded also from the other side of the cable, which means the normal sensor end became now the sensor entrance. The motivation of this additional measurement was to assess the improved localisation accuracy of both leakage spots by the Three-Stake method, which was discussed in paragraph 4.3.4.

A square wave with a period of 5 μs and an amplitude of 100 mV were used in both experiments to illustrate that a leakage spot is also clearly observable for lower voltage amplitudes. The load condition of the sensor was an open-circuit.

Figure 5.6 gives a visual overview of the location and size of the three leakage spots. The location of the resistance clamps at the entrance and end of the sensor are also shown.

5.2. Sensor 2: conductive rubber for detection of kerosene

During the previous research, additional sensors were designed to detect mineral oil- and fuel-based liquids, such as engine oil or kerosene, which were described in paragraph 2.3.2 (H. Pfeiffer, 2012a). An electrically conductive metal-rubber composite was used for the detection of those liquids. Currently, a conductive rubber is studied to detect and localise a kerosene leakage spot by DC resistance and TDR measurement. Similar to the water percolation sensor discussed in the previous paragraph, a conducting wire was helically wound around the rubber to allow TDR measurements to establish a twisted pair cable.
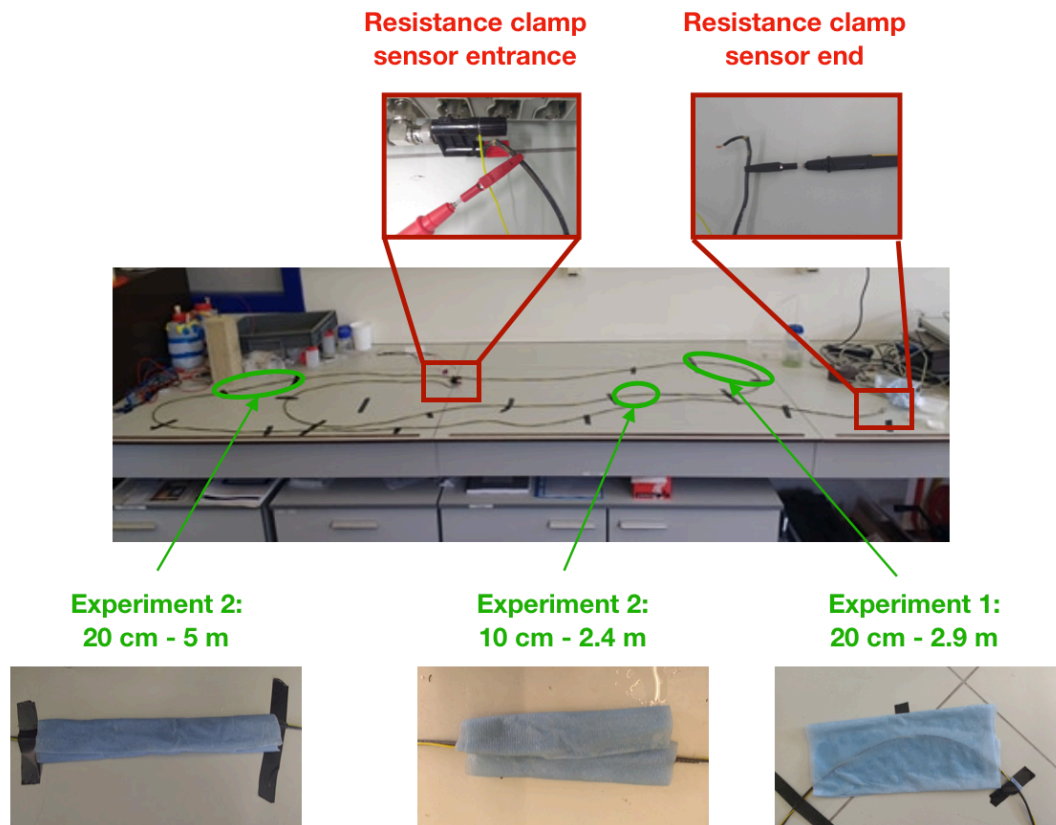
Figure 5.6. Overview of the locations and size of each of the three leakage spots applied in the third series of water leakage experiments. Both leakage spots of experiment 2 were present simultaneously. The location of the clamps applied for the DC resistance measurements are also shown at the entrance and end of the sensor.

It has however to be emphasised that in contrast to the water sensor, where the active sensing material was just between copper cables non-affected by water interaction, here, one part of the twisted cable will be affected directly by the liquid and in this way, one expects a much stronger effect.

Figure 5.7 shows the renewed sensor design appropriate for lab-conditions. For an implementation at industrial sites, probably a somewhat more robust design would be developed. According to the manufacturing data of the rubber sensor, the suggested lay-up and composition of the sensor is given in table 5.4. The sensor is made of a silicone rubber in which graphite coated nickel filler particles are dispersed. These particles form a conductive network and hence, sigmoidal-like behaviour of the DC resistance can be expected when sufficiently kerosene is absorbed as a result of the loss of electrical percolation conductivity after rubber swelling. Because the set-up and analysis of most measurements is similar to the those performed for the water sensor, often a reference to paragraph 5.1 will be made.

5.2.1. Materials cost of the sensor

In order to allow comparison of the designed kerosene sensor to the commercially available alternatives mentioned in paragraph 2.2, the materials cost of the sensor per meter was calculated. The diameter and price per unit length of each layer was supplied by the manufacturer's data and allowed an estimation of the complete sensor's materials cost.
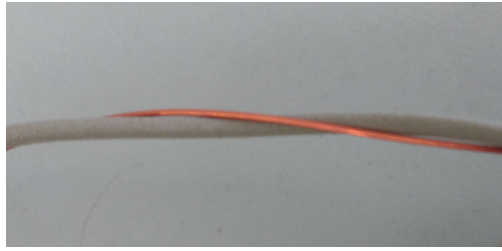
Figure 5.7. Detail of the investigated conductive rubber sensor for the detection of kerosene. An isolated (lacquer) conductive wire (metallic brown) was helically wound around a central rubber wire (light grey).

Table 5.4. Suggested lay-up and composition of the kerosene detecting conductive rubber sensor based on the manufacturing data.

layer	Composition	Dimensions	Manufacturer/source
inner conductor	silicone rubber filled with nickel coated graphite particles	1.6 x 1.4 mm	(Holland Shielding Systems BV, 2018)
outer conductor	enamel coated copper wire	diameter: 0.214-0.226 mm	(Conrad, 2018)

5.2.2. TDR signature of the measuring set-up

TDR baseline signature

As discussed in paragraph 4.1, a complete measuring system for TDR consists of a wave generator, an oscilloscope, connecting cables and the DUT. The same set-up as for the water percolative sensor discussed in paragraph 5.1 was used. The rubber sensor was connected to the oscilloscope by the splitter and BNC-to-banana conductor. The rubber wire was chosen as signal conductor, whereas the helical outer conductor acted as the return conductor. An open-circuit load was applied at the end of the sensor.

For all experiments, a square wave was chosen with a period of 5 µs and an amplitude of 100 mV. The lower voltage was used to study whether the power supplied to the sensor was still large enough to detect a leakage, because the rubber shows a significant attenuation, which was negligible for the water sensor. Additionally, a lower voltage improves the safety in fuel-like kerosene environments where sparks because of sudden electrical discharge must be avoided. The oscilloscope signal was averaged using 512 samples.

Wave propagation velocity and TOF

The same analysis as for the water sensor discussed in paragraph 5.2.1 was executed. The reflected voltage wave was recorded, the reflection coefficient at the entrance of the sensor was calculated and the wave propagation velocity was derived based on the different methods summarised in paragraph 4.3.4 for the determination of the TOF. The length of the sensor was measured with a measuring tape. However, the impedance spectrum was not measured.

Uncertainty on wave propagation velocity, TOF and effective permittivity

Uncertainty of the influencing parameters can severely jeopardise the accuracy of the localisation of the discontinuity. Hence, the uncertainty on the measured TOF and sensor length will be

calculated to assess the uncertainty on the derived length/location. The same analysis was done as for the water sensor.

Lumped parameter model

Finally, the characteristic impedance and consequently the reflection coefficient at the sensor's entrance is estimated based on the materials electromagnetic properties of the constituing layers of the sensor. The formulas derived for the equivalent parameters, especially the ones reported in table 3.2, will be used to model the sensor as a transmission line. The analysis will be more complicated than for the water sensor because of the significant resistive attenuation along the conductive rubber sensor.

5.2.3. Kerosene sorption by silicone rubber

It was already seen during research within the NDT group of the Department of Materials Engineering of KU Leuven that the used rubber absorbs kerosene well, which causes the percolative conductive filler network to be disrupted. To assess the order of magnitude of the absorption, a 5 cm long sample of the rubber with a weight of 0.191 g (measured with a Gemini Sartorius BP211S balance) was immersed for 1.5 hours in kerosene. The weight of the sample was recorded after the sorption measurement to assess the relative mass sorption of kerosene. The kerosene was taken from the fuel tank of the OO-SFZ Airbus 330 from Brussels Airlines.

5.2.4. Kerosene leakage detection and localisation

The series of experiments carried out within this section allow to answer the core research question of this thesis. Is leakage detection of kerosene possible with TDR, and can the leakage spot be localised based on the received voltage reflectogram by TDR? All kerosene leakage experiments can be grouped into two main series of experiments. During both series, the DC resistance will also be monitored in most of the experiments to detect the leakage when the percolation threshold has been reached and hence, to confirm the current leakage detection ability of the sensor based on only the DC resistance.

For all leakage experiments, the same set-up as discussed in paragraph 5.2.1 for the TDR signature of sensor, was used, which consists of a wave generator, a connecting coaxial cable, an oscilloscope and the sensor (DUT). Additionally, a Fluke 177 Multimeter was connected with clamps to the entrance and end of the sensor to monitor the DC resistance. The influence of the clamps on the TDR signature of the sensor was also examined. Each leakage spot was created by immersing the sensor in a weighing boat of approximately 4 cm wide filled with kerosene. Figure 5.8 shows such a leakage spot. For all leakage experiments, kerosene was taken from the fuel tank of the OO-SFZ Airbus 330 from Brussels Airlines.
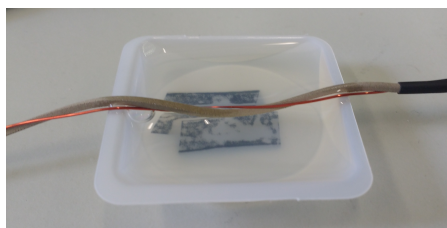
Figure 5.8. Illustration of the leakage spot created by immersing the rubber sensor in a 4 cm wide weighing boat filled with kerosene.

Series 1: leakage spots at 4 different locations

Four random leakages spots were chosen, which were applied in four separate experiments. However, the distance between them was at least 0.5 m to allow clear distinction between the different spots. The leakage spots were located at a distance of 0.30 m, 1.45 m, 1.75 m and 2.64 m. In between each experiment, sufficient time was allowed to assure complete drying of the sensor. A complete drying was assumed when the DC resistance measured over the sensor had approximately reached the value recorded before the experiment. The DC resistance could only be measured for the leakage spots of 1.45 m and 2.64 m, because the sensor had not been completely dried at the time of initiation of the other experiments. The DC resistance was monitored for 15 minutes every (half of a) minute. The voltage reflectogram was recorded every 1 minute for 15 minutes. Depending on the experiment, the reflectogram was saved again after times between 30 and 90 minutes. Figure 5.9 gives a visual overview of the location and size of each leakage spot applied. The lay-out of the sensor looks messy, but one could argue that in practical applications, one would also expect all kinds of bends and turns.
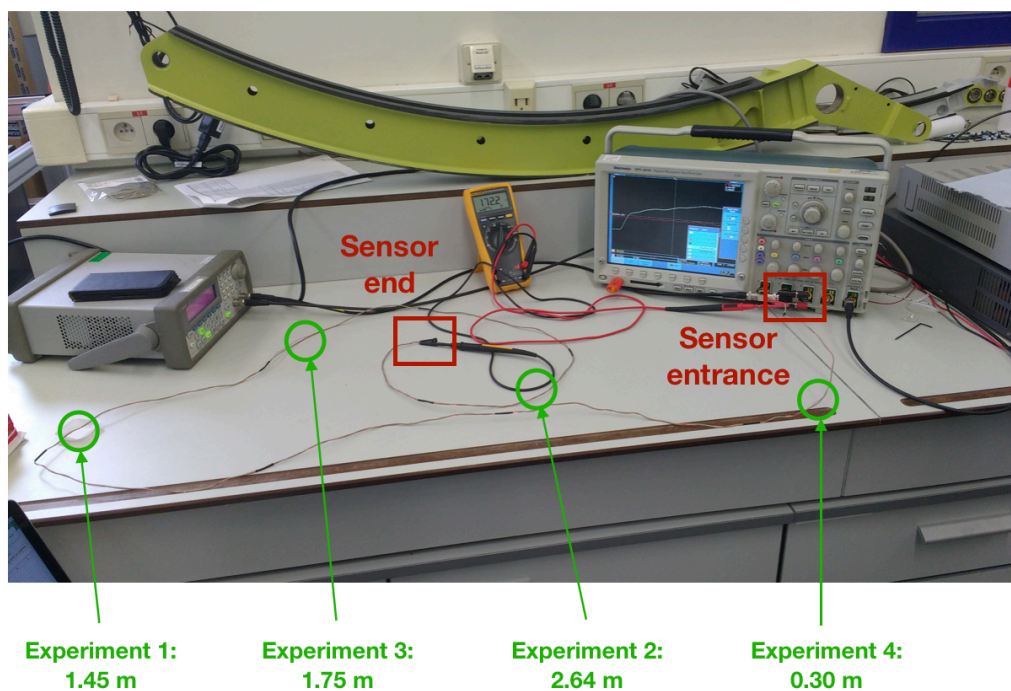
Figure 5.9. Overview of the locations of each of the four leakage spots applied in the first series of kerosene leakage experiments. The location of the clamps applied for the DC resistance measurements are also shown at the entrance and end of the sensor.

Series 2: two simultaneous leakage spots

The DC resistance and voltage reflectogram were monitored every minute. The same kerosene as for the previous case was used.

Two leakage spots were applied simultaneously. The first leakage spot was created at a distance of 0.80 m from the sensor entrance to study whether a significant difference with the dry sensor will be detected first in the DC resistance or in the TDR signal. For an accurate determination of the evolution in time of both signals, the DC resistance and voltage reflectogram are recorded every 15 seconds during the first 10 minutes of the experiment. After 10 minutes, when the DC resistance reached a value of the multimeter's maximal detection range, the second leakage spot was applied at 2 m rom the sensor entrance to assess the detectability of the sensor when a leakage spot was already present at the same sensor on a location closer to the sensor entrance.

The voltage reflectogram was monitored 15 minutes and 1 hour after the creation of the second leakage spot. Both leakage spots are indicated in figure 5.10.
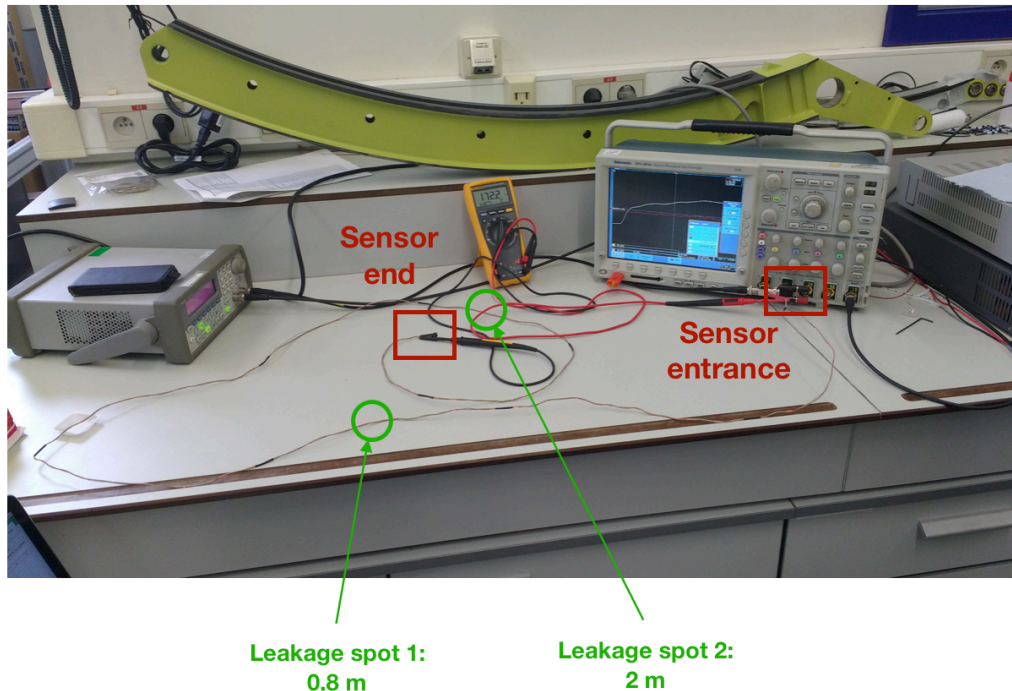
Figure 5.10. Overview of both locations of the leakage spots applied in the second series of kerosene leakage experiments. The second leakage spot was applied 10 minutes after the first one. The location of the clamps applied for the DC resistance measurements are also shown at the entrance and end of the sensor.

5.3.   Conclusions

An overview of all experiments carried out within this research was elaborated in this chapter. Two sensors were studied. The first one was a redesigned version of the TiCN/PVA percolation sensor discussed in paragraph 2.3.2 for the detection of water. The second one was a conductive metal-silicone rubber composite in which nickel coated graphite filler particles are dispersed. To allow TDR, an appropriate coaxial cable was required and hence, a conducting copper wire was helically wound around both the water and rubber sensor to establish a twisted-pair cable design. For both sensors, the TDR signature was recorded by monitoring the voltage reflectogram and the wave propagation velocity was estimated together with the time of flight based on the different methods discussed in paragraph 4.3.4 supplemented by a suggested new sigmoidal fitting method. The integral materials cost was estimated based on the manufacturer's datasheets and by performing Scanning Electron Microscopy to verify the lay-up of the water sensor.

The core research question of this thesis is to assess the detectability and localisability of a leakage spot by TDR. Hence, a series of leakage experiments were initiated. For the water sensor, three series of experiments were carried out, which consist of 4 leakage spots of a different size and at a different position, 3 leakage spots of the same size at different positions and finally two simultaneous leakage spots of the same size at a different position. For the kerosene sensor, two series of experiments were performed. A first consisted of 4 leakage spots of the same size at

different locations along the sensor, whereas for the second series 2 simultaneous leakage spots of the same size were applied at different positions.

The results of the sensor characterisation and the leakage experiments will be discussed in the next chapters together with a model of both sensors and the effect of the leakages on the reflected voltage wave based on a lumped circuit approach.

Chapter 6

Characterisation water sensor

During previous research, the percolation based water sensor described in paragraph 2.3.2 was intensively studied (H. Pfeiffer, 2014). Currently, a renewed, conceptual design of the sensor by replacing the nylon by a viscose textile and by helically winding an outer conductor around the inner wire is used to combine the percolation threshold based DC resistance method and TDR measurements. This chapter elaborates a complete characterisation of the water sensor by calculating its materials cost and determining the TDR signature for both the dry sensor and when leakage spots are applied. The suggested lay-up based on data supplied by the manufacturers is verified by Scanning Electron Microscopy and Energy Dispersive Spectroscopy. The time of flight, wave propagation velocity and permittivity are estimated based on both traditional and proposed new methods to allocate a characteristic time point to the sensor entrance and end. The detectability and localisability of a single and multiple leakage spots at different positions along the sensor is assessed. Finally, dielectric spectroscopy is used to map the dielectric behaviour of PVA and TiCN at room conditions and for a series of relative humidities.

6.1. Dimensional and compositional characterisation of the sensor's cross-section by Scanning Electron Microscopy

6.1.1. Viscose-based design

Figure 6.1a and 6.1b show the (detail of the) cross-section of the viscose-based water sensor obtained by Scanning Electron Microscopy (SEM). A bundle of wires was clearly seen around which an isolating layer was applied together with a spongy textile layer on top of it. Finally, 2 layers were present on top of the spongy layer. Figure 6.1c shows the cross-section of the outer conductor obtained by SEM. A bundle of wires was present, but during grinding and polishing wear-out of the wires occurred.

Energy Dispersive Spectroscopy (EDS) was used to determine the composition of each layer by executing both spot and area analyses, which allowed together with the measured layer thicknesses an estimation of the sensor's lay-up. The observed lay-up confirmed the suggested one by the manufacturer's data defined in table 5.1. Table 6.1 gives an overview of the measured composition (at%) of each layer. A mapping of the distribution of the elements detected in the viscose-based inner conductor and the outer conductor can be found in Appendix A.1. Figure 6.2 contains an illustration of the total sensor lay-up together with its materials composition and dimensions.

The PVC ($C_2H_3Cl)_n$ layer contained significant traces of calcium and some magnesium. Calcium-zinc particles are sometimes added as heat stabilisers, whereas $CaCO_3$ is the most commonly used filler to lower the cost of PVC (S. Patrick, 2004; C. P. Sugumaran, 2015). $Al_2(OH)_6$ and $Mg(OH)_2$ are widely used flame retardants. Viscose rayon ($C_6H_{10}Cl_5)_n$ is a textile made of regenerated cellulose fibres, which is commonly used for clothing and industrial yarns (Polymerdatabase, 2018). The traces of silicon probably originated from the grinding and

polishing. The composition found for the PVA/TiCN layer is approximately equal to 80 wt% TiCN, which was the predefined amount chosen for this sensing layer. PVA has $(C_2H_4O)_n$ as formula.

(a)

(b)

(c)

(d)
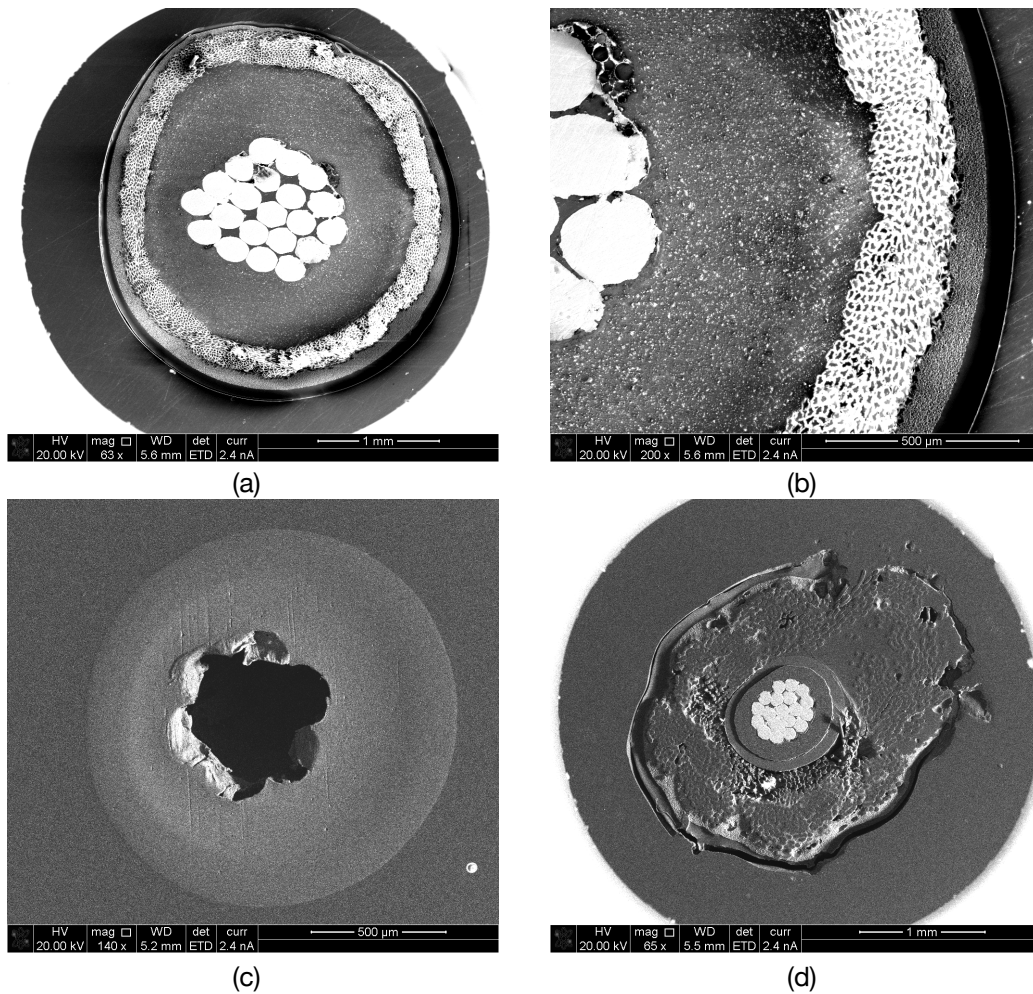
Figure 6.1a and 6.1b. Cross-section of the viscose-based water sensor (with a detail of the viscose-PVA/TiCN-PVA layer included). Figure 6.1c. Cross-section of the outer conductor (the bundle of wires wear out during grinding and polishing. Figure 6.1d. Cross-section of the nylon-based water sensor. All images were obtained by SEM.

Table 6.1. Composition of each layer of the viscose-based water sensor obtained by EDS.

Layer	Composition [at%] (error)	Materials
bundle of wires	Cu: 100(2)	copper
isolating layer	C: 60(10) - O: 20(11) - Cl: 10(1.5) - Ca: 10(1.9) - Mg: 0.6(8.8)	PVC with $CaCO_3$ filler
spongy layer	C: 80(7) - O: 17(12) - Si: 3(2.8) - Cl: 0.3(6.7)	viscose rayon
PVA/TiCN percolating composite	C: 58(7) - O: 14(12) - Ti: 29(2)	PVA with TiCN particles
PVA protection	C: 80(4) - O: 20(13)	PVA
outer conductor	C: 66(12) - O: 11(12) - Cl: 21(1) - Ca: 1.5(4.2)	PVC (around copper)

Layer	Layer thickness
HELICAL OUTER WIRE	
PVC insulation	0.5 mm
Cu wire - 7 strands	0.63 mm diameter
CENTRAL INNER WIRE	
PVA topcoating	0.08 mm
PVA/Ti0.7C0.3N 20/80 wt% sensing coating	0.10 mm
viscose insulation	0.23 mm
PVC insulation	0.56 mm
Cu wire - 21 strands	1.20 mm diameter

1.63 mm

3.14 mm
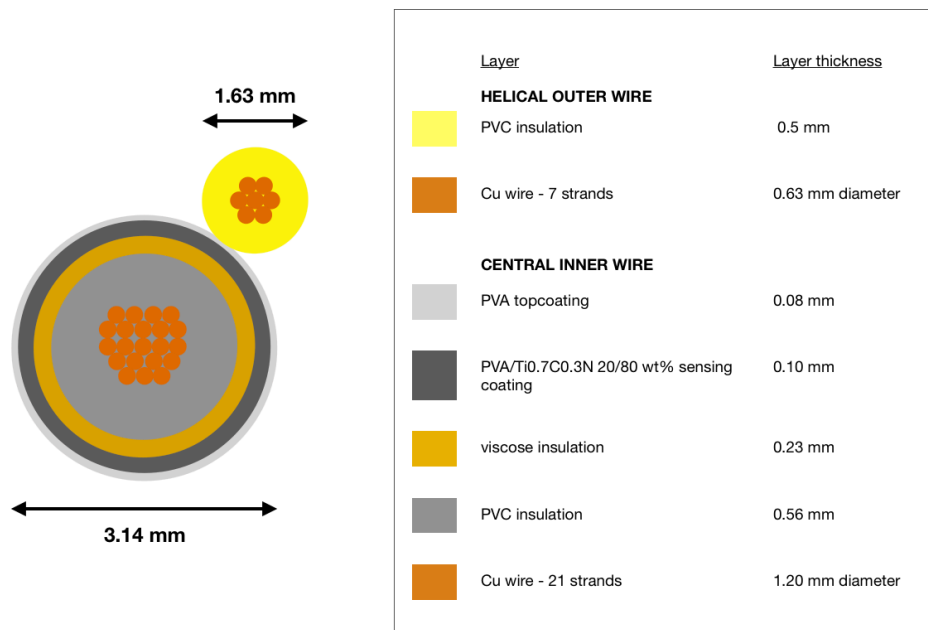
Figure 6.2. Illustration of the cross-section of the viscose-based water sensor based on the cross-sections imaged with SEM. The viscose layer is together with the PVC insulation and copper wires denoted as inner conductor.

6.1.2. Nylon-based design

For comparison with the old sensor design, which is used in Lufthansa aircrafts, a cross-section of the nylon-based water sensor was also made. Figure 6.1d shows this cross-section imaged with SEM. The sensor lay-up is similar to the viscose-based sensor, except for the inner conductor, which consisted of layered FEP or PTFE tapes instead of PVC isolation. The inner conductor was surrounded by a thick textile-like layer, which was nylon. The 2 layers present on top of the nylon were again a PVA/TiCN and a PVA layer. In the original design, no outer conductor was included, which is not included in the illustration in figure 6.3 of the total sensor lay-up together with its materials composition and dimensions.

The observed lay-up suggested by the manufacturer's data was again confirmed by EDS, as is shown in table 6.2. A mapping of the distribution of the elements detected in the nylon-based inner conductor can be found in Appendix A.1.

The isolating layer contained a lot of trace elements of which some are unexpected (antimony, zinc). No explanation for their presence was found in literature or in the manufacturer's datasheets. The outer jacket of the inner conductor clearly consists of PTFE or FEP based on the significant amount of fluor present. The textile layer is made of nylon for which the carbon/oxygen ratio is 6/1 for the widely used nylon 6 and nylon 66 types. The traces of silicon probably originated from grinding and polishing. The composition found for the PVA/TiCN layer is approximately equal to 80 wt% TiCN, which was again the predefined amount chosen for this sensing layer.

6.2. Materials cost of the sensor

The materials cost for each layer and the complete sensor was estimated based on the price per length supplied by the manufacturers and is given in table 6.3 and 6.4 for respectively the nylon-based and viscose-based sensor.

6.2.1. Nylon-based sensor

The largest contribution to the total price are the PVA/TiCN sensing layer (39 %) and the inner conductor (35 %). The contribution of both the PVA protecting layer and the outer conductor are negligible. A total price based on the materials cost of € 0.92/m was estimated for the complete sensor.

Layer	Layer thickness
PVA topcoating	0.02 mm
PVA/Ti0.7C0.3N 20/80 wt% sensing coating	0.08 mm
nylon insulation	0.63 mm
FEP or PTFE inslulation	0.09 mm
2 FEP/PI/FEP tapes - insulation	0.17 mm
Cu wire - 19 strands	0.49 mm diameter

2.46 mm
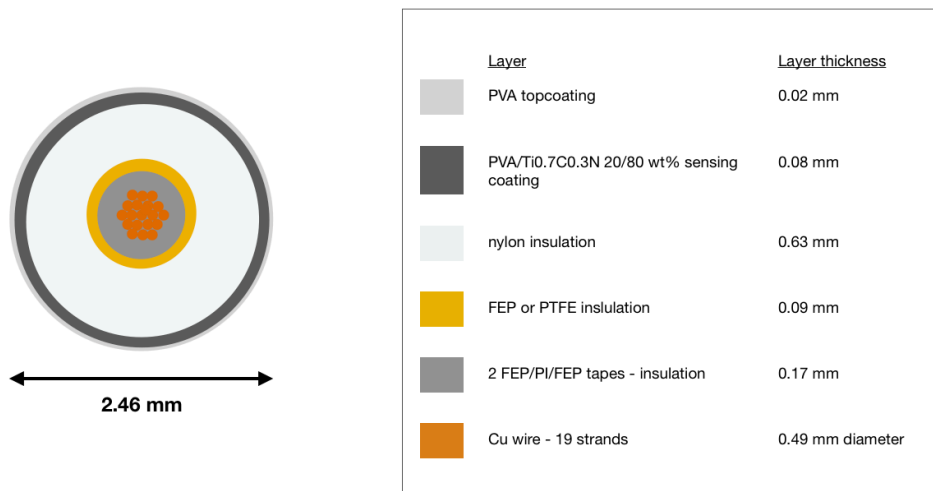
Figure 6.3. Illustration of the cross-section of the nylon-based water sensor based on the cross-sections imaged with SEM. The FEP/PTFE layers are together with the copper wires denoted as the inner conductor.

Table 6.2. Composition of each layer of the nylon-based water sensor obtained by EDS.

Layer	Composition [at%] (error)	Materials
bundle of wires	Cu: 73(2) - C: 22(12) - O: 4.9(12)	copper
isolating layer	C: 95(7) - O: 1.4(52) - Zn: 0.9(6.5) - Sb: 0.8(7) - S: 0.7(3.2) - Si: 0.3(6.2)	FEP/PI
jacket inner conductor	C: 62(8) - F: 29(9) - O: 6.6(12.8) - S: 1.1(4.1) - Si: 0.5(6) - Zn: 0.5(9.5)	FEP/PTFE
textile layer	C: 80(4) - O: 20(14) - Si: 0.2(5.1)	nylon
PVA/TiCN percolating composite	C: 54(7) - O: 18(12) - Ti: 28(2)	PVA with TiCN particles
PVA protection	- (too thin)	PVA

6.2.1. Viscose-based sensor

The largest contribution to the total price is the inner conductor (58 %), followed by the PVA/TiCN sensing layer (31 %). The contribution of both the PVA protecting layer and the outer conductor are again negligible. A total price based on the materials cost of € 1.72/m was estimated for the complete sensor, which is twice the estimated price for the nylon sensor. The viscose-based sensor has a 25 % larger diameter than the nylon-based sensor, but the main reason for the doubled materials cost is the expensive viscose-based inner conductor. Nevertheless, only the sensing layer has to be coated onto the inner conductor and no embedding of the inner conductor in the nylon cord is required and hence, this probably lowers the machinery and production costs, which makes the viscose-based design advantageous again.

Table 6.3. Materials cost for the complete nylon-based sensor and each composing layer.

Layer	Price [€/m]	Contribution to total sensor price [%]	Manufacturer/source
inner conductor	0.32	35	(Holland Shielding Systems BV, 2018)
nylon cord	0.06	7	(CheapRope, 2018)
PVA/TiCN percolating composite	0.36	39	(Acros Organics, 2018) (HC Starck, 2018)
PVA protection	0.07	7	(Acros Organics, 2018)
outer conductor	0.11	12	(Farnell, 2014)
total sensor cost	**0.92**		

Table 6.4. Materials cost for the complete viscose-based sensor and each composing layer.

Layer	Price [€/m]	Contribution to total sensor price [%]	Manufacturer/source
inner conductor	0.99	58	(Kabel Schmidt, 2018)
PVA/TiCN percolating composite	0.53	31	(Acros Organics, 2018) (HC Starck, 2018)
PVA protection	0.09	5	(Acros Organics, 2018)
outer conductor	0.11	6	(Farnell, 2014)
total sensor cost	**1.72**		

The price for both the nylon-based and viscose-based sensor is an order of magnitude lower compared to the cost of € 14-40/m for the commercially available sensors discussed in paragraph 2.2. However, the materials cost should be understood as the marginal cost of the sensor, which is the cost for an extra sensor produced and hence, fixed costs as machinery, construction of the production facility and labour, the latter one being also a marginal cost, were not included. Nevertheless, the estimation of the materials costs confirms the developed sensor to be a low-cost alternative to the currently available commercial leakage sensors.

6.3. TDR signature of the measuring set-up

6.3.1. TDR baseline signature

Within this thesis research, only the viscose-based sensor was studied, without loss of generality. Figure 6.4 shows the TDR voltage reflectogram measured for the dry sensor. Both the sensor entrance and end are clearly recognised and no significant resistive attenuation is seen along the sensor (nearly constant reflected voltage between the sensor entrance and end). A DC resistance of the copper inner and outer conductor of respectively 1.1±0.1 Ω and 1.6±0.1 Ω was observed over the complete sensor length, whereas the value for the PVA/TiCN sensing layer was 27.7±0.1 kΩ. A DC resistance out of the multimeter's detection limit was observed when measuring between both conductors, indicating no conductive path in between the conductors was present for the sensor, which was intended by the sensor design.

A length of 7.93±0.20 m was measured for the sensor via a measuring tape. The outer conductor was helically wound around the rubber wire and an inclination angle of 7.5 ° was measured. The splitter and the BNC-to-banana connector were assumed to coincide and hence, the point in time when the voltage wave was detected by the oscilloscope equals the point in time for which the sensor entrance was reached.
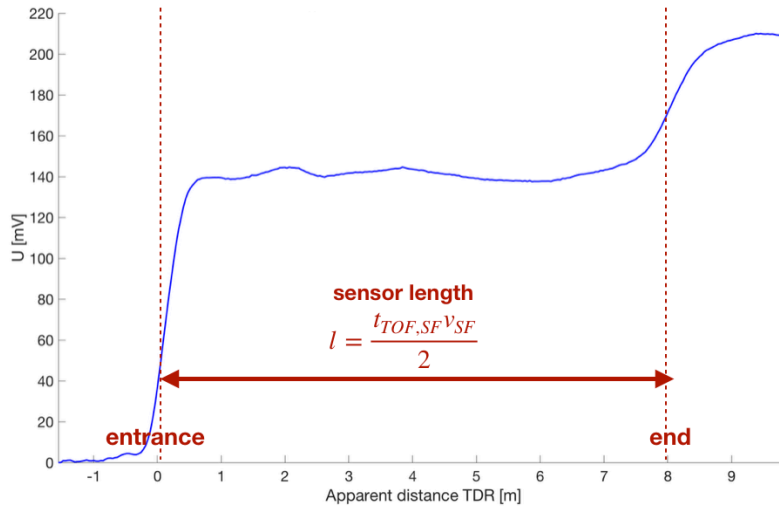
Figure 6.4. TDR signature of the water sensor. Both the entrance and end of the sensor are indicated. The apparent distance between them is calculated by using the time interval between the entrance and end determined by the sigmoidal fitting (SF) method, which allows the calculation of the time of flight (TOF) and the wave propagation velocity (v).

Influence of signal conductor

Normally, the inner conductor was used as the signal conductor, whereas the outer conductor functioned as the return conductor (and is connected to the ground). Figure 6.5 shows the influence in the sensor's TDR signature if the function of both conductors was reversed. A small difference was observed, which probably was an artefact inherent to the process of changing the contacts. However, by always using the same conductor as the signal conductor, it was assured that no differential voltages compared to the baseline were introduced.

Impedance spectrum

Figure 6.6 contains the impedance spectrum measured for the sensor connected to the impedance analyser by a 1 m long RG 58 C/U coaxial cable. The total impedance measured at the entrance of the spectrum analyser was seen to be dominated by the reactance. For 5.2 MHz a sharp singularity was observed for the impedance. This was caused by resonance of the voltage wave on the sensor set-up. The occurrence of standing waves was discussed in paragraph 3.2.5 and is seen when the measured voltage reaches a minimum at the entrance of the analyser, which causes a minimum in the measured impedance. In case of an open-circuit load, an antinode in the voltage must present at the sensor end, whereas a node should be present at the analyser entrance. Because of the non-zero attenuation/resistive contribution along the sensor, the voltage did not reach a zero value at the resonance frequency. The assumption of the phenomenon of resonance occurring was confirmed by the frequency for which the first antinode was found, which equalled 9.3 MHz (almost two times the first harmonic frequency), because the first antinode occurs for a wavelength half of the one for the first harmonic frequency. Additionally, the second harmonic frequency was found to be 15.8 MHz, which is approximately three times the first harmonic frequency, as was expected (a three times smaller wavelength is present for the second harmonic compared to the first harmonic).
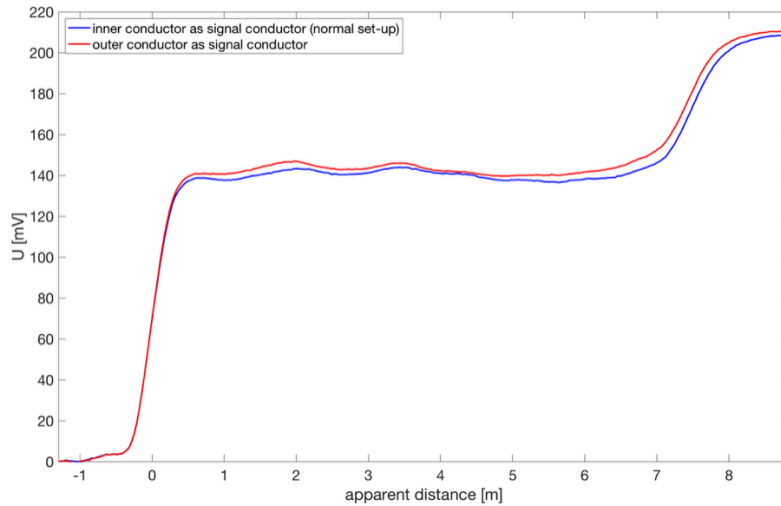
Figure 6.5. Influence of the choice of the inner or outer conductor as the signal conductor on the sensor's TDR signature.

The resonance frequency (first harmonic) can be used to estimate the phase velocity of the sensor, which is directly related to the wave propagation velocity derived by the tangent line method, which was discussed in paragraph 4.3.4 (N. Giaquinto, 2015). A modification to equation (4.10) had to be made because of the combined distance travelled along the sensor and coaxial cable should exactly equal one-fourth of the resonance wavelength.

$$\frac{1}{4} = f_{res} \sum_i \frac{l_i}{v_i} \tag{6.1}$$

By using both the sensor and coaxial cable length together with a wave propagation velocity along the coaxial cable of $0.66c$, a phase velocity of $1.86 \cdot 10^8$ m/s was found, which is almost equal to the velocity of $1.84 \cdot 10^8$ m/s obtained by the tangent line method in next paragraph (Huber+Suhner, 2007).
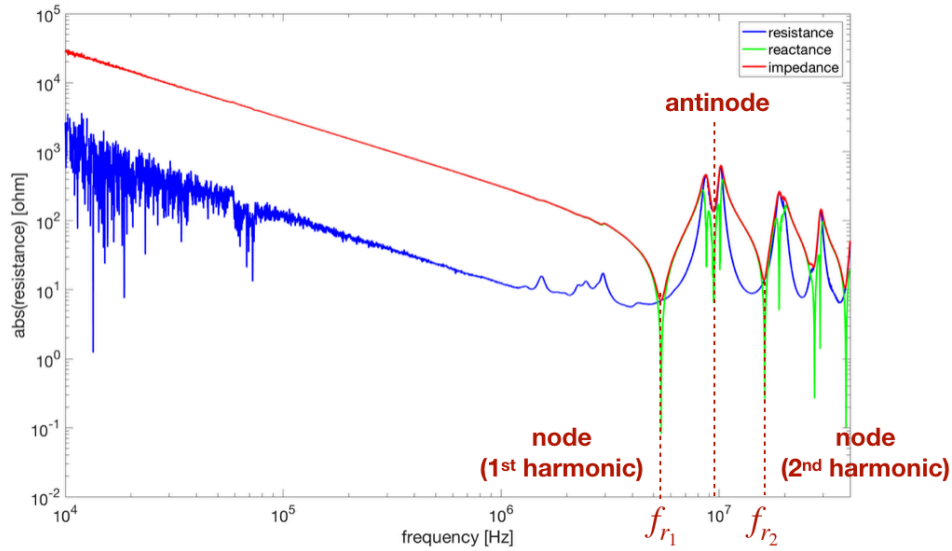
Figure 6.6 Impedance spectrum of the water sensor connected to a 1 m RG 58 C/U coaxial cable. The first and second harmonic frequency are indicated, which are the nodes of impedance measured at the entrance of the analyser, together with the first antinode.

Influence of wave frequency

Normally, a wave period of 5 μs (or a frequency of 200 kHz) was used. However, it can be assumed that an upper limit in the allowable frequency exists above which no clear recognition of the sensor's voltage reflectogram can be done anymore. Figure 6.7a shows the wave period for the applied square wave. The limiting frequency can be estimated based on the TOF along the sensor, which equalled 90 ns. Hence, a minimal period of approximately 200 ns was estimated. Figure 6.7b illustrates the influence of the chosen wave frequency on the recorded TDR voltage reflectogram of the sensor. For frequencies above 5 MHz, clear recognition of the sensor entrance and end was not longer possible. However, for frequencies above 1.8 MHz already a difference with the voltage reflectogram obtained for 200 kHz was seen. This was caused by the ringing/overshoot of the voltage wave at the sensor end: due to back-and-forth reflections between the sensor entrance and end, the steady state voltage, which equals two times the amplitude of the square wave, is only reached after multiple times the TOF of the sensor. From the inset in figure 6.7a, a maximal frequency of 2 MHz was estimated below which the overshoot had become negligible before the next square wave started and hence, interacted with the ringing signal.

In conclusion, a maximal frequency of 1.8 MHz could be used in practice to assure a detection of the complete sensor's TDR signature. The use of an as low frequency as possible could be thought to be more appropriate. However, higher frequency components are necessary to assure a sharp edge of the square wave, which allows a higher time resolution and the detection of smaller discontinuities along the sensor.

Influence of rise time

Equation (4.3) showed the time resolution and hence, the detection limit of a discontinuity to be dependent on the rise time of the signal. For the used set-up, a maximal rise time for the wave generator and oscilloscope of respectively 8 ns and 1 ns were reported. Equation (4.8) allows the calculation of the upper limit of the combined rise time of the total measurement set-up, which equalled approximately 8 ns and indicated the rise time of the wave generator to be the limiting

factor of the time resolution. Next paragraph shows the experimental rise time to vary between 6.4 ns and 16.5 ns (which is higher than the measurement rise time and was caused by the dispersion of the wave along the sensor) at respectively the sensor entrance and end. Hence, by using the wave propagation velocity determined by sigmoidal fitting method, which is discussed in the next paragraph, the time resolution varied between 0.56 m and 1.44 m at respectively the sensor entrance and end. However a single discontinuity can normally be seen if the voltage wave passes along it in a time frame at least equal to one-fifth or one-tenth of the signal's rise time , which means two discontinuities can be resolved as long as their inter-distance is 0.056 and 0.144 m respectively for the sensor entrance and end (Electronic Device Failure Analysis Society, 2004).

The frequency spectrum of the applied wave is mainly determined by its rise time. Ideally, a square wave has a zero rise time resulting in an infinite frequency spectrum. A realistic square wave has a more trapezoid-like behaviour. Shorter rise times mean higher frequency components. The Fourier coefficients for the applied wave depend on both the rise time and the sampling frequency. Figure 6.8a and 6.8b illustrate the difference between the frequency spectrum obtained for an idealised square wave with zero rise time and a more realistic trapezoid-like wave with a rise time of 8 ns and a sampling frequency of 2 GHz, which were the parameters present within the used measurement set-up. A higher rise time means a faster attenuation of the higher frequency components and a more harmonic spectrum with less singularities.

Influence of bends

For the dry sensor, no significant reflections are expected along the sensor, because of the similar characteristic impedance along the complete sensor. Hence, a flat reflectogram should be seen between the sensor entrance and end (the ringing phenomenon only occurs after the first reflection from the sensor end). However, figure 6.9 shows small increases/decreases distributed along 3 areas on the sensor. The variations were attributed to the bends present in the sensor lay-out. The relation between the positions of these variations along the sensor and the locations of the bends was also shown.

The influence of bends could be twofold. First, stresses were locally introduced due the bending, especially for a stiff composite as the sensor (TiC and TiN have a Young's modulus of respectively 31-462 GPa and 248 GPa) (W. Martienssen, 2005). O. Steiner et al. found that stresses of 10 MPa in $BaTiO_3$ introduced an increase of 10 % in the relative permittivity (O. Steiner, 1999). However, also for lower stresses below 1 kPa P. Chakraborty et al. observed a 5-10 % change in the relative permittivity of 25-50 μm thick cured resins used for 3D printing, for which 60-65 % of the increase occurred for a stress of only 1 kPa (P. Chakraborty, 2017).

Secondly, bends cause locally partial reflections of the voltage wave. Equations (3.2) and (3.3) indicate a different expression for the reflection and transmission coefficient of the n- and p-component of the electric field depending on the angle of incidence and refraction. The reflection coefficient can reach all values between -1 (complete negative reflection) and 1 (complete positive reflection), which is illustrated in figure 6.10a and 6.10b. The angle of incidence (depending on the orientation between the voltage wave propagating in TEM mode and the sensor interface) and refraction can vary between 0 and 90 °. The calculation was made for the copper/PVC interface. The characteristic impedance of the sensor seen by the wave propagating in the PVC is different because of the changed lumped circuit parameters. Especially the equivalent resistance increased significantly due to the change from the conductive copper to the isolating PVC layer. A characteristic impedance of approximately 1.2 kΩ was found for the PVC layer, whereas a value of 117 Ω was calculated in paragraph 8.1 for the complete sensor. Hence, a negative reflection was expected at the beginning of each bend due to the angle of incidence which obtained high values,

whereas the angle of refraction was assumed to be low, which was based on Snell's law of refraction in which the real part of the permittivity for the copper conductor was assumed to be nearly zero.
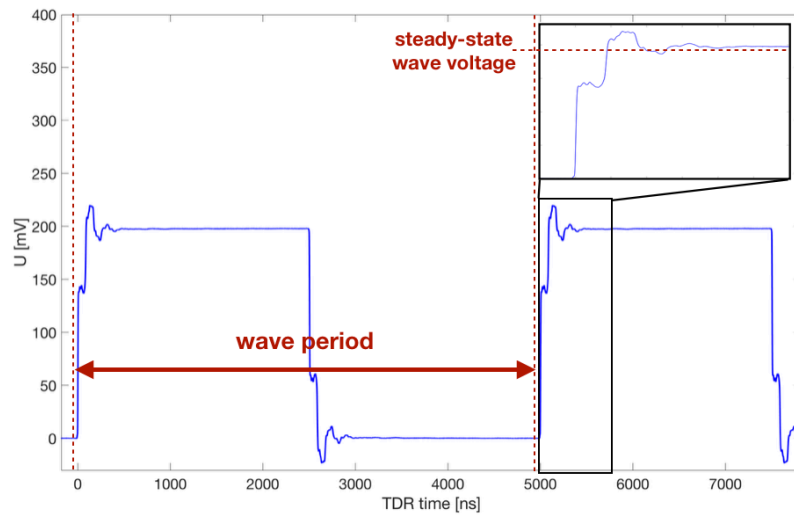
(a)
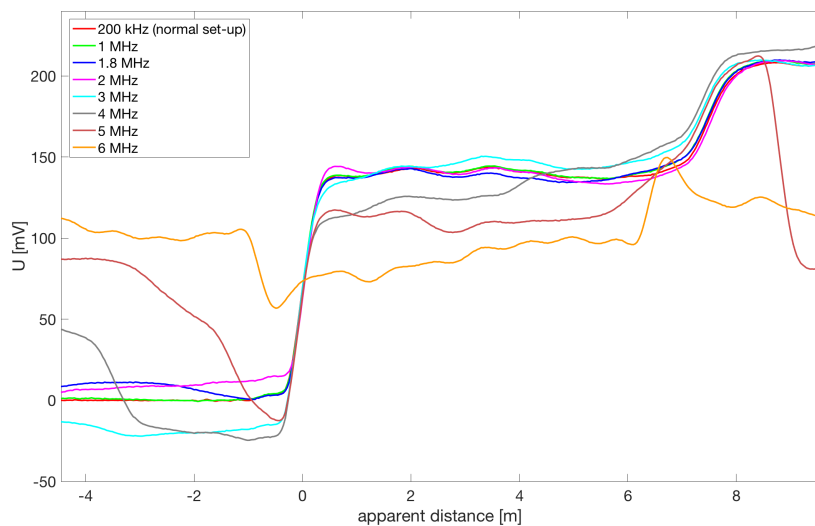
(b)

Figure 6.7a. Illustration of the wave frequency (inverse of the wave period) for the applied square wave. After each change of zero to the voltage amplitude of the wave, the reflectogram of the sensor can be recognised, for which the complementary reflectogram is seen at the end of the square wave. The inset shows the reflectogram of the sensor in which the phenomenon of overshoot/ringing is clearly seen: due to back-and-forth reflections between the sensor entrance and end, the steady state voltage, which equals two times the amplitude of the square wave, is only reached after multiple times the TOF of the sensor. Figure 6.7 b. Influence of the wave frequency on the sensor's TDR signature.
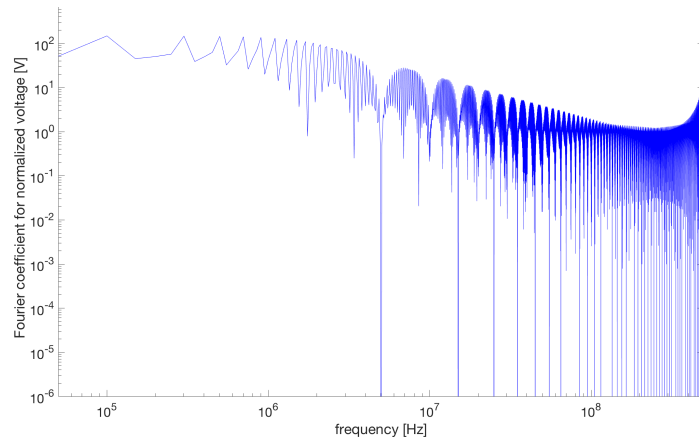
(a)
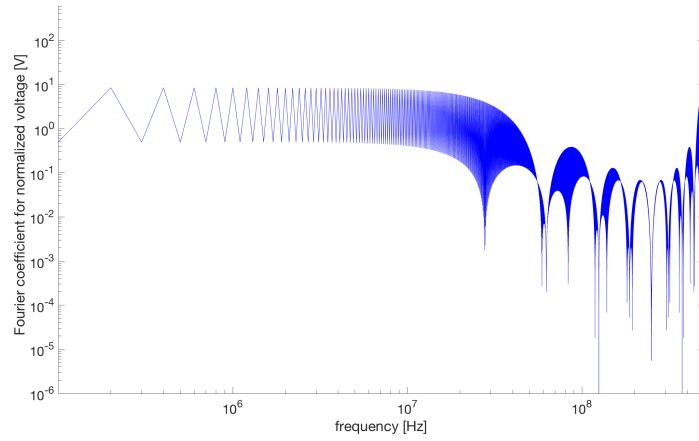
(b)

Figure 6.8. Frequency spectrum of an idealised square wave with zero rise time (a) and of a more realistic trapezoid-like wave with a rise time of 8 ns and a sampling frequency of 2 GHz (b) used in the measurement set-up.
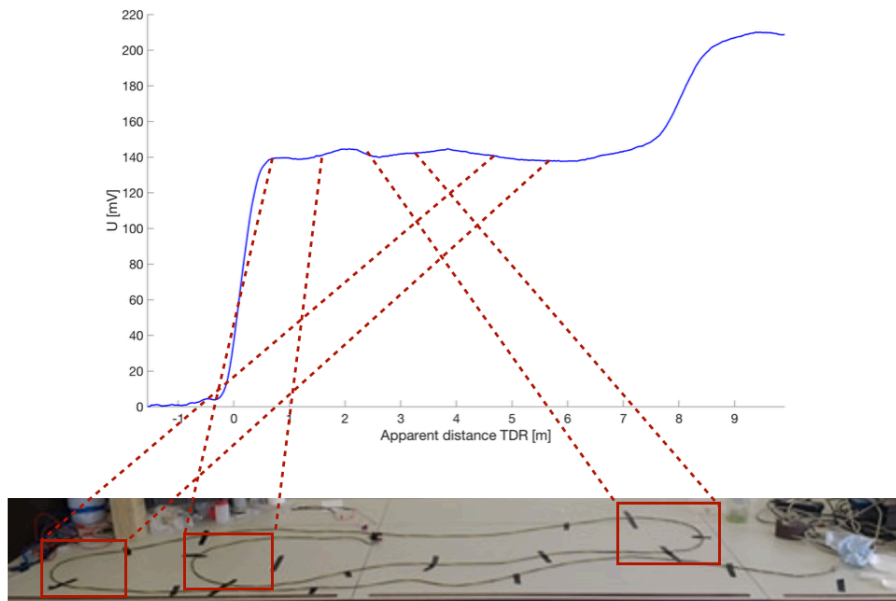
Figure 6.9. Relation between bends present in the sensor lay-out and distributed variations from the expected constant reflected TDR voltage along the sensor.
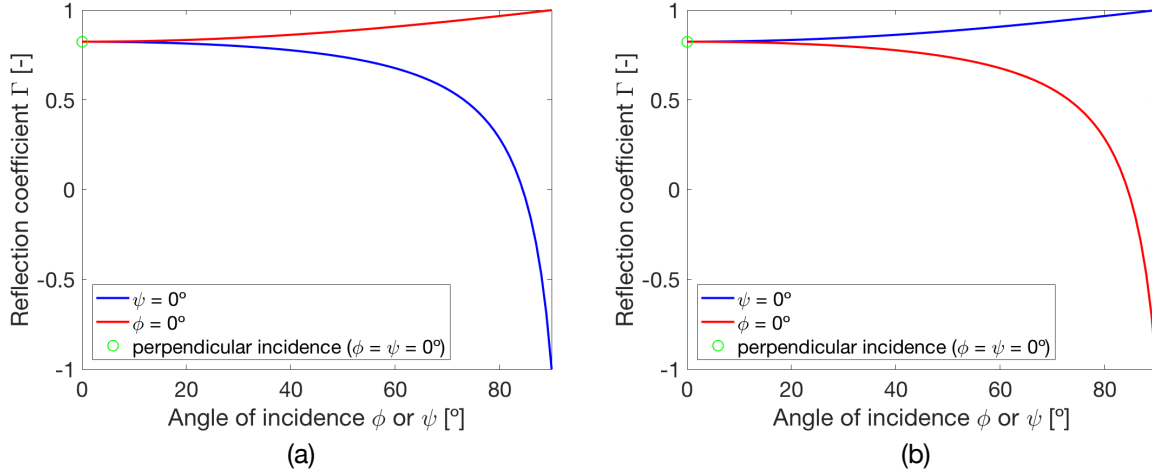
Figure 6.10. Influence of bends on the reflection coefficient of the n- (a) and p-component (b) of the electric field at the copper wire/PVC isolation interface for angles of incidence ϕ and refraction ψ varying between 0º and 90º .

6.3.2. Wave propagation velocity and TOF

The traditional maximum-derivative (MD), tangent line (TL) and zero-crossing (ZC) method were combined with the proposed new maximum and sigmoidal fitting method. The maximum-derivative method uses the time point of maximal derivative in the voltage. For the zero-crossing method, the time point at which a minimum in the voltage occurs before each significant increase or decrease in the voltage (which is at a discontinuity) is chosen. The value of maximal derivative is further used for the tangent line method in which the time point of intersection between the horizontal tangent line drawn at the ZC time point and the tangent line constructed at the MD time point is assigned. The sigmoidal fitting method uses the time calculated as the inflection point of equation (5.1) to attribute a characteristic time. For the maximum method, the maximal voltage observed in the reflectogram, which was seen in the region of overshoot at each discontinuity, was chosen as characteristic time. The time points determined by all five methods are shown in figure 6.11a and 6.11b for respectively the sensor entrance and exit. Next, these time points were used to calculate the time of flight (TOF), which was in turn used in combination with the sensor length to calculate the wave propagation velocity

The 10-90 % rise time at the sensor entrance and end was calculated directly from the sigmoidal fitting function defined by equation (5.1). Equation (6.2) allows the determination of the rise time based on the fitted p_2 parameter, which is called the scaling parameter. Because of the excellent sigmoidal fit of the entrance and satisfactory fit of the end, the values for both the sensor entrance and end matched well with the values observed for the experimental voltage reflectogram (6.6 ns and 13.6 ns for respectively the sensor entrance and end). The less good estimation for the rise time at the sensor end based on the scaling parameter was caused by the significant decrease in the reflectogram just before the sensor end was detected, which was the basis for the ZC method.

$$t_{10-90\%} \approx \frac{4.4}{p_2} \tag{6.2}$$

The rise time at the end was twice as high as at the entrance, which can be explained by the dispersion occurring along the sensor: the steep edges of the square wave are smoothened due to the faster propagating high frequency components. The uncertainty originated from the fitting

procedure for the scaling parameter and is represented by the half width of the 95 % confidence interval.

The 10-90 % rise time and the DC resistance are listed in table 6.5 together with the TOF, wave propagation velocity and permittivity determined by the different methods for the TOF. The uncertainty on the wave propagation velocity was determined by using equation (5.2) in which the uncertainty on both the sensor length and the TOF are taken into account. For the MD, MAX, ZC and TL method, no uncertainty was attributed because the characteristic time points are based on only one time, not a fitted value and hence, an uncertainty is only attributable to the uncertainty on the sensor length. The relative permittivity followed from equation (4.13) and its uncertainty was assigned by equation (5.3). The time point determined by the TL method can also be directly derived from the scaling parameter in the SF method according to equation (6.3)

$$ t_{TL} = -\frac{2}{p_2} + t_{SF} \tag{6.3} $$

Table 6.6 contains the fitted parameters for the SF method at the sensor entrance and end. Figure 6.11a and 6.11b indicates the time points chosen respectively the sensor entrance and end for all methods for the determination of the TOF.

A first important conclusion is that all five methods except the MAX and SF method resulted in similar TOF and wave propagation velocities. Typically, a wave propagation velocity equal to half of the velocity of light is found in cables (Megger, 2013). For PVC and nylon insulations, typical values of respectively 35-58 % and 47-53 % of the velocity of light were reported in literature (PIC Wire, 2018). The wave propagation velocity determined with the MD method was equal to the one calculated form the TL method, which was in turn lower then velocity derived from the ZC method. The latter relation is in accordance with the in paragraph 4.3.4 discussed literature, but normally a lower velocity derived from the MD than the TL method should be found (G. M. D'Aucelli, 2017; N. Giaquinto, 2015; D. A. Robinson, 2005). The TL method is related to the phase velocity, whereas the MD method has a connection with the group velocity, the latter always being lower than the former. This is confirmed by the dispersion behaviour: the high frequency components propagate faster along the line (rather with the phase velocity) and the time distance between the mean frequency components (which propagate rather with the group velocity) increases along the sensor and hence, the time difference between the time point calculated with the MD and TL method increases. However, the observed velocities for the MD, TL and ZC method all have closely related values and hence, uncertainty on their values and on the derivatives could be the cause of the difference with literature. The SF method offered a very accurate guess of the velocity obtained from the experimental datapoints for the TL method.

Secondly, the proposed SF method is a valid alternative to the traditional MD and TL method. The SF is advantageous over the MD and TL method by averaging over the data points of the reflection due to the fitting procedure instead of determining the characteristic time based on the derivative at one characteristic time. Small local variations and fluctuations in the derivative can seriously influence the characteristic time. The influence of the evaluation scheme of the derivative at time t (either based on the data points for t_{i-1} and t_i, either for t_i and t_{i+1} or an average based on t_{i-1} and t_{i+1}) showed no significant difference in the value of the time point determined by the MD and TL method. Additionally, the TL time point was accurately estimated with the SF method.

Table 6.5. Characterisation of the dry water sensor based on the DC resistance, 10-90 % rise time, TOF, wave propagation velocity and permittivity. The maximum-derivative (MD), tangent line (TL), zero-crossing (ZC), sigmoidal fitting (SF) and maximum method (MAX) were applied.

Property	Value	Method used
DC resistance inner conductor	$1.1\pm0.1\ \Omega$	-
DC resistance outer conductor	$1.6\pm0.1\ \Omega$	-
DC resistance inner/outer conductor	out of limit	-
DC resistance PVA/TiCN coating	$27.7\pm0.1\ \Omega$	
length	7.93 ± 0.20 m	-
10-90 % rise time at entrance	6.3 ± 0.4 ns	sigmoidal fitting
10-90 % rise time at end	16.6 ± 0.5 ns	sigmoidal fitting
TOF	86.4 ns	maximum-derivative (MD)
	86.4 ns (85.8 ns)	tangent-line (TL) (estimated by sigmoidal fitting)
	84.8 ns	zero-crossing (ZC)
	90.4 ± 0.3 ns	sigmoidal fitting (SF)
	93.6 ns	maximum (MAX)
wave propagation velocity	$1.84.10^8$ m/s	maximum-derivative (MD)
	$1.84.10^8$ m/s ($1.85.10^8$ m/s)	tangent-line (TL) (estimated by sigmoidal fitting)
	$1.87.10^8$ m/s	zero-crossing (ZC)
	$1.75\pm0.05.10^8$ m/s	sigmoidal fitting (SF)
	$1.69.10^8$ m/s	maximum (MAX)
relative permittivty	2.93 ± 0.17	sigmoidal fitting

Table 6.6. Fitted parameters in the sigmoidal fit for the water sensor entrance and end, based on equation (5.1).

Parameter	p_1 [V]	p_2 [ns^{-1}]	p_3 [V]	t_0 [ns]
sensor entrance	6.98	695.10^{-3}	0	47.8
sensor end	3.63	266.10^{-3}	7.34	138.3

Starting from the inflection point of the SF method, one could say the uncertainty on the wave propagation velocity does not merely result from the fitting procedure of the sigmoidal parameter, but especially on the uncertainty on the choice of the correct/appropriate characteristic time point. The real appropriate time point is situated between the one used for the ZC and SF method. Hence, a lager uncertainty on the time of 7.2 ns was found, based on the average time difference between the time points obtained with the ZC and SF method for both the sensor entrance and end, which resulted in an uncertainty on the wave propagation velocity for the SF method of $0.32.10^8$ m/s.
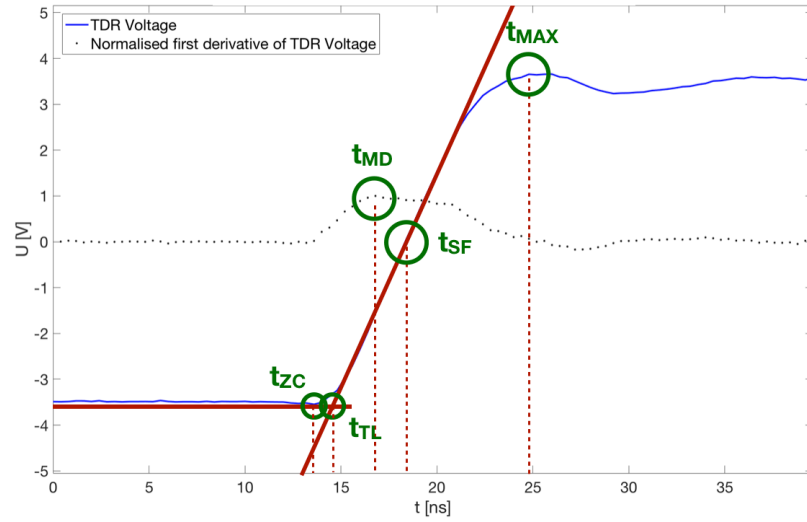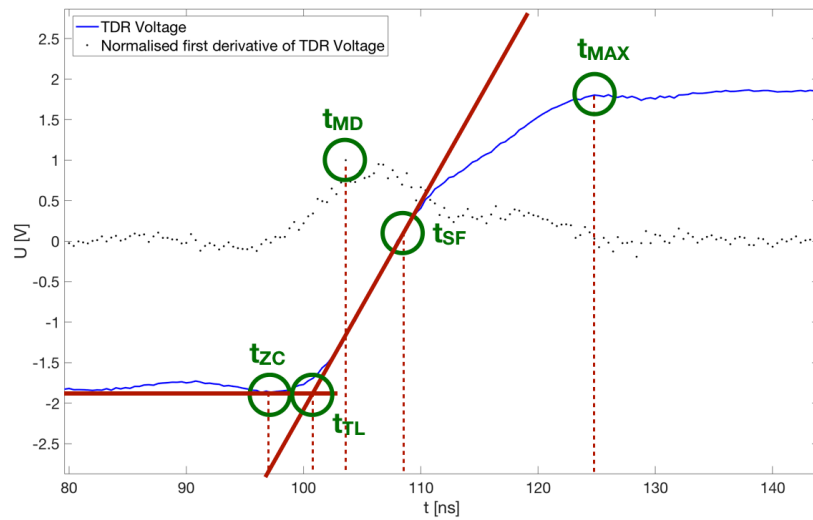
Figure 6.11a. Determination of the characteristic time for the water sensor entrance. Figure 6.11b. Determination of the characteristic time for the water sensor end. The maximum-derivative (MD), tangent line (TL), zero-crossing (ZC), sigmoidal fitting (SF) and maximum method (MAX) were considered, each of them resulting in a different characteristic time. The derivative of the TDR signal, which was normalised for a clear representation together with the TDR voltage, is also shown.

6.4. Water sorption by viscose

A relative mass absorption of 30 % was reached by the viscose wire after 45 minutes of immersion in water. However, the PVC and copper wires were not expected to absorb significantly water and hence, the relative mass increase by considering only the viscose jacket was more appropriate, which equalled 194 %. The large water uptake could be explained by both the free space between the woven viscose textile fibres and the interaction of the water molecules with the polar hydroxyl functional groups present in cellulose (J. Borch, 2001; Polymerdatabase, 2018). When only the viscose jacket was immersed in water, a relative mass increase of even 391 % was reached. However, this value will be lower for the viscose jacket present in the wire: the other layers constrain the dimensional changes due to the swelling and probably the fibres were also partially impregnated by the TiCN coating, which seals of the access to water.

Figure 6.12 shows the diffusion of the water along the viscose jacket. After 1-2 minutes, the water spread out along the complete piece of wire, whereas only the part between the 2 indicated marks was immersed. Hence, a diffusion rate of 2-4 cm/min was observed. However, within the sensor, diffusion along the vapour phase is prohibited because of the PVA/TiCN layer above the viscose jacket. Nevertheless, the viscose layer should be taken into account to model the influence of the water absorption on the dielectric behaviour of the complete sensor.
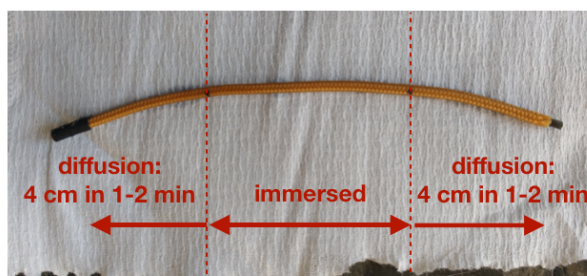
Figure 6.12. Illustration of the high diffusion rate of water along the viscose jacket. The middle part was immersed in water. However, the water spread out along the rest of the jacket in 1-2 minutes.

6.5. Dielectric characterisation of PVA/TiCN, PVA and TiCN by dielectric spectroscopy

Dielectric spectroscopy is a powerful characterisation tool to map the dielectric properties and phase transitions of materials. Impedance analysis is commonly used for frequencies in the range of 10 Hz - 100 MHz, whereas a radio-frequency reflectometer is appropriate for MHz - GHz measurements (F. Kremer, 2003). The permittivity is directly derived from the applied cyclic electric field and the measured current density between the two (parallel) electrodes. Two types of processes can be detected by dielectric spectroscopy: either relaxation processes, for which a peak in the imaginary part of the permittivity is observed together with a step-like decrease in the real part for increasing frequencies, either conductive processes, for which the imaginary part of the permittivity decreases with increasing frequency. For purely ohmic conductive processes, no frequency-dependence of the real part of the permittivity is seen in the latter case. The different dielectric model functions discussed in paragraph 4.6.2 can be used to model the dielectric behaviour.

6.5.1. Literature review on the dielectric behaviour of TiCN and PVA

Multiple authors reported on the dielectric behaviour of PVA. Figure 6.13a and 6.13b give a comprehensive overview of the data found for the real and imaginary part of the permittivity of PVA (T. A. Abdel-Baset, 2016; O. G. Abdullah, 2011; D. D. Sandu, 1985; M. H. Suhail, 2016; M. J. Uddin, 2012; E. A. Van Etten, 2014). However, large variations in the data were observed based on temperature and molecular weight of the studied PVA. Both the real and imaginary part were found to decrease with increasing molecular weight, whereas higher values for both were seen for higher temperatures. D. Lu et al. used PVA as a humidity sensing film for which the RH dependent permittivity in the GHz range is shown in figure 6.14 (D. Lu, 2014). A clear increase towards the permittivity of (un)bound water was seen, which was reported in paragraph 4.6.2. For TiCN, no data was found in literature. However, negative values of the real part of the permittivity of TiN

were reported for frequencies up to PHz (J. A. Briggs, 2017; S. T. Sundari, 2013). A value for both the real and imaginary part of the permittivity equal to 70 was observed for 70 wt% TiC used as absorbing particles in epoxy (Y. Wang, 2014). Despite the fact that TiC and TiN are isomorphic materials, they both have a face cubic centred structure at room temperature in which carbon and nitrogen reside in the octahedral interstitials, a completely different dielectric behaviour was seen in the scarce literature data.

The above summary on the dielectric behaviour of PVA and TiCN made clear a lot of variation on the reported data existed and that the properties are very dependent on the exact materials system specifications (mainly molecular weight and temperature). Hence, dielectric spectroscopy was indispensable for an accurate assignment of the dielectric properties of the studied PVA/TiCN percolative composite.

6.5.2. Temperature-low frequency (< 10⁷) scans

Figure 6.15 compares the obtained spectrum over a temperature range of -100 to 250 °C and a frequency range of 0.1 Hz to 10 MHz of the imaginary part of the permittivity for respectively the PVA/TiCN layer at room RH (50 -60 %) and after equilibration in a saturated salt solution of K_2SO_4.

Very high values for the imaginary part of the permittivity were observed because of the conductive behaviour of the TiCN particles, which is directly related to the imaginary part of the permittivity. The presence of water was detected for both conditions: a relaxation peak at the melting point of water was clearly visible. However, for the composite at room RH an additional relaxation for the low-density hexagonal ice phase was seen together with a phase transition around 100 °C which was unknown, but could be attributed to the liquid-gas transition of water (F. Kremer, 2003). The large increase in conductivity after the melting point of ice due to the liquid water molecules caused a significant increase in the imaginary part of the permittivity. For the K_2SO_4 conditions, the additional relaxations where not longer seen: the dielectric behaviour of the PVA/TiCN composite was completely dominated by the water molecules, which is a confirmation of the hygroscopic behaviour of PVA (G. S. Kulagina, 2007; I. Pitropakis, 2015; A. A. Tager, 1971).

The relaxation time was used to determine the glass transition of the phases present in the PVA/TiCN composite. W. Tala Taza reported the glass transition temperature of PVA to be independent of the added vol% of TiCN (W. Tala Taza, 2012). However, water seriously decreases the glass transition temperature because of its plasticising effect. According the Fox-Flory relation, the glass transition of PVA varies between a value of 80 °C for pure PVA and - 135 °C for pure water (J. Raul, 1995). The glass transition followed from the empirical Vogel-Fulcher-Tammann relation, which shows a good fit for alpha-relaxations. These alpha-relaxations are related to a reorientation of the main chain molecules of the polymer, which can be seen as a 'cage reorientation' of the polymer. An Arrhenius relation is accurate to fit beta-relaxations, which are related to relaxations of the side groups of the main chain and hence, can be seen as fluctuations within the 'main chain cage' (F. Kremer, 2003). The presence of the (hexagonal) ice phase was confirmed by the Arrhenius fit, whereas the presence of the water phase was verified by its glass transition of approximately - 135 °C, which was derived from the Vogel-Fulcher-Tammann fit. The glass transition of the PVA/water phase was found to be around - 30 °C and followed the Vogel-Fulcher-Tammann relation. Based on the mass absorption of the PVA/TiCN composite for 50% RH reported by G. De Lescluze and the data on the influence of the mass fraction of water, a glass transition temperature of -10 to -20 °C was estimated, which is in accordance with the observed value (G. De Lescluze, 2017; J. Raul, 1995). The glass transition temperature of pure PVA could not be observed, because it was masked by the presence of the water phase (J. Raul, 1995).
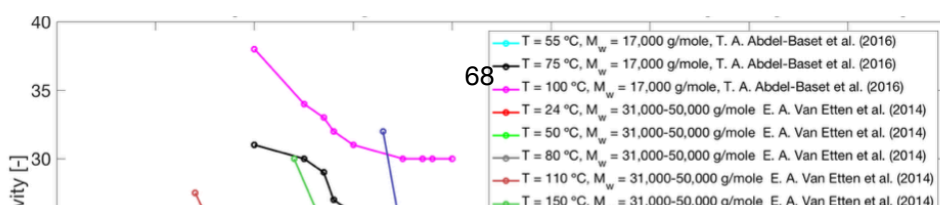
Figure 6.13. Summary of literature data found on the real (a) and imaginary (b) part of the permittivty of PVA.
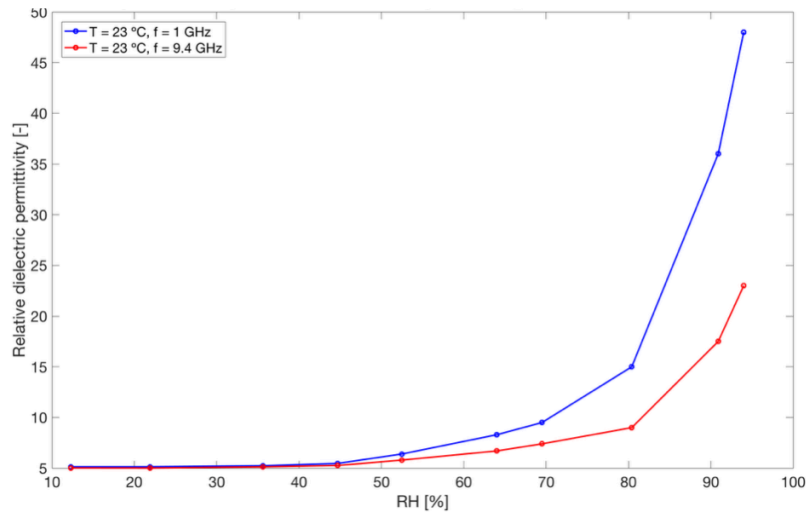
Figure 6.14. Influence of RH on the permittivty of PVA in the GHz range (D. Lu, 2014).

6.5.3. Low frequency (< 10^6) scans in a humidity chamber

Figure 6.16a and 6.16b show the steady-state real (a) and imaginary (b) part of the relative permittivity reached after equilibration in each of the used saturated salt solutions. Both real and imaginary part had the same order of magnitude. Only for the KCl solution, a significant increase in the permittivity was observed, which was attributed to both higher real (due to the higher polarity) and imaginary (due to the higher conductivity) part of the permittivity of water. The permittivity still reached very high values, which is due to the metallic-like dielectric behaviour of the TiCN particles. However, the RH at which a significant increase occurred, can be in fact related to the lyotropic percolation threshold. Figure 2.5b showed this threshold to occur at a RH of about 80 % at room temperature. Hence, a relation between the change in dielectric properties and the lyotropic percolation threshold is assumed. It was already explained in paragraph 2.3.1 that microcapacitor networks are formed in the vicinity of the percolation threshold, which caused an exponential increase in the permittivity according to equation (2.4) (C. W. Nan).

The dielectric behaviour of pure PVA was also tested for room conditions and after equilibration in both P_2O_5 and K_2SO_4 to study the influence of the TiCN particles. The equilibrium real and imaginary part of the relative permittivity are shown in figure 6.17a and 6.17b. Again, the influence of water on both parts of the permittivity was clearly visible. Especially for the lower frequency components, a significant increase was observed, probably due to the much higher conductivity of water compared to PVA. The real part equalled approximately 3 and 3.3 for respectively room conditions and K_2SO_4. The value at room conditions was in good accordance with the value reported by O. G. Abdullah et al. and M. H. Suhail et al. (O. G. Abdullah, 2011; M. H. Suhail, 2016).
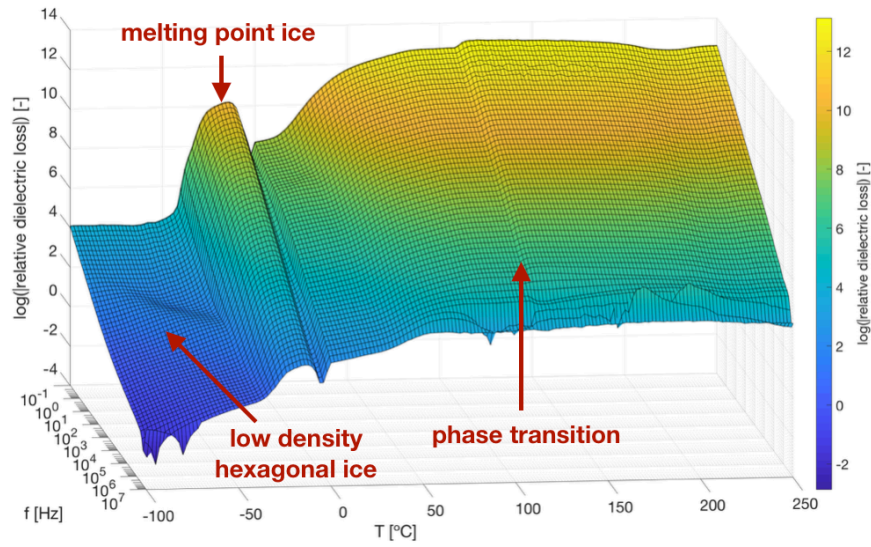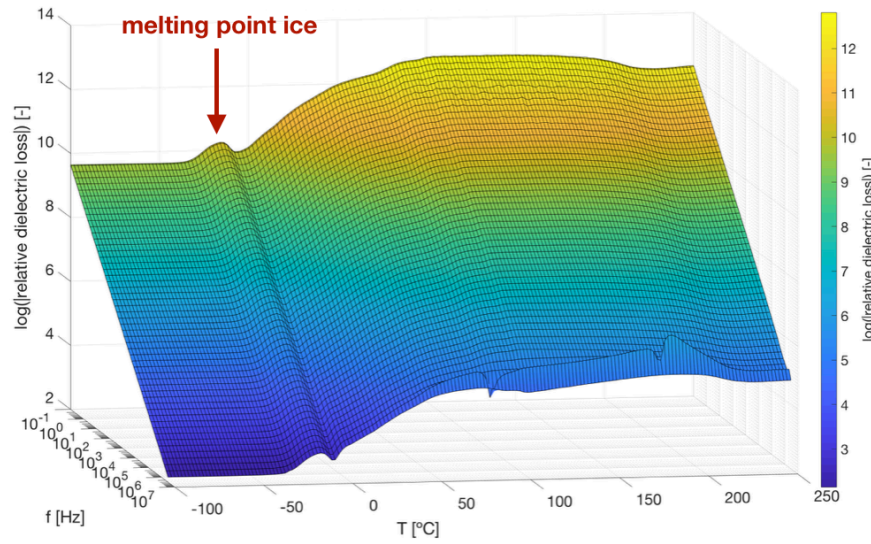
Figure 6.15. Imaginary part of the relative permittivity as function of frequency and temperature for the PVA/TiCN coating after equilibration at room conditions (50-60 % RH) (a) and in K_2SO_4 (b).
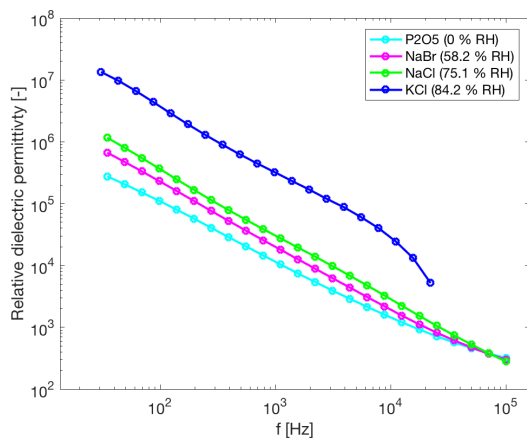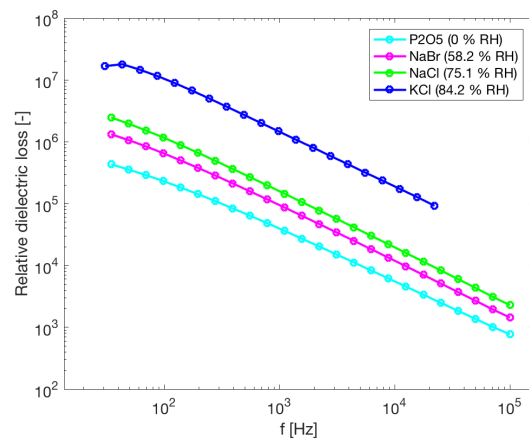
Figure 6.16. Real (a) and imaginary (b) part of the relative permittivity of the PVA/TiCN coating at room temperature after equilibration in different saturated salt solutions.
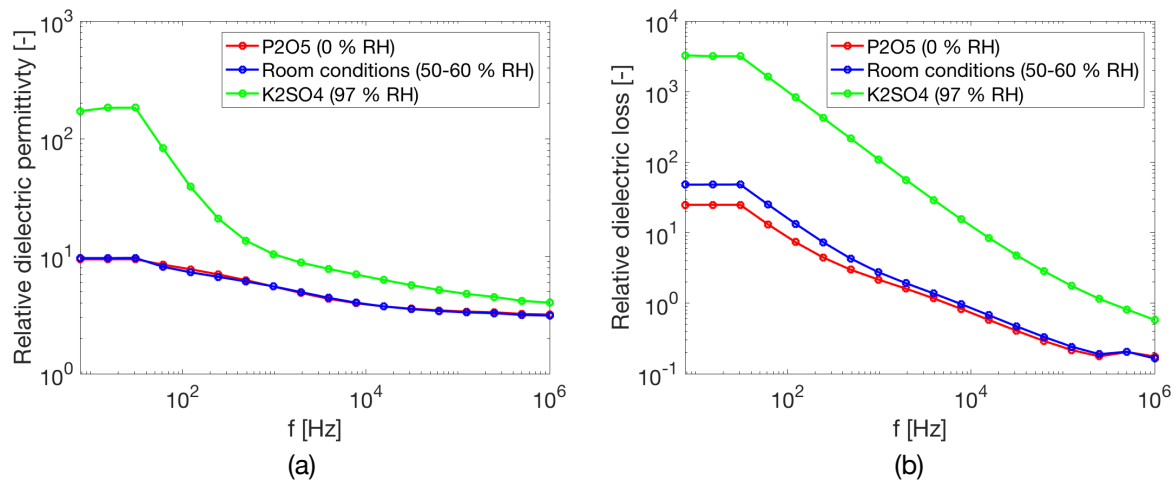
Figure 6.16. Real (a) and imaginary (b) part of the relative permittivity of the PVA at room temperature after equilibration in different saturated salt solutions.

The imaginary part was found to be negligible at MHz frequencies, which was also stated by the mentioned authors. However, the permittivity for humidities adjusted by K_2SO_4 did not increase in the expected order of magnitude. Figure 6.14 showed a permittivity of 40-50 at a RH of nearly 100 %, which is ten times higher than the observed value (D. Lu, 2014). The electrode set-up was thought to be the cause of the low values: the PVA naturally wants to swell, however is constrained by the fixed inter-electrode distance. Hence, the driving force for absorption is mechanically countered and less absorption than expected for equilibrium occurred. Nevertheless, if the electrodes were allowed to expand, an apparent permittivity lower than the real value would still be observed: the Labview processing software assumes a constant inter-electrode distance and hence a larger distance, which influences the denominator of the capacitance, should be corrected by a higher permittivity, which influences the numerator of the capacitance. However this positive correction on the permittivity was not made because the software did not take the swelling into account.

The evolution of the real and imaginary part of the permittivity was monitored for 3 frequencies and is shown for the real part in figures 6.17a, 6.17b and 6.17c for respectively equilibration at room conditions, in K_2SO_4 and P_2O_5. After room conditions, the sample was placed in the K_2SO_4 solution followed by the P_2O_5 salt. Hence, an increase and decrease should be respectively observed for the second and third experiment, which was indeed seen, due to the transition to the maximal and minimal possible water content in the PVA at respectively a RH of 100 % and 0 %. The drying kinetics were monitored for approximately 11 hours. For the high frequency components, a steady-state permittivity value was reached after this measuring time, whereas for the low frequency components this was not the case (except for in K_2SO_4). The slow drying kinetics (compared to the change in TDR signature of the sensor observed in the leakage experiments discussed in the next paragraph) were attributed to the long diffusion distance: the sample was only accessible to water from the sides because of the constraining electrodes (an inter-electrode distance of maximal 0.5 mm was present), whereas in the leakage experiments the complete surface of the layers was accessible to water.

6.5.4. Temperature-high frequency (> 10^6) scans

A relative density of 97.2 % of the theoretical density was found for the Spark Plasma Sintered TiCN disc. The small fraction of air should be taken into account when calculating the permittivity of pure TiCN based on the data obtained for the TiCN/air composite. The simple linear mixing

model, which will be given by equation (8.5), was proven to be appropriate (C. Vanga Bouanga, 2011).

Due to a long-duration breakdown of the high frequency measurement set-up, dielectric spectroscopy was not possible at GHz frequencies for the TiCN and PVA. Hence, chapter 8 will use the dielectric data obtained in the MHz range to model the sensor.

(a)

(b)

(c)
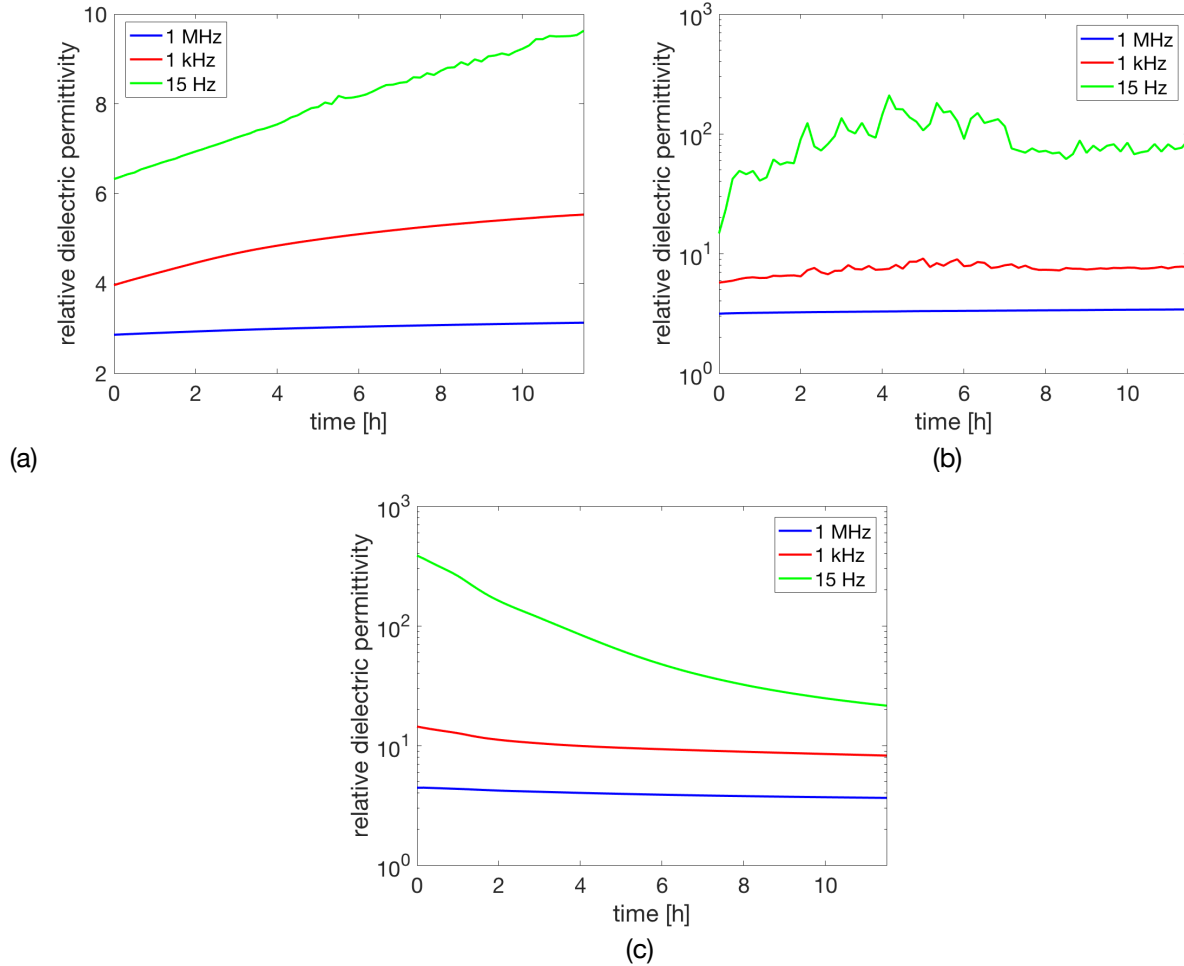
Figure 6.17. Evolution of the real permittivity of PVA at room temperature when equilibrated at room conditions, in K_2SO_4 and in P_2O_5. The experiments were conducted in this sequence of solutions.

6.6. Water leakage detection and localisation

Previous paragraph explained why a significant absorption of water and hence, a significant change in local dimensional and electromagnetic properties of the sensor can be expected when a leakage spot of water is intentionally applied. For every experiment, the sensor's baseline TDR voltage reflectogram was recorded and all changes in the reflectogram over time were compared to this baseline. The wave propagation velocity was also recalculated for each experiment to take any changes on the sensor over time into account.

6.6.1. Series 1: leakage spots of different size

The evolution of the DC resistance for the first three experiments is shown in figure 6.18. The expected fuse-like behaviour was seen and the lyotropic percolation threshold was found to occur after 65-70 minutes. The observed change in resistance from 10-100 kΩ to 1-10 MΩ was in accordance with previous research (G. De Lescluze, 2017; H. Pfeiffer, 2012a; I. Pitropakis, 2015; W. Tala Taza, 2012). However, the characteristic drop immediately after the percolation threshold from 10 to 3-4 MΩ due to the formation of a conductive percolation network by the water molecules was not observed. A too large time interval between successive resistance measurements was stated as the cause of this discrepancy. In all 3 cases, the leakage spot could be detected by monitoring the change in DC resistance.

Another important conclusion drawn from this first series of leakage experiments is the influence of the leakage spot size on the behaviour of the DC resistance change. For small leakage spots, a clear fuse-like transition was observed, whereas for the larger spots, a more step-wise change in the logarithm of the resistance was found. The local variations in the concentrations of water and percolative filler particles along the sensor in the area of a leakage spot was assumed to be the cause: multiple partial interruptions of the percolation network occurred before locally the percolation threshold was clearly passed. However, a change of one order of magnitude in the frame of MΩ was seen at the time for which in the experiments for smaller leakage spots the lyotropic percolation threshold was clearly observed based on the fuse-like behaviour.

The recorded (differential) TDR voltage reflectograms did not allow the clear detection, and certainly not the localisation, of each of the leakage spots. For all 4 experiments, noise-like differential reflectograms were found, which is illustrated by figure 6.18 for the leakage spot at a distance of 2.7 from the sensor entrance with a size of 0.14 m. At the time of the experiments, it was thought that TDR was not an appropriate technique to detect leakages on the sensor. However, later experiments, which are discussed in the next paragraphs, clearly showed the detectability and localisability of the leakage spots by TDR. Hence, it was assumed that an inappropriate measurement set-up was used for these first series of experiments (concerning the sampling frequency, sample averaging and calibration). However, the undetectable leakage spot with a size of 4 cm could be explained by the insufficient time resolution of the measurement set-up: the rise time was too high to detect such a small leakage spot, which was shown in paragraph 6.3.1. For the larger leakage spots, the distributed character of the leakage spot was thought to be the cause of regions of positive and negative differential voltage variations. Within the area of the leakage spot, the local characteristic impedance depends on the water concentration, which varies along the sensor. Hence, multiple internal reflections of the voltage wave will cause a diffuse character of the detected reflectogram in the area of the leakage. However, the series of experiments discussed in the next paragraphs clearly show detection of larger distributed leakage spots to be possible.

To illustrate the order of water absorption by the sensor, figure 6.20 shows a detail of the sensor after a leakage experiment. Significant swelling of the PVA layer was observed. However, long-time reuse of the sensor for other leakage experiments could be assured by the fact that only a small fraction of 10-20 vol% of the PVA migrates to the water phase and hence, after drying most of the initial PVA layer will be restored (G. S. Kulagina, 2007 ; A. A. Tager, 1971).
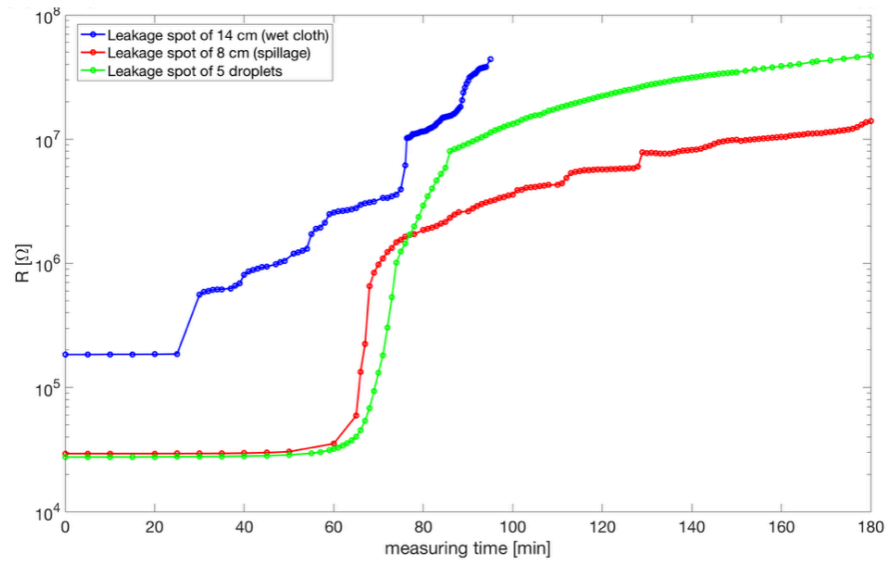
Figure 6.18. Time evolution of the DC resistance for the first three experiments of the first series of water leakage experiments.
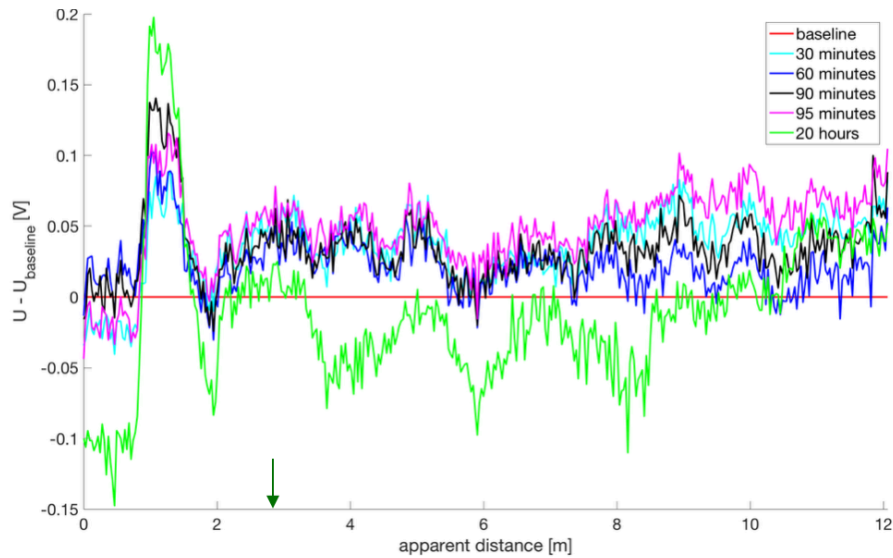
Figure 6.19. Time evolution of the differential TDR voltage reflectogram for the leakage spot at a distance of 2.7 m from the sensor entrance. The leakage spot is indicated by a green arrow.
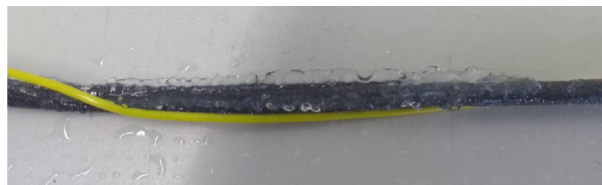
Figure 6.20. Illustration of the large swelling of the PVA (transparent) protecting and PVA/TiCN (black) sensing layer of the water sensor due to the water absorption.

6.6.2. Series 2: leakage spots of same size at 3 different locations

Figures 6.21 and 6.22 show the obtained (differential) TDR voltage reflectograms for which a maximal difference with the sensor's baseline was seen in each experiment. In both experiments, the 3 leakage spots were all clearly recognised and a distinction between the location of each of the 3 leakage spots was possible. Because of the non-averaged data, no further analysis based on the discussed methods for the determination of the TOF was possible. However, the apparent distance of each leakage spot was estimated by using the time point for which half of the observed maximal differential voltage was seen for each discontinuity (SF method), which means for the sensor entrance and each leakage spot. A maximal error on the position of approximately 0.3 m was found. However, the finite size of the leakage spot could have introduced the error on the location because it is unsure whether the centre or the start of the leakage spot was applied at the predefined distances. Also the diffusion of the water along the sensor could have caused an increase of the leakage spot. A diffusion via the vapour phase of 0.004 m/min was observed in previous research by W. Tala Taza (W. Tala Taza, 2012).
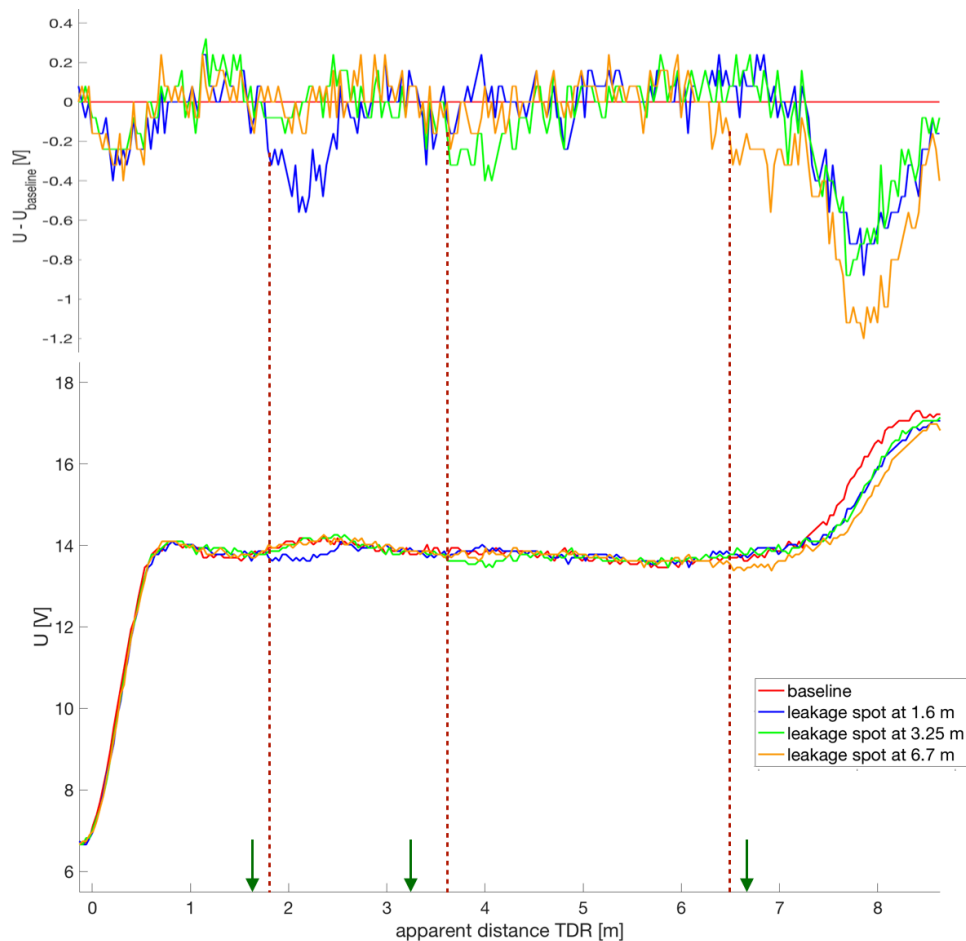
Figure 6.21. TDR voltage reflectogram (bottom) together with the differential TDR voltage reflectogram (top) for the water sensor during the first experiment in which 3 leakage spots of approximately 20 cm wide were separately applied. The leakage spots are indicated by a green arrow and were applied at a distance of respectively 1.6 m, 3.25 m and 6.7 m from the sensor entrance. The estimated leakage locations are indicated by a dashed red line and were determined by visual selection of the inflection point of the differential voltage at each leakage spot. (Data obtained within the PhD research of Sevilia Sunetchiieva.)
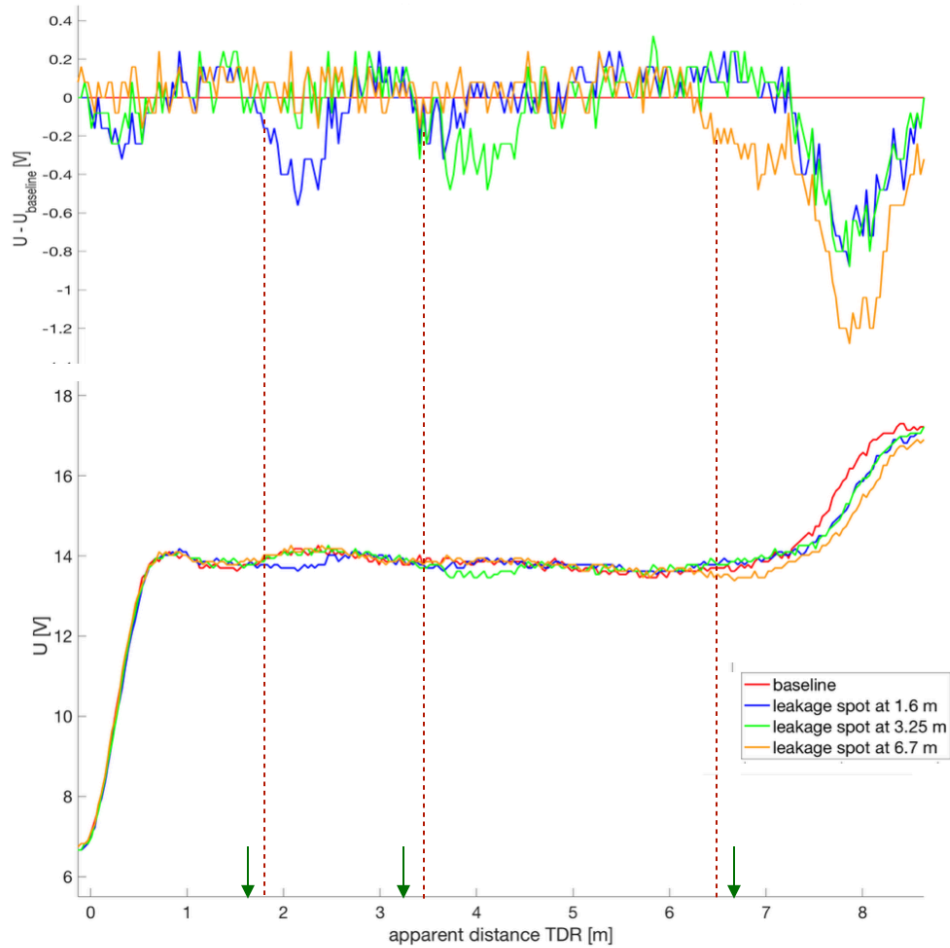
Figure 6.22. TDR voltage reflectogram (bottom) together with the differential TDR voltage reflectogram (top) for the water sensor during the second experiment in which 3 leakage spots of approximately 20 cm wide were separately applied. The leakage spots are indicated by a green arrow and were applied at a distance of respectively 1.6 m, 3.25 m and 6.7 m from the sensor entrance. The estimated leakage locations are indicated by a dashed red line and were determined by visual selection of the inflection point of the differential voltage at each leakage spot. (Data obtained within the PhD research of Sevilia Sunetchiieva.)

For the leakage spots located at 1.6 m and 3.25 m from the sensor entrance, an overestimation of the location was found, whereas for the spot at 6.7 m an underestimation was observed. The spread-out of the leakage spot would have caused an underestimation, whereas the locally decreased wave propagation velocity due to the water uptake, which follows from equation (4.24), would have resulted in an overestimation. The sensor had sufficiently dried within half of a day to allow the initiation of a new leakage experiment.

All leakage spots introduced a negative differential voltage peak, which indicates the increase in permittivity due to water absorption to dominate the decrease in permittivity due to the swelling of the water absorbing PVA/TiCN and PVA layer, which was also confirmed by dielectric spectroscopy in the previous paragraph. Finally, a large differential TDR voltage peak could always be observed after a leakage spot around the sensor end. The local shift in the open-circuit peak of the sensor end was caused by the locally decreased wave propagation velocity, according to equation (4.17), due to the presence of water. Hence, a larger apparent distance for the sensor end was observed, because the wave propagation velocity on the dry sensor was used.

Nevertheless, the experiments confirmed both the detectability and localisability of the leakage spots by TDR. The maximal differential voltages observed at a leakage spot were about 4 to 6 % of the amplitude of the applied voltage wave and were 1.5-2 times higher than the voltage amplitude variations caused by electromechanical noise along the sensor. Also the reproducibility of the TDR method was illustrated: almost no difference was observed between the detection and localisation of each of the 3 leakage spots in both experiments.

6.6.3. Series 3: leakage spots of same size at close distance and 2 simultaneous leakage spots

First experiment

Figure 6.23a contains the TDR voltage reflectogram obtained for a leakage applied at a distance of 2.90 m from the sensor entrance. The time evolution of the DC resistance is shown in figure 6.23c and is compared to the time evolution of the differential TDR voltage reflectogram in figure 6.23b. The leakage spot was clearly detected and a maximal differential voltage of 5 % of the amplitude of the applied voltage wave was observed.

A significant (> 2 mV) increase of the differential TDR voltage occurred after 50-60 minutes and after 80 minutes a steady-state value was reached. A comparison with the time at which a fuse-like increase of the DC resistance occurred was made to assess the simultaneity of the time after which a leakage could be observed based on either the TDR, either the DC resistance measurement. Unfortunately, a linear increase of the DC resistance was observed instead of the fuse-like behaviour. This was explained as for the larger leakage spots in the first series of water leakage experiments to be caused by the distributed character of the leakage: multiple positions within the leakage spot were possible at which locally the percolation network was interrupted by the water uptake. Each of these events did not have to occur necessarily at the same time because of the possible difference in local free volume, diffusion behaviour, concentration of TiCN particles and layer thickness. Hence, a (continuous) series of events was rather seen than the intended fuse-like behaviour. Nevertheless, a change of 2-3 MΩ was observed after 60 minutes. If at this time, locally the percolation network was completely interrupted, for which the lyotropic percolation threshold was reached, it could be concluded that the significant change in TDR occurred 10 minutes before this threshold. The first series of leakage experiments concluded the lyotropic percolation threshold to occur after 65-70 minutes, which justifies the assignment of the time at which the lyotropic percolation threshold took place.

Several possible causes of the earlier detection of the leakage by TDR can be found. First, the permittivity change of the PVA layer will be the dominant factor on the total permittivity change, which will be explained and illustrated in paragraph 8.1.3, because of the negligible contribution of the PVA/TiCN layer's permittivity to the equivalent series capacitance. For the fuse-like DC resistance behaviour, only the PVA/TiCN sensing layers plays a role. Because of the application of water at the circumference of the sensor, diffusion will cause the local concentration of water to be always higher in the PVA layer. Based on Birchak's mixing model, given in equation (4.15), a continuous increase in the total permittivity of the PVA/water composite during the leakage experiment can be expected, whereas a critical concentration of water exists below which the percolation network stays intact (K. Kupfer, 2005). Additionally, the diffusion within the vapour phase allows a faster spread-out of the water in the PVA layer than in the PVA/TiCN layer, where diffusion through only the solid composite or liquid water phase is possible (W. Tala Taza, 2012).
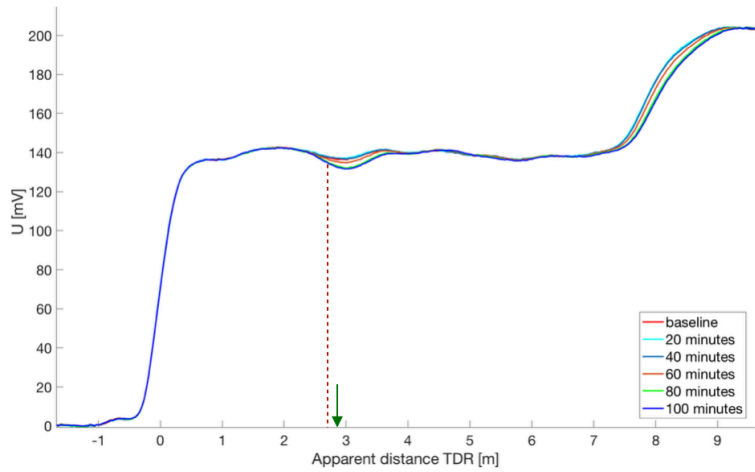
(a)
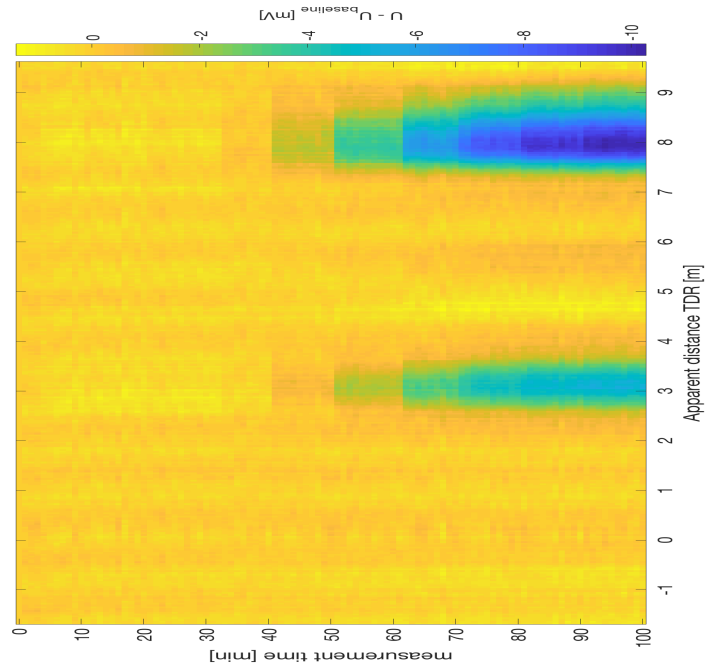
(b)
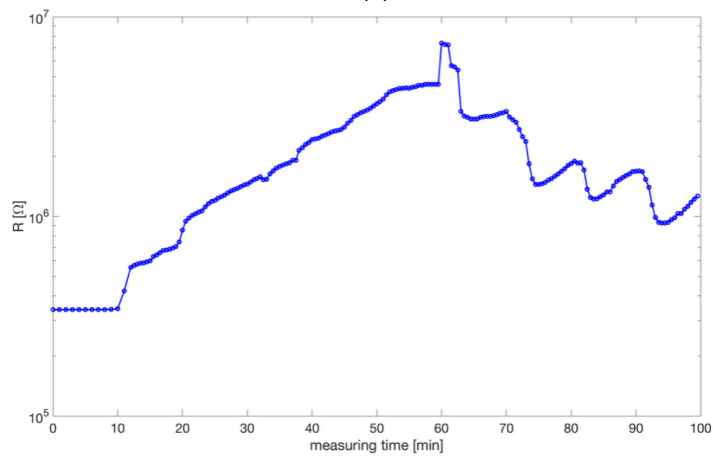
(c)

Figure 6.23. Time evolution of the TDR voltage reflectogram (a), differential TDR voltage reflectogram (b) and DC resistance for a water leakage spot at a distance of 2.90 m from the sensor entrance. The estimated leakage locations are indicated by a dashed red line and were determined by visual selection of the inflection point of the differential voltage at each leakage spot. The leakage spot is indicated by a green arrow.

Secondly, it was assumed by previous research that the critical RH level for the occurrence of the lyotropic glass transitions and lyotropic percolation threshold are related (G. De Lescluze, 2017; H. Pfeiffer, 2012b; H. Pfeiffer 2014). The change in the derivative of the free volume with increasing water concentrations at the glass transition temperature will cause a faster decrease of the attracting forces between the PVA molecules and hence, a higher local mobility of the polymer chains is accompanied by a higher diffusion rate of mainly unbound water molecules (G. De Lescluze, 2017; R. M. Hodge, 1996; G. S. Kulagina, 2007). For higher water concentrations, the conductive path between the randomly dispersed filler particles can locally not longer be sustained and hence, the percolation network is broken, which can be seen in the fuse-like increase of the DC resistance. Hence, the DC resistance increase will only be seen for higher water concentrations in contradiction to the permittivity change which continuously occurs in the PVA layer.

The superposition of the cyclic variation in and the monotonic decrease of the DC resistance was not observed in the previous leakage experiments and could be attributed to a problem with the multimeter. However, for sufficiently large concentrations of water present in the sensor, the conductivity is partially restored by the ions contained by the tap water. This assumption clearly requires further research for confirmation.

Second experiment

The inability to detect multiple leakage spots simultaneously present at the sensor could seriously jeopardise the commercialisation and application of the sensor in industrial environments. Hence two leakage spots were applied at the same time on the sensor. The results of the second experiment in which a second leakage spot was applied at a distance of 5 m from the sensor entrance 60 minutes after the first leakage spot had been introduced at a distance of 2.40 m from the sensor entrance, are shown in figure 6.24a and 6.24b. The first leakage spot was clearly observed after 60-120 minutes. Also 60-120 minutes were required for detection of the second leakage spot. The experiment showed the detection of an additional leakage spot, which is located behind another leakage spot on the sensor, to be possible. The first leakage spot barely influenced the detected differential TDR voltage for the second leakage spot: like in the first experiment a negative change of 4-5 mV was observed, which is an important observation concerning the applicability in large engineering structures.

For the first leakage, only a differential TDR voltage of 2 mV was observed. The smaller leakage spot size of 10 cm instead of the normally used 20 cm is the cause. It was concluded that the width of this leakage spot was below the time/spatial resolution of the measurement set-up. Paragraph 6.3.1 showed that a minimal leakage spot width of 0.05-0.14 m was required, depending on its position along the sensor, if a differential voltage of one-tenth of the nominal differential voltage for a leakage spot was assumed to be the detection limit.

A MOHR 100 nanopulsor was tested once for the detection of a 4 cm wide leakage spot (same set-up as the other experiments for a wet cloth wrapped around the sensor). The lower rise time of 60-100 ps allowed a time resolution of about 1 cm (MOHR, 2017). Again, a negative voltage peak of 4-5 mV was observed for the leakage spot. Hence, the spatial resolution of the normally used TDR measurement set-up was concluded to be between 0.10 and 0.20 m (neglecting the spread-out of the leakage spot during the performed experiments).
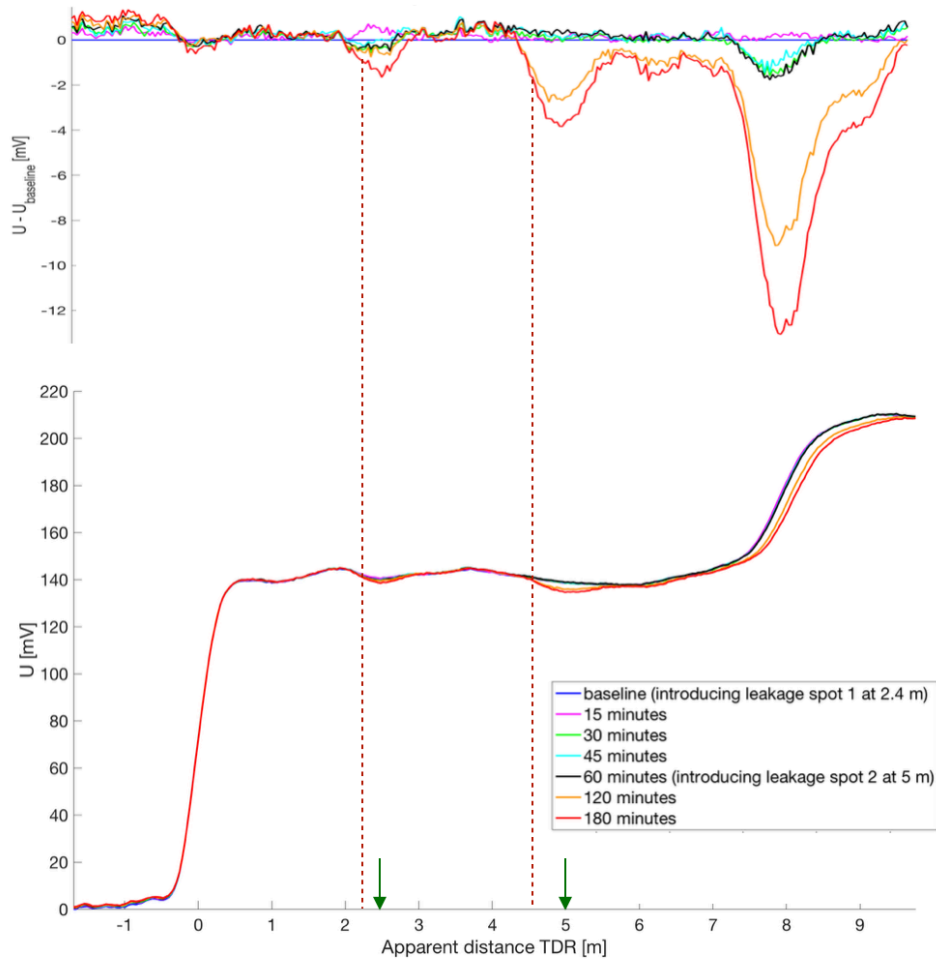
Figure 6.24. Time evolution of the (differential) TDR voltage reflectogram for two water leakage spots simultaneously present at a distance of respectively 2.40 m and 2.90 m from the sensor entrance. The estimated leakage locations are indicated by a dashed red line and were determined by visual selection of the inflection point of the differential voltage at each leakage spot. The leakage spots are indicated by a green arrow.

Localisation of all 3 leakage spots

The five discussed methods for the determination of the TOF were used for the localisation of the 3 leakage spots within the series of experiments. For each leakage spot, a characteristic time point was determined based by applying the MD, TL, MAX and SF method to the differential voltage (to filter the influence of bends out). The ZC method could not be used because the characteristic voltage drop just before a discontinuity was not clearly observable. Figure 6.25 illustrates the determination of the characteristic time point for each method for the leakage spot applied at a distance of 2.90 m from the sensor entrance. The fitted sigmoidal differential voltage for the SF method together with the (differential) TDR voltage reflectogram observed at the other leakage spots can be found in appendix A.3.

The locations of the leakage spot derived from all methods are given in table 6.6 whereas the error for each method at each leakage spot is shown in figure 6.26. Table 6.7 contains the mean error and its 95 % confidence interval for each methods based on these 3 leakage spots.

A distinction between all leakage spots could clearly be made based on only the estimated locations for all methods, except for the leakage spots at 2.40 and 2.90 m the TL methods could

not offer a clear distinction. Generally, an underestimation of the leakage location was seen. The error increased along the sensor. The average error of approximately 0.30 m was similar for the MD, TL and SF methods. However, the variation of the error was significantly smaller for the SF method. The MAX method always seriously underestimated the leakage locations and hence, should not be used to localise water leakage spots along the sensor. The proposed SF method showed less variation due to its fitting procedure, in which averaging was done over the local variations in the differential voltage, and offers a valid alternative to the traditional MD and TL method.
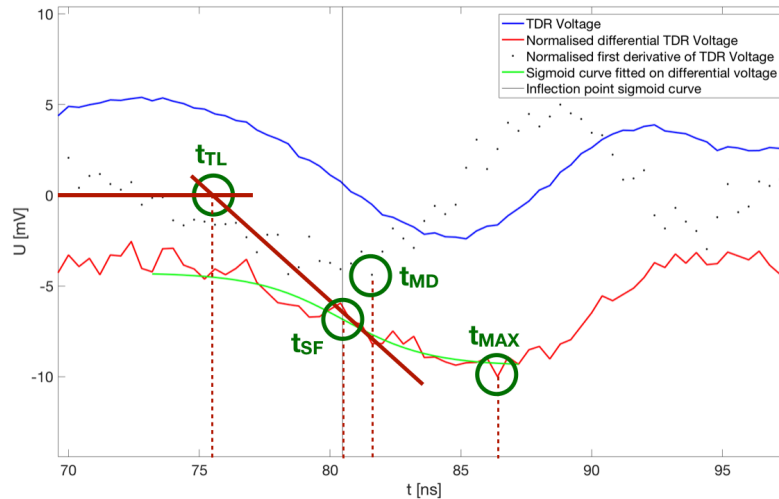
Figure 6.25. Determination of the characteristic time for the water leakage spot at a distance of 2.90 m from the sensor entrance. The maximum-derivative (MD), tangent line (TL), sigmoidal fitting (SF) and maximum method (MAX) were considered, each of them resulting in a different characteristic time. The derivative of the TDR signal, which was normalised for a clear representation together with the TDR voltage, is also shown.

Table 6.6. Estimated leakage locations together with the real locations at which the water leakages were applied for the third series of water leakage experiments.

Leakage spot (real location)	2.40 m	2.90 m	5 m
sigmoidal fitting	2.18 m	2.59 m	4.61 m
maximum-derivative	2.20 m	2.75 m	4.55 m
tangent line	2.43 m	2.50 m	4.49 m
maximum	1.63 m	2.23 m	3.91 m
zero-crossing	-	-	-
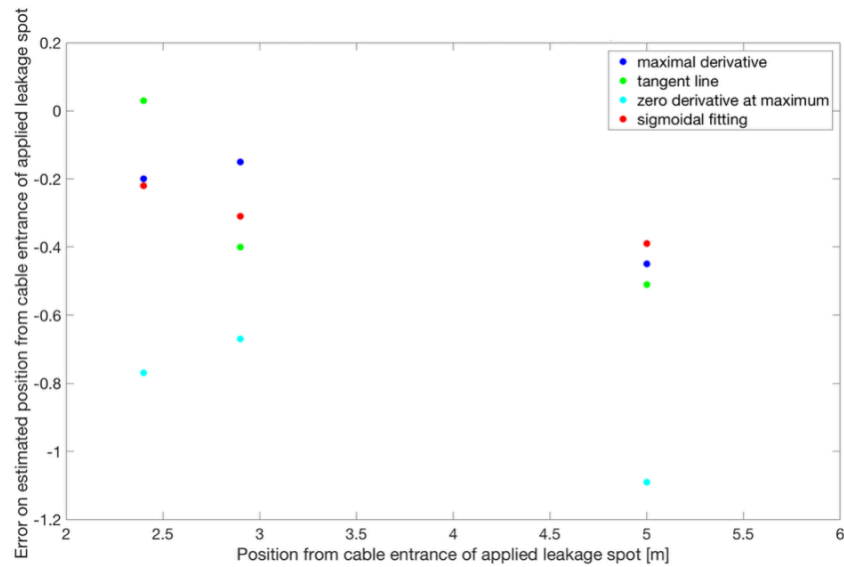
Figure 6.26. Error on the leakage positions determined by the maximal-derivative, tangent line, maximum and sigmoidal fitting method for each of the 3 leakage spots applied in the third series of water leakage experiments.

Table 6.7. Mean error and 95 % uncertainty interval for each of the 5 studied methods for the determination of the leakage location based on the third series of water leakage experiments.

Leakage spot (real location)	Mean error
sigmoidal fitting	-0.31±0.11 m
maximum-derivative	-0.26±0.21 m
tangent line	-0.29±0.37 m
maximum	-0.84±0.28 m
zero-crossing	-

Three-Stake method

The Three-Stake method discussed in paragraph 4.3.4 was also tested for an improved localisation of the leakage spots (Megger, 2013). Figure 6.27 shows the TDR voltage reflectogram obtained at the end of the second experiment measured from the normal sensor end. Both leakage spots were detectable and a smaller differential voltage was seen for the first leakage spot, which was now seen to be located the furthest from the newly used sensor entrance. The observed differential voltages were similar to the ones observed with the normal sensor entrance. The locations of both leakage spots detected with the normal and reversed sensor entrance are shown in table 6.8 together with the corrected estimation based on combining both distances found for each leakage spot according to the Three-Stake method. The SF method was used to visually assess the time points of the leakage spots. For both leakage spots, an improvement in localisation was observed. Especially for the second leakage spot, a remarkable increase in the accuracy of the leakage spot location was seen. Hence, the Three-Stake method improves without any doubt the localisation accuracy of a leakage spot based on TDR measurements.

Table 6.8. Apparent locations of both simultaneously present leakage spots on the water sensor determined by attaching the measurement set-up to both the sensor entrance and end. The Three-Stake method was used for an improved localisation according to equation (4.7) and (4.8) (Megger, 2013).

Leakage spot (real location)	2.40 m	5 m
measured from sensor entrance	2.2 m	4.6 m
measured from sensor end	5.5 m	2.8 m
improved guess based on Three-Stake method	2.3 m	4.9 m

(d)
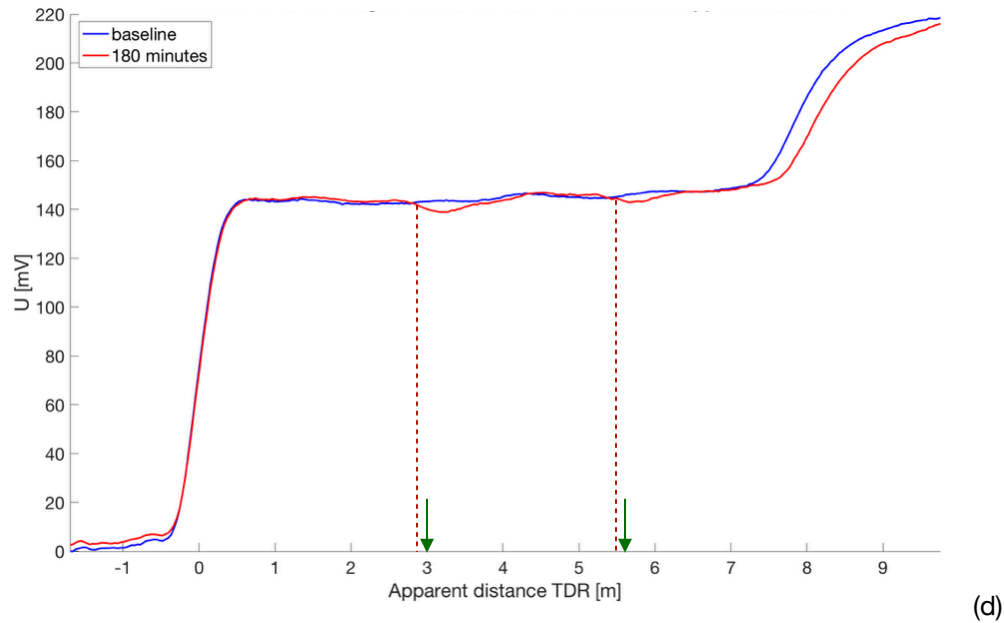
Figure 6.27. Time evolution of the (differential) TDR voltage reflectogram for two water leakage spots simultaneously present at a distance of respectively 3 m and 5.60 m from the sensor entrance. The normal sensor end was now attached to the measurement set-up (Three-Stake method). The estimated leakage locations are indicated by a dashed red line and were determined by visual selection of the inflection point of the differential voltage at each leakage spot. The leakage spots are indicated by a green arrow.

Influence of resistance clamps

Contrary to the kerosene sensor, no significant influence of the resistance clamps on the sensor's TDR signature was observed. The much stiffer structure of the water sensor was assumed to be the cause: less flexibility was present and the PVA/TiCN sensing layers provided most of the composite's stiffness.

6.7. Conclusions

A redesign of the viscose-based sensor was studied for the spatial detection of water. Its lay-up and dimensional properties were determined by Scanning Electron Microscopy and Energy Dispersive spectroscopy. The materials cost was estimated at € 1.72/m, which is significantly lower than the commercially available alternatives. The TDR signature was obtained for the dry sensor. No significant attenuation was seen along the sensor. A minimal frequency of 1.8 MHz for the square wave was observed to allow complete and clear recognition of the sensor in the detected TDR voltage reflectogram. A theoretical spatial resolution of 0.05-0.10 m was derived for the currently used measurement set-up to allow a complete detection of a leakage spot. The wave propagation velocity was determined based on both traditional and the new proposed sigmoidal fitting method, which was proven to be a valid alternative to the commonly used traditional maximum-derivative and tangent line method.

Two equal series of three leakage spots applied at different locations along the sensor could all be clearly detected and an accurate localisation based on the proposed sigmoidal fitting method was possible. A negative reflection of approximately 4-6 % of the applied voltage wave amplitude at a leakage spot was found to be caused by the increase in the permittivity of the PVA matrix due to the water absorption, which was confirmed by dielectric spectroscopy. The PVA swelling acted as a second order effect, which did not cause a fuse-like complete reflection as will be seen for the rubber sensor in next chapter. A second leakage spot was possible to be detected when it was applied behind a leakage spot closer to the sensor entrance. The Three-Stake method suggested in literature seriously improved the localisation accuracy of the leakage spots.

The fuse-like increase of the DC resistance was found to occur 10-15 minutes after the significant change in the differential TDR voltage was observed, because a larger diffusion distance was present for the water to reach the percolative PVA/TiCN layer. Hence, a larger water concentration in the TDR influencing PVA protective layer was always present. Additionally, no critical local water concentration existed to see a significant change in the recorded TDR signal, whereas for the DC resistance, the lyotropic percolation threshold had to be locally exceeded.

Chapter 7

Characterisation kerosene sensor

During previous research, additional sensors were designed to detect oil- and fuel-based liquids, which were described in paragraph 2.3.2 (H. Pfeiffer, 2014). Currently, a conductive rubber is studied to detect and localise a kerosene leakage spot by DC resistance and TDR measurement. This chapter elaborates a complete characterisation of the kerosene sensor by calculating its materials cost and determining the TDR signature for both the dry sensor and when leakage spots are applied. The time of flight, wave propagation velocity and permittivity are estimated based on both traditional and proposed new methods to allocate a characteristic time point to the sensor entrance and end. The detectability and localisability of a single and multiple leakage spots at different positions along the sensor is assessed. Finally, the influence of the clamps attached to the sensor to allow measurement of the DC resistance is studied.

7.1. Materials cost of the sensor

Figure 7.1 illustrates the lay-up of the sensor based on datasheets supplied by the manufacturer (Conrad, 2018; Holland Shielding Systems BV, 2018). The inner conductor consists of a silicone rubber in which nickel coated graphite filler particles are dispersed and has a rectangular base with a semi-circular top. The outer conductor is an enamel coated copper wire which was helically wound around the inner conductor to allow TDR measurements. The outer conductor has a significantly smaller diameter compared to the inner conductor.
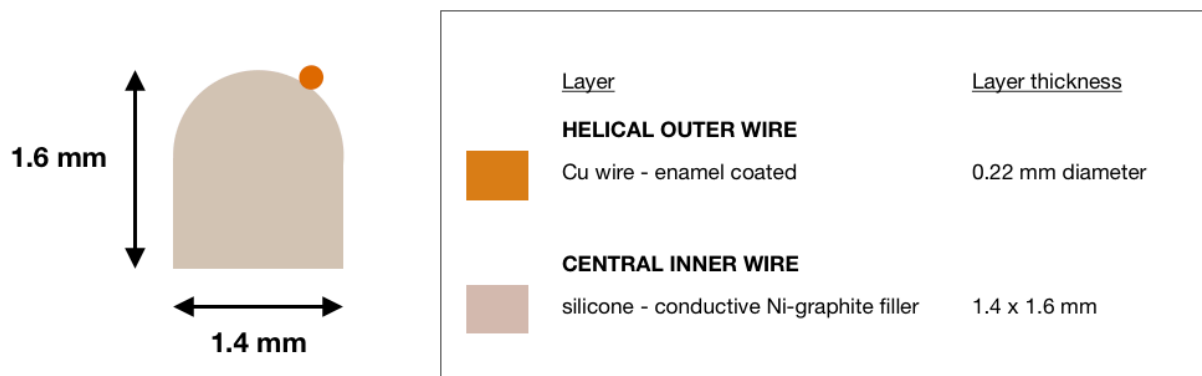
Figure 7.1. Illustration of the lay-up of the rubber sensor based on datasheets supplied by the manufacturer.

The materials cost for each layer and the complete sensor was estimated based on the price per length supplied by the manufacturers and is given in table 7.1. The percolative rubber wire makes up 75 % of the total price and a materials cost of € 0.25/m was estimated for the complete sensor, which is one-fourth and one-seventh of the materials cost of respectively the nylon and viscose based water sensor. The price is an order of magnitude lower compared to the cost of € 14-40/m for the commercially available sensors discussed in paragraph 2.2. However, the materials cost should be understood as the marginal cost of the sensor, which is the cost for an

extra sensor produced and hence, fixed costs as machinery, construction of the production facility and labour, the latter one being also a marginal cost, were not included. Nevertheless, the estimation of the materials costs confirms the developed sensor to be a low-cost alternative to the currently available commercial leakage sensors. Moreover, discounts are not yet considered.

Table 7.1. Materials cost for the complete kerosene sensor and each composing layer.

Layer	Price [€/m]	Contribution to total sensor price [%]	Manufacturer/source
inner conductor	0.19	75	(Holland Shielding Systems BV, 2018)
outer conductor	0.06	25	(Conrad, 2018)
total sensor cost	**0.25**		

7.2. TDR signature of the measuring set-up

7.2.1. TDR baseline signature

Figure 7.2 shows the TDR voltage reflectogram measured for the dry sensor. Similar to the water sensor, the sensor entrance is clearly recognised, whereas the sensor end is masked by the resistive attenuation along the sensor. The attenuation is caused by the higher resistance of the silicone rubber. Conductive nickel coated graphite particles are dispersed in the silicone to increase the conductivity, however a conductivity still lower than for the copper conductors used in the water sensor is present. A DC resistance of the rubber inner conductor of 150.6±0.1 Ω was observed over the complete sensor length, whereas the value for the copper outer conductor was 1.2±0.1 Ω. A DC resistance out of the multimeter's detection limit was observed when measuring between both conductors, indicating no conductive path in between the conductors was present for the sensor, which was intended by the sensor design.

A length of 2.96±0.07 m was measured for the sensor. As for the water sensor, the splitter and the BNC-to-banana connector were assumed to coincide and hence, the point in time when the voltage wave was detected by the oscilloscope equals the point in time for which the sensor entrance was reached.

7.2.2. Wave propagation velocity and TOF

The same analysis as for the water sensor discussed in paragraph 6.1.3 was executed. The traditional maximum-derivative (MD), tangent line (TC) and zero-crossing (ZC) method were combined with the proposed new maximum and sigmoidal fitting method. The sigmoidal fitting method used the time calculated as the inflection point of equation (5.1) to attribute a characteristic time to both the sensor entrance and end. For the maximum method, the maximal voltage seen in the reflectogram at the entrance, which was seen in the region of overshoot at each discontinuity, was chosen as characteristic time. The time points determined by all five methods are shown in figures 7.3a and 7.3b for respectively the sensor entrance and exit. Next, these time points were used to calculate the time of flight (TOF), which was in turn used in combination with the sensor length to calculate the wave propagation velocity.
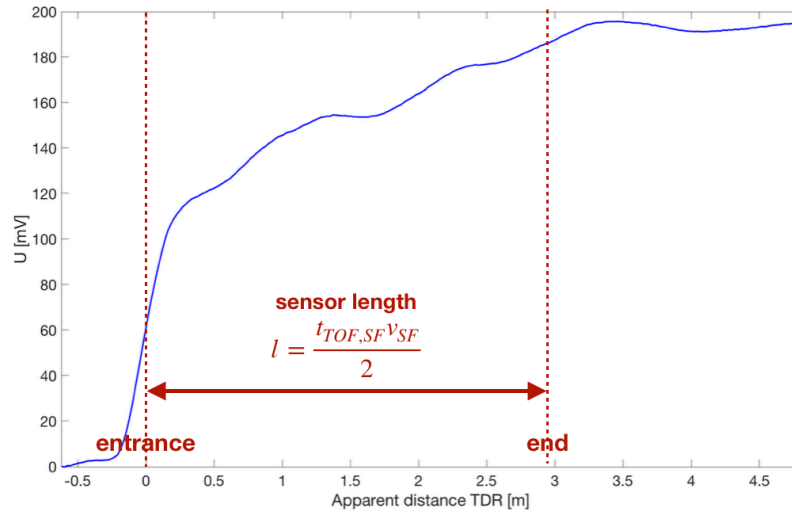
Figure 7.2. TDR signature of the kerosene sensor. Both the entrance and end of the sensor are indicated. The apparent distance between them is calculated by using the time interval between the entrance and end determined by the sigmoidal fitting (SF) method, which allows the calculation of the time of flight (TOF) and the wave propagation velocity (v).

The 10-90 % rise time at the sensor entrance and end was calculated by using equation (6.2) in which its value was directly related to scaling parameter of the sigmoidal fitting. As for the water sensor, the rise time at the end was twice as high as at the entrance, which can be explained by the dispersion occurring along the sensor: the steep edges of the square wave are smoothened due to the faster propagation of higher frequency components. The uncertainty originated from the fitting procedure for the scaling parameter and is represented by the half width of the 95 % confidence interval.

The 10-90 % rise time and the DC resistance are listed in table 7.2 together with the TOF, wave propagation velocity and permittivity determined by the different methods for the TOF. The uncertainty on the wave propagation velocity was determined by using equation (5.2) in which the uncertainty on both the sensor length and the TOF are taken into account. The ZC method could not be used for the rubber sensor because the resistive attenuation masked the local valley in the TDR voltage reflectogram, which is characterised by the ZC method. For the MD, MAX and TL method, no uncertainty was attributed because the characteristic time points are based on only one time, not a fitted value and hence, an uncertainty is only attributable to the uncertainty on the sensor length. The relative permittivity followed from equation (4.13) and its uncertainty was assigned by equation (5.3).

Table 7.3 contains the fitted parameters for the SF method at the sensor entrance and end.

A first important conclusion is that all five methods except the MAX method resulted in similar TOF and wave propagation velocities. The MAX method might be less appropriate for the rubber sensor because the time point of maximal overshoot is masked by the attenuation, which is the best seen at the sensor entrance. Typically, a wave propagation velocity equal to half of the velocity of light is found in cables (Megger, 2013). For silicone rubbers, typical values between 53 ad 69 % of the velocity of light were reported in literature (PIC Wire, 2018). However, the high permittivity of the sensor due to the percolative graphite filler network, which was discussed in paragraph 2.3.1. for other dielectric ceramics, decreased this value to about one-third of the velocity of light. The wave propagation velocity determined with the MD method was lower than the one calculated form the TL method, which is in accordance with the in paragraph 4.3.4 discussed literature (G. M. D'Aucelli, 2017; N. Giaquinto, 2015; D. A. Robinson, 2005). The TL

method is related to the phase velocity, whereas the MD method has a connection with the group velocity, the latter always being lower than the former. This is confirmed by the dispersion behaviour: the high frequency components propagate faster along the line (rather with the phase velocity) and the time distance between the mean frequency components (which propagate rather with the group velocity) increases along the sensor and hence, the time difference between the time point calculated with the MD and TL method increases (as can be seen in table 7.2). Hence, a difference in wave propagation velocity for both methods arose. This also results in an increase of the rise time at the sensor end compared to the sensor entrance, which was observed and given in table 7.2.

Table 7.2. Characterisation of the dry kerosene sensor based on the DC resistance, 10-90 % rise time, TOF, wave propagation velocity and permittivity. The maximum-derivative (MD), tangent line (TL), zero-crossing (ZC), sigmoidal fitting (SF) and maximum method (MAX) were applied.

Property	Value	Method used
DC resistance inner conductor	$150.6 \pm 0.1\ \Omega$	-
DC resistance outer conductor	$1.2 \pm 0.1\ \Omega$	-
DC resistance inner/outer conductor	out of limit	-
length	2.96 ± 0.07 m	-
10-90 % rise time at entrance	6.1 ± 0.4 ns	sigmoidal fitting
10-90 % rise time at end	12.8 ± 0.7 ns	sigmoidal fitting
TOF	56.4 ns	maximum-derivative (MD)
	52.9 ns (51.6 ns)	tangent-line (TL) (estimated by sigmoidal fitting)
	-	zero-crossing (ZC)
	54.6 ± 0.4 ns	sigmoidal fitting (SF)
	59.0 ns	maximum (MAX)
wave propagation velocity	$1.05 \cdot 10^8$ m/s	maximum-derivative (MD)
	$1.12 \cdot 10^8$ m/s ($1.15 \cdot 10^8$ m/s)	tangent-line (TL) (estimated by sigmoidal fitting)
	-	zero-crossing (ZC)
	$1.08 \pm 0.04 \cdot 10^8$ m/s	sigmoidal fitting (SF)
	$1.00 \cdot 10^8$ m/s	maximum (MAX)
relative permittivty	7.66 ± 0.45	sigmoidal fitting

Table 7.3. Fitted parameters in the sigmoidal fit for the kerosene sensor entrance and end, based on equation (5.1).

Parameter	p_1 [V]	p_2 [ns^{-1}]	p_3 [V]	t_0 [ns]
sensor entrance	$117 \cdot 10^{-3}$	$724 \cdot 10^{-3}$	0	75.9
sensor end	$21 \cdot 10^{-3}$	$345 \cdot 10^{-3}$	$173 \cdot 10^{-3}$	130.5
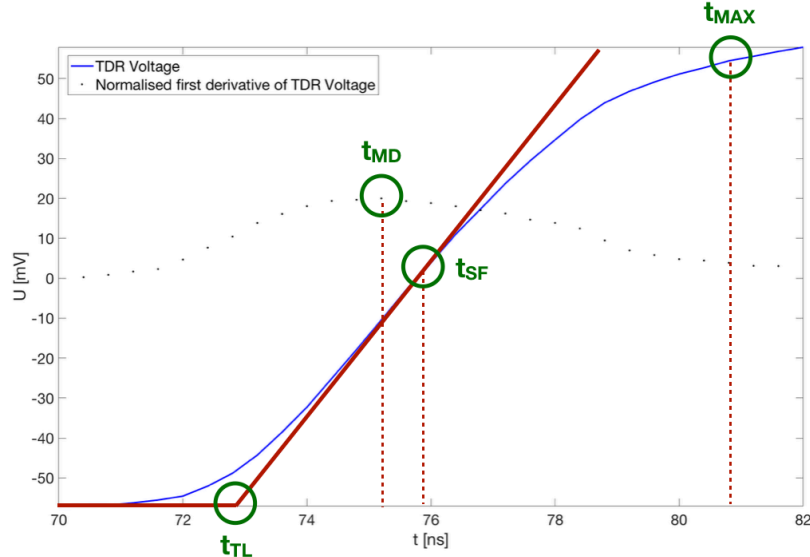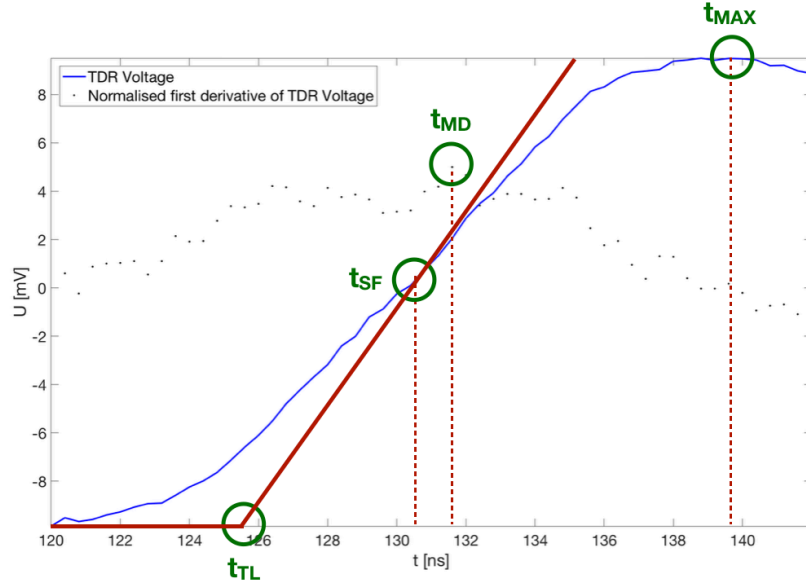
Figure 7.3a. Determination of the characteristic time for the kerosene sensor entrance. Figure 7.3b. Determination of the characteristic time for the kerosene sensor end. The maximum-derivative (MD), tangent line (TL), sigmoidal fitting (SF) and maximum method (MAX) were considered, each of them resulting in a different characteristic time. The derivative of the TDR signal, which was normalised for a clear representation together with the TDR voltage, is also shown.

Secondly, the proposed SF method is a valid alternative to the traditional MD and TL method. The SF is advantageous over the MD and TL method by averaging over the data points of the reflection due to the fitting procedure instead of determining the characteristic time based on the derivative at one characteristic time. Small local variations and fluctuations in the derivative can seriously influence the characteristic time. The influence of the evaluation scheme of the derivative at time t (either based on the data points for t_{i-1} and t_i, either for t_i and t_{i+1} or an average based on t_{i-1} and t_{i+1}) showed no significant difference in the value of the time point determined by the MD and TL method. Additionally, the TL time point was accurately estimated with the SF method. Hence, the SF method was used for all apparent distance calculations on the sensor during leakage experiments.

Starting from the inflection point of the SF, one could say the uncertainty on the wave propagation velocity does not merely result from the fitting procedure of the sigmoidal parameter, but especially on the uncertainty on the choice of the correct/appropriate characteristic time point. The real appropriate time point is situated between the one used for the TC and SF method. Hence, a larger uncertainty on the time of 2.0 ns was found, based on the average time difference between the time points obtained with the TC and SF for both the sensor entrance and end, which resulted in an uncertainty on the wave propagation velocity for the SF method of $0.10.10^8$ m/s. This uncertainty was used within the leakage experiments to calculate the uncertainty on the estimated location of the leakage spot based on only the SF method.

7.3. Kerosene sorption by silicone rubber

A relative mass absorption of 16.9 % was reached by the sensor after 1.5 hours of immersion in kerosene. By calculating the relative density of the rubber sensor, which equals 1.89, the volumetric swelling can be estimated based on a relative density of 0.8 for kerosene. By assuming no density change for the pure rubber phase, a volumetric swelling of nearly 40 % was found. J. L. Graham observed a volumetric swelling of 5-9 % for nitride rubber in JP-5 Jet fuel enriched with 10 vol% of aromatics (J. L. Graham, 2006). However, the order of magnitude of the swelling is strongly dependent on the rubber-solvent system. The degree of cross-linking, type of solvent, and temperature together with the rubber's molecular weight, glass transition temperature and chemical composition all influence this behaviour (E. V. Takeshita, 2012). E. V Takeshita et al. observed a relative mass swelling of 12 % and 25 % after respectively 5 and 15 minutes for styrene-butadiene rubber in toluene. C. Nohilé, P. I. Dolez and T. Vu-Khanh indicated the similarity between the Hansen solubility parameters of the rubber and the solvent as the major driving force for swelling (C. Nohilé, 2008). However, also the diffusion together with the ad- and absorption behaviour played a major role. For perchloroethylene in butyl rubber, a relative volumetric swelling of even 391 % was found.

Physically, the rubber swelling is explained by an equilibrium between the driving osmotic pressure for dissolving the polymer in the solvent and the isotropic restoring elastic force exerted by the cross-linked network of the polymer chains after vulcanisation (G. Strobl, 2007).

Chemical resistance charts for rubber indicated the silicone rubber to be unsatisfactory resistant to kerosene, jet fuel A (which is commercial jet fuel) and RJ-1 (which is rocket fuel) and doubtfully resistant to Skydrol. Nevertheless, the silicone rubber shows a satisfactory resistance to water and other polar solvents (Mykin, 2018).

7.4. Kerosene leakage detection and localisation

Previous paragraph explained why a significant absorption of kerosene and hence, a significant change in local dimensional and electromagnetic properties of the sensor can be expected when a leakage spot of kerosene is intentionally applied. For every experiment, the sensor's baseline TDR voltage reflectogram was recorded and all changes in the reflectogram over time were compared to this baseline. The wave propagation velocity was also recalculated for each experiment by the SF method to take any changes on the sensor over time into account.

7.4.1. Series 1: leakage spots at 4 different locations

Four random leakages spots were chosen, which were applied in four separate experiments. The leakage spots were located at a distance of 0.30 m, 1.45 m, 1.75 m and 2.64 m from the sensor entrance. The DC resistance could only be measured for the leakage spots of 1.45 m and 2.64 m, because the sensor had not been completely dried at the time of initiation of the other experiments. The sensor was observed to have sufficiently dried (which means a change in the DC resistance of several orders of magnitude on a logarithmic scale could clearly be observed during a new experiment) after 3 days, which is longer than for the water sensor. The lower vapour pressure of kerosene, approximately 3.5 times lower than for water, explains the slower drying kinetics (Engineering Toolbox, 2018b). However, the interaction (which depends on the Hansen solubility parameters) of the solvent with the absorbing matrix plays also an important role.

Figure 7.4a-7.4d show the measured differential TDR voltage reflectograms together with the TDR voltage reflectogram during each experiment. Each of the four experiments allowed the detection of the leakage. However, for leakage spots located at a larger distance from the sensor entrance, the change in TDR voltage was lower because of the attenuation of the applied voltage wave along the sensor. A voltage of approximately 2 times the applied voltage was observed for each leakage spot, which indicated a local reflection coefficient of nearly 1. This was caused by an exponential increase of one or more of the electromagnetic properties of the sensor. The interruption of the percolation network of the graphite filler particles was assumed to be the major cause. An exponential decrease of the conductivity, as described by equations (2.2) and (2.3), occurred because of the transition from conductive graphite particles to isolating kerosene dominated electric properties of the rubber. Paragraph 8.3.3 of the next chapter tries to estimate the change of the reflection coefficient at a kerosene leakage spot by using the lumped circuit approach.

Contrary to the water sensor, the change in electromagnetic properties of the rubber sensor at a leakage spot is a 'first order effect,' because the exponential change in resistance is directly influencing the local characteristic impedance of the main conductors, whereas for the water sensor the change only occurs in the permittivity of the material between the main conductors. The glass transition also does not play an important role for the rubber sensor, because elastomers normally have a glass temperature below room temperature. However the swelling of the rubber started already before the lyotropic percolation threshold of the graphite filled rubber was reached and caused a decrease in the equivalent capacitance: both the increase of the inter-wire conductor distance and the decrease in the permittivity due to the rubber swelling have a negative effect on the capacitance.

For the leakage spot at a distance of 1.45 m and 2.64 m from the sensor entrance, the time evolution of the DC resistance was monitored, which is shown respectively in figure 7.5a and 7.6a. A fuse-like transition was seen with a change in the DC resistance from hundreds of ohm to out of the multimeter's detection range (> 60 MΩ). This change over 5 orders of magnitude was also seen within the previous research of H. Pfeiffer et al. for a kerosene detecting rubber sensor (H. Pfeiffer, 2014). However, a less sharp sigmoidal change from 10 kΩ tot 3 MΩ was reported over a time frame of 4 hours, in which the sigmoidal behaviour started to increase faster after 40 minutes. A different sensor design (a conductive tap containing ethylene propylene rubber mixed with graphite powder) was indicated as the reason for the slower absorption kinetics. Hence, the currently used silicone rubber allows a faster detection of the leakage. For the silicone sensor, the lyotropic percolation threshold occurred 8-9 minutes after the application of kerosene to the sensor, which is highly sufficient to support maintenance operations.

(a)

(b)

(c)

93
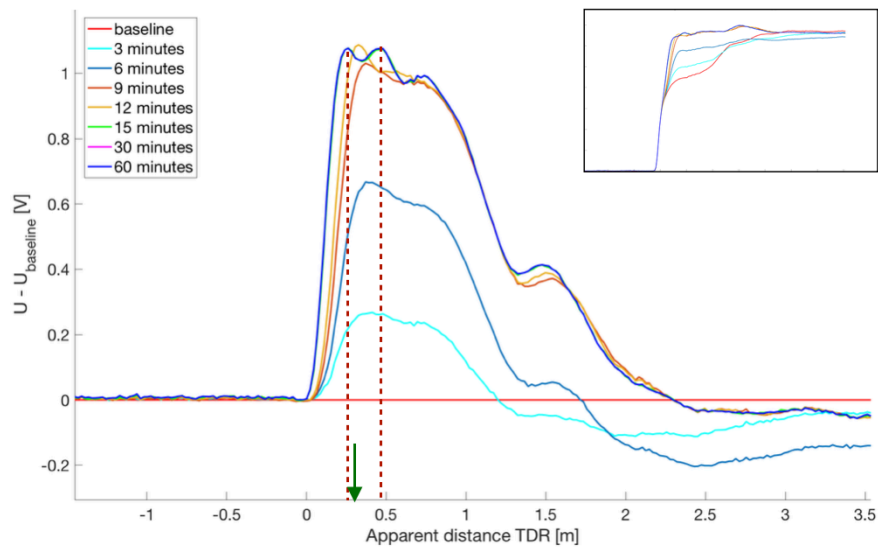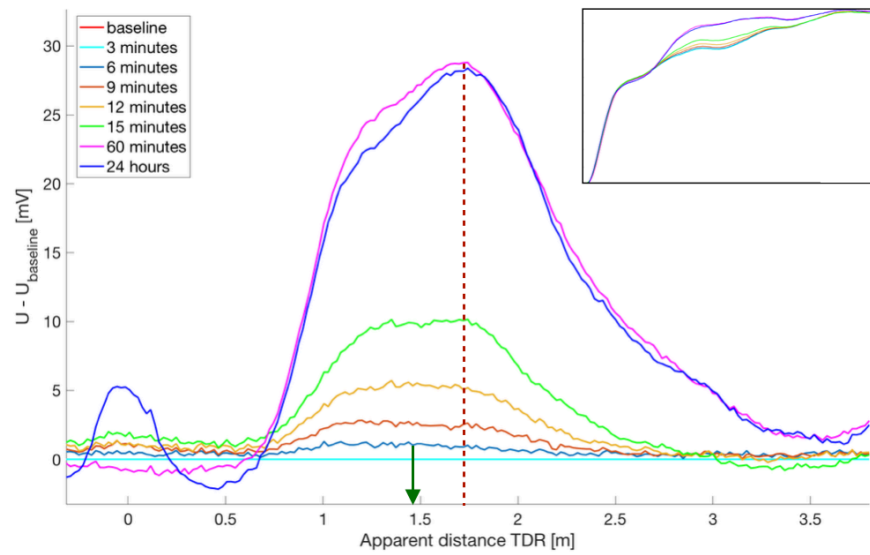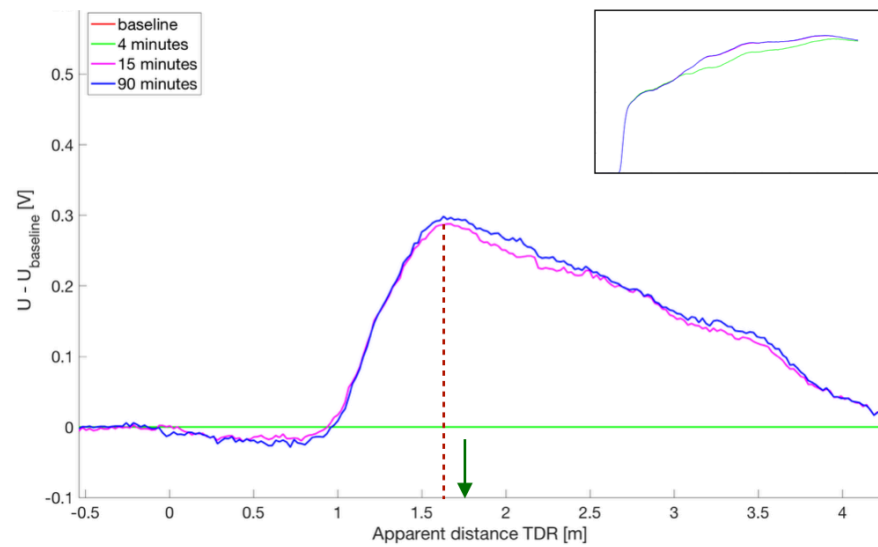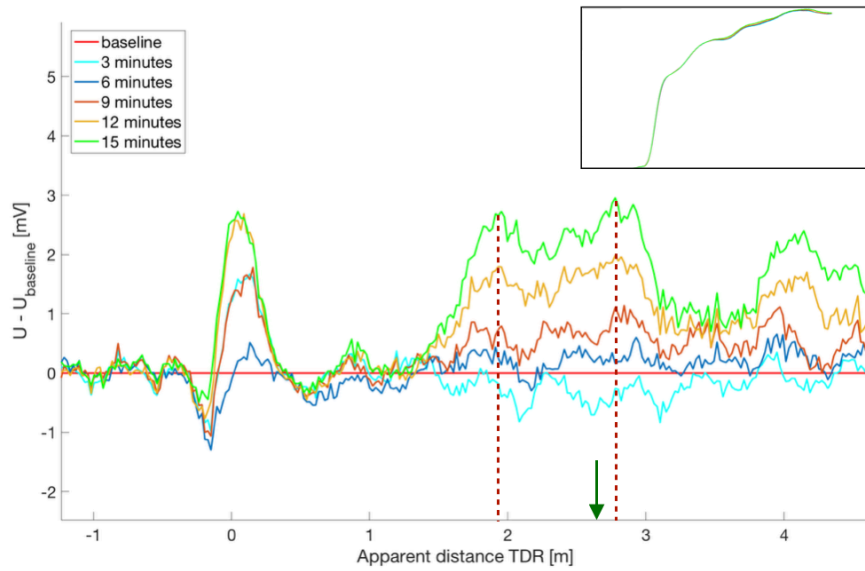
(d)

Figure 7.4. Time evolution of the differential TDR voltage reflectogram for the rubber sensor when a kerosene leakage spot of 4 cm was applied. The leakage spots are indicated by a green arrow and were applied at a distance of respectively 0.30 m (a), 1.45 m (b), 1.75 m (c) and 2.64 m (d) from the sensor entrance. The estimated leakage positions are shown by a red dashed line based on the position of maximal differential TDR voltage. The inset contains for each figure the time evolution of the TDR voltage reflectogram, which also shows a clear detection of the leakage spot was possible. However, for accurate localisation, the differential TDR voltage is the most appropriate to examine. All differential TDR voltages were determined with respect to the baseline of the dry sensor, measured at the beginning of each leakage experiment.

Figure 7.5b and 7.6b confirm a significant change in the differential TDR signal (chose to be above 50 % of the final differential voltage because of the values recorded for other non-leakage positions along the sensor, which were attributed as noise due to local mechanical or electromagnetic perturbations) to nearly coincide with the fuse-like increase of the DC resistance indicating the lyotropic percolation threshold of the rubber sensor was reached.

The locations of the leakage spot derived from the SF method, for which the time difference between the characteristic point of the sensor entrance determined by this method and the time point of maximal differential TDR voltage are used, are given in table 7.4. For a correct determination of the location of the leakage, a sigmoidal fitting procedure should be performed on the differential TDR voltage. However, the attenuation along the sensor significantly masked the sigmoidal change at the leakage discontinuity, which was not a problem for the water sensor. Hence, the accuracy of this modified SF method based on the maximal differential TDR voltage time point was studied. The uncertainty was chosen to be the average time distance between the characteristic time point of both the sensor entrance and end determined by the SF and TL method. This time difference is approximately equal to the time distance between the time point determined by the SF and MAX method and hence, the real location of the leakage spot should always be contained by this uncertainty interval: the uncertainty more or less corrects the used time point of maximal differential TDR voltage to the time point of the leakage discontinuity required for the SF method.
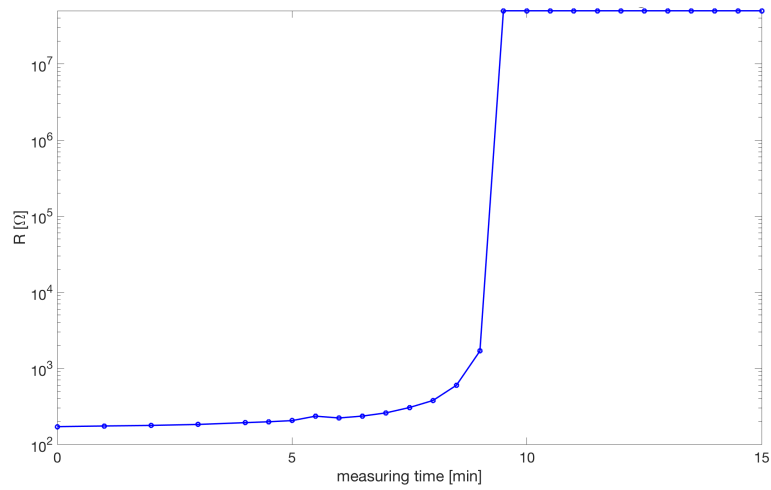
(a)
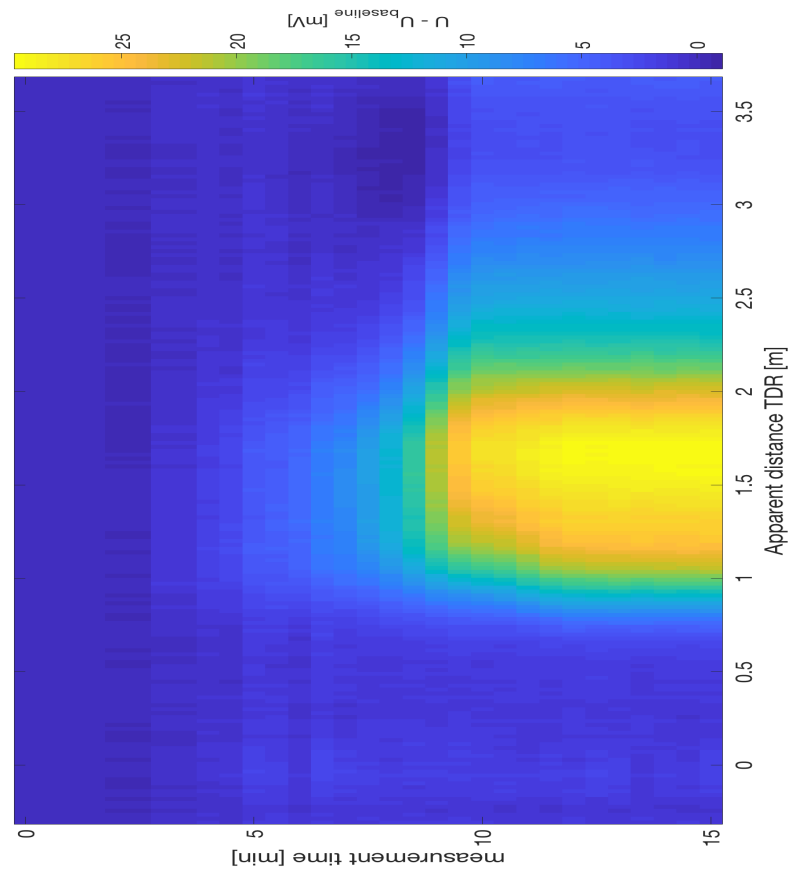
(b)

Figure 7.5a. Time evolution of the DC resistance. Figure 7.5b. Time evolution of the differential TDR voltage reflectogram. Both the fuse-like increase in the DC resistance and the significant change in the TDR voltage (assumed to be at 50 % of the final maximal differential voltage) occurred after 8-9 minutes. The kerosene leakage spot was applied at a distance of 1.45 m from the sensor entrance.

For the leakage spot applied at 0.30 m (figure 7.4a), two closely positioned peaks in the differential TDR voltage were observed. However, the peak after 12 minutes was chosen because probably spreading or a local perturbation of the leakage spot caused the apparent splitting or expansion of the leakage. For the leakage spot applied at 2.64 m, a similar phenomenon was seen: 2 clear peaks separated by approximately 0.80 m were observed. However, the differential TDR signal after 24 hours, which is not included in figure 7.4d, showed the second peak to have further increased. Hence, this peak position was chosen for the distance determination.

All real leakage position were included within the uncertainty interval of he estimated leakage spot.
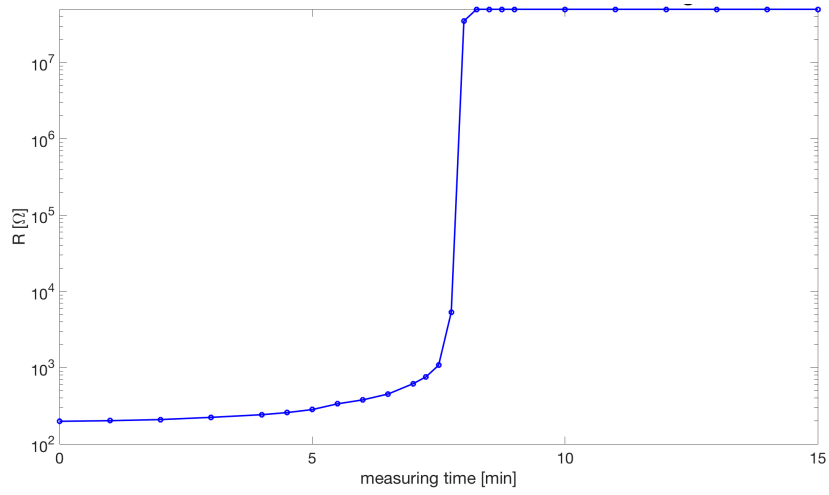
(a)
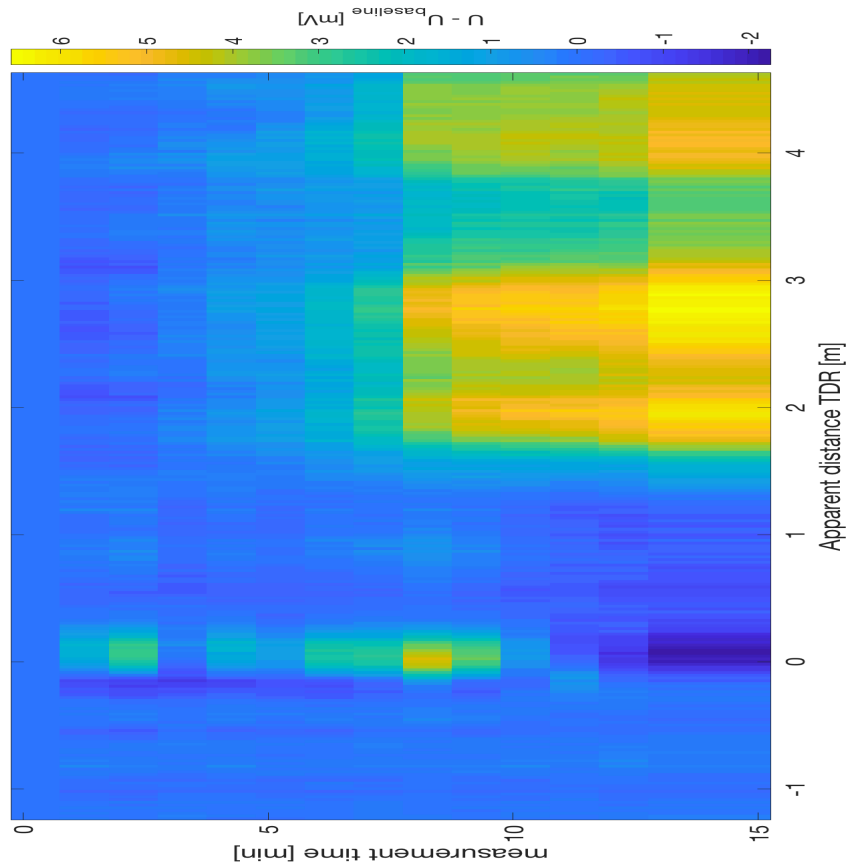
(b)

Figure 7.6a. Time evolution of the DC resistance. Figure 7.6b. Time evolution of the differential TDR voltage reflectogram. Both the fuse-like increase in the DC resistance and the significant change in the TDR voltage (assumed to be at 50 % of the final maximal differential voltage) occurred after 8 minutes. The kerosene leakage spot was applied at a distance of 2.64 m from the sensor entrance.

Table 7.4. Estimated leakage locations together with the real locations at which the kerosene leakages were applied.

Leakage spot (real location)	0.30 m	1.45 m	1.75 m	2.64 m
estimated location	0.27 m	1.52 m	1.84 m	2.82 m
uncertainty interval	[0.26 m; 0.30 m]	[1.42 m; 1.73 m]	[1.66 m; 2.02 m]	[2.54 m; 3.10 m]

Figure 7.7 shows the error on the estimated leakage location together with the uncertainty on the estimated location. The error increased with increasing distance along the sensor of the leakage spot. However, the error was always smaller than the uncertainty and hence, it could be concluded that the SF method in combination with the maximal differential TDR voltage allows an accurate localisation of the leakage spot when the uncertainty on the characteristic time point of the sensor entrance and end is taken into account.
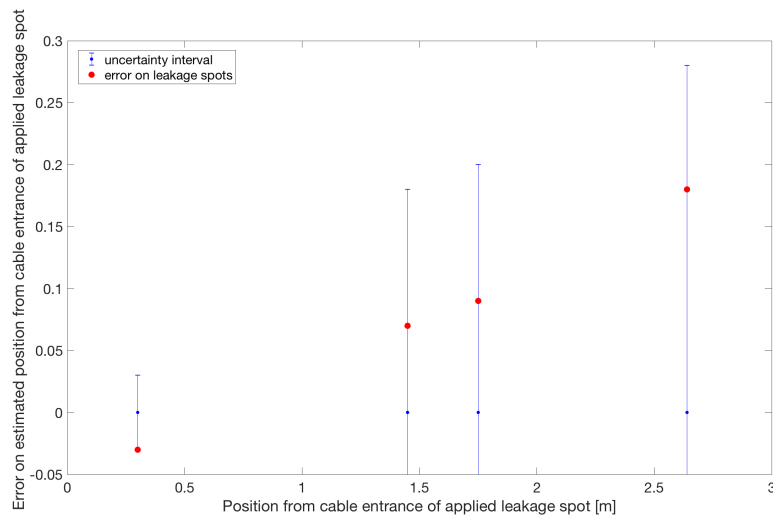
Figure 7.7. Error on the estimated leakage locations together with the uncertainty interval on the estimated locations of the applied kerosene leakage spots.

After 15 minutes, the change in differential voltage seemed to have reached a steady state value. Hence, the differential curves for longer time are sometimes not visible (figure 7.4a), because they are coinciding with the curve for 15 minutes. However, 7.4b shows a significant increase of the differential TDR voltage after 1 hour or 24 hours. This time behaviour can be location-dependent along the sensor apparently. It was concluded that for the practical application of the TDR measurement to detect an immersion leakage spot, inspection intervals of at least 1 hour are appropriate.

A distinction between all leakage spots could clearly be made based on only the estimated locations. The maximal and minimal real distance between two applied leakage spots was respectively 0.30 m and 1.15 m. Even for the smallest distance, a difference in leakage location of approximately 0.30 m could be assessed. Hence, the proposed SF method applied to the peak in the TDR differential voltage allows accurate localisation and detection of the leakage position, whereas only based on a visual inspection of the differential TDR voltage, the localisation of the leakage spot is difficult to perform due to the influence of the leakage spot on the TDR signal over distances far larger than the real width of the applied leakage spot. Because of the 'first order

effect' of the kerosene on the TDR voltage reflectogram, a leakage spot as small as a couple of centimetres could be detected and localised, which was impossible for the water sensor with the currently used wave generator and oscilloscope.

7.4.2. Series 2: two simultaneous leakage spots

The inability to detect multiple leakage spots simultaneously present at the sensor could seriously jeopardise the commercialisation and application of the sensor in industrial environments. Hence two leakage spots were applied at the same time at the sensor. The first one was applied at a distance of 0.80 m from the sensor entrance, the second one at a distance of 2 m after 10 minutes.

Figure 7.8a contains the differential TDR voltage reflectogram. The first leakage spot could be clearly seen after 8-10 minutes. The second spot was not detectable after 20 minutes because it was masked by the further increase of the differential peak at the first leakage spot. Nevertheless, by inspecting the difference between the differential TDR voltage reflectogram obtained after 20 minutes and 1 hour, the second leakage spot could be observed. Localisation was cumbersome, but in combination with the TDR voltage reflectogram, the position of maximal difference (compared to the reflectogram after 20 minutes) for the second leakage spot could be determined.

In order to assess the simultaneity of the significant increase in the differential TDR voltage and the fuse-like increase of the DC resistance, both the reflectogram and resistance were recorded every 15 seconds for 10 minutes. Figure 7.8b shows the time evolution of the differential TDR voltage, whereas the change in differential TDR voltage at the location of maximal difference compared to the baseline together with the change in DC resistance over time are given by figure 7.8c. As for the other leakage experiments with kerosene, a significant change in the differential TDR voltage was observed after 7.5-8 minutes. The DC resistance also showed a fuse-like increase after 8 minutes. Hence, the hypothesis of the simultaneously occurring significant change in differential TDR voltage and DC resistance was confirmed, which was caused by the disruption of the percolative graphite filler network by the kerosene. The local change of conductor- to an isolator-like behaviour of the rubber wire is the origin of the nearly complete reflection of the applied voltage wave.

Based on equation (2.2) and (2.3), the conductivity of the rubber wire is expected to increase according to a power law when the percolative network is interrupted. Hence, a linear change of the differential TDR voltage on a logarithmic scale can be predicted. Figure 7.8c and 7.8d respectively show the time evolution of the logarithm of the differential TDR voltage and the change in the logarithm of the differential TDR voltage at the location of maximal difference compared to the baseline together with the change in DC resistance over time. The expected linear increase in the logarithm of the differential TDR voltage was indeed observed. However, after 8 minutes it reached a stable value, indicating the graphite network was locally completely disrupted at the leakage spot. A leakage spot will always mask the presence of another leakage spot further along the sensor because of the shift of the voltage reflectogram to lower times, which introduces a differential voltage. The decreased permittivity is the reason for this phenomenon: the wave propagation velocity will locally increase at the leakage spot according to equation (4.18). After 20 minutes, the differential TDR voltage attained a steady state value at the first leakage spot. After 1 hour, no significant difference compared to after 20 minutes was seen.
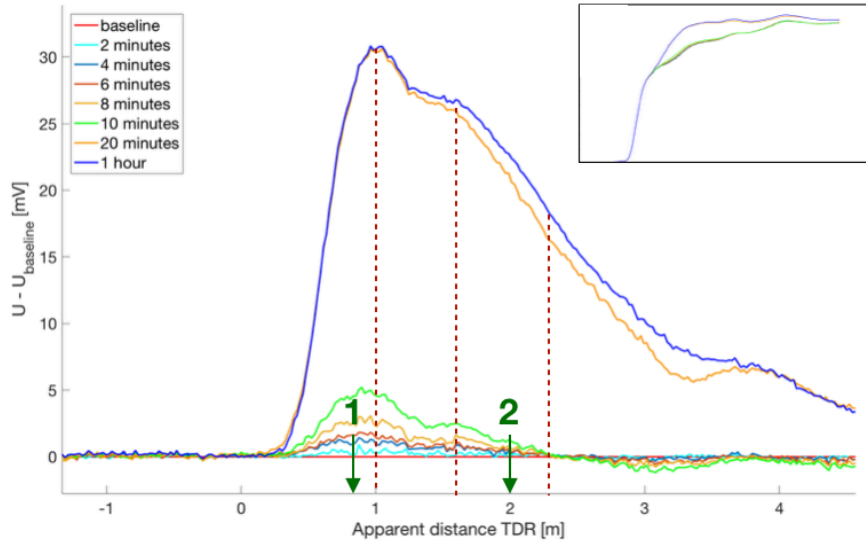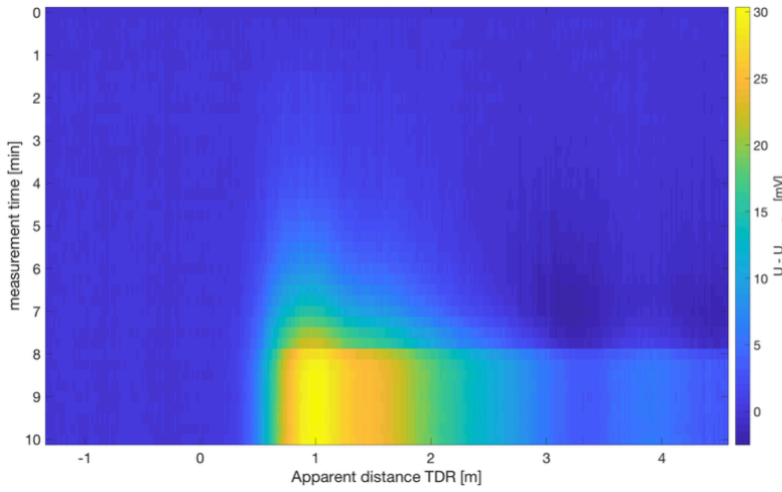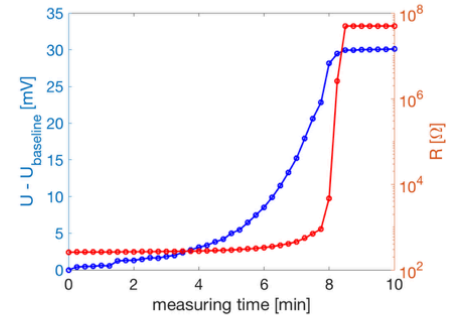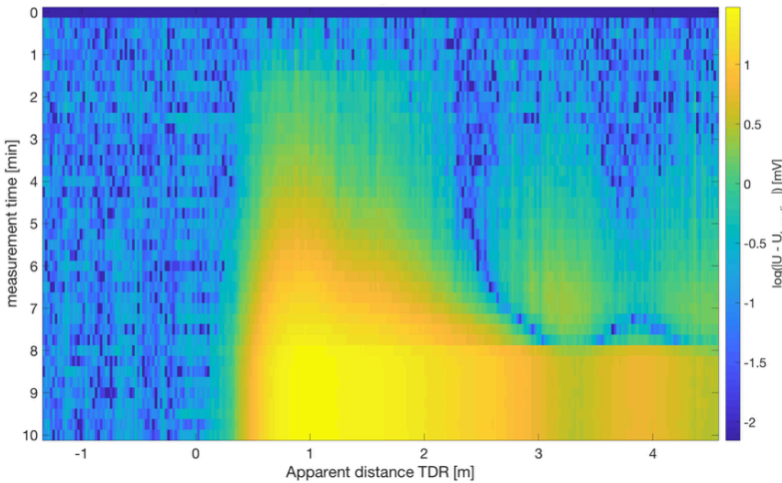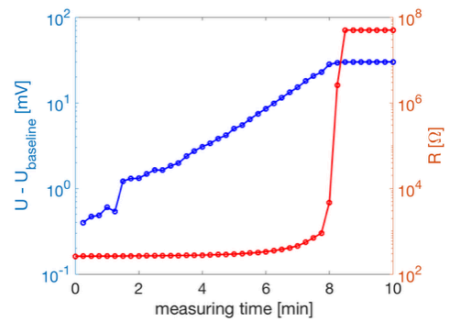
Figure 7.8. Time evolution for the experiment in which 2 leakage spots were simultaneously present at the sensor of the differential TDR voltage (inset of the TDR voltage) (a) and (b), DC resistance (c) together with the logarithmic change of the differential TDR voltage (d) and (e). Figure (c) and (d) show the evolution of the differential TDR voltage at the location of maximal difference. The first leakage spot was applied at a distance of 0.80 m, whereas the second leakage spot was applied after 10 minutes at a distance of 2 m.

Table 7.5 contains the estimated locations of both leakage spots together with the uncertainty on their values. For an accurate localisation, the changed wave propagation velocity in the area of the leakage spot should be taken into account according to equation (4.17). However, the influence of the initially 4 cm wide leakage spot on the velocity was neglected and hence, the velocity determined for the baseline at the start of the experiment could be used. Both applied leakage spots were for this experiment not included within the uncertainty interval. For the second leakage spot a large overestimation was even observed, which was in contradiction to the estimated influence of the locally increased wave propagation velocity. It was concluded that the choice of the time point for the second leakage spot was not accurate and was cumbersome due to the masking by the resistive attenuation along the line and the small increase (relative to the amplitude resolution) in differential TDR voltage at this second leakage spot.

Table 7.5. Estimated leakage locations together with the real locations at which the kerosene leakages were applied for the experiment in which two leakage spots were simultaneously applied.

Leakage spot (real location)	0.80 m	2 m
estimated location	0.92 m	2.28 m
uncertainty interval	[0.83 m; 1.01 m]	[2.05m; 2.50 m]

7.4.3. Influence of resistance clamps

Figure 7.9 shows the voltage reflectogram for the dry sensor when clamps were attached to the sensor to allow measurement of the DC resistance. Especially the negative influence of the clamp at the sensor entrance was clearly seen. This was caused by the introduction of local stresses and bends at the connection of the resistance clamp to the sensor, because of the low Young's modulus of the elastomeric silicone rubber. The influence of bends on the local reflection coefficient was already illustrated in paragraph 6.10. O. Steiner et al. found that stresses of 10 MPa in $BaTiO_3$ introduced an increase of 10 % in the relative permittivity (O. Steiner, 1999). However, also for lower stresses below 1 kPa P. Chakraborty et al. observed a 5-10 % change in the relative permittivity of 25-50 µm thick cured resins used for 3D printing, for which 60-65 % of the increase occurred for a stress of only 1 kPa (P. Chakraborty, 2017). If only the permittivity changed by the clamping, the observed negative reflection could be explained by the increase in permittivity. However, also the resistance was probably influenced due to the dimensional change in the sensor's cross-section.

To conclude, the flexibility of the rubber sensor allows its application in geometrically complex environments, but does also introduce a change in the sensor's TDR signature. Hence, the baseline should, in contradiction to the water sensor where nog significant influence was observed, always be recorded when the resistance clamps already have been attached to the sensor in order to allow the detection of differential TDR voltages only caused by leakage spots.
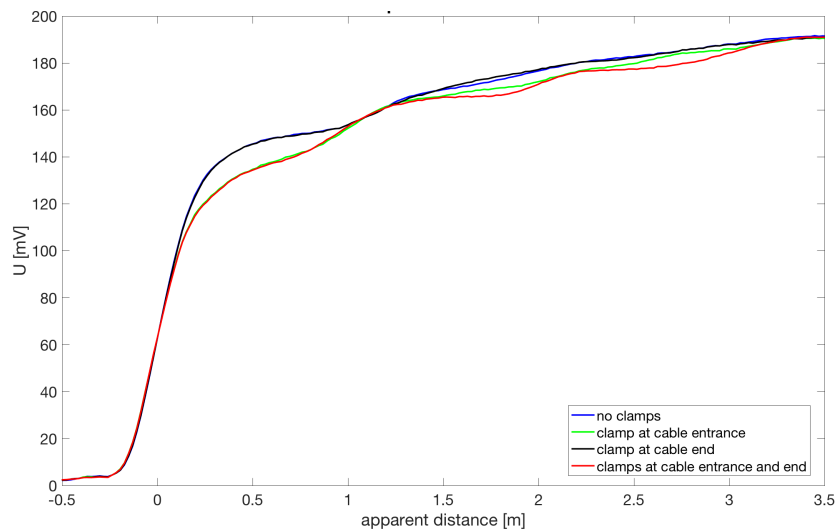
Figure 7.9. Influence of the resistance clamps on the sensor's TDR signature.

7.5. Conclusions

A new design of the rubber sensor was studied for the detection of kerosene. The sensor consisted of a silicone rubber in which conductive nickel coated graphite filler particles were dispersed. The materials cost was estimated at € 0.26/m, which is significantly lower than the commercially available alternatives. The TDR signature was obtained for the dry sensor. Different to the water sensor, significant attenuation along the sensor was seen, which masked the detection of subsequent leakage spots. The wave propagation velocity was determined based on both traditional and the new proposed sigmoidal fitting method, which was proven to be a valid alternative to the commonly used traditional maximum-derivative and tangent line method.

The four leakage spots separately applied at different locations along the sensor could all be clearly detected and an accurate localisation based on the peak in the differential TDR voltage in combination with the sensor entrance was possible by using the proposed sigmoidal fitting method. The nearly complete reflection of the applied voltage wave at a leakage spot was found to be caused by the interruption of the percolative graphite network by the absorption of kerosene. The rubber swelling acted as a 'first order effect', whereas for the water sensor the 'second order effect' of the water absorption introduced a smaller reflection as it only affected the permittivity between the main conductors. A second leakage spot was more difficult but still possible to be detected when it was applied behind a leakage spot closer to the sensor entrance. However, the localisation of the second leakage spot was cumbersome and less accurate.

The fuse-like increase of the DC resistance was found to coincide with the significant change in the differential TDR voltage, because both phenomena were caused by the interruption of the percolative graphite network. Finally, it was concluded that the baseline of the dry sensor should always be recorded after the attachment of the clamps for the resistance measurement, because these significantly influence the TDR signal.

Chapter 8

Lumped circuit modelling

Chapters 6 and 7 concluded that both accurate, precise and sensitive detection and localisation of water and mineral-oil base liquids such as kerosene is possible with respectively the PVA/TiCN and rubber sensor, both of them percolation-based. A negative reflection was observed on the water sensor, whereas a positive reflection was present for the rubber sensor. To assure these reflections originate from the water or kerosene uptake, a rigorous estimation of the order of magnitude of the reflection caused by the leakage is elaborated in this chapter. The model is based on the lumped circuit approach discussed in chapter 3 and allows to determine the characteristic impedance of both sensors and of the leakage spot. The dimensional data obtained from the manufacturer's data sheets and Scanning Electron Microscopy are combined with both literature and experimental data on the electromagnetic properties of the sensors. For the water sensor, the permittivity data obtained with the dielectric spectroscopic measurements will be used to estimate a range of change of capacity due to the water leakage to verify whether this interval contains the experimentally observed value of the capacity.

8.1. Sensor 1: PVA/TiCN for detection of water

8.1.1. Reflection coefficient of the dry sensor

At the sensor entrance, an increase in voltage of 140 mV was observed, which is equal to a reflection coefficient of 0.40 if a square wave with an amplitude of 100 mV was applied. At the sensor end, an increase in voltage of 200 mV was observed compared to before the sensor entrance, which is approximately equal to a reflection coefficient of 1 if a square wave with an amplitude of 100 mV was applied and was caused by the open-circuit load. Figure 8.1 summarises the increase in voltage and the reflection coefficient at the entrance and end of the sensor.
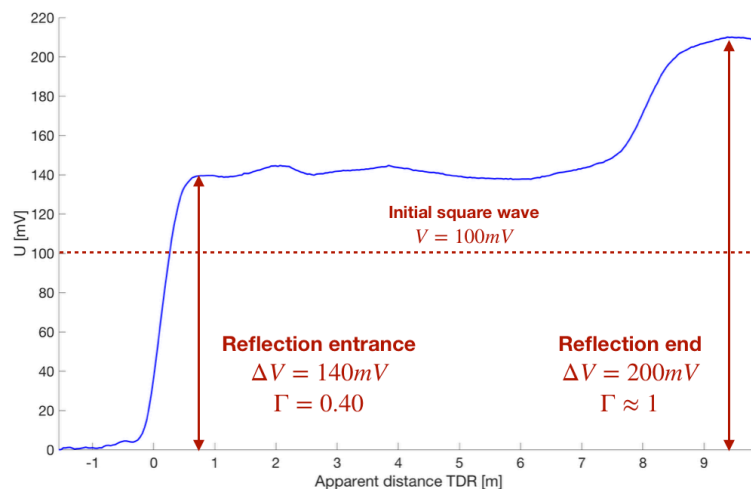
Figure 8.1. Reflection of the applied voltage square wave at the entrance and end of the water sensor.

The transmission line formulas for the 4 lumped circuit parameters were calculated for the parallel wires, twisted pair and coaxial transmission line. The exact formulas were given in table 3.2 and were used to predict the reflection coefficient at the sensor entrance. The SEM data on the sensor's cross-section given in chapter 6 allowed the estimation of the layer thicknesses and lay-up of the composite sensor. Both the inner and outer conductor consisted of wound copper strands, which were simplified by assuming a circular cross-section (no literature was found on significant influences of strand wires on the lumped circuit parameters). A correction on the formulas for a parallel wires transmission line had to be made because of the unequal diameters of both conductors. The correction was based on using a geometric mean for both diameters and is given in equations (8.1)-(8.3) (D. P. Kothari, 2009). The chosen symbols represent the same physical properties as defined in table 3.2.

$$\frac{\pi \varepsilon}{\ln \sqrt{\frac{(2D - d_1)(2D - d_2)}{d_1 d_2}}} \tag{8.1}$$

$$\frac{\mu}{\pi} \ln \sqrt{\frac{(2D - d_1)(2D - d_2)}{d_1 d_2}} \tag{8.2}$$

$$\text{for all } \frac{d}{2} \text{ use } \frac{1}{2}\sqrt{d_1 d_2} \tag{8.3}$$

All used dimensional data and electromagnetic properties are given in table 8.1. The relative magnetic permeability of the sensor was chosen to be 1, because of the insignificant magnetic properties of all constituting materials (also for TiCN a negligible value was found based on the data on both TiC and TiN) (Engineering Toolbox, 2018a; T. Makarova, 2004; W. Martienssen, 2005; Reade, 2018). Additionally, a small air gap between the two conductors should be considered. Visually, a value of 0.5 mm was seen, but its value was varied to illustrate the influence of this parameter. A comparison of the obtained characteristic impedance for air gaps between 0 and 1 mm is made in table 8.3 for the parallel wires transmission line, because the modelling of the sensor indicated the parallel wires were the most appropriate to model the studied sensor. This can be seen in table 8.2, which compares the parallel wires, twisted pair and coaxial cable model for transmission lines. The effective frequency approach introduced by J.A. Strickland was used based on the observed rise time of 5.76 ns at the sensor entrance calculated with the sigmoidal fitting method and resulted in a value of 60.8 MHz (J. A. Strickland, 1970). The equivalent resistive contribution was neglected based on the conductivity of copper used for the conducting wires, which equals $5.96.10^7$ S/m (W. Martienssen, 2005).

For the conductance, supplementary conductivity data for PVC and PVA were consulted in literature and are summarised in appendix C.1 (B. K. Sarker, 2006; M. H. Suhail, 2016; M. J. Uddin, 2012). Based on these data, the isolating jacket of the copper wires were together with the pure PVA considered as non-conductive and hence, the equivalent conductance was also neglected in the model.

The total relative electric permittivity experimentally calculated in chapter 6 was used and because of the uncertainty on its value, equation (8.4) is used to calculate the influence of the relative permittivity's uncertainty on the characteristic impedance.

$$\Delta Z_0 = \left| \frac{\partial Z_0}{\partial \varepsilon} \right| \Delta \varepsilon = \left| -\frac{j\omega Z_0}{2(G' + j\omega C')} \right| \frac{\partial C'}{\partial \varepsilon} \tag{8.4}$$

Table 8.1. Dimensional data and electromagnetic properties used for the calculation of the lumped circuit parameters for the water sensor, where X is the width of the air gap between the 2 wires.

Lumped circuit parameter	Dimensional data	Electromagnetic data
C'	$d_1 = 2r_1 = 2a = 1.20mm$ $d_2 = 2r_2 = 0.63mm$	$\varepsilon_r = 2.93$ $\Delta\varepsilon_r = 0.17$
L'	$D = 2.385 + Xmm$ $b = 2.07 + Xmm$ $X = 0.5mm$	$\mu_r = 1$
R'	assumed to be negligible compared to the other parameters based on the conductivity data of copper	
G'	assumed to be negligible compared to the other parameters based on the conductivity data of PVC, viscose, PVA and air	

Table 8.2. Lumped circuit parameters and characteristic impedance calculated for the water sensor by using the parallel wires, twisted pair and coaxial cables model for transmission lines (X = 0.5 mm).

Lumped circuit parameter	Parallel wires	Twisted pair	Coaxial wires
C' [F/m]	$4.74.10^{-11}$	$4.30.10^{-11}$	$2.99.10^{-10}$
L' [H/m]	$6.87.10^{-7}$	$7.57.10^{-7}$	$1.09.10^{-7}$
R' [Ω/m]		≈ 0	
G' [S/m]		≈ 0	
Z_0 [Ω]	120	133	19.1

Table 8.3. Characteristic impedance of the water sensor calculated with the parallel wires transmission line and different widths of air gap.

Width of air gap (X)	Characteristic impedance
0 mm	104 Ω
0.3 mm	1
0.4 mm	118 Ω
0.5 mm	120 Ω
0.6 mm	123 Ω
1 mm	134 Ω

Based on the experimentally observed reflection coefficient of 0.40 and by taking a 50 Ω characteristic impedance for the BNC-to-banana connector into account, a characteristic impedance of 117 Ω should be found for the water sensor. Hence, the used model with an air gap of 0.5 mm resulted already in an accurate guess for the parallel wires model: only a relative error of 3 % was calculated. However, table 8.3 indicated a more accurate value of 0.4 mm for the air gap: the relative error attained a value of only 0.4 %. To illustrate the influence of the air gap, its

value was calculated for which the twisted pair model is accurate. If no air gap is present, which visually seems unrealistic, the twisted pair is more appropriate.

Table 8.2 clearly indicates the coaxial transmission line model to be inaccurate for the studied sensor. This can be understood based on the electric field present between the two electrodes in a coaxial cable: the complete dielectric is polarised because the outer electrode is present along the complete circumference of the wire. Hence, a serious overestimation on the charge storing capacity of the sensor is made and the characteristic impedance is far too low. The parallel wires and twisted pair models return more similar results, because the only difference between the formulas for both models is the use of a corrected inter-wire distance in the parallel wires model due to the significant diameter of the wires compared to the width of the dielectric. The analysis indicated that the correction made for this finite diameter of the wires was an accurate improvement. However, by decreasing the width of the air gap, the twisted pair model became more accurate and resulted in a similar value for the experimentally observed characteristic impedance for an air gap of 0 mm. Nevertheless, it was visually clearly seen that an air gap is present for the sensor due to the repetitive use of the sensor: mechanical loads and the partial dissolution and drying of the PVA in water weakened the adhesion of the outer conductor to the sensor. Hence, the parallel wires model was chosen as the most appropriate one for the water sensor. Figure 8.2 shows the distribution and intensity of the electric field for coaxial and parallel wires. Comparison with the sensor lay-out in figure 6.2 clearly shows that the sensor is more similar to the parallel wires than to the coaxial wire model (J. Nagel, 2013; C. W. Trueman, 2002).

(a)   (b)
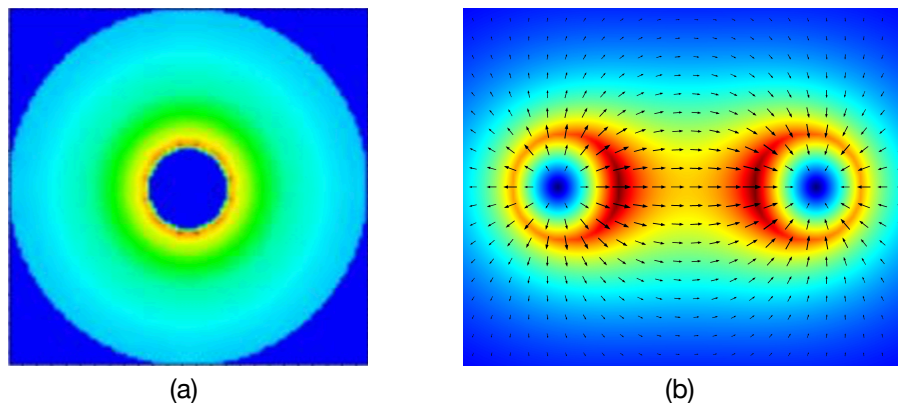
Figure 8.2a. Distribution of the electric field for coaxial wires (C. W. Trueman, 2002). Figure 8.2b. Distribution of the electric field for parallel wires (J. Nagel, 2013). For both figures, the intensity increased from blue to red in the colour code.

The relative permittivity value was based on only one TDR measurement. Hence, an uncertainty is present, for which the effect was taken into account by equation (8.4). The uncertainty of 0.17 introduces an uncertainty of 3.5 Ω, which results in a relative error of -0.1 % if the originally assumed air gap width of 0.5 mm was used. Hence, the assumed width of 0.5 mm could also have been correct. Consequently, the modelled dimensions and electromagnetic properties allow a very accurate prediction on the sensor's reflection coefficient at the entrance.

8.1.2. Permittivity model for the dry sensor

A relative permittivity of 2.93 was derived from the wave propagation velocity based on the sigmoidal fitting. However, to predict the change in permittivity when water is absorbed, a good prediction of each layer's permittivity is necessary. By combining literature data for the dielectric properties of PVC, PVA, TiCN, viscose and the $CaCO_3$ filler, a combined permittivity is calculated

by assuming a series capacity model and a volumetric mixing model. Literature data on the dielectric permittivity and dielectric loss for PVA and TiCN are given in appendix C.1, whereas for PVC and CaCO₃ data are reported in appendix C.2. For viscose, no frequency-dependent permittivity values were found in literature and hence, the dielectric constant at 1kHz was used (J. Borch, 2001). If possible, the permittivity values were chosen as close as possible to the calculated effective frequency of 60.8 MHz.

Mixing models for permittivity

Multiple mixture models were reported in literature. Gladstone and Dale defined the simplest possible mixing rule for the composite's permittivity ε_C purely based on the volume fraction of each component (E. Tuncer, 2002; C. Vanga Bouanga, 2011).

$$\varepsilon_C = \sum_i \phi_i \varepsilon_i \tag{8.5}$$

This approach is exact for layered structures where the electric field runs parallel to the layers. For layered structures perpendicular to the electric field, equation (8.6) is valid.

$$\varepsilon_C = \left(\sum_i \frac{\phi_i}{\varepsilon_i} \right)^{-1} \tag{8.6}$$

Wiener stated that all possible mixture models will result in a value situated between the bounds defined by equation (8.5) and (8.6) (A. Sihvola, 2008). More complicated models are either based on a mean field or an effective medium approach. Bruggeman's asymmetric formula for higher volume fractions of fillers (above 20 %) is a mean field approach, which means the matrix material can clearly be distinguished from the filler material (E. Tuncer, 2002).

$$\frac{\varepsilon_C - \varepsilon_f}{\varepsilon_m - \varepsilon_f} \left(\frac{\varepsilon_m}{\varepsilon_C} \right)^n = (1 - \phi_f) \tag{8.7}$$

The exponent n is a shape factor with a value between 0 and 1 and equals 1/3 for spherical particles. The shape factor is dependent on geometry of the filler particles. The shape factor is also directly related to the percolation threshold (A. Sihvola, 2008). To assess the order of homogeneity seen by a wave propagating along the sensor, one should look to the wavelength present. Based on the effective frequency, a wavelength of approximately 3 m was calculated, which is orders of magnitude larger than the layer thicknesses. Hence, it was expected that the sensor's dielectric was seen as homogeneous matter by the propagating wave.

For water containing composites, Birchak's model offers a simple approximation and was originally created for estimating the permittivity of soil, which is also a composite matter (K. Kupfer, 2005).

$$\varepsilon_C = \left(\sum_i \phi_i \sqrt{\varepsilon} \right)^2 \tag{8.8}$$

Selection of an appropriate mixing model

The sensor can best be described as a composite made of concentric layers. Hence, equation (8.6) is expected to give the most accurate results. However, a comparison with equation (8.5) was made. For the PVC, EDS analysis showed the presence of 22 vol% CaCO₃, which is assumed to be dispersed in the PVC matrix. Hence, Bruggeman's model described in equation (8.7) is appropriate. The calculated value was situated between the Wiener bounds. For the TiCN/ PVA percolative sensing layer, this model is also applicable. Unfortunately, no dielectric data on TiCN could be obtained within this thesis and no literature data on the dielectric behaviour of

TiCN was found for MHz frequencies. Hence, the dielectric spectrum obtained by dielectric spectroscopy in chapter 6 could not be verified based on a mixture rule between PVA and TiCN.

All used dielectric data are summarised in table 8.4. A comparison is made between the parallel and perpendicular layers model together with the experimentally observed value in table 8.5. The influence of water at room conditions (50-60 % RH) is estimated based on Birchak's model given in equation (4.15). The observed permittivity of pure PVA by dielectric spectroscopy is recalculated with this model to the value for dry PVA. A volume fraction of water of 0.08 was assumed for 50 % RH based on the sorption isotherms reported by G. S. Kulagina. (G. S. Kulagina, 2007). Two types of water can be present: either bound, either free water. Their properties and physical difference was explained in paragraph 4.6.2. G. S. Kulagina also showed the first 30 vol% of water to be present as bound water, hence the permittivity of bound water was used to determine the permittivity op pure PVA. A relative density of 1.27 was reported by A. G. Supri for PVA with a molecular weight between 89 and 98 kg/mole (A. G. Supri, 2012). The viscose was assumed to be dry at room conditions because of the slow diffusion of water through the PVA and when water reaches this region, probably the percolative network had already been disrupted (F. Muller-Plathe, 1998).

Dielectric spectroscopy showed in chapter 6 that the permittivity of the percolative TiCN/PVA composite is 3-4 orders of magnitude larger than for pure PVA.The microcapacitor network of conductive TiCN causes the sensing layer to behave more as a metal (infinite permittivity). Hence, this layer was again neglected for the permittivity of the composite in the series capacitance model.

The models for the permittivity of layered structures were derived for parallel plates, because the effect of the non-uniformity or directionality of the electric field is already included in the formulas for coaxial or parallel wires. Hence, the volume fraction can be replaced by the layer's thickness. Implementation of the air gap of 0.4 mm found in the previous part of this chapter resulted in far too low permittivities. If the twisted pair model would have been used, the implementation of an air gap was not wished for an accurate prediction of the sensor's reflection coefficient. Hence, it was assumed that locally the outer conductor was tightly connected to the sensor wire. However table 8.5 shows that this assumption leads to an overestimation of the permittivity for the composite. Hence, the data on the permittivity of the pure PVA and viscose rayon layer were assumed to be accurate and all other incorrectly estimated data or the neglected air gap are combined in one constant, which is not varied when the influence of water in a leakage is modelled in the next paragraph .

To conclude, the perpendicular layers model gave, when the uncertainty on the permittivity was taken into account, quite accurate results (relative error of 5.8 %) and was used further to model the influence of a leakage spot on the water sensor. The parallel layers model totally overestimated the permittivity because the extremely high permittivity of the PVA/TiCN layer is not neglected in this model.

8.1.3. Reflection coefficient of a local water spot

The leakage experiments discussed in paragraph 6.6 indicated a detected local decrease in the measured reflectogram of 4-5 mV (or 10-15 Ω when the nanopulsor was used) when a square wave with an amplitude of 100 mV was applied. A lattice diagram, which is given in figure 8.3, was used to calculate the reflection coefficient of a leakage discontinuity (S. H. Hall, 2009). The lattice diagram clearly illustrates the detected decrease in voltage to not only originate from the expected reflection at the leakage discontinuity, but also the partial reflection at the sensor

entrance must be taken into account. Each discontinuity causes a partial reflection (V_0^-) and transmission (V_0^+) of the voltage wave. Hence, the detected decrease in voltage caused by the leakage consisted of two contributions: the partial reflection at the leakage spot and the partial transmission at the sensor entrance.

Table 8.4. Overview of the dielectric data collected from experiments and literature for each of the layers in the water sensor.

Layer	Relative Permittivity		Remark	Source
	dry	50 % RH		
PVC(CaCO$_3$) inner conductor	3.5	-	$\varepsilon_m = 2.8, \varepsilon_f = 7, \phi = 0.22$ dielectric loss negligible Bruggeman's mixing model (spherical fillers)	(C. T . Dervos, 2005) (National Physical Laboratory, 2017)
viscose rayon	2.67	-	at 1 kHz, assumed dry	(J. Borch, 2001)
PVA/TiCN	-	3.10^3	at 1 MHz	experiments
PVA	1.59	3.13	at 1 MHz Birchak's mixing model for pure PVA (assume bound water) $\phi = 0.08$	experiments
PVC outer conductor	2.8	-	dielectric loss negligible	(C. T . Dervos, 2005) (National Physical Laboratory, 2017)

Table 8.5. Effective dielectric permittivity of the water sensor determined from experiments (wave propagation velocity), the parallel layers and perpendicular layer model (as a reference: $\varepsilon_r \approx 80$ for free water molecules).

Permittivity model	Calculated value for ε_r
experimental value	2.93
parallel layers (8.5)	206.96
perpendicular layers (8.6)	3.10

The reflection coefficient was directly used for the calculation of the characteristic impedance of a leakage spot based on equation (3.10). The absorption of water will only influence the permittivity of the sensor, because the dimensional changes caused by the swelling are present in both the equivalent capacitance and inductance and hence, cancel out. The permittivity of the sensor in a region of water leakage then directly follows from equation (8.9), where 1 refers to the dry sensor and 2 refers to the sensor at the local leakage spot.

$$\varepsilon_2 = \varepsilon_1 \left(\frac{Z_1}{Z_2} \right)^2 \tag{8.9}$$

It was found that the relative permittivity increased from 2.93 to 3.55-3.71 (depending on the exact value of the reflection coefficient). Hence, it was already concluded that the combined effect of the high permittivity of water and the swelling due to the water absorption, which are two

contradictory factors, results in a negative reflection of the applied voltage wave at the leakage spot.
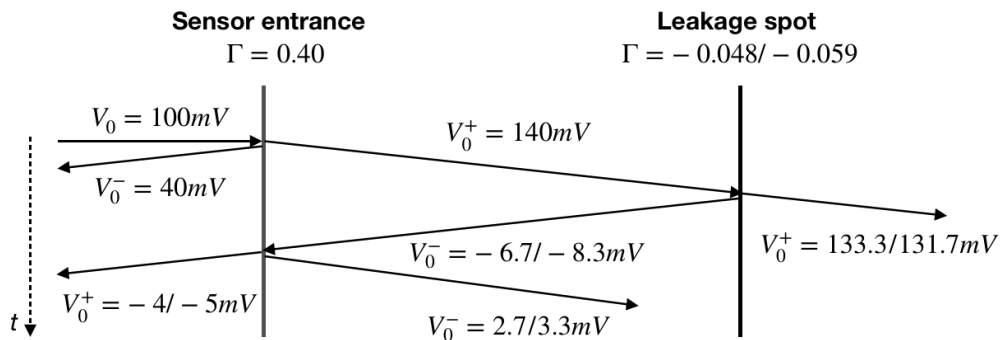
Figure 8.3. Lattice diagram of the reflected and transmitted fraction of the applied square voltage wave when a water leakage spot is present on the sensor. Two impedance discontinuities are present: the first at the sensor entrance, the second at the leakage spot. Each discontinuity causes a partial reflection (V_0^-) and transmission (V_0^+) of the voltage wave. The detected voltage by the oscilloscope over time is the sum of all reflected and transmitted waves at the sensor entrance. For the leakage spot, the total detected voltage consists of the initially applied wave, the reflected wave at the sensor entrance and the partially transmitted reflection of the leakage spot.

An accurate quantification of the dimensional change is challenging and nearly impossible, because the volumetric expansion due to the water absorption is unknown and no data were found in literature. Hence, two limiting cases were considered for which the observed permittivity should be situated between these two bounds.

The first limiting case consists of the assumption that swelling is absent. This means the PVA molecules are simply replaced by the water molecules or that the capillary network inside the PVA is sufficiently large to facilitate the total amount of absorbed water. The local free volume in between the PVA molecules does not increase because the water present is of the type free water (R. M. Hodge, 1996). Hence, a maximal water volume fraction of 0.5 was chosen directly from the water/PVA phase diagram at 20 °C based on the PVA-rich boundary of the two-phase region (G. S. Kulagina, 2007; A. A. Tager, 1971). The phase diagram constructed by G. S. Kulagina together with the influence of the water volumetric content on the glass transition temperature is included in appendix C.3.

The second limiting case consists of the assumption that complete swelling is present. This means the water molecules are simply added to the PVA, but no interaction occurs and hence a mixture of the two separately added fractions of PVA and water in equilibrium is present. The local free volume in between the PVA molecules does again not increase because the water present is of the type free water (R. M. Hodge, 1996). Realistically, this case applied to bound water molecules, but the expansion of the PVA's free volume will again decrease the volume fraction of water present in the system that was derived from the PVA/water phase diagram. Hence, to assume a limiting case, bound water molecules were used for the first 35 vol% of water absorbed, after which any additional water molecule was considered to be free.

For the viscose, the dimensional change was estimated based on the relative mass absorption discussed in paragraph 6.4 when the viscose protected wire was immersed in water. The relative mass change of 1.95 is equal to a water volume fraction of 0.75. J. Borch reported a relative density for the viscose rayon of 1.53 (J. Borch, 2001).

The permittivity of both the viscose and PVA layer were calculated with Birchak's model (8.8) based on the data for free water and dry PVA or dry viscose.

The change in thickness of the viscose and PVA layer were calculated and the results for the two discussed limiting cases are given in table 8.6. The experimental permittivity for the dry sensor was used to calculate a constant which implements the permittivity contributions of all (non-absorbing) layers except the viscose and pure PVA layer. Dielectric spectroscopy showed the permittivity of the PVA/TiCN composite in a K_2SO_4 humidity regulated environment to be still 3 orders of magnitude higher than the other layers and hence, can still be neglected. It can be concluded that the observed relative permittivity of the sensor at a leakage spot is situated between the 2 limiting cases. However, the uncertainty in the permittivity data found in literature and the detected reflection coefficient should be taken into account and hence, when both PVA and viscose absorb water, the selection of the most appropriate limiting case is seriously hindered. The permittivity of the wet sensor was also always larger than for the dry sensor, which was confirmed by the leakage experiments. The need to take the swelling and water absorption of the viscose into account is clearly illustrated.

Table 8.6. Effective dielectric permittivity of the water sensor at a leakage spot determined from experiments (wave propagation velocity) and for the two limiting cases discussed (no swelling and complete swelling)

Permittivity model	Only PVA layer absorbs	Both PVA and viscose layer absorb
experimental value	3.5-3.7±0.2	
limiting case 1: no swelling	3.1±0.1	3.7±0.1
limiting case 2: complete swelling	3.0±0.1	3.5±0.1

8.2. Sensor 2: conductive rubber for detection of kerosene

8.2.1. Reflection coefficient of the dry sensor

At the sensor entrance, an increase in voltage of 118 mV was observed, which is equal to a reflection coefficient of 0.18 if a square wave with an amplitude of 100 mV was applied. At the sensor end, an increase in voltage of 195 mV was observed compared to before the sensor entrance, which is approximately equal to a reflection coefficient of 1 if a square wave with an amplitude of 100 mV was applied and is caused by the open-circuit load. Figure 8.4 summarises the increase in voltage and the reflection coefficient at the entrance and end of the sensor.

The transmission line formulas for the 4 lumped circuit parameters were calculated for the parallel wires, twisted pair and coaxial transmission line. The exact formulas were given in table 3.2 and the correction applied by equation (8.3) for the non-similar diameter of the rubber and helical outer wire was also taken into account. Figure 8.5 shows that the rubber wire has not a circular cross-section, but rather a semi-circular top with a rectangular-like side and base. Hence, a correction based on a mean radius was implemented to allow use of the formulas for the lumped circuit parameters derived for circular wires. The centre of mass was calculated with equation (8.10) and was inserted in equation (8.11) to estimate a mean radius. A transformation to polar coordinates was used. $R(\theta)$ denotes the local radius as function of the polar angle, $2b(y)$ is the local width as function of the height y and $\bar{x}$ and $\bar{y}$ are respectively the x- and y-coordinate of the centre of mass. $\bar{R}$ is the equivalent mean radius. The complete approach is illustrated in figure 8.5.

$$\bar{x} = 0.7mm \quad \text{and} \quad \bar{y} = \frac{\int_0^{1.6} 2b(y)y\,dy}{\int_0^{1.6} 2b(y)\,dy} = 0.73mm \tag{8.10}$$

$$\bar{R} = \frac{\int_0^{2\pi} R(\theta)\,d\theta}{\int_0^{2\pi} d\theta} = 0.79mm \tag{8.11}$$
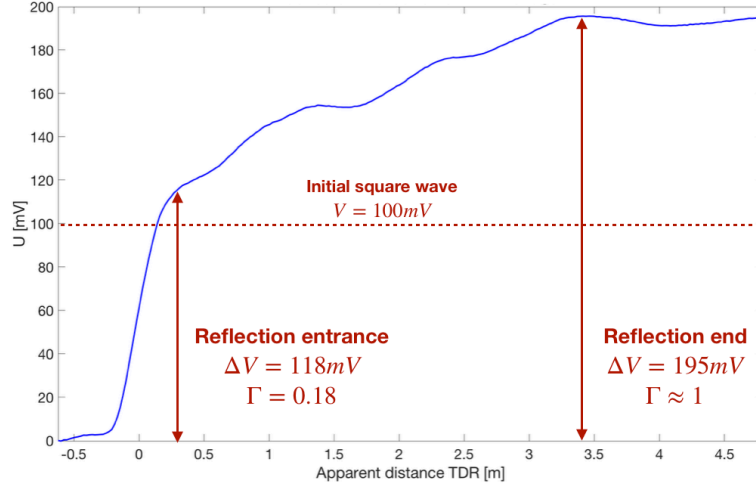
Figure 8.4. Reflection of the applied voltage square wave at the entrance and end of the rubber sensor.
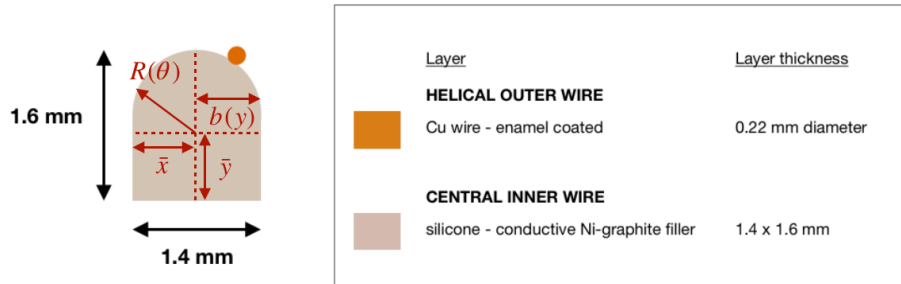
Figure 8.5. Parameters used for the calculation of a mean equivalent radius for the rubber wire.

By simply calculating the area of the rubber's cross-section and deriving the mean radius by assuming a circular cross-section, a radius of 0.80 mm was found. Hence, the more exact approach of the mean radius by calculating the centre of mass resulted in approximately the same mean radius. Hence, the mean radius approach based on a purely circular cross-section is a valid simplification.

Because of the significant attenuation along the rubber wire, the equivalent resistance will not longer be negligible. Its value depends on the frequency, which pose a complex problem since a nearly infinite frequency spectrum is present in a square wave, as was shown in figure 6.6a. Hence, the effective frequency approach introduced by J. A. Strickland was used based on the observed rise time of 6.08 ns at the sensor entrance calculated with the sigmoidal fitting method. (J. A. Strickland, 1970). An effective frequency of 57.8 MHz was found. The specific resistance reported in literature for graphite was considered (Holland Shielding Systems BV, 2018; W. Martienssen, 2005). The total relative permittivity calculated in chapter 7 was used and because of

111

the uncertainty on its value, equation (8.4) was used to calculate the influence of the uncertainty on the relative permittivity on the characteristic impedance.

All dimensional data and used electromagnetic properties are given in table 8.7. The relative magnetic permeability of the sensor was chosen to be 1, because of the insignificant magnetic properties of all constituting materials (also for graphite a negligible value was found) (Engineering Toolbox, 2018a; T. Makarova, 2004; W. Martienssen, 2005; Reade, 2018). Additionally, a small air gap between the two conductors should be considered. Visually, a value of 0.5 mm was seen, but its value was varied to illustrate the influence of this parameter. A comparison of the obtained characteristic impedance for air gaps between 0.5 and 1 mm is made in table 8.8 for the twisted pair transmission line, because the modelling indicated the twisted pair to be the most appropriate model for the studied sensor. The values of the 4 lumped equivalent parameters were not reported here for the other two models, but the approach of calculation was the same as the one used in paragraph 8.1 for the water sensor.

Based on the experimentally observed reflection coefficient of 0.18 and by taking a 50 Ω characteristic impedance for the BNC-to-banana connector into account, a characteristic impedance of 72 Ω should be found for the rubber sensor. Hence, the used model with an air gap of 0.5 mm resulted already in an accurate guess: only a relative error of -5 % was calculated. However, table 8.8 indicated a more accurate value of 0.6 mm for the air gap.

Table 8.7. Dimensional data and used electromagnetic properties for the calculation of the lumped circuit parameters for the rubber sensor, where X is the width of the air gap between the 2 conductors.

Lumped circuit parameter	Dimensional data	Electromagnetic data
C'	$\dfrac{d_1}{2} = 0.79mm$	$\varepsilon_r = 7.66$ $\Delta\varepsilon_r = 0.45$
L'	$\dfrac{d_2}{2} = 0.11mm$	$\mu_r = 1$
R'	$D = 0.9 + Xmm$ $X = 0.5mm$	$f_{eff} = 57.8MHz$ $\rho_{graphite} = 1.4.10^{-5}\Omega m$
G'	assumed to be negligible compared to the other parameters based on the conductivity data of air and the enamel coating	

Table 8.8. Characteristic impedance of the rubber sensor calculated with the twisted pair transmission line and different widths of air gap

Width of air gap (X)	Characteristic impedance
0.5 mm	69 Ω
0.6 mm	72 Ω
0.7 mm	74 Ω
0.8 mm	77 Ω
0.9 mm	80 Ω
1 mm	80 Ω

The relative permittivity value was based on only one TDR measurement. Hence, an uncertainty is present, for which the effect was taken into account by equation (8.4). The uncertainty of 0.45 introduced an uncertainty of 2.1 Ω, which resulted in a relative error of -1.6 %. Consequently, the modelled dimensions and electromagnetic properties allow a very accurate prediction on the sensor's reflection coefficient at the entrance.

8.2.2. Attenuation of the dry sensor

In contrast to the water sensor, the resistive attenuation along the rubber sensor is significant. Hence, an estimation of the attenuation constant is useful. Figure 8.6 shows a distributed reflection of 59 mV along a distance of 2.2 m on the sensor. Equation (8.12) allows the calculation of the attenuation coefficient, which is the real part of the complex propagation constant. The voltage amplitude after the sensor entrance that was left for resistive reflection was 82 mV.

$$\Delta V = V_0 \left(1 - e^{-2\alpha l} \right) \tag{8.12}$$

The attenuation constant has a value of 0.29, which can be verified based on the lumped parameters by using equation (3.8). A value of 0.43 was found, which is much higher than the value calculated from the experimental data. This can be explained by the large influence of bends, which may mask the total reflected voltage because of the resistive attenuation, or ageing due to the repetitive sensor use for the multiple leakage experiments. Also the effective frequency used at the sensor entrance is probably not longer valid, because of the dispersion behaviour along the sensor, which decreases the rise time. If the effective frequency decreased an order of magnitude, an attenuation constant of 0.31 was found, which is close to the observed value. The fitted reflected voltage due to the attenuation is shown in figure 8.6.

8.2.3. Reflection coefficient of a local kerosene spot

Unlike for the water sensor, it can be assumed that the absorption of kerosene will directly influence the conductivity of the rubber wire by interrupting the percolative graphite/nickel filler network. This 'first order effect' is caused by the rubber swelling, which was discussed in chapter 7, and will increase the characteristic impedance of the sensor some orders of magnitude compared the water sensor where the swelling acts as a 'second order effect' by changing the permittivity (J. L. Graham, 2006; C. Nohilé, 2008; E. V. Takeshita, 2012). The sorption experiment showed a relative mass increase of 16.9 % after immersion in kerosene, hence a volume expansion can be expected of the sensor.

According to equation (8.3), this will have a decreasing influence on the resistance, but the size effect is expected to be negligible compared to the change in conductivity. Additionally, the capacity will decrease because of both the lower relative permittivity of kerosene compared to silicone rubber (respectively 1.8 and 3.2) and the swelling (KAB Electro-Acoustics, 2018). The combined effect of all mentioned changes in lumped circuit parameters will cause an increase of the characteristic impedance. Assuming the change in conductance from the graphite particles to kerosene (conductivity of 5.10^{-11} S/m) as the main influence, a characteristic impedance of approximately $2.2.10^6$ Ω at the location of kerosene absorption is calculated (QSStudy, 2018). This implies a reflection coefficient of nearly 1, which was indeed observed in the TDR signal monitored at the sensor entrance when a kerosene leakage was applied at a distance of 0.30 m from the entrance and was shown in figure 6.6a.
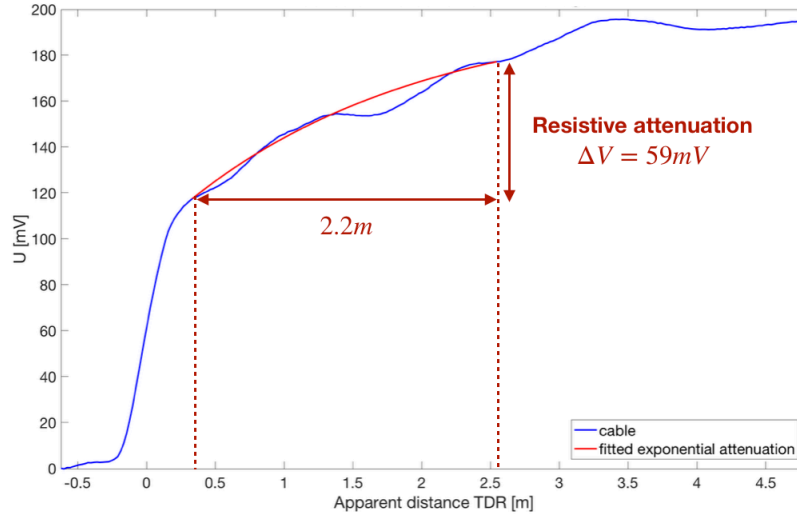
Figure 8.6. Resistive attenuation along the rubber sensor.

8.3. Conclusions

A lumped circuit approach was elaborated within this chapter to predict the reflection coefficient of both the water and kerosene sensor in dry conditions. The transmission line formulas summarised in chapter 3 were applied by modelling the sensors as parallel wires, a twisted pair or a coaxial wire. Literature data and dielectric spectroscopy data were combined with Scanning Microscopy data to estimate the electromagnetic and dimensional properties of each layer present in the sensors. The parallel wire model was the most accurate for the water sensor, whereas for the kerosene sensor the twisted pair model was found to be the most accurate. In both models, a small air gap was included to mimic the effect of the lost connection between the sensor and the outer conductor at certain positions along the sensor. For the water sensor, the experimentally observed effective permittivity of the layer composite was estimated by considering the sensor as a circuit of series capacitances. A relative error on the experimentally observed characteristic impedance for both sensors of respectively 3 % and -5.8 % was found, which shows the strength and accuracy of the lumped circuit approach.

The effect of a leakage spot on the local reflection coefficient at the leakage discontinuity was estimated and compared to the experimentally observed value from the voltage reflectogram. A water leakage always results in a negative voltage reflection and was explained by the increase in the permittivity of the PVA and viscose layer due to water absorption. The two considered limiting cases of no swelling and complete swelling confirmed the experimental value to be situated between these bound. Additionally, the importance of implementing the water absorption by the viscose layer for an accurate estimation of the effect on the sensor's permittivity was shown. For the kerosene sensor, the interruption of the percolative graphite/nickel filler network always results in a positive reflection due to the significant increase in sensor resistance. The transition of a conducting percolative wire to a kerosene dominated conductivity results in a nearly complete reflection of the incident voltage wave at the leakage spot on the sensor.

Chapter 9

Limitations, future research and applicability to large engineering structures

9.1. Limitations and future research

A detailed characterisation of the lay-up, electromagnetic properties and TDR signature of the water and kerosene sensor developed at the Department of Materials Engineering of KU Leuven during the last decade was elaborated within this thesis. Numerous leakage experiments were performed to assess the detectability and localisability of the leakage spots along both sensors. A comprehensive understanding of the sensor's behaviour in the dry state and wetted state was obtained and multiple conclusions were drawn concerning the applicability of the sensor to large engineering structures. However, a critical awareness of the limitations of the conducted research is indispensable to assess the possibilities, assets and drawbacks of the studied sensor. Based on the limitations and shortcomings of the performed research, some questions remain unanswered, whereas multiple improvements and opportunities for the sensor design and measurement set-up exist.

- The studied sensors were designed for the detection of only water and kerosene. However, the detection of liquids like Skydrol and other common industrial solvents can also be desirable depending on the service environment. The silicone rubber sensor is expected to also detect other carbon-based solvents because of its apolar organic structure. The principle of detection and the design of the sensor can be tailored for any possible liquid by choosing an appropriate sensing and solvent absorbing material.

- The short inspection length of the kerosene sensor could be expected to limit the industrial implementation in large engineering structures. However, contrary to the distribution of water leakage spots in large areas, kerosene leakages are expected to occur in the direct vicinity of the fuel tanks, which expand over a smaller area and have limited dimensions. Hence, a couple of meters of the kerosene sensor should be sufficient to monitor the sealings at the supply valves of the fuel tanks.

- The detection and localisation along the kerosene sensor was observed to be more difficult and less accurate, especially when multiple leakage spots were present along the same sensor, which can pose a serious drawback for the application of the sensor in real structures. Nevertheless, due to the low sensor cost, it can be expected that during a close inspection of the area in which a leakage spot was detected, the sensor will partially be replaced by a new dry one, and hence, detection of additional leakages spot along the same sensor are made possible again.

- To improve the lumped circuit model of both sensors, further characterisation of the electromagnetic properties of the composing materials is recommended. Especially for the water sensor, a detailed characterisation of each layer by dielectric spectroscopy is necessary to asses accurately each layer's contribution to the total change in the recorded sensor's TDR signal when water is absorbed. The permittivity should be measured for each layer before and after water absorption to take the volumetric expansion of the layers due to the water uptake into account. Volumetric sorption isotherms could be constructed by measuring the dimensional change for a series of relative humidities and can then be used for the series capacitance model of the layered sensor. By assessing more accurately the dominant layers influencing the TDR signal, an optimised design of the sensor is possible by changing the thickness and composition of each layer. The outer conductor could also be imbedded or integrated into the coated inner conductor, such that a strong but flexible sensor design is obtained for which no air gaps are possible between the two conductors. The complete sensor can for example be embedded in a PVA jacket to obtain a sealed design that stills allows water absorption.

- A higher spatial resolution, and hence detection ability of leakages spots can be reached by using a nanopulsor to decrease the rise time of the used square wave significantly. However, the cost of this specialised equipment reaches ten times the price for the currently used measurement set-up and hence, the advantage of detecting a leakage spot with a size of a couple of cm instead of 10 cm can be questioned. In large engineering structures, a repair of the water-damaged structure is normally done only in the case of a significant size of the leakage spot. Additionally, the inspection and repair of an engineering structure is done over of 0.1-1 m or even tens of meters long distances.

- In-service monitoring of the sensor is the next step to assess its applicability to large public and industrial engineering structures. Automatisation and processing of the TDR and DC resistance measurements for a sensor network distributed over large areas should be executed. Automated data logging facilities and wireless solutions, such as radio-frequency identification chips were already implemented by MTM in an operational aircraft in the frame of a project (H. Pfeiffer, 2014).

- The influence of electromechanical noise should be investigated together with the influence of temperature, stresses and vibrations on the monitored TDR signal. The relation between the significant change in the TDR signal, DC resistance, the lyotropic percolation threshold and the lyotropic glass transition should be further elaborated.

- To allow commercialisation and decrease the production costs, a further optimisation can be carried out in order to decide whether the nylon-based or viscose-based sensor design is from a financial point of view the best choice. A cost analysis is necessary to balance the higher materials cost of the viscose-based sensor compared to the longer production times of the nylon based sensor, the latter one caused by the additional embedding step of the inner conductor in the nylon cord. An automated production line should be initialised to keep the fixed production costs low and allow industrially relevant production quantities.

9.2. Applicability to large engineering structures

The main goal of this thesis research was to assess the applicability of TDR for leakage damage detection in large engineering structures. The water and kerosene sensor are currently applied in

airliners of Lufthansa and in pipe lines of BASF (H. Pfeiffer, 2014). The DC resistance is monitored to detect a (significant) leakage spot along the sensor. However, localisation is currently only limited to the pin-pointing of the specific sensor line in a distributed network along which a leakage is present. However, the exact location of the leakage spot can only be determined by inspecting the complete line, which requires expensive and time-intensive manual inspection by engineers and technicians. Figure 9.1 shows the lay-out of such a distributed sensor network along the floor beams of an airliner's fuselage (R. Windey, 2016). Nevertheless, the sensor already saves many labour hours and inspection costs by indicating the area of the total floor structure in which the leakage is present. The developed sensor is not only advantageous over commercially available leakage detector sensors (which were discussed in paragraph 2.2) concerning their much lower cost (€ 1-2/m compared to € 10/m), but also their smaller diameter (2-3 mm compared to at least 5-10 mm) allows integration of the sensor in between the floor panels, which is cumbersome for commercial sensors. Figure 9.1b shows the water sensor installed in between the floor panels of a commercial airliner Boeing D-ABIX 737-530 (H. Pfeiffer, 2014).

distributed sensor network

(a)   (b)
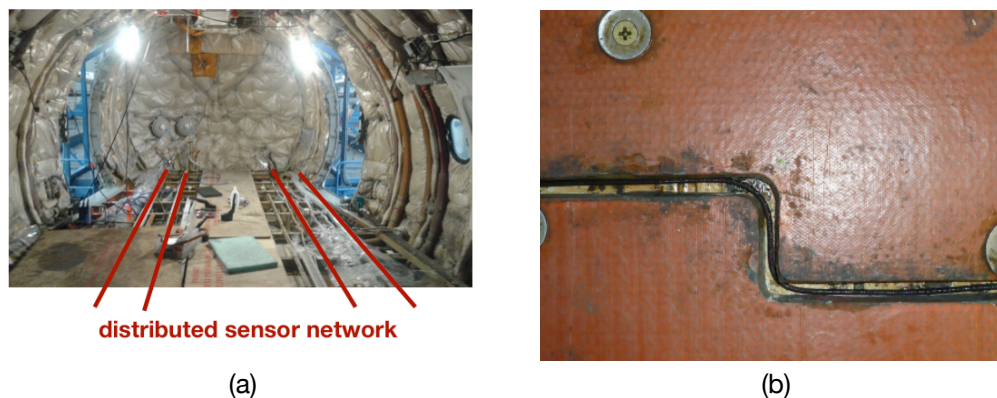
Figure 9.1a. Fuselage of an Airbus 330 of Brussels Airlines in which the floor panels have been removed for inspection. Illustration of the installation of a distributed sensor network is included (R. Windey, 2016). Figure 9.1b. Detail of the floor panels of an airliner for which the sensor was installed in between (Boeing D-ABIX 737-530) (H. Pfeiffer, 2014).

Because of the diffusion of water in the vapour phase, leakage spots located at a distance of 10-20 cm to the sensor are also detectable because the hygroscopic PVA will already absorb significant amounts of water for relative humidities above 60-70 %, which is a major advantage over most point-like operating water sensors.

The accurate localisation of the leakage spot can be performed by connecting a TDR measurement set-up to the sensor network. Geometric influences like bends and bumps were shown to be insignificant for both the leakage detection and localisation if the differential TDR signal was compared to the sensor's baseline, which must be measured after the installation of the sensor. Multiple leakage spots were found to be detectable along the sensor, which is important to allow simultaneous inspection of multiple areas of possible leakages. The negligible resistive attenuation along the water sensor allows large inspection lengths, normally limited to 20-30m within an airliner's fuselage.

For the kerosene sensor, as explained in the previous paragraph, the short inspection lengths do not pose a real threat to the industrialisation of the sensor, because of the localised character of kerosene leakages. Also the fact that the sensor will be partially replaced in the area of leakage to assure the detection of additional leakage spots along the complete sensor length offers a solution to the short inspection lengths. The low voltage amplitudes required to detect a leakage are an extra asset in areas in which inflammable liquids like kerosene are used.

However, the continuous monitoring of the sensor's TDR signal is not desirable because of the high cost, significant dimensions and cumbersome implementation of commercially available wave generators and oscilloscopes. Resistance meters are much less expensive and smaller in size and hence, a continuous monitoring of the DC resistance will be accompanied by a periodic inspection by TDR. Figure 9.2 illustrates such a suggested inspection scheme for the combined DC resistance/TDR system. A fuse-like increase in the DC resistance above a specified threshold (MΩ) will trigger an alarm to alert the maintenance technician that a critical leakage spot is present along a specific sensor of the distributed sensor network. Next, A TDR inspection of the indicated sensor line is performed to localise the leakage spot. After repair, the TDR signal is inspected again to verify whether all leakages have been removed along this specific sensor. A new TDR inspection will be executed when the DC resistance has passed the critical threshold again. If a leakage spot remains detected at the same location even after repair, 2 possible conclusions can be drawn. Either no complete repair was executed and the leakage kept existing, either the sensor has not dried yet and remains saturated. In the latter case, the wet sensor should be replaced by a dry one to properly detect a new leakage spot. The labour and materials costs for the opening of the floor panels and the repair or replacement of floor beams in the airliner's fuselage exceed the materials cost of a new sensor by orders of magnitude and hence, the sensor will be always replaced to assure its detection ability during the intensive 6-yearly D-checks of the fuselage (R. Windey, 2016).
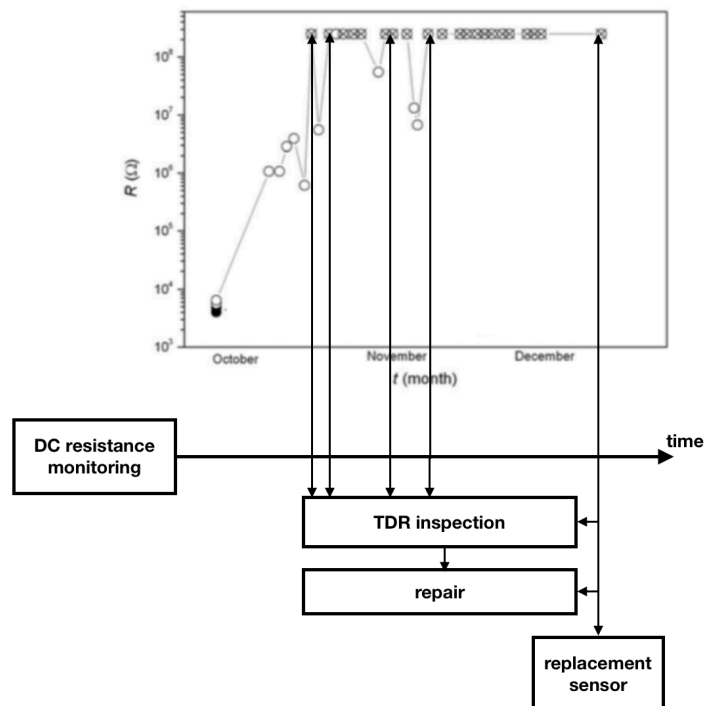
Figure 9.2. Illustration of the suggested DC resistance monitoring and TDR inspection scheme for leakage detection along a long-distance pipe line. (DC resistance measurements supplied by H. Pfeiffer).

Chapter 10

General conclusions

Leakages can cause major damage and long-duration downtimes in industrial structures and public transport facilities. Hence, early detection and localisation of leakages in industrial structures and public transport facilities by Structural Health Monitoring is indispensable to avoid major water damage and long-duration downtimes. Time Domain Reflectometry (TDR) was combined with DC resistance measurements for sensors tailored for water and kerosene detection, which were developed at the Department of Materials Engineering at KU Leuven. The fuse-like increase at the lyotropic percolation threshold of the DC resistance only allows detection of the leakage spot and localisation is made possible by using TDR. The water sensor was made of a percolative PVA/TiCN sensing layer coated onto a viscose-based wire, whereas a percolative silicone rubber in which nickel coated graphite particles were dispersed was used for kerosene. An outer conductor was helically wound around both sensors to allow TDR measurements.

Leakage spots of water and kerosene applied at different locations along both sensors were clearly detected. The evolution of the sensor's TDR voltage reflectogram was monitored during each experiment and compared with the reflectogram recorded for the dry sensor, which is called the baseline, to allow detection and localisation. A minimal leakage spot size of 10 cm was required for the water sensor to allow detection, whereas a 4 cm wide leakage spot was clearly detected for the kerosene sensor. A new method for the determination of the time of flight along the sensor based on a sigmoidal fitting procedure of the differential TDR signal was compared to traditional methods for the localisation of the leakage spot. The sigmoidal fitting method was found to accurately localise the leakage spot for both sensors, which was cumbersome for the traditional methods on the kerosene sensor due to its resistive attenuation. The detection of two leakage spots simultaneously present on both sensors was possible, however a smaller differential voltage was observed for the kerosene sensor due to its resistive attenuation.

A lumped circuit model based on the dimensional and electromagnetic properties of the sensor's constituting layers accurately predicted the reflection of the applied voltage wave at both the sensor entrance and the applied leakage spot. The local increase in the permittivity of the PVA layer due to the water absorption was assumed to be the main cause of a negative voltage reflection for the water sensor at a leakage spot. However, additional measurements on the changes in dimensional and dielectric properties of each constituting layer of the sensor by dielectric spectroscopy were suggested for future research. For the kerosene sensor, the fuse-like increase of the resistance due to the kerosene-induced disruption of the percolative graphite network was suggested to introduce a positive reflection of the complete voltage.

It was concluded that TDR under the conditions of a percolation threshold offers a sensitive detection and accurate localisation solution for leakage monitoring in large engineering structures like fuselages of aircrafts and pipelines. Its combination with DC resistance monitoring allows the lay-out of a distributed sensor network in these structures for low-cost, flexible and continuous Structural Health Monitoring. Geometric influences like bends and bumps together with static electromechanical influences were filtered out of the sensor's TDR signal by comparison to the sensor's baseline. The sensor's low materials cost of approximately € 1-2/m makes it clearly advantageous over the currently available commercial leakage sensors.

Appendices

A.   Additional literature to chapter 3

A.1. Maxwell's equations

The foundation of all electromagnetic theory is described by Maxwell's equations. The differential form of Maxwell equations is given in equations (A.1) through (A.4):

$$\nabla \times \vec{E} + \frac{\partial \vec{B}}{\partial t} = 0 \qquad \text{(Faraday's law)} \tag{A.1}$$

$$\nabla \times \vec{H} = \vec{J} + \frac{\partial \vec{D}}{\partial t} \qquad \text{(Ampère's law)} \tag{A.2}$$

$$\nabla . \vec{D} = \rho \qquad \text{(Gauss's law for electricity)} \tag{A.3}$$

$$\nabla . \vec{B} = 0 \qquad \text{(Gauss's law for magnetism)} \tag{A.4}$$

where ρ denotes the electric charge density. The magnetic flux intensity $\vec{B}$ is dependent on the magnetic field intensity $\vec{H}$ and magnetisation density $\vec{M}$. The permeability of free space is denoted by μ_0.

$$\vec{B} = \mu_0 \left(\vec{H} + \vec{M} \right) \tag{A.5}$$

The electric flux density $\vec{D}$ depends on the electric field intensity $\vec{E}$ and the electric polarisation density $\vec{P}$. The permittivity of free space is denoted by ε_0.

$$\vec{D} = \varepsilon_0 \vec{E} + \vec{P} \tag{A.6}$$

Supplementary relations that comprehend the properties of media other than free space are required. These include the finite conductivity of a material in equation (A.7), where $\vec{J}$ denotes the current density and σ denotes the conductivity of the medium, the magnetic properties of a material in equation (A.8) and finally the response of a dielectric to an applied electric field in equation (A.9). The permittivity of a medium is written as the product of the relative permittivity and permittivity of free space, respectively denoted as ε_r and ε_0. Similarly, the permeability of a medium is written as the product of the relative permeability and permeability of free space, respectively denoted as μ_r and μ_0.

$$\vec{J} = \sigma \vec{E} \tag{A.7}$$

$$\vec{B} = \mu_r \mu_0 \vec{H} \tag{A.8}$$

$$\vec{P} = \varepsilon_0 (\varepsilon_r - 1) \vec{E} \tag{A.9}$$

A.2. Telegrapher's equations

All interconnects can be treated as transmission lines consisting of a signal and return conductor. Basically, the transmission line is divided in N equal differential elements, as shown in figure A.1 (F. Farahmand, 2012b), which can each be characterised by 4 equivalent or lumped parameters: a resistance R' [Ω/m], a capacitance C' [F/m], an inductance L' [H/m] and a conductance G' [S/m] per unit length. In this lumped parameter approach, the series inductance will take the changes in the magnetic field into account caused by the changing current in the closed loop formed by the transmission line. The effect of the changing voltage, dielectric properties of the medium in between the conductors and their close spacing is represented by a shunt capacitance. A series resistance takes the attenuation along the conducting lines due to the DC resistance and the skin effect into account. Finally, any losses due to the conductive properties of the dielectric are taken into account by a conductance in parallel with the capacitance. The equivalent circuit for the Nth differential element with length Δz is given in figure A.1 (F. Farahmand, 2012b).
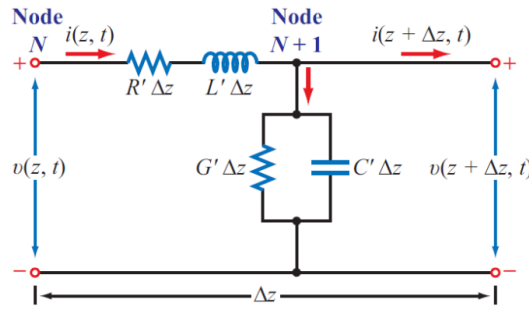
Figure A.1. Illustration of the equivalent circuit parameters required to describe the current and voltage in each differential element (F. Farahmand, 2012b).

In each differential element, Kirchhoff's voltage (A.10) and current law (A.11) can be applied to derive a relation between the current $i(z, t)$ and voltage $v(z, t)$ at the entrance and exit of the Nth differential element. The equivalent parameters are assumed to be time-independent.

$$R'\Delta z\, i(z, t) + L'\Delta z \frac{\partial i(z, t)}{\partial t} + v(z + \Delta z, t) - v(z, t) = 0 \tag{A.10}$$

$$i(z, t) = G'\Delta z\, v(z + \Delta z, t) + C'\Delta z \frac{\partial v(z + \Delta z, t)}{\partial t} + i(z + \Delta z, t) \tag{A.11}$$

By refining the division into $N \to \infty$ differential elements, the length of the differential elements $\Delta z \to 0$ and by applying the limit definition for derivatives, equations (A.10) and (A.11) become a pair of coupled linear differential equations, better known as the telegrapher's equations.

$$\frac{\partial v(z, t)}{\partial z} = -\left(R'i(z, t) + L'\frac{\partial i(z, t)}{\partial t} \right) \tag{A.12}$$

$$\frac{\partial i(z, t)}{\partial z} = -\left(G'v(z, t) + C'\frac{\partial v(z, t)}{\partial t} \right) \tag{A.13}$$

By introducing the phasor notation commonly used for AC circuits (A.14), equations (A.12) and (A. 13) become time-independent. The imaginary unit is denoted by j.

$$v(z, t) = \Re\left[V(z)e^{j\omega t} \right] \quad \text{and} \quad i(z, t) = \Re\left[I(z)e^{j\omega t} \right] \tag{A.14}$$

$$\frac{dV(z)}{dz} = -\left(R' + j\omega L' \right) I(z) \tag{A.15}$$

$$\frac{dI(z)}{dz} = -\left(G' + j\omega C'\right) V(z) \tag{A.16}$$

These coupled linear differential equations can be uncoupled (A.18) by taking the derivative of (A.13) with respect to the time and substituting this expression in equation (A.12) for the voltage, and vice versa for the current. All constant parameters are combined in one constant γ (A.17) and consists of a real part, which is called the attenuation constant and has units of [Np/m], and a complex part, which is called the phase constant and has units of [rad/m].

$$\gamma = \alpha + j\beta = \sqrt{(R' + j\omega L')(G' + j\omega C')} \tag{A.17}$$

$$\frac{d^2V(z)}{dz^2} - \gamma^2 V(z) = 0 \quad \text{and} \quad \frac{d^2I(z)}{dz^2} - \gamma^2 I(z) = 0 \tag{A.18}$$

The equations in (A.18) are very similar to the wave equations for the electric and magnetic field. By also introducing the phasor notation for the electric and magnetic field, these wave equations are equivalent to the equations given in (A.18) with the next relationship between γ, ε and μ occurring:

$$-\gamma^2 = \varepsilon\mu\omega^2 \Leftrightarrow \alpha = 0 \quad \text{and} \quad \beta = \omega\sqrt{\varepsilon\mu} \tag{A.19}$$

Hence, the solutions of the second-order linear differential equations for $V(z)$ and $I(z)$ are of the same form as the solutions for the electric and magnetic field. These are standing waves caused by the interference of a forward-propagating and back-propagating wave, respectively denoted by + and -.

$$V(z) = V_0^+ e^{-\gamma z} + V_0^- e^{\gamma z} \quad \text{and} \quad I(z) = I_0^+ e^{-\gamma z} + I_0^- e^{\gamma z} \tag{A.20}$$

The characteristic impedance Z_0 is defined as the ratio of the coefficients of the forward-propagating voltage and current wave.

$$Z_0 = \frac{V_0^+}{I_0^+} = -\frac{V_0^-}{I_0^-} = \sqrt{\frac{R' + j\omega L'}{G' + j\omega C'}} \tag{A.21}$$

Finally, the time- and position-dependent expressions for the voltage and current can be given.

$$v(z,t) = V_0^+ e^{-\alpha z} \cos(\omega t - \beta z) + V_0^- e^{\alpha z} \cos(\omega t + \beta z) \tag{A.22}$$

$$i(z,t) = \frac{1}{Z_0} \left[V_0^+ e^{-\alpha z} \cos(\omega t - \beta z) - V_0^- e^{\alpha z} \cos(\omega t + \beta z) \right] \tag{A.23}$$

B.   Additional figures to chapter 6

B.1. Element mappings of the sensor's cross-section obtained by EDS

26% C K	
11% O K	
3% MgK	
3% AlK	
4% SiK	
26% ClK	
10% CaK	
6% TiK	
11% CuK	
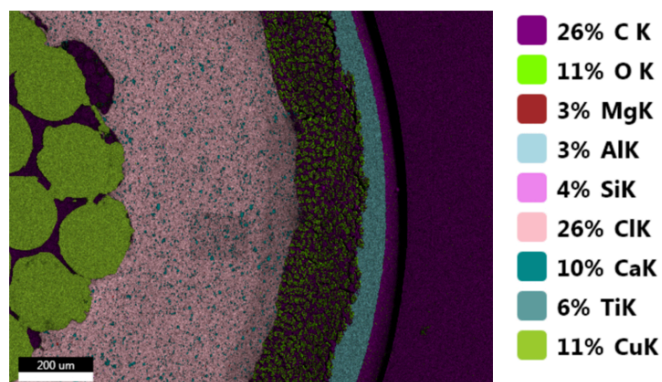
Figure B.1. Elemental mapping of the cross-section of the viscose-based water sensor obtained by EDS.

30% C K	
10% O K	
6% F K	
25% SiK	
5% S K	
5% SbL	
8% TiK	
9% CuK	
2% ZnK	
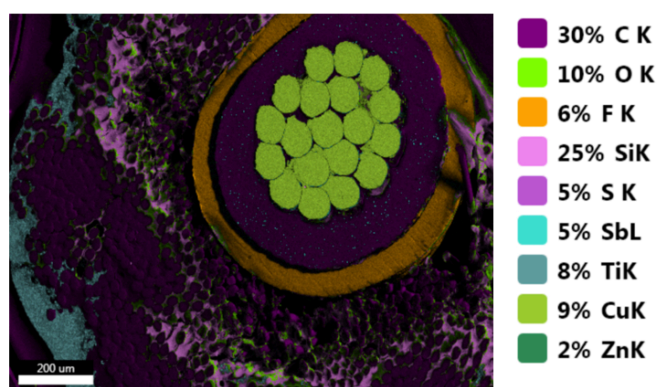
Figure B.2. Elemental mapping of the cross-section of the nylon-based water sensor obtained by EDS.

47% C K	
12% O K	
4% MgK	
32% ClK	
5% CaK	
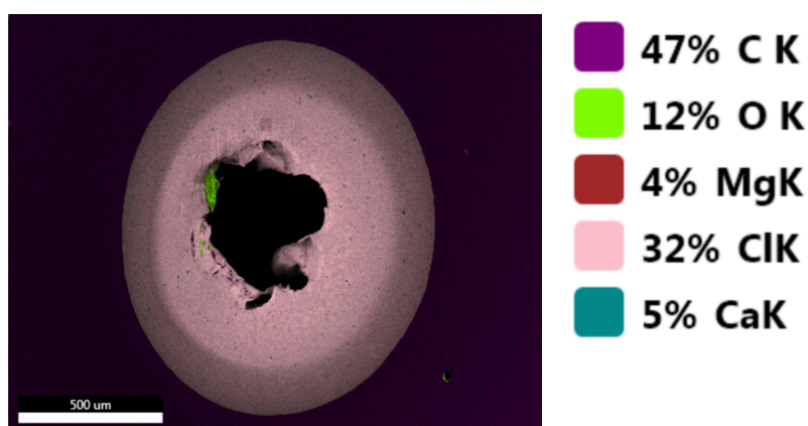
Figure B.3. Elemental mapping of the cross-section of the outer conductor obtained by EDS. The bundle of copper wires wear out during grinding and polishing and hence, was not seen.

B.2. Fitted differential TDR voltage reflectogram for the leakage spots at a distance of 2.40 m and 5 m from the sensor entrance
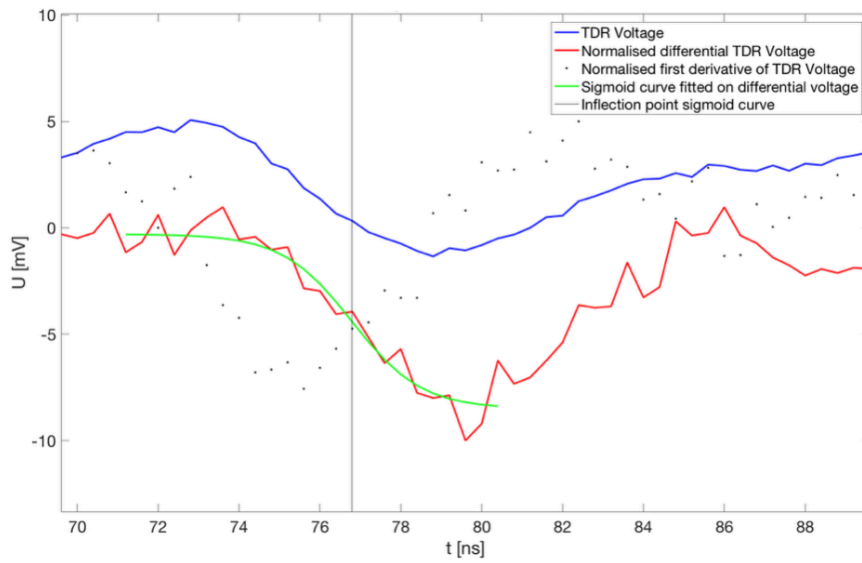
Figure B.4. Fitted differential TDR voltage reflectogram for the leakage spot at a distance of 2.40 m from the sensor entrance.
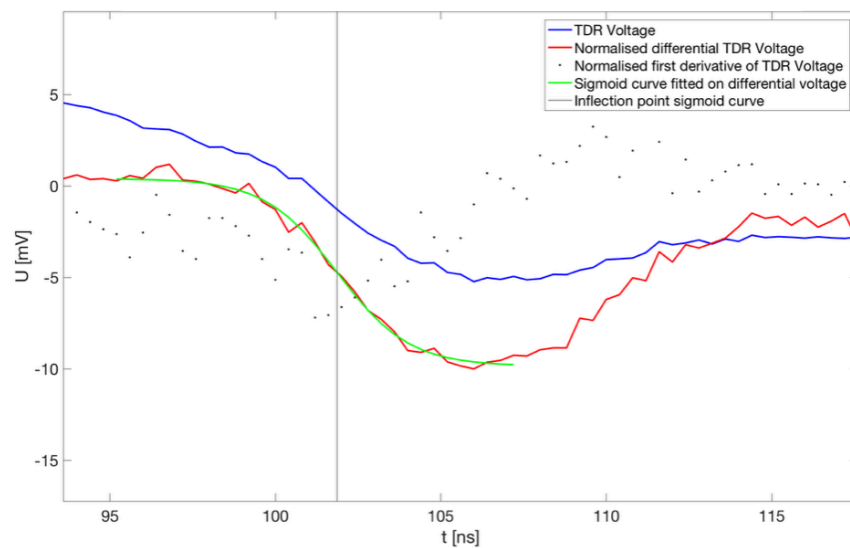
Figure B.5. Fitted differential TDR voltage reflectogram for the leakage spot at a distance of 5 m from the sensor entrance.

C.   Additional figures l to chapter 8

C.1. Literature data on the conductivity of PVA and PVC
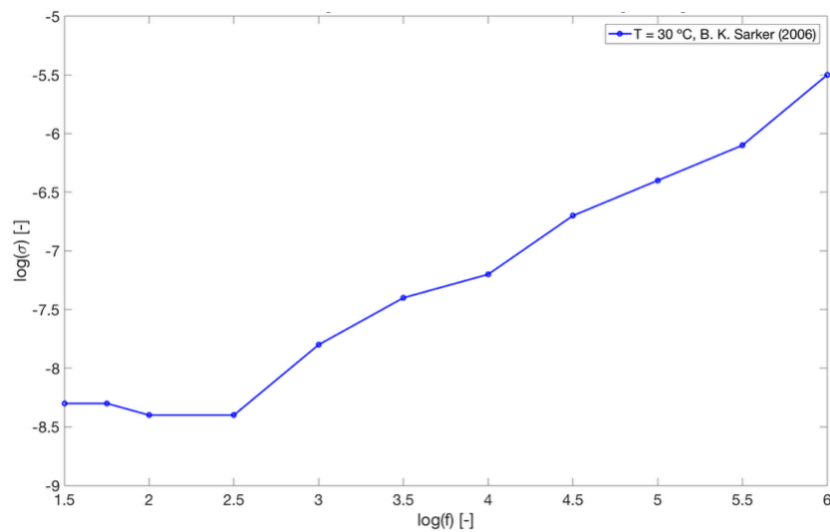
Figure C.1. Frequency dependence of the conductivity of PVC (B. K. Sarker, 2006).

\
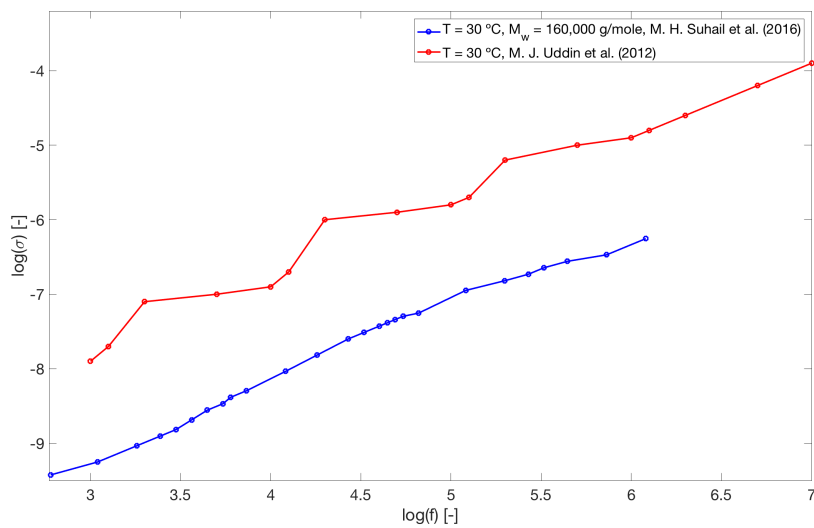
Figure C.2. Frequency dependence of the conductivity of PVA (M. H. Suhail, 2016; M. J. Uddin, 2012).

C.2. Literature data on the permittivity of PVC and CaCO₃
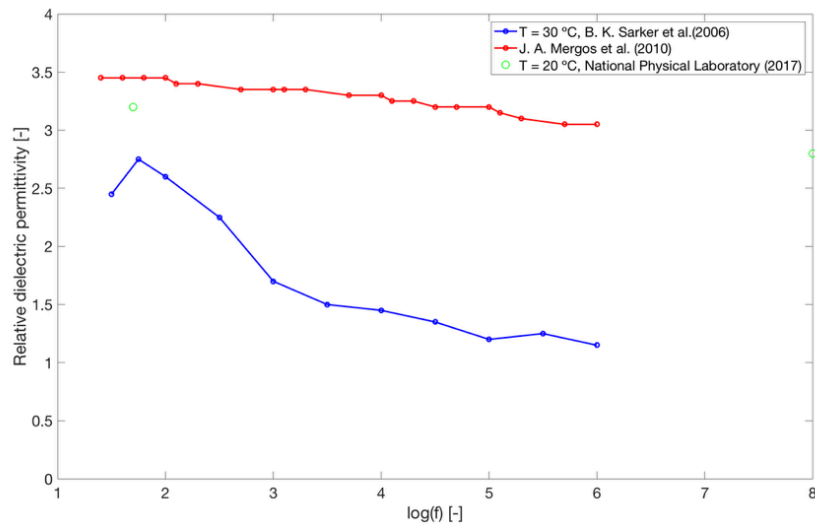
Figure C.3. Frequency dependence of the relative dielectric constant of PVC (J. A. Mergos, 2005; National Physical Laboratory, 2017; B. K. Sarker, 2006).
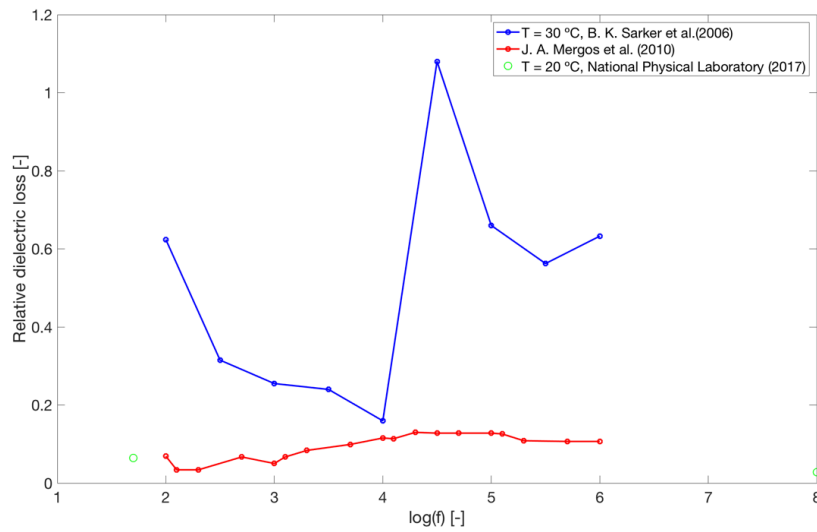
Figure C.4. Frequency dependence of the relative dielectric loss of PVC (J. A. Mergos, 2005; National Physical Laboratory, 2017; B. K. Sarker, 2006).
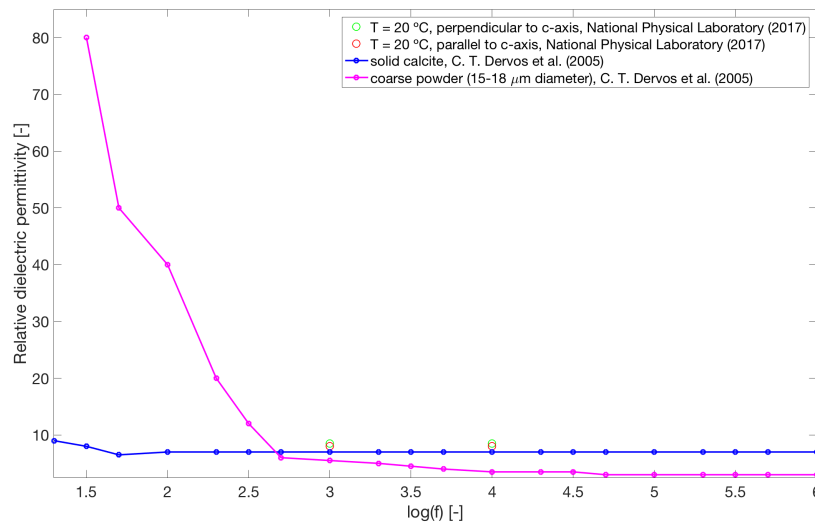
Figure C.5. Frequency dependence of the relative dielectric constant of PVC (C. T . Dervos, 2005; National Physical Laboratory, 2017).
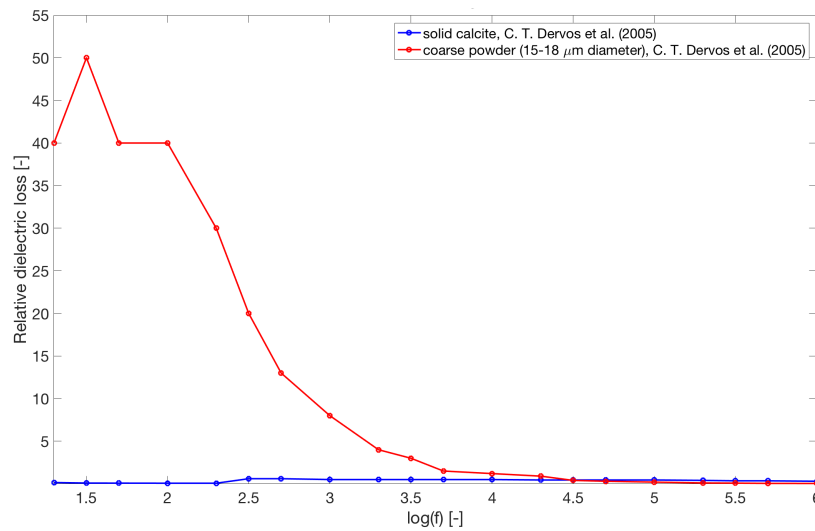
Figure C.6. Frequency dependence of the relative dielectric loss of PVC (C. T . Dervos, 2005; National Physical Laboratory, 2017).

C.3. Literature data on phase diagram of the binary PVA/water system
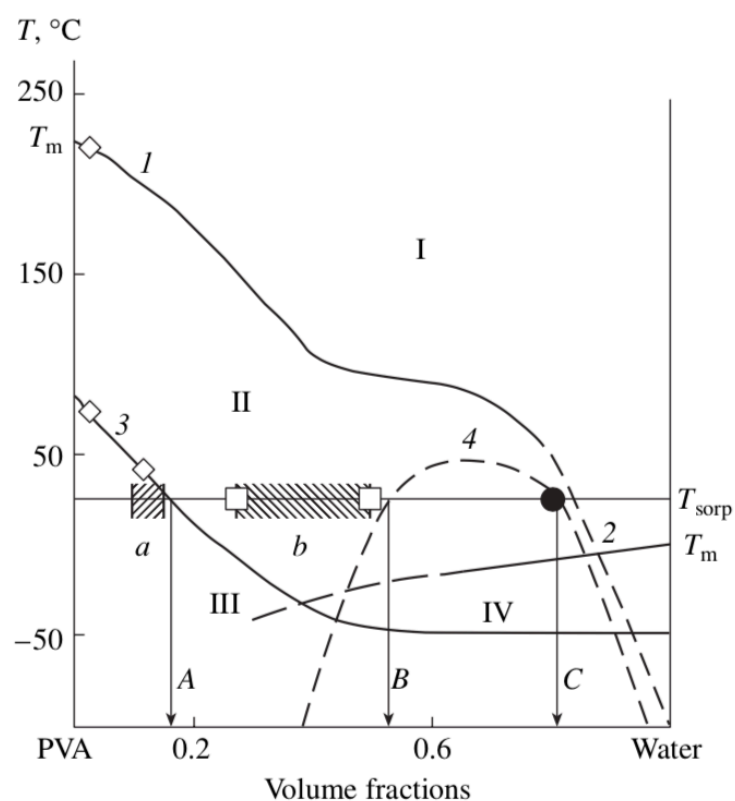
Figure C.7. Phase diagram for the binary water/PVA system. (C. (G. S. Kulagina, 2007). The liquidus line of PVA (1), the liquidus line of water (2), the concentration dependence of the glass-transition temperature (3) and the curve of equilibrium swelling (4) are included.

References

x

| (T. A. Abdel-Baset, 2016) | T. A. Abdel-Baset and A. Hassen (2016). Dielectric relaxation analysis and Ac conductivity of polyvinyl alcohol/polyacrylonitrile film. *Physics B: Condensed Matter*, *499*, 24-28. |

(O. G. Abdullah, 2011)   O. G. Abdullah, S. A. Hussen and A. Alani (2011). Electrical Characterization of Polyvinyl Alcohol Films Doped with Sodium Iodide. *Asian Transactions on Science & Technology*, *1*(4), 1-4.

(Acros Organics, 2018)   Acros Organics (2018). *Poly(vinyl alcohol), 95.5-96.5% hydrolyzed, M.W. approx. 85,000-124,000*.
[12/04/2018, Acros Organics: http://www.acros.com/DesktopModules/Acros_ Search_ Results/ Acros_Search_Results.aspx search_type=CatalogSearch& SearchString=pva].

(Agilent Technologies, 2000)   Agilent Technologies (2000). *Agilent 33250A 80 MHz Function / Arbitrary Waveform Generator*.
[10/02/2018, MTU: http://www.ece.mtu.edu/labs/EElabs/EE3306/ Revisions_2008/agt33250aman.pdf].

(Agilent Technologies, 2017a)   Agilent Technologies (2017). *Agilent Time Domain Reflectometry Theory*.
[07/11/2017, Agilent Technologies: http://literature.cdn.keysight.com/litweb/pdf/ 5966-4855E.pdf].

(Agilent Technologies, 2017b)   Agilent Technolgies (2017). *Agilent High Precision Time Domain Reflectometry*.
[06/11/2017, Agilent Technologies: http://arpg-serv.ing2.uniroma1.it/mostacci/ didattica/lab_meas_high_freq/store/TimeDomainReflectometry/Agilent_ AN1304-7_TDRhighPrecision.pdf].

(E. M. Amin, 2013)   E. M. Amin, N. C. Karmakar, and B. Winther-Jensen (2013). Polyvinyl-Alcohol (Pva)-Based RF Humidity Sensor in Microwave Frequency. *Progress In Electromagnetics Research B*, *54*, 149-166.

(A. Andryieuski, 2015)   A. Andryieuski, S. M. Kuznetsova, S. V. Zhukovsky, Y. S. Kivshar and A. V. Lavrinenko (2015). Water: Promising Opportunities For Tunable All-dielectric Electromagnetic Metamaterials. *Scientific Reports*, *5*, 13535.

(Aquentis, 2017)   Aquentis (2017). *Water Detection Sensing Cable 10 Metres*.
[27/10/2017, Aquentis: http://www.aquentis.com/index.php?route=product/ product&path=59_70&product_ id=98].

(Aquilar Ltd., 2008)   Aquilar Ltd (2008). *TraceTek Leak Detection Systems.*
[26/10/2017, Aquilar Ltd.: http://tracetek.uk.com.php].

(Aquilar Ltd., 2017)   Aquilar Ltd (2017). *Aquilar leak detection solutions*.
[27/10/2017, Aquilar Ltd.: http://www.aquilar.co.uk].

(J. Behari, 2005)   J. Behari (2005). *Microwave Dielectric Behavior of Wet Soils*. New Delhi, India: Anamaya Publishers.

(L. Bengtsson, 2017)   L. Bengtsson (2017). *New design ideas for TDR-based liquid level detectors*. Paper presented at Instrumentation and Measurement Technology Conference (I2MTC) on 22-25/05/2017 in Turin, Italy.

(E. Bogati, 2011)   E. Bogatin (2011). Esssential Principles of Signal Integrity. *IEEE Microwave Magazine, 12*(5), 34-41.

(J. Borch, 2001)   J. Borch, M. B. Lyne, R. E. Mark and C. Habeger (2001). *Handbook of Physical Testing of Paper*. Boca Raton, USA: CRC Press.

(A. Boudenne, 2005)	A. Boudenne, L. Ibos, M.Fois, J. C. Majesté and E. Géhin (2005). Electrical and thermal behavior of polypropylene filled with copper particles. *Composites Part A: Applied Science and Manufacturing*, *36*(11), 1545-1556.
(J. A. Briggs, 2017)	J. A. Briggs et al. (2017). Temperature-dependent optical properties of titanium nitride. *Applied Physics Letters*, *110*.
(K. W. Burkes, 2015)	K. W. Burkes, E. B. Makram and R. Hadidi (2015). Water Tree Detection in Underground Cables Using Time Domain Reflectometry. *IEEE Power and Energy Technology Systems Journal*, *2*(2), 53-62.
(Y. Cai, 2010)	Y. Cai, Z. Wang, R. Dias and D. Goyal (2010). *Electro Optical Terahertz Pulse Reflectometry - an Innovative Fault Isolation Tool*. Paper presented at 60th Electronic Components and Technology Conference (ECTC) on 01-04/06/2010 in Las Vegas, USA.
(A. Cataldo, 2011)	A. Cataldo, E. De Benedetto and G. Cannazza (2011). *Broadband Reflectometry for Enhanced Diagnostics and Monitoring Applications*. Heidelberg, Germany: Springer-Verlag.
(A. Cataldo, 2012)	A. Cataldo, E. De Benedetto, G. Cannazza and N. Giaquinto (2012). *Performance evaluation of a TDR-based system for detection of leaks in buried pipes*. Presentation at Instrumentation and Measurement Technology Conference (I2MTC) on 13-16/05/2012 in Graz, Austria.
(A. Cataldo, 2017a)	A. Cataldo, E. De Benedetto, C. Huebner and D. Trebbels (2017). TDR application for moisture content estimation in agri-food materials. *IEEE Instrumentation and Measurement Society*, *20*(3), 26-31.
(A. Cataldo, 2017b)	A. Cataldo, E. De Benedetto, G. Cannazza, E. Piuzzi and E. Pittella (2017). TDR-Based Measurements of Water Content in Construction Materials for In-the-Field Use and Calibration. *IEEE Instrumentation and Measurement Society*, *99*, 1-8.
(M. Cauwe, 2006)	M. Cauwe, J. De Baets and A. Van Calster (2006). *High-frequency Characterization of Embedded Active Components in Printed Circuit Boards*. Paper presented at 8th Electronics Packaging Technology Conference (EPTC) on 06-08/12/2006 in Singapore, Singapore.
(P. Chakraborty, 2017)	P. Chakraborty, N. B. Gundrati, C. Zhou and D. D. L. Chung (2017). Effect of stress on the capacitance and electric permittivity of three-dimensionally printed polymer, with relevance to capacitance-based stress monitoring. *Sensors and Actuators A: Physical*, *263*, 380-385.
(CheapRope, 2018)	CheapRope (2018). *2mm Braided Nylon Cord*. [17/04/2018, CheapRope: https://www.cheaprope.co.uk/braided-nylon-cord p-779.html].
(M. K. Chen, 2006)	M. K. Chen, C. C. Tai and Y. J. Huang (2006). Nondestructive Analysis of Interconnection in Two-Die BGA Using TDR. *IEEE Transactions on Instrumentation and Measurement*, *55*(2), 400-405.
(B. E. Clothier, 1994)	B. E. Clothier and S. R. Green (1994). Rootzone processes and the efficient use of irrigation water. *Agricultural Water Management*, *25*(1), 1-12.
(Conrad, 2018)	Conrad (2018). *BELI-BECO M 20 Koperdraad gelakt 100 m*. [23/03/2018, Conrad: http://www.produktinfo.conrad.com/datenblaetter/ 1400000-1499999/001437325-da-01-de-KUPFERLACKDRAHT_LOETBAR.pdf].
(J. D. Cooper, 2016)	J. D. Cooper (2016). *Soil Water Measurement: A Practical Handbook*. Chichester, UK: John Wiley & Sons.
(S. Corey, 2000)	S. Corey and D. Smolyansky (2000). *Electrical Package Characterization Using Differential TDR Techniques*. Paper presented at 9th IEEE Topical Meeting on Electrical Performance of Electronic Packaging on 23-25/10/2000 in Scottsdale, United States.
(R. P. Cruz, 2004)	R. P. Cruz (2004). *Flip Chip Advanced Package Solder Joint Embrittlement Fault Isolation Using TDR*. Paper presented at 5th International Symposium on Quality Electronic Design on 22-24/03/2004 in San Jose, United States.

(G. M. D'Aucelli, 2017)	G. M. D'Aucelli, E. Piuzzi and A. Cataldo (2017). *Transmission Line Simulator for TDR-Based Measurements*. Presentation at Instrumentation and Measurement Technology Conference (I2MTC) on 22-25/05/2017 in Turin, Italy.
(F. N. Dalton, 1986)	F. N. Dalton and M. T. Van Genuchten (1986). The time-domain reflectometry method for measuring soil water content and salinity. *Geoderma*, *38*(1-4), 237-250.
(A. Dawson, 2008)	A. Dawson (2008). *Water in Road Structures: Movement, Drainage & Effects*. Berlin, Germany: Springer Science + Business Media.
(Electronic Device Failure Analysis Society, 2004)	Electronic Device Failure Analysis Society (2004). *Microelectronics Failure Analysis.* Materials Park, USA: ASM International.
(G. De Lescluze, 2017)	G. De Lescluze (2017). *Phase diagram for a ternary mixture of conducting ceramics and water showing percolation conductivity in a hydrophilic matrix* [pdf]. Leuven: KU Leuven.
(R. Degraeve, 1998)	R. Degraeve et al. (1998). New Insights in the Relation Between Electron Trap Generation and the Statistical Properties of Oxide Breakdown. *IEEE Transactions on Electron Devices*, *45*(4), 904-911.
(R. Degraeve, 2004)	R. Degraeve et al. (2004) Analytical Percolation Model for Predicting Anomalous Charge Loss in Flash Memories. *IEEE Transactions on Electron Devices*, *51*(9), 1392-1400.
(C. T . Dervos, 2005)	C. T. Dervos, J. A. Mergos and A. A. Losfides (2005). Characterization of insulating particles by dielectric spectroscopy: Case study for $CaCO_3$ powders. *Materials Letters*, *59*(22), 2842-2849.
(H. T. Devarajulu, 2017)	H. T. Devarajulu, M. Xie, C. Hu, D. Goyal, E. Kato and M. Hashimoto (2017). *Improving Terahertz signal travel distance for fault isolation*. Paper presented at IEEE 67th Electronic Components and Technology Conference on 30/05-02/06/2017 in Orlando, USA.
(EEWeb, 2017)	EEWeb (2017). *Twisted Pair*. [17/12/2017, EEWeb: https://www.eeweb.com/tools/twisted-pair].
(Engineering Toolbox, 2018a)	Engineering Toolbox (2018), *Permeability*. [15/03/2018, Engineering Toolbox: https://www.engineeringtoolbox.com/permeability-d_1923.html].
(Engineering Toolbox, 2018b)	Engineering Toolbox (2018). *Vapor Pressure common Liquids*. [18/05/2018, Engineering Toolbox: hhttps://www.engineeringtoolbox.com/vapor-pressure-d_312.html].
(Farnell, 2014)	Farnell (2014). *MC6A-1/0.6T2-RD-100 - Wire, Solid, Equipment, PVC, Red, 23 AWG, 0.28 mm², 328 ft, 100 m*. [22/03/2018, Farnell: http://www.farnell.com/datasheets/1863191.pdf?_ga=2.115750850. 535410024.1521707470—1220639252.1521707470].
(F. Farahmand, 2012a)	F. Farahmand (2012). *Introduction to transmission lines, part I* [ppt]. Rohnert Park, USA: Sonoma State University.
(F. Farahmand, 2012b)	F. Farahmand (2012). *Introduction to transmission lines, part II* [ppt]. Rohnert Park, USA: Sonoma State University.
(Federal public Service Mobility and Transport - Air Accident Investigation Unit, 2012)	Federal public Service Mobility and Transport - Air Accident Investigation Unit (2012). *Incident to Avro RJ100 registered OO-DWK on 27 October 2009.* Brussel
(P. A. Ferré, 1998)	P. A. Ferré, J. D. Redman and D. L. Rudolph (1998). The dependence of the electrical conductivity measured by time domain reflectometry on the water content of a sand. *Water Resources Research*, *34*(5), 1207-1213.
(P. Fornasini, 2008)	P. Fornasini (2008). *The Uncertainty in Physical Measurements*. New York, USA: Springer Science + Business Media.

(N. Giaquinto, 2015)	N. Giaquinto et al. (2015). *Accuracy Analysis in the Estimation of ToF of TDR Signals*. Paper presented at Instrumentation and Measurement Technology Conference (I2MTC) on 11-14/05/2017 in Pisa, Italy.
(J. L. Graham, 2006)	J. L. Graham, R. C. Striebich, K. J. Myers, D. K. Minus and W. E. Harrison (2006). Swelling of Nitrile Rubber by Selected Aromatics Blended in a Synthetic Jet Fuel. *Energy Fuels*, *20*(2), 759-765.
(L. Greenspan, 1977)	L. Greenspan (1977). Humidity Fixed Points of Binary Saturated Aqueous Solutions. *Journal of research of the National Bureau of Standards - A. Physics and Chemistry*, *81*(1), 89-96.
(HW Group, 2017)	HW group (2017). *HWg-WLD: Water leak detector for a 2D area*. [27/10/2017, HW group: https://www.hw-group.com/products/HWg-WLD/WLD_water_leak_detection_ en.html].
(S. V. Gupta, 2013)	S. V. Gupta (2013). *Measurement Uncertainties*. Heidelberg, Germany: Springer.
(S. H. Hall, 2009)	S. H. Hall and H. L. Heck (2009). *Advanced Signal Integrity for High-Speed Digital Designs*. Hoboken, USA: John Wiley & Sons.
(H. M. Hashemian, 2006).	H. M. Hashemian (2006). *Maintenance of Process Instrumentation in Nuclear Power Plants*. Berlin, Germany: Springer-Verlag.
(HC Starck, 2018)	HC Starck (2018). *Titaniumcarbonitride*. [12/04/2018, HC Starck: https://www.hcstarck.com/titanium_carbonitride].
(Helukabel, 2018)	Helukabel (2018). *Formulas of electrotechnic and electronic*. [13/04/2018, Helukabel: http://www.helukabel.com/media/publication/de/cor_docs/ qt_23/QT_COR-DOCS_ X_107_Formulas_of_electrotechnic_and_electronic.pdf].
(R. M. Hodge, 1996)	R. M. Hodge, G. H. Edward and G. P. Simon (1996). Water absorption and states of water in semicrystalline poly (vinyl alcohol) films. *Polymer*, *37*(8), 1371-1376.
(Holland Shielding Systems BV, 2018)	Holland Shielding Systems BV (2018). *5750-P series - Elektrisch geleidende rubber profielen*. [21/03/2018, Holland Shielding Systems BV: https://hollandshielding.nl/P-Elektrisch-geleidende-rubber-profielen].
(C. W. Hsue, 1997)	C. W. Hsue and T. W. Pan (1997). Reconstruction of Nonuniform Transmission Lines from Time-Domain Reflectometry. *IEEE Transactions on Microwave Theory and Techniques, 45*(1), 32-38.
(L. Huakang, 2017)	L. Huakang, L. Kehong, J. Qiu and G. Liu (2017). Analysis of time domain reflectometry for crack intermittency detection in circuit board. *Structural Control Health Monitoring*, *21*(6), 1030-1042.
(Huber+Suhner, 2007)	Huber+Suhner (2007). *HUBER+SUHNER® DATA SHEET Coaxial Cable: RG_58_C/U*. [18/04/2018, Richardson RFPD: http://www.richardsonrfpd.com/resources/RellDocuments/SYS_25/22510015 _dataSheet.pdf].
(G. Joshi, 2006)	G. Joshi and S. M. Pawde (2006). Effect of molecular weight on dielectric properties of polyvinyl alcohol films. *Applied Polymer Science*, *102*(2), 1014-1016.
(S. B. Jones, 2002)	S. B. Jones, J. M. Wraith and D. Or (2002). Time domain reflectometry measurement principles and applications. *Hydrological Processes*, *16*(1), 141-153.
(D. H. Jung, 2013)	D. H. Jung, et al. (2013). *Fault Isolation of Short Defect in Through Silicon Via (TSV) based 3D-IC*. Paper presented at International 3D Systems Integration Conference (3DIC) on 02-04/10/2013 at San Jose, United States.
(KAB Electro-Acoustics, 2018)	KAB Electro-Acoustics (2018). *Dielectric Constants of Common Materials*. [05/05/2018, KAB Electro-Acoustics: https://www.kabusa.com/Dilectric-Constants.pdf].

(Kabel Schmidt, 2018)   Kabel Schmidt. (2018). *Einadrig Textilumfl. Leitung 1x0,75qmm Gold*.
                             [12/03/2018, Kabel Schmidt: https://www.kabel-schmidt.de/Stoffkabel-230V/
                             Textilumflochtene-Einzelader-leitung/Einadrig-textilumfl-Leitung-1x0-75qmm-
                             gold.html].

(H. Kaden, 1959)   H. Kaden (1959). *Wirbelströme und Schirmung in der Nachrichtentechnik*. Berlin,
                             Germany: Springer-Verlag.

(Key Publishing Ltd., 2005) Key Publishing Ltd. (2005). Finding Fuel Leaks. *Airports International, 38*(2), 35.

(Keysight Technologies, 2017) Keysight Technologies (2017). *Time Domain Analysis Using a Network Analyzer*.
                             [08/11/2017, Keysight Technologies: http://literature.cdn.keysight.com/litweb/
                             pdf/5989-5723EN.pdf].

(K. K. Kim, 2015)   K. K. Kim et al. (2015). Highly sensitive and stretchable multidimensional strain
                             sensor with prestrained anisotropic metal nanowire percolation networks. *Nano
                             Letters*, *15*(8), 5240-5247.

(D. P. Kothari, 2009)   D. P. Kothari and I. J. Nagreth (2009). *Modern Power System Analysis*. New
                             Delhi, India: Tata McGraw-Hill.

(E. Kowalczuk, 2014)   E. Kowalczuk, A. Bhattacharya, K. C. Lee, J. alton, M. Igarashi and S. Barbeau
                             (2014). *Fault localisation of defects using Electro Optical Terahertz Pulse
                             Reflectometry and 3D EM modelling with Virtual Known Good Device*. Paper
                             presented at International 3D Systems Integration Conference (3DIC) on
                             01-03/12/2014 in Kinsdale, Ireland.

(F. Kremer, 2003)   F. Kremer and A. Schönhals (2003). *Broadband Dielectric Spectroscopy*. Berlin,
                             Germany: Springer-Verlag.

(G. S. Kulagina, 2007)   G. S. Kulagina, A. E. Chalykh, V. K. gerasimov, K. A. Chalykh and T. P. Purvaeva
                             (2007). Sorption of Water by Poly(vinyl alcohol). *Polymer Science A*, *49*(4),
                             654-662.

(K. Kupfer, 2005)   K. Kupfer (2005). *Electromagnetic Aquametry*. Heidelberg, Germany: Springer-
                             Verlag.

(K. Kurokawa, 1965)   K. Kurokawa (1965). Power Waves and the Scattering Matrix. *IEEE Transactions
                             on Microwave Theory and Techniques, 13*(2), 194-202.

(K. C. Lee, 2015)   K. C. Lee, J. Alton and M. Igarashi (2015). *Fast Feature Based Non-Destructive
                             Fault Isolation in 3D IC Packages Utilizing Virtual Known Good Device*. Paper
                             presented at 41st International Symposium for Testing and Failure Analysis on
                             1-5/11/2015 in Portland, USA.

(J. Lekner, 2016)   J. Lekner (2016). *Theory of Reflection*. Cham, Switzerland: Springer International
                             Publishing Switzerland.

(T. Li, 2013)   T. Li, X. Dong, C. C. Chan, K. Ni, S. Zhang and P. P. Shum (2013). Humidity
                             Sensor With a PVA-Coated Photonic Crystal Fiber Interferometer. *IEEE Sensors
                             Journal*, *13*(6), 2214-2216.

(Y. Li, 2012)   Y. Li, P. Wagenaars, P. A. A. F. Wouters, P. C. J. M. van der Wielen, and E. F.
                             Steennis (2012). Power cable joint model: Based on lumped components and
                             cascaded transmission line approach. *International Journal on Electrical
                             Engineering and Informatics, 4*(4), 536-552.

(D. R. Lide, 2003)   D. R. Lide (2003). *CRC Handbook of Chemistry and Physics.* Boca Raton, USA:
                             CRC Press.

(S. Lilley, 2015)   S. Lilley (2015). *Escape to Failure - The Qantas Flight 32 Uncontained Engine
                             Failure.*
                             [12/10/2017, NASA Safety Center: https://nsc.nasa.gov/SFCS/
                             SystemFailureCaseStudy/Details/154].

(L. T. Lim, 1999)   L. T. Lim, I. J. Britt and M. A. Tung (1999). Sorption and Transport of Water Vapor
                             in Nylon 6,6 Film. *Journal of Applied Polymer Science*, *71*(2), 197–206.

(C. P. Lin, 2015)   C. P. Lin, S. H. Tang, C. H. Lin and C. C. Chung (2015). An Improved Modeling of TDR Signal Propagation for Measuring Complex Dielectric Permittivity. *Journal of Earth Science*, *26*(6), 827-834.

(C. P. Lin, 2017)   C. P. Lin, Y. J. Ngui and C. H. Lin (2017). A novel TDR signal processing technique for measuring apparent dielectric spectrum. *Measurement Science and Technology*, *28*(1), 015501.

(D. Lu, 2014)   D. Lu, Y. Zheng, A. Penirschke, A. Wiens, W. Hu and R. Jakoby (2014). *Humidity Dependent Permittivity Characterization of Polyvinyl-Alcohol Film and its Application in Relative Humidity RF Sensor*. Paper presented at 44th European Microwave Conference (EuMC) on 06-09/10/2014 in Rome, Italy.

(T. Makarova, 2004)   T. Makarova (2004). Magnetic Properties of Carbon Structures. *Semiconductors*, *38*(6), 615-638.

(W. Martienssen, 2005)   W. Martienssen and H. Warlimont (2005). *Springer Handbook of Condensed Matter and Materials Data*. Heidelberg, Germany: Springer.

(J. Martinez-Vega, 2007)   J. Martinez-Vega (2007). *Dielectric Materials for Electrical Engineering*. Hoboken, USA: John Wiley & Sons.

(Megger, 2013)   Megger (2013). *Fault Finding Solutions*.
                           [22/11/2017, Electrical Engineering Portal: http://electrical-engineering-portal.com/download-center/books-and-guides/power-substations/megger-fault-finding-solutions].

(J. A. Mergos, 2010)   J. A. Mergos, M. D. Athanassopoulou, T. G. Argyropoulos, C. T. Dervos and P. Vassiliou (2010). *The Effect of Accelerated UV-Ageing on the Dielectric Properties of PVC, PTFE and HDPE*. Paper presented at International Conference on Solid Dielectrics on 04-09/07/2010 in Potsdam, Germany.

(S. Miau-Bin, 1990)   S. Miau-Bin (1990). Fracture Monitoring within Concrete Structure by Time Domain Reflectometry. *Engineering Fracture Mechanics*, *35*(1-3), 313-320.

(MOHR, 2017)   MOHR (2017). *Operator's manual: CT100B Series*.
                           [20/02/2018, MOHR: http://www.mohr-engineering.com/tdr-cable-tester-documents-CT100.php].

(F. Muller-Plathe, 1998)   F. Muller-Plathe (1998). Diffusion of Water in Swollen Poly(vinyl alcohol) Membranes Studied by Molecular Dynamics Simulation. *Journal of Membrane Science*, *141*, 147-154.

(Mykin, 2018)   Mykin (2018). *Rubber Chemical Resistance Chart*.
                           [06/05/2018, Mykin Inc.: http://mykin.com/rubber-chemical-resistance-chart-6].

(J. Nagel, 2013)   J. Nagel (2013). *The Beauty of Electromagnetics*.
                           [06/05/2018, J. Nagel: http://www.drjamesnagel.com/EM_Beauty.htm].

(C. W. Nan, 2010)   C. W. Nan, Y. Shen and J. Ma (2010). Physical Properties of Composites Near Percolation. *Annual Review of Materials Research*, *40*, 131-151.

(National Physical Laboratory, 2017)   National Physical Laboratory (2017). Dielectric properties of materials.
                           [23/03/2018, National Physical Laboratory: http://www.kayelaby.npl.co.uk/general_physics/2_6/2_6_5.html].

(Nexans, 2003)   Nexans (2003). *Type ASNE 0261 200°C Operating Temperature*.
                           [12/04/2018, Nexans: http://www.nexans.com/Poland/2007/Aircraft.pdf].

(C. Nohilé, 2008)   C. Nohilé, P. I. Dolez and T. Vu-Khanh (2008). Parameters controlling the swelling of butyl rubber by solvents. J*ournal of Applied Polymer Science*, *110*(6), 3926-3933.

(J. Obrzut, 2006)   J. Obrzut and R. Nozaki (2006). *TDR permittivity measurements of dielectric films*. Paper presented at Instrumentation and Measurement Technology Conference (IMTC) on 24-27/04/2006 in Sorrento, Italy.

(G. Pandey, 2013)	G. Pandey, H. Deffor, E. T. Thostenson and D. Heider (2013). Smart tooling with integrated time domain reflectometry sensing line for non-invasive flow and cure monitoring during composites manufacturing. *Composites A: Applied Science and Manufacturing*, *47*, 102-108.
(T. A. Papadopoulos, 2013)	T. A. Papadopoulos, A. I. Chrysochos and G. K. Papagiannis (2013). Narrowband power line communication: Medium voltage cable modeling and laboratory experimental results. *Electric Power Systems Research*, *102*, 50-60.
(R. Papazyan, 2007)	R. Papazyan, P. Pettersson and D. Pommerenke (2007). Wave Propagation on Power Cables with Special Regard to Metallic Screen Design. *IEEE Transactions on Dielectrics and Electrical Insulation*, *14*(2), 409-416.
(Pasternack, 2018)	Pasternack (2018). *BNC to Banana Adapters*. [18/04/2018, Paternack: https://www.pasternack.com/bnc-to-banana-adapters-category.aspx].
(S. Patrick, 2004)	S. Patrick (2004). PVC Compounds and Processing. *Rapra Review Report*s, *15*(3), 12-27.
(J. O. Payero, 2006)	J. O. Payero, D. D. Tarkalson and S. Irmak (2006). Use of Time Domain Reflectometry for Continuous Monitoring of Nitrate-Nitrogen in Soil and Water. *Applied Engineering in Agriculture*, *22*(5), 689-700.
(Y. Peng, 2013)	Y. Peng, H. Miao and Z. Peng (2013). Development of TiCN-based cermets: Mechanical properties and wear mechanism. *International Journal of Refractory Metals and Hard Materials*, *39*, 78–89.
(Pentair, 2016)	Pentair (2016). *Cables and sensors.* [26/10/2017, Pentair: https://www.pentairthermal.com/products/leak-sensing-systems/cables-and-sensors/].
(R. A. Peterson, 1998)	R. A. Peterson, A. R. Greenberg, L. J. Bond and W. B. Krantz (1998). Use of ultrasonic TDR for real-time noninvasive measurement of compressive strain during membrane compaction. *Desalination*, *2-3*, 115-122.
(H. Pfeiffer, 2012a)	H. Pfeiffer et al. (2012). Liquid detection in confined aircraft structures based on lyotropic percolation thresholds. *Sensors and Actuators B*, *161*(1), 721-798.
(H. Pfeiffer, 2012b)	H. Pfeiffer, P. Heer, H. Sekler, M. Patitsa, I. Pitropakis and M. Wevers (2012). *Structural Health Monitoring in an Operational Airliner: An Intermediate Report on Leakage Monitoring with Percolation Sensors.* Paper presented at 6th European Workshop on Structural Health Monitoring on 04/07/2012 in Dresden, Germany.
(H. Pfeiffer, 2014)	H. Pfeiffer, P. Heer, M. Winkelmans, W. Taza, I. Pitropakis and M. Wevers (2014). Leakage monitoring using peroclation sensors for revealing structural damage in engineering structures. *Structural Control and Health Monitoring*, *21*, 1030-1042.
(H. Pfeiffer, 2017)	H. Pfeiffer (2017). *Aviation science at KU Leuven, an overview on activities, expertises and capabilities.* Paper presented at Flemish Aerospace Group's Technology Day on 23/10/2017 in Leuven, Belgium.
(PIC Wire, 2018)	PIC Wire (2018). *Cable velocity factor*. [18/05/2018, PIC Wire: https://www.picwire.com/technical/tech-papers/velocity-factor].
(I. Pitropakis, 2015)	I. Pitropakis (2015). *Dedicated Solutions for Structural Health Monitoring of Aircraft Components* [pdf]. Leuven: KU Leuven.
(D. Pommerenke, 2002)	D. Pommerenke and S. Sakaguchi (2002). Application of Maxwell Solvers to PD Propagation - Part I: Concepts and Codes. *IEEE Electrical Insulation Magazine*, *18*(5), 15-21.
(QSStudy, 2018)	QSStudy (2018). *Electrical Conductivities of Kerosene*. [05/05/2018, QSStudy: http://www.qsstudy.com/chemistry/electrical-conductivities-of-kerosene].
(Radiodetection, 2017)	Radiodetection (2017). *The ABCs of TDRs*. [08/11/2017, Radiodetection: https://www.radiodetection.com/sites/default/filesTheABCsofTDRsApplication Note.pdf].

(J. Rault, 1995)	J. Rault, R. Gref, Z. H. Ping, Q. T. Nguyen and J. Néel (1995). Glass transition temperature regulation effect in poly(vinyl alcohol) - water system. *Polymer*, *36*(8), 1655-1661.
(Raychem, 2017)	Raychem (2017). *TraceTek Leak Detection Systems - Brochure TT3000 and TT5000.* [27/10/2017, Raychem Ltd.: http://www.etracetek.com/tracetek/environmental_applications/pipeline/hydrocarbon_chemical_systems_with_piping/double_containment/Short%20System/PDF%20Files/TT3000%20and%205000 %20Brochure.pdf].
(Reade, 2018)	Reade (2018). *Magnetic Properties & Susceptibilities (Typical) Chart*. [15/03/2018, Reade: https://www.reade.com/reade-resources/reference-educational/reade-reference-chart-particle-property-briefings/31-magnetic-properties-a-susceptibilities-chart].
(J. Reynaert, 2017)	J. Reynaert - Brussels Airlines (2017). *Research & innovation at Brussels Airlines.* Presentation at Flemish Aerospace Group's Technology Day on 23/10/2017 in Leuven, Belgium.
(N. B. Rithin Kumar, 2013)	N. B. Rithin Kumar, S. Pai, V. Crasta and B. Shreeprakash (2013). *Studies of the effect of nanoparticle dopants and blending of different polymers on Physical, Electrical, Optical and Micro structural properties of PVA - a Review*. Paper presented at International Conference on Advanced Nanomaterials & Emerging Engineering Technologies on 24-26/07/2013 in Chennai, India.
(RLE Technologies, 2017)	RLE Technologies (2017). *Liquid & Water Leak Detection Equipment*. [27/10/2017, RLE Technologies: https://rletech.com].
(D. A. Robertson, 2005a)	D. A. Robinson, D. R. Bolton, P. A. S. Cruickshank and G. M. Smith (2005). *Centimetre resolution time domain reflectometry using ultra-short millimetre wave pulses*. Paper presented at Joint 30th International Conference on Infrared and Millimeter Waves and 13th International Conference on Terahertz Electronics on 19-23/09/2005 in Williamsburg, USA.
(D. A. Robinson, 2005b)	D. A. Robinson, M. G. Schaap, D. Or and S. B. Jones (2005). On the effective measurement frequency of time domain reflectometry in dispersive and nonconductive dielectric materials. *Water Resources Research, 41*(2), W02007.
(D. D. Sandu, 1985)	D. D. Sandu, P. Gasner, O. Rusu and M. G. Serbian (1985). *Complex permittivity evaluation for poly(vinyl alcohol) and poly(methyl methacrilate) at microwave frequencies by a TDR method*. Paper presented at Symposium on Antenna Technology and Applied Electromagnetics on 09-12/08/1998 in Ottowa, Canada.
(B. K. Sarker, 2006)	B. K. Sarker, A. B. M. O. Islam, F. Ahmed and A. H. Bhuiyan (2006). Optical and Dielectric Properties of PVC, PVA and Their Blends. *Polymers & Polymer Composites*, *14*(7), 741-746.
(Sartorius, 2001)	Sartorius (2001). *YDK01,YDK01-0D,YDK01LP - Density Determination Kit*. [02/04/2018, Dublin City University: https://www.dcu.ie/sites/default/files/mechanical_engineering/pdfs/manuals/Density%20Determination%20Kit(a).pdf].
(M. Shafiq, 2013)	M. Shafiq, L. Kutt, F. Mahmood, G. A. Hussain and M. Lehtonen (2013). *An improved technique to determine the wave propagation velocity of medium voltage cables for PD diagnostics* . Paper presented at 12th International Conference on Environment and Electrical Engineering on 05-08/05/2013 in Wroclaw, Poland.
(C. Siegmund, 1999)	C. Siegmund and H. Leuenberger (1999). Percolation theory, conductivity and dissolution of hydrophilic suppository bases (PEG systems). *International Journal of Pharmaceutics*, *189*(2), 187-196.
(A. Sihvola, 2008)	A. Sihvola (2008). *Electromagnetic Mixing Formulas and Applications*. Padstow, UK: TJ International.
(O. Steiner, 1999)	O. Steiner, A. K. Tagantsev, E. L. Colla and N. Setter (1999). Uniaxial Stress Dependence of the Permittivity of Electroceramics. *Journal of the European Ceramic Society*, *19*, 1243-1246.

(R. D. Straw, 2000)   R. D. Straw (2000). *The ARRL Antenna Book*. Newington, USA: American Radio Relay League.

(J. A. Strickland, 1970)   J. A. Strickland (1970). *Time-Domain Reflectometry Measurements.* Beaverton, USA: Tektronix.

(G. Strobl, 2007)   G. Strobl (2007). *The Physics of Polymers.* Heidelberg, Germany: Springer-Verlag.

(C. P. Sugumaran, 2015)   C. P. Sugumaran (2015). *Experimental study on dielectric and mechanical properties of PVC cable insulation with SiO2/ CaCO3 nanofillers*. Paper presented at IEEE Conference on Electrical Insulation and Dielectric Phenomena (CEIDP) on 18-21/10/2015 in Ann Arbor, USA.

(M. H. Suhail, 2016)   M. H. Suhail, M. Ghazi and M. Al-Hamdany (2016). Electrical and Dielectic Properties of PVA: CuI Nanocomposites. *Emerging Research in Management & Technology*, *5*(6), 124-129.

(S. Sun, 2009)   S. Sun et al. (2009). A Novel TDR-Based Coaxial Cable Sensor for Crack/ Strain Sensing in Reinforced Concrete Structures. *IEEE Transactions on Instrumentation and Measurement*, *58*(2), 2714 - 2725.

(S. T. Sundari, 2013)   S. T. Sundari, R. Ramaseshan, F. Jose, S. Dash and A. K. Tyagi (2013). *Temperature dependence of dielectric constants in Titanium Nitride*. [19/03/2018, Cornell University Library: https://arxiv.org/abs/1308.0470].

(A. G. Supri, 2012)   A. G. Supri, S. J. Tan, H. Ismail and P. L. Teh (2012). Enhancing Interfacial Adhesion Performance by Using Poly(vinyl alcohol) in (Low-Density Polyethylene)/Natural Rubber)/(Water Hyacinth Fiber) Composites. *Journal of Vinyl and Additive Technology*, *19*(1), 47-54.

(A. A. Tager, 1971)   A. A. Tager, A. A. Anikeyeva, L. V. Adamova, V. M. Andreyeva, T. A. Kuz'mina and M. V. Tsilipotkina (1971). The effect of temperature on the water solubility of polyvinyl alchohol. *Polymer Science U.S.S.R*, *13*(3), 751-758.

(E. V. Takeshita, 2012)   E. V Takeshita, F. A. Piantola, S. M. A. U. de Souza, R. C. R. Nunes and A. A. U. de Souza (2012). Quantification of styrene-butadiene rubber swelling as a function of the toluene content in gasoline: A new method to detect adulterations in fuels. *Journal of Applied Polymer Science*, *127*(4), 3053-3062.

(W. Tala Taza, 2012)   W. Tala Taza (2012). *Performance of Percolation-Threshold Based Sensors for Detecting Aqueous Liquids* [pdf]. Leuven: KU Leuven.

(M. Y. Tay, 2012)   M. Y. Tay, L. Cao, M. Venkata, L. Tran, W. Donna and W. Qiu (2012). *Advanced Fault Isolation Technique Using Electro-optical Terahertz Pulse Reflectometry*. Paper presented at 19th IEEE International Symposium on Physical and Failure Analysis of Integrated Circuits (IPFA) on 02-06/07/2012 in Singapore, Singapore.

(Tektronix, 2009)   Tektronix (2009). *Test Equipment Solutions Datasheet*. [08/05/2018, Tektronix: http://www.testequipmenthq.com/datasheets/TEKTRONIX-DPO4034-Datasheet.pdf].

(Tektronix, 2017)   Tektronix (2017). *TDR Impedance Measurements: A Foundation for Signal Integrity.* [05/11/2017, Tektronix: www.tek.com/dl/55W_14601_2.pdf].

(TeraView, 2017)   TeraView (2017). *Terahertz Applications*. [15/12/2017, TeraView: http://www.teraview.com/products/thz-reflectometry/index.html].

(TPub, 2017)   TPub (2017). *Standing Waves on a Transmission Line*. [17/12/2017, TPub: http://www.tpub.com/neets/book10/41k.htm].

(C. W. Trueman, 2002)   C. W. Trueman (2002). *User's Guide for Program LAPL*. [06/05/2018, C. W. Trueman, https://users.encs.concordia.ca/~trueman/lapl/index.htm].

(I. Tsuyumoto, 2011)   I. Tsuyumoto and Y. Iida (2011). Percolation-Type Chemical Sensor: Electrical- and Humidity-Sensing Properties of Carbon–Montmorillonite Composites. *International Journal of Applied Ceramic Technology, 8*(4), 793–799.

(TTK, 2017) TTK (2017). *Sense Cables*.
[27/10/2017, TTK: http://www.ttkuk.com].

(True Path Technologies, 2017) True Path Technologies (2017). *WLD Sensing and Conn Cable (water)*.
[27/10/2017, True Path Technologies: http://truepathtechnologies.com/shop/hwgroup-products/wld-sensing-and-conn-cable-water/].

(I. Tsuyumoto, 2011) I. Tsuyumoto, Y. Iida and H. Hori (2011). Gas sensor for volatile organochlorine compounds using percolation conduction of organic montmorillonite-carbon composites. *International Journal of Applied Ceramic Technology*, *8*(6), 1408-1413.

(E. Tuncer, 2002) E. Tuncer, Y. V. Serdyuk and S. M. Gubanski (2002). Dielectric Mixtures: Electrical Properties and Modeling. *IEEE Transactions on Dielectrics and Electrical Insulation*, *9*(5), 809-828.

(M. J. Uddin, 2012) M. J. Uddin, J. Sannigrahi, M. G. Masud, D. Bhadra and B. K. Chaudhuri (2012). High Dielectric Permittivity and Percolative Behavior of Polyvinyl Alcohol/Potassium Dihydrogen Phosphate Composites. *Journal of Applied Polymer Science*, *125*(3), 2363-2370.

(USPTO, 2015) USPTO (2015). *Sensor for detecting liquid spilling*.
[13/12/2017, USPTO: http://patft.uspto.gov/netacgi/nph-Parser?Sect1=PTO1&Sect2=HITOFF&d=PALL&p=1&u=%2 Fnetahtml%2FPTO%2Fsrchnum.htm&r=1&f=G&l=50&s1=8,963,565.PN.&OS=PN/8,963,565&RS=PN/8,963,565].

(E. A. Van Etten, 2014) E. A. Van Etten, E. S. Ximenes, L. T. Tarasconi, I. T. S. Garcia, M. M. C. Forte and H. Boudinov (2014). Insulating characteristics of polyvinyl alcohol for integrated electronics. *Thin Solid Films*, *568*, 111-116.

(D. Vandepitte, 2017) D. Vandepitte (2017). *Aviation research at KU Leuven and future opportunities.* Presentation at Flemish Aerospace Group's Technology Day on 23/10/2017 in Leuven, Belgium.

(C. Vanga Bouanga, 2011) C. Vanga Bouanga, S. Savoie, H. Couderc, M. F. Fréchette and E. David (2011). *The dielectric permittivity of ceramic powders used in composite polymers*. Paper presented at Conference on Electrical Insulation and Dielectric Phenomena (CEIDP) on 16-19/10/2011 in Cancun, Mexico.

(K. Versteele, 2017) K. Versteele - Sabena Aerospace (2017). *Innovation and R&D in MRO.* Presentation at Flemish Aerospace Group's Technology Day on 23/10/2017 in Leuven, Belgium.

(A. Von Hippel, 1954) A. Von Hippel (1954). *Dielectrics and Waves*. Hoboken, USA: John Wiley & Sons.

(Q. Wang, 2014) Q. Wang, F. Zhou, Z. Zhou, L. K. Y. Li and J. Yan (2014). Electrochemical performance of TiCN coatings with low carbon concentration in simulated body fluid. *Surface & Coatings Technology*, *253,*199–204.

(Y. Wang, 2014) Y. Wang, F. Luo, W. Zhou and D. Zhu (2014). Dielectric and electromagnetic wave absorbing properties of TiC/epoxy composites in the GHz range. *Ceramics International*, *7B*, 10749-10754.

(F. Wenzel, 2014) F. Wenzel and J. Zschau (2014). *Early Warning for Geological Disasters Scientific Methods and Current Practice*. Heidelberg, Germany: Springer.

(R. Windey, 2016) R. Windey, M. Wevers, A. Vanaerschot and J. Reynaert (2016). *Corroded floor structure in wet areas of A320 family* [pdf]. Leuven: KU Leuven.

(T. Worzyk, 2009) T. Worzyk (2009). *Submarine Power Cables: Design, Installation, Repair, Environmental Aspects*. Berlin, Germany: Springer-Verlag.

(W. Yuan, 2007) W. Yuan, W. Zhu, P. Win, C. K. Wang, H. B. Tan and A. Y. S. Sun (2007). *Packaging Failure Isolation with Time-Domain Reflectometry (TDR) for Advanced BGA Packages*. Paper presented at 8th International Conference on Electronic Packaging Technology on 14-17/08/2007 in Shangai, China.

(K. P. Yoo, 2010) K. P. Yoo, L. T. Lim, N. K. Min, M. J. Lee, C. J. Lee and C. W. Park (2010). Novel resistive-type humidity sensor based on multiwall carbon nanotube/polyimide composite films. *Sensors and Actuators B: Chemical*, *45*(1), 120-125.

(X. Zeng, 2007)   X. Zeng, J. He, M. Wang and M. Abdulla (2007). New Closed-Form Formula for Series Inductance and Shunt Capacitance Based on Measured TDR Impedance Profile. *IEEE Microwave Wireless Components Letters*, *17*(11), 781-783.